Data-Independent Acquisition Mass Spectrometry Measurement of Protein Networks in the Aging Human Lens and Lens Influx Pathways

By

Lee Stevenson Cantrell

Dissertation
Submitted to the Faculty of the
Graduate School of Vanderbilt University
in partial fulfillment of the requirements
for the degree of

DOCTOR OF PHILOSOPHY

In

Chemical & Physical Biology

May 12, 2023

Nashville, Tennessee

Approved:

Kevin L. Schey, Ph.D.
Richard M. Caprioli, Ph.D.
Renã A. S. Robinson, Ph.D.
Ken S. Lau, Ph.D.
Hassane S. Mchaourab, PhD.

ACKNOWLEDGEMENTS

This work would not have been possible without the financial support of the Vanderbilt Biomedical Research Education and Training program, the Chemical-Biology Interface Pre-Doctoral Training Grant through the National Institutes of Health, the National Science Foundation Graduate Research Fellowship, the Vanderbilt University Graduate School, the American Society for Mass Spectrometry, and the National Association for Eye Research. I am especially indebted to Dr. Kevin Schey and Dr. Zhen Wang for ongoing support in technical, biological, and professional development in support of my career goals.

I am grateful for all members of the Schey research group who provided thoughtful conversation and a supportive work environment through my training. Each of the members of my Dissertation Committee has provided extensive professional guidance and taught me a great deal about research as I have progressed through my training. I would especially like to thank Dr. Renã Robinson, the chair of my committee. In addition to advocating for the development of my research, she has consistently supported my development towards a career in mass spectrometry proteomics. I wish to acknowledge students around me who have championed successes and come together in difficult times. I also wish to acknowledge the late Jorge Bahena, a friend and fellow pre-doctoral trainee who exemplified strength in difficult projects and life circumstances.

Above all, I could not complete this Dissertation project without the support of my family. I would like to thank my parents and brother who supported my decision to move across the country to continue my studies, celebrated my successes with me, and provided a sounding board on the bad days. Most importantly, I wish to thank my fiancé, Chloe, who has supported the long hours pipetting, coding, and writing as I worked towards this project's completion. Without her consistent love, presence, and support, this work may never have been completed.

TABLE OF CONTENTS

LIST OF TABLES

LIST OF FIGURES

ABBREVIATIONS

AGC	Active Gain Control
ARNC	Age Related Nuclear Cataract
ARVCF	Armadillo Repeated Protein in Velio Cardio Facial syndrome
ASCT2	Neutral Amino Acid Transporter B(0)
AQP	Aquaporin
BASP1	Brain Acid Soluble Protein 1
BCA	Bicinchoninic Acid
BMC	Basal Membrane Complex
BRP	Basic Reverse Phase
BSA	Bovine Serum Albumin
CaM	Calmodulin
CAPN3	Calpain-3
CASI	Continuous Accumulation of Selected Ions
CDH2	N-Cadherin
CID	Collision Induced Dissociation
CLIC5	Chloride Intracellular Channel Protein 5
CODEX	Co-detection by imaging
CRYAA	Alpha-A Crystallin
CRYAB	Alpha-B Crystallin
CRYB	Beta Crystallin
CRYG	Gamma Crystallin
CTN	Catenin
Cx	Connexin
DDA	Data-Dependent Acquisition
DHA	Dehydroalanine (chapter 1) or Dehydroascorbic Acid (chapter 5)
DHB	Dehydrobutyrine
DIA	Data-Independent Acquisition
EAAT	Excitatory Amino Acid Transporters
ECD	Electron Capture Dissociation
ESI	Electrospray Ionization
FAIMS	Field Asymmetric Ion Mobility Spectrometry
FDR	False Discovery Rate
FT-ICR	Fourier Transform-Ion Cyclotron Resonance
GCLC	Glutamate Cysteine Ligase Catalytic Subunit
GGCT	Gammaglutamyl Cycloransferase
GPF	Gas-Phase Fractionated
GJA	Gap Junction Alpha
GLUT	Facilitative Glucose Transporter
GLYT	Sodium- and Chloride-Dependent Glycine Transporter
GRIFIN	Galectin-Related-Inter-Fiber-Protein
GRIN	Gradient of Refraction Index
GSEA	Gene Set Enrichment Analysis
GSH	Glutathione
HCD	Higher Energy Collision Induced Dissociation
HPLC	High-Performance Liquid Chromatography
HSP	Heat Shock Protein
sHSP	Small Heat Shock Protein
IAA	Iodoacetamide

IIT	Ion Injection Time
IMS	Imaging Mass Spectrometry
LC	Liquid Chromatography
LCM	Laser Capture Microdissection
LDHAL6B	L-Lactate Dehydrogenase
LTQ	Linear Trapping Quadrupole
MCS	Microcirculation System
MIMS	Multi-Isotope Imaging Mass Spectrometry
MIP	Major Intrinsic Protein (Aquaporin 0)
MRI	Magnetic Resonance Imaging
MRP	Multidrug Resistant Protein
MS	Mass Spectrometry
MS/MS	Tandem Mass Spectrometry
MuDPIT	Multi-Dimensional Protein Identification Technology
NaDC3	Sodium-Dependent Dicarboxylate Transporter 3
NADPH	Nicotinamide Adenine Dinucleotide Phosphate
nanoPOTS	nanodroplet Processing in One pot for Trace Samples
NCE	Normalized Collision Energy
OAT	Organic Anion Transporter
OFZ	Organelle Free Zone
PASEF	Parallel-Accumulation Serial Fragmentation
PCA	Principal Component Analysis
PC#	Principal Component Axis #
PET	Positron Emission Tomography
PPI	Protein-Protein Interaction
PSEA	Protein Set Enrichment Analysis
PTM	Post-Translational Modifications
r/a	Normalized radius relative to equatorial diameter
QE	Q-Exactive
QqQ	Triple Quadruople
QTOF	Quadrupole Time of Flight
r/a	Normalized radius
SCOPE-MS	Single Cell Proteomics with Mass Spectrometry
SEM	Scanning Electron Microscopy
SIMS	Secondary-Ion Mass Spectrometry
SVCT2	Sodium-Coupled Vitamin C Transporter 2
SWATH-MS	Sequential Window Acquisition of All Theoretical Mass Spectra
TEAB	Triethylammonium Bicarbonate
TIMS	Trapped Ion Mobility Spectrometry
TMEM47	Transmembrane Protein 47
TMM	Trimmed Means of M-Values
TRPV	Transient Receptor Potential Cation Channel Subfamily V
UPS	Ubiquitin Proteasome System
XCT	Cysteine/Glutamate Transporter
X_c^-	Cysteine/Glutamate Transporter Complex
2DGE	2-Dimensional Gel Electrophoresis
4F2	4F2 Cell-Surface Antigen Heavy Chain

1. CHAPTER 1

INTRODUCTION AND LITERATURE REVIEW

1.1. General Eye Anatomy

The eye is a complex system of highly organized components which, when functional, enable visual perception of focused light stimulus (Figure 1-1) (Land & Fernald, 1992). Light enters the eye first through the cornea at the anterior surface of the eye. The iris and pupil form an aperture where the iris muscle adjusts the amount of light transmitting through the pupil. Light then travels through the aqueous humor which provides a metabolic energy source to the lens positioned posterior to the aqueous humor. The lens is responsible for further focusing of light to the retina with distance accommodation facilitated by the ciliary muscle at the lens equator. In response to objective distance from the eye, the ciliary muscle applies or releases tension to modulate lens thickness. Between the lens and retina, the vitreous humor is a transparent and more viscous medium that supports eye structure and light travel. Finally, the retina is a light-sensitive nerve layer that lines the eye posterior and transduces light signal as impulses that travel along the optic nerve to the brain.

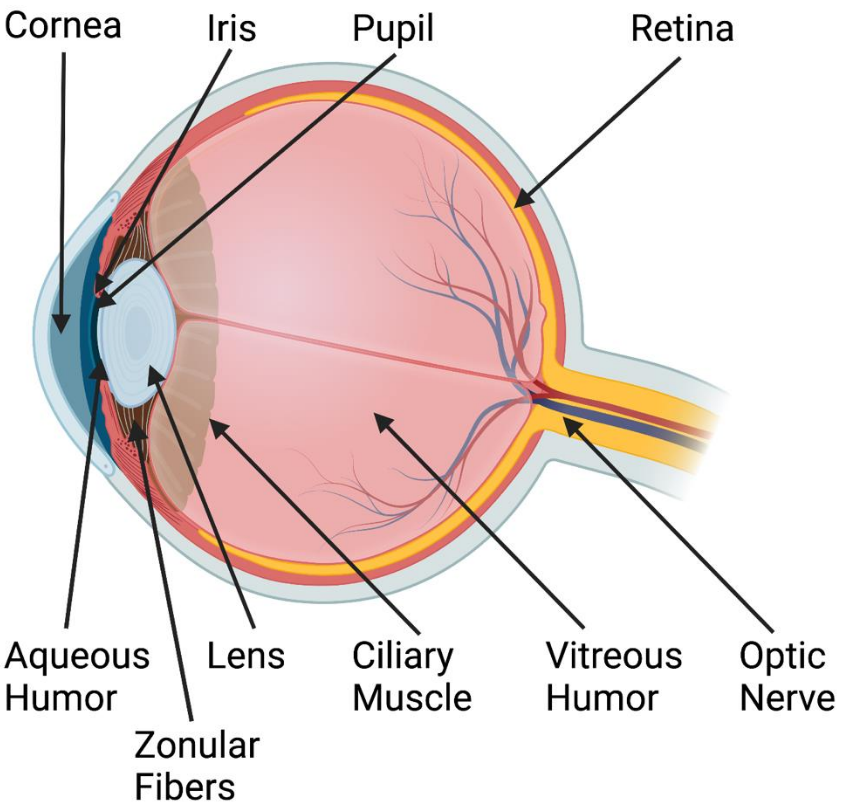

Figure 1-1 - Cartoon depiction of eye structure with labeled components. Drawn in BioRender.

1.2. Lens development and structure

The lens is a transparent tissue lacking blood vessels or innervation, positioned behind the cornea of the eye, responsible for focusing and transmission of light to the retina (Augusteyn, 2007). The adult human lens is an oblate spheroid surrounded by a collagenous capsule with approximate dimensions of 9.6 mm diameter on the equatorial axis and 4.2 mm on the polar axis (Hoffer, 1993) (Figure 1-2). Prior to maturation, the lens is established *in utero* as part of eye formation. The lens originates from the induction of the surface ectoderm and optic vesicle, formed approximately 3 weeks post-gestation (Li & Ding, 2017). The optic vesicle contacts the surface ectoderm, causing ectodermal thickening to form the lens placode. The lens placode is then invaginated to form the lens pit concurrent with optic vesicle invagination to form the optic cup approximately 5 weeks post-gestation. At six weeks post-gestation, the lens pit separates from the surface ectoderm to become the lens vesicle and descends into the optic vesicle. At this point, differentiation of cells in the lens vesicle accelerate. Anterior lens vesicle cells, further from the optic cup, differentiate into the anterior subcapsular epithelium which remains intact throughout life. Posterior lens vesicle cells simultaneously elongate to form primary fiber cells, which will be retained throughout life as the center of the lens fiber cell organization. These cells grow forward towards the anterior epithelium and eventually reach the anterior wall where their maturation as primary fiber cells is completed. Primary fiber cells are formed by week 7 post gestation. As fibers elongate, the lumen of the lens vesicle gets progressively narrower and eventually becomes a sphere filled with crescent shape fiber cells (Figure 1-2). Post-maturation, primary fiber cell cross-sectional area is heterogenous with cross sectional areas of 80 +/- 68 μm^2, a consequence of developmental processes rather than aging (Shestopalov & Bassnett, 2000).

Epithelial cells located at the equator makeup a germinative zone in fiber cell development, from which fiber cells secondary to the formation of primary fiber cells will differentiate throughout life (Li & Ding, 2017). Epithelial cells are most mitotically active at this germinative zone while anterior cells are non-mitotic. Epithelial cells then migrate to the transitional zone where cells are post-mitotic but have not yet begun to elongate (Rafferty & Rafferty, 1981), but the molecular causation of this migration is unknown. Cells in the transitional zone continue towards the lens core as additional growth rings are formed and simultaneously begin elongation towards the anterior and posterior poles to form the oblate spheroid structure. The anterior cell tip grows towards the anterior subcapsular epithelium and the posterior poles toward the posterior capsule, meeting fibers coming from all radial directions of the lens. Elongation is suggested to be supported by microtubule structures (Piatigorsky et al., 1973) and as cells elongate, they maintain a similar cross-sectional area to their transitional cell cross-section (Beebe et al., 1982). It is estimated that elongation is caused by the increase of ion permeability, namely potassium by Na/K-ATPases (Beebe & Cerrelli, 1989). Hydrostatic pressure accumulation is balanced by increased water permeability, resulting in increase in cell volume. As the first secondary fiber cells reach the anterior and posterior poles of the lens, a suture interface between elongated fiber cells is formed while primary fiber cells disconnect from the capsule and subcapsular epithelium in an uncoordinated series of events (Shestopalov & Bassnett, 2000). After the first growth layer of secondary fiber cells is formed, continuous differentiation of new growth rings of fiber cells occurs throughout life.

The structure of lens fiber cells should not be denoted as fusiform but instead as incomplete meridians with columns extending to outward tapers (Kuszak, Zoltoski, & Sivertson, 2004). The cross section of lens fiber cells is hexagonal in shape to allow efficient cellular organization, reducing extracellular space as additional fibers are added to the lens. On the hexagonal structure, there is broad side parallel to the germinative epithelium and a narrow fiber cell width along the axis of fiber growth cells. The broad side of these cells increases proportional to the radius of the growth shell secondary fiber cells reside in as shown by 3D-CAD projections from Kuszak (Kuszak, Zoltoski, & Sivertson, 2004). The continuous addition of fibers paired to spatial restraints in the eye is believed to be responsible for gradual radial compaction of lens fibers, which degrades the geometric integrity of the fiber, increases the cellular density of the lens and subsequently reduces elasticity (Bassnett & Costello, 2017; Freel et al., 2003). Loss of elasticity is not solely due to growth of the lens but is thought to be multifactorial; not dictated solely by genetic aging processes (Fisher & Pettet, 1973; Glazier, 2022). The functional consequence of reduced elasticity being less effective accommodation of the eye lens – presbyopia – with the most significant decreases in visual accommodating power occurring between the ages of 20 and 50.

As described, fiber cells are organized in concentric growth rings. While fiber cells are differentiated with hexagonal structures, maturation and cellular compaction leads to the decrease in extracellular space between fiber cells and the organization of cells is mildly altered to have less geometric homogeneity (Bassnett & Costello, 2017). The transition of cellular packing is approximately correlated with cellular age and functionality. Using correlative transmission electron microscopy and scanning electron microscopy on vibratome sectioned human lenses, the positioning of several regions was assigned by Costello et al. (V. L. Taylor et al., 1996). These regions and their proportional contribution to lens diameter can be grossly described in order of increasing cellular age as embryonic nucleus (3%), fetal nucleus (45%), juvenile nucleus (12%), adult cortex (24%) and cortex (16%). The name of each region is descriptive of the age of these growth rings relative to human age, except for cortex fibers which are the youngest fiber cells at the lens periphery. Congruent to these findings, fiber cells of the fetal nucleus are formed at an approximate 1.36 million cells/year: an order of greater than any other region of the lens. It was also noted that the embryonic nucleus is composed of approximately 800 fiber cells while the adult nucleus is composed of approximately 4.5 million fiber cells. Finally, the size of each cell was calculated with cross section area estimated to range from 5 µm circular diameter in the fetal nucleus to 2.24 x 14 µm in the cortex.

Secondary fiber cells meet at the anterior and posterior in organized structures referred to as sutures (Kuszak, Zoltoski, & Tiedemann, 2004). The patterned shape of suture is defined in part by the lens subject species (Kuszak et al., 1984). The elongated shape of fiber cells and their hexagonal shape necessitates a high order of spatial organization along the entire fiber to minimize extracellular space, maximize intercellular contact area, and minimize plasma membrane mediated light refraction (Kuszak, Zoltoski, & Tiedemann, 2004). The simplest possible suture model is a point suture wherein fiber cells reach confluence at a single point at the anterior and posterior pole. However, more complex suture patterns are needed to accommodate the accumulation of fiber cells in the mammalian lens. The murine and bovine lens each demonstrate a simple Y shaped suture which is formed by the extension of a fiber cell to a branch off an anterior Y shape tree of fiber cell endings to a corresponding branch on the posterior Y suture. Kuszak et al. demonstrated with electron microscopy and computational modeling that fibers do not extend their crescent shape perfectly in line with light on the polar axis, but instead are skewed in an S-shape along the axis perpendicular to light travel. The extent of skew is contingent to the length of fiber cells, which, in Y shape suture is dependent on a sinusoidal function with equatorial positioning defining the shortening or lengthening of the cell (V. L. Taylor et al., 1996). Sutures in the human lens take a more complex asymmetric “star” shape with additional branch points originating on the length each arm of the bovine Y suture. The complexity of the star suture largely comes from the accumulation of additional growth shells of fiber cells. In the embryonic human lens, a Y suture is formed in initial growth shells, but branch points accumulate as the number of fiber cells in a growth layer increase with correlation to the circumference of the growth shell.

The entirety of the lens is enclosed within an elastic collagen capsule. In addition to retaining tension for the ciliary muscle stretching of the lens, the capsule is permeable to molecules up to 166 kDa, but restricts the movement of larger colloidal particles (Kastner et al., 2013). The capsule is approximately 3.5 µm thick at the posterior pole, 7 µm at the equator and 11-15 µm at the anterior, a measurement that increases with age (Barraquer et al., 2006). Lens elasticity is conferred by membrane-like collagen IV and laminin structure. The capsule is directly attached to zonular fibers which are intermediates between the lens and ciliary muscle (Land & Fernald, 1992). When ciliary muscle is in a relaxed state, zonular fibers are pulled tight and flatten the lens for the accommodation of far-distance objects (Banh et al., 2006). When the ciliary muscle constricts, the lens adopts a more relaxed spheroid geometry and is best suited for near vision focusing.

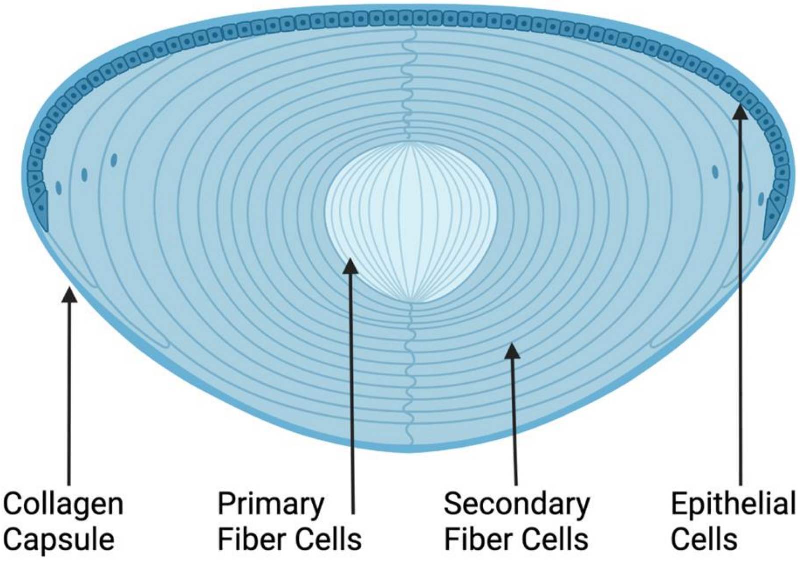

Figure 1-2 - Cartoon depiction of the lens with major cell types noted. Drawn in BioRender.

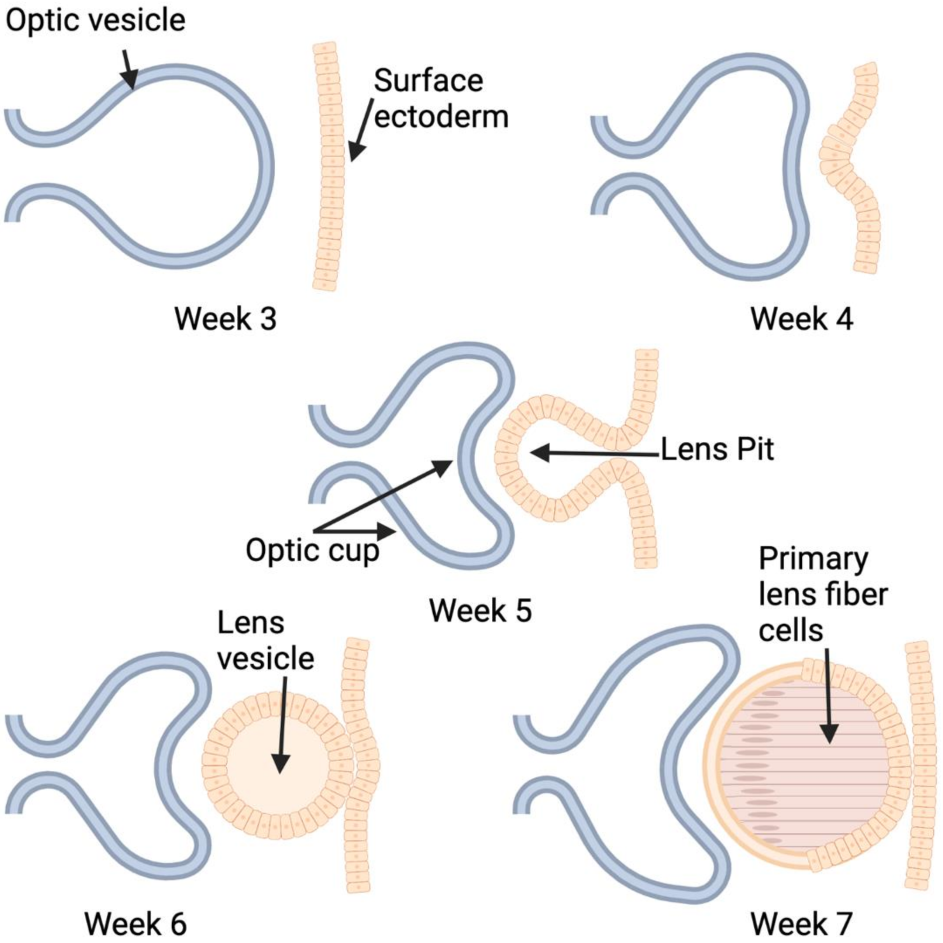

Figure 1-3 - Cartoon of lens development in utero with estimated time post germination in humans. Figure adapted from Li & Ding, 2016.

1.3. Lens transparency

As described, the lens is transparent, allowing for transmission of light to the retina with focusing accommodation meditated by the ciliary muscle that tensions and relaxes zonular fibers. To establish transparency, fiber cells maintain a high order of organization and the tight packing of fiber cells minimizes intracellular space to reduce light scattering. Light scattering is further inhibited in the lens by degradation of organelles shortly after fiber cell maturation (Varadaraj et al., 1999). Minimal light scattering persists but is thought to be caused primarily by fiber cell membranes. In addition to focusing of light through a transparent lens, the lens must correct for the path light takes through the cornea to reach the retina.

Light refraction is increased when light enters the eye off center of the cornea (Vaghefi et al., 2015). To account for this spherical-structure-induced refractive difference, a gradient of refractive index (GRIN) is established in the lens wherein fibers have heterogenous light refraction to correct for the travel of light through the lens. The lens GRIN is established largely by the differential expression of abundant crystallin proteins relative to the content of water in the lens (Vaghefi et al., 2015). Crystallins make up to 90% of the dry mass of the human lens and vary in concentration from 240-600 mg/mL in the cortex to inner nucleus core respectively (Slingsby et al., 2013). As the primary component of the lens proteome, crystallins must be thermodynamically stable, soluble proteins adaptive to environmental stresses for many years. The primary members of the crystallin family are α, β, and γ. Alpha-crystallin, the most abundant crystallin in secondary fiber cells, is subdivided into A and B subunits: CRYAA and CRYAB, respectively. Each subunit of CRYA serves a functional role in the lens as small heat shock protein (sHSP)(Rao et al., 1995). Like other sHSPs, CRYA is not expected to contribute to active re-folding of proteins but instead to the prevention of misfolding pre-emptively or in response to misfolding stress (S.-Y. Wu et al., 2016). The elimination of CRYA is reported to decrease lens size, supporting its putative contribution towards lens ultrastructure (S.-Y. Wu et al., 2016). Mutation of the sHSP domain induces light scattering cataract demonstrating its importance in the prevention of misfolding and aggregation induced cataract (S.-Y. Wu et al., 2016). Beta- and gamma-crystallin form a second superfamily of lens crystallins. Unlike CRYA, CRYB and CRYG are composed of a more heterogenous group of subunits sharing 30% sequence similarity (Slingsby & Clout, 1999). Each member of the CRYB and GRYG superfamily have two domains composed of approximately 40 residue Greek key motifs. Highly symmetric CRYB motifs between proteins leads to the formation of monomeric and high order oligomer complexes with primarily structural purpose. A survey of amino acids in CRYG revealed a high quantity of high refractive index residues suggesting that they make a significant contribution to the increased refractive power of the lens, especially in the embryonic nucleus of the lens, where CRYG is abundantly expressed (H. Zhao et al., 2011).

Finally, in addition to the expression of proteins in the lens, the distribution of proteins therein is partially mediated by a syncytium which facilitates macromolecule diffusion within growth layers of the lens (Shi et al., 2009). Typically identified in eukaryotic cells and in prokaryotic muscle development, partial fusion of mononucleate cells by process of adhesion and hemichannel formation results in aqueous pore formation between cells. Lens syncytium formation is incomplete in that pores do not expand indefinitely, establishing partial partitions between fiber cells. While previously thought to contribute to the transport of small molecules to the oldest fiber cells of the lens (Mathias et al., 1981), Bassnett et al. show that diffusion of proteins between cells primarily occurs in growth layers (Shi et al., 2009). In this way, growth layers of fibers cells share cytoplasmic proteins, and their distribution is thought to be homogenous, consistent with Le Chatelier’s principle. Bassnett expands on this finding to support that LIM2, an abundant lens membrane protein, is essential for the formation of these syncytia but is not essential for the formation of gap junctions from connexins 46 and 50 for the transport of small molecules between cells.

1.4. Fiber cell organelle loss

Lens fiber cells degrade their organelles as a part of fiber cell maturation, a process hypothesized to prevent light scattering (Bassnett, 2002). Organelle degradation was first shown more than 120 years ago (Rabl, 1899) and has been observed in various lenses including bovine, primate, rodent and avian species (Bassnett, 2002). Loss of nuclei in fiber cells is a rapid process that coincides with the disappearance of other cytoplasmic organelles, as demonstrated by confocal imaging experiments (Bassnett & Beebe, 1992). Matured lens fibers lack organelles and inherent to the organization of fibers, the lens establishes an organelle-free zone (OFZ) composed of all organelle-free fiber cells including primary fiber cells. By E21, the chick OFZ increases in diameter a sufficient width to establish transparency in the entirety of the pupil. As anticipated, the disruption of OFZ-formation results in congenital cataract blindness (Satoh et al., 2021, p. 1; W.-L. Wang et al., 2010).

In tandem to nuclear degradation, the mitochondria and endoplasmic reticulum are known to degrade. Mitochondrial degradation can be indicated by the lack of rhodamine 123 in mitochondria-less fiber cells (Bassnett, 1992; Bassnett & Beebe, 1992), while mitochondrial marker proteins BAP37 and prohibitin were simultaneously degraded (Dahm et al., 1998) supporting organelle degradation. Complementarily, resident-protein of the endoplasmic reticulum, protein disulfide isomerase (Bassnett, 1995), was also rapidly degraded in as little as 2-4 hours (Bassnett, 1992). While the degradation of nuclear function precedes organelle degradation (Dahm et al., 1998), nuclear breakdown is relatively slow relative to mitochondrial and endoplasmic reticulum degradation. Nuclei first change from an elongated shape to a spherical form concurrent to DNA condensation at the periphery before holes appear in the lamina. After holes appear in the lamina, filamentous cytoplasmic components enter the nucleus which eventually subdivides into membrane vesicles before nuclear contents become indistinguishable from the cytoplasm (Kuwabara & Imaizumi, 1974).

Fiber cell organelle loss has frequently been compared to apoptosis, especially regarding the change in nucleus structure and the cleavage of characteristic cytoplasmic and nuclear substrates (Dahm et al., 1998; Modak & Bollum, 1970; Wride, 2011). Caspases, members of the cysteine protease family, play a key role in apoptosis. Proteolytic activation of effector caspases by regulatory caspases causes cleavage of substrate proteins including poly(ADP-ribose) polymerase, lamin B, DNA fragmentation factor and spectrin (Alnemri et al., 1996). While apoptosis results in cell death and removal, fiber cell differentiation with organelle degradation must be more attenuated than classical apoptosis as the cell does not disintegrate or get exported as nuclear waste. This may be demonstrated by the remodeling of the actin/spectrin cytoskeleton in fiber differentiation (Clark et al., 1999; Wenke et al., 2016) instead of complete substrate cleavage by caspase effector molecules. It has been also shown that αB-crystallin is a negative regulator of effector caspase-3 indicating some endogenous control of caspase and thus, apoptotic activity in the crystalline lens (Kamradt et al., 2001).

While fiber cell organelle degradation occurs in a rapid series of events at a defined boundary line to the OFZ, the trigger of degradation is not well established. As the endoplasmic reticulum and mitochondria are degraded early in organelle degradation, it is expected that a distinct triggering event to the destruction of these organelles precedes that for the nucleus. Several mechanisms have been suggested including triggering by a gradient of diffusible or time-degraded molecule (Bassnett & Mataic, 1997). In progressively older fiber cells, the partial pressure of oxygen is decreased which challenges mitochondrial function to produce reactive oxygen species that exceed the capabilities of cellular antioxidants which may lead to mitochondrial lipid peroxidation and excess mitochondrial calcium concentration (Murphy & Steenbergen, 2008). Simultaneously, hypoxia upregulates the unfolded protein response pathway in the endoplasmic reticulum, an indication of endoplasmic reticulum stress, also causing calcium leak to the cytosol. The combined accumulation of calcium abundance and reactive oxygen species formation may lead to increased mitochondrial permeability, a key feature of apoptosis (Deniaud et al., 2008). Previous reports support the role of calcium as a secondary messenger for proapoptotic mitochondrial membrane permeabilization, resulting in the release of proapoptotic factors such as cytochrome c, smac/DIABLO, apoptosis-inducing factor, and endonuclease G. The role of the latter 3 elements has not been well established in nuclear degradation of fiber cells, but cytochrome c is inhibited by α-crystallin (Kamradt et al., 2001) and is uncoupled from the degradation of the nucleus in lens fiber cells (Sanders & Parker, 2002), suggesting that an alternate trigger is responsible for nuclear degradation. More recent studies suggest that degradation of cyclin-dependent kinase inhibitor p27 activates cyclin-dependent kinase 1, resulting in nuclear lamin phosphorylation, dissociation of the nuclear membrane and entry of lysosomes that liberate DNA to cleave chromatin in nuclear degradation (Rowan et al., 2017). What remains unknown in this proposed method for nuclear degradation is the sequence of events that precede p27 degradation, though this may be mediated by upregulation of the ubiquitin proteasome system.

The most important takeaway for long term homeostasis of lens function is that organelles, including those that synthesize new proteins, correctly fold, respond to improperly folded proteins, and provide energy for the cell, are degraded while their constituent fiber cell body is not degraded. Thus, proteins in the lens must be sustained without organelle machinery from the time of degradation in fiber maturation through death of the organism. Further, the generation of ATP is not mediated by mitochondrion and is otherwise be established largely by anaerobic glycolysis either dependent or independent of the pentose phosphate pathway.

1.5. Lens Physiology

After degradation of organelles and the machinery required to synthesize new protein, normal function of the mature fiber cell is mediated by proteins and protein complexes in the lens. The discussion here is directed towards plasma membrane and cytoskeleton organization, metabolism and glucose transport systems in the lens, glutathione mediated redox, calcium transport, water transport and the barrier that hinders transport of small molecules therein, established with age. Convection of small molecules in the lens is carried out by a hypothesized microcirculation system (MCS) and is discussed at length in the following section.

1.5.1. Lens membrane and cytoskeletal organization

As previously mentioned, secondary lens fiber cells adopt an elongated fiber-like shape with hexagonal cross-sections (Kuszak, Zoltoski, & Sivertson, 2004). These cells are not symmetrical hexagons and contain a broad side which adjoins cells of different growth layers and a narrow side which creates cell-to-cell contacts between cells within the same concentric growth ring. Elongated fiber cells in the bovine lens reach at least 15 mm in length and are approximately 10 µm wide on the broad side and 3 µm on the narrow side. The contribution of these fibers to a species-dependent suture system is briefly described in the lens development and structure section. The cell-to-cell contacts of fiber cells has been established by electron microscopy studies which reveal smooth surfaces broken up by interdigitations between fiber cells, named according to their approximate physical characteristics (V. L. Taylor et al., 1996). Ball and socket joints are composed of small globular structures protruding from the cell membrane from a cylindrical “stalk” (the ball) and residing in a complimentary socket joint in the adjacent cell, primarily along the broad side of fiber cells (Biswas et al., 2010). Alternative interdigitation structures include tongue-and-groove, flap and imprint, and interlocking edge junctions. The functional consequence of these interdigitations is thought to be like a ship to dock, keeping the extracellular space between fiber cells to a minimum to better establish GRIN and minimize light scattering (V. L. Taylor et al., 1996).

Aside from physical characteristics of the membrane, cell-to-cell contacts are established in the lens to mediate adhesion, and intercellular transport. The most abundant protein in the lens fiber cell membrane is Aquaporin-0 (AQP0), also known as major intrinsic protein (MIP) (Schey et al., 2017). Consistent with naming convention, AQP0 is a water channel responsible for regulation of water permeability between fiber cells. Other measured water transport proteins in the lens include Aquaporin-5 (AQP5), expressed in fiber cells and epithelial cells, and Aquaporin-1 (AQP1), a member of the epithelial cell membrane. A second primary component of the lens membrane is connexin gap junction proteins 46 and 50, also referred to as gap junction alpha 3/8 (GJA3, GJA8) respectively (Berthoud & Beyer, 2009; Valiunas & White, 2020). Connexin 43 has also been identified as a predominant gap junctional protein in the lens epithelium but is not represented in the fiber cell proteome (Berthoud et al., 2014). As in other tissues, connexins contribute to passive intercellular diffusion of small molecules between cells as established by gap junction connectivity. As passive diffusion channels, it is anticipated that the intercellular transport of small molecules is primarily accommodated by gap junction proteins, but substrate specific small molecule, active or facilitated transporters have also been identified throughout the lens (J. C. Lim et al., 2013; Mathias & Rae, 1985; Shahidullah et al., 2018).

The second most abundant lens membrane protein is lens fiber membrane intrinsic protein (LIM2), which is lens tissue specific (Shi et al., 2011, p. 2). When phosphorylated, LIM2 has demonstrated the ability to form a complex with calmodulin (CaM) and is required to maintain transparency in the lens. LIM2 is a relative of a wider gene family containing peripheral myelin protein 22, epithelial membrane proteins 1-3, and claudins. Each protein is a 4-pass transmembrane protein and at least LIM2 is putatively responsible for cell-to-cell adhesion property in complex with galectin-3 (Shi et al., 2011, p. 2). Previous studies also suggest that LIM2 is required for establishment of the lens syncytium. Finally, it was shown by SEM and proteomic analysis that the depletion of LIM2 from the fiber cell proteome degrades cytoskeletal networks, reflected in more heterogenous cell morphology and increased intercellular resistance (Shi et al., 2009).

In addition to the functional needs supported by transporters in the lens fiber cell membrane, several integral or peripherally associated membrane proteins further support intercellular adhesion. Essential for fiber cell differentiation, neural cell adhesion molecules (NCAM) 140 and 120 are expressed throughout the lens epithelium and fiber cells with decreasing concentrations in cell growth rings of increasing age. N-, B-, and E-cadherins are also expressed in the lens (Atreya et al., 1989; Leong et al., 2000; Nishi et al., 1997; Pontoriero et al., 2009; Watanabe et al., 1989). The inhibition of N-cadherin function blocks fiber cell differentiation and diminishes the protein-protein interactions of the cadherin-catenin complex with actin cytoskeleton (Leong et al., 2000). Several integrins have been detected in lens fiber cells including β1,3,4 and laminin receptor α6 (Walker & Menko, 2009). Integrin β1 is partially responsible for adhesion of fiber cells to the basement membrane capsule; aside from contributions to development of the lens vesicle, other functions of integrin proteins in the lens are not well established. Galectin-related-inter-fiber-protein (GRIFIN) is an additional protein with assumed responsibility for cell adhesion. Unlike galectin 3, GRIFIN is not anticipated to bind lactose or other carbohydrates in mammals but does in fish and birds. The rationale for species-deterministic functional differences and structural significance of GRIFIN in the lens remains to be identified (Ruiz et al., 2018). Finally, secreted protein acidic and rich in cysteine has been identified as a protein involved in cell-to-cell adhesion and necessary for epithelial differentiation to elongating fiber cells, but the ligand substrate and molecular basis for functionality of this protein have not been established (Scavelli et al., 2015).

The lens cytoskeleton is largely responsible for the structure and polarization of elongated lens fiber cells and its long-term structural maintenance (Clark et al., 1999). Like other tissues, the lens possesses microfilaments, microtubules, and intermediate filaments. Unlike other tissues, the lens has adapted several structural elements to form specialized filaments unique to the lens, including beaded filament structural proteins 1 and 2.

Actin microfilaments are found throughout the lens and have previously been established as necessary for differentiation and elongation of fiber cells (C. Cheng et al., 2017). While it was hypothesized that actin networks contribute explicitly to lens accommodation, actin is found in both accommodating lenses such as the human lens, and non-accommodating lenses as in rodents (Rao & Maddala, 2006). For the most part, β- and γ- actin are the only actin family members in the lens whereas muscle-type α-actin is found in lens epithelial explants with posterior subcapsular cataract (Nagamoto et al., 2000). Actin serves a critical role in polarization of differentiating fiber cells by organizing the distribution of adhesion complexes, ion transporters, and ion channels (Rajasekaran & Rajasekaran, 2003). Cell junctions are composed of actin-binding proteins α-actinin, α-, β-, and γ-catenin, N- and B-cadherins, band 4.1 paxillin, plakoglobin, spectrin, and vinculin (Berthoud & Beyer, 2009; Straub et al., 2003). These actin-binding adherent junction proteins are not homogenously distributed and instead localize in spatially defined regions at fiber cell tips, suggesting specificity of assembled complexes and a functional role in subcellular distribution. The adhesion complexes formed here between the anterior apical tip of fiber cells and epithelium are not replicated in the posterior where an alternative actin-based adhesion complex: the basal membrane complex (BMC) is formed between posterior fiber tips and the posterior capsule (Lu et al., 2008).

Microtubules are responsible for organization of organelles and are involved in cell division and fiber cell elongation (Piatigorsky et al., 1973). Thus, the primary role of tubulin and microtubule complexes is established in epithelial and maturing fiber cells. The polarized microtubule network is degraded after degradation of polarization centers, such as the centrosome, in organelle degradation as a process in lens maturation (Logan et al., 2018). In addition to absence of centrosomes, the contribution of tubulin to lens biology is limited by the absence of ATP generated by mitochondrial glycoloysis.

Intermediate filaments are named for their size relative to smaller microfilament and microtubule cytoskeletal elements (Herrmann et al., 2007). Six classes of intermediate filament proteins are defined including: acidic and basic keratins, type III which may form homo- or heteropolymer assemblies and includes vimentin, type IV which includes neurofilament proteins, type V nuclear lamins, and type VI beaded filament proteins including filensin and phakinin. All intermediate filament proteins share some similarity, with a central rod α-helix domain flanked by two non-α-helical domains. Intermediate filament proteins in the lens include vimentin, filensin, and phakinin (Z. Wang et al., 2010; Wenke et al., 2016). Vimentin is the only intermediate filament protein measured in both epithelial cells and fiber cells, suggesting that it has some role in fiber cell formation from epithelial cells (Sandilands, Prescott, Carter, et al., 1995). Vimentin is degraded from the cortex before and after organelle degradation concurrent to generation of beaded filament protein structures in organelle-containing fiber cells. Thus, beaded filament protein networks are significantly more abundant than vimentin in mature secondary fiber cells (Z. Wang et al., 2020). Beaded filament proteins filensin (BFSP1) and phakinin (BFSP2) are not measured in epithelial cells, but are essential for maintenance of lens transparency, maintaining interdigitations between fiber cells, establishing fiber cell maturation state, and long-range stacking organization of fiber cells (Quinlan et al., 1996). Remodeling of intermediate filament structures in the lens is not organism or age-dependent and is instead a result of cell maturation (Z. Wang et al., 2020; Wenke et al., 2016).

1.5.2. Lens metabolism and glucose transport

Epithelial cells and differentiating fiber cells in the lens retain organelles, and thus share some resemblance to metabolic regulation in canonical cell systems. For these cells, it is possible to generate ATP by aerobic glycolysis, which is much more efficient than alternative methods. However, the avascular nature of the lens restricts the availability of oxygen in the lens center, thus alternative metabolic control is necessary. This observation was experimentally modeled by first culturing the bovine lens in aerobic and anaerobic conditions in glucose media (Kinoshita, 1965). Transparency was maintained in each cultured lens. Further, oxygenated incubation of bovine lens in glucose-deficient media does induce cortical cataract. Finally, 400 mg/dL glucose supplementation to replacement vitreous humor in diabetic vitrectomy procedures has been shown to reduce post-operative cataract in respect to 100 mg/dL irrigating solution (Haimann & Abrams, 1984). Taken together, glucose is essential in transparency maintenance and anaerobic ATP generation is sufficient for lens homeostasis.

The functional alternative to aerobic glycolysis is anaerobic glycolysis and the hexose monophosphate shunt pathway (Figure 1-4) (Kinoshita, 1965). In both pathways, glucose first enters the lens and is converted to glucose-6-phosphate by hexokinase, consuming one unit of ATP. It is believed that anaerobic glycolysis is more active than the hexose monophosphate shunt pathway. In anaerobic glycolysis, glucose-6-phosphate is isomerized to fructose-6-phosphate before being phosphorylated to fructose-1,6-bisphospate by phosphofructokinase-1, consuming a second unit of ATP. Aldolase then breaks the 6-carbon sugar unit into one unit of glyceradehyde-3-phosphate and one unit of dihydroxyacetone phosphate, which is converted by triose phosphate isomerase to a second unit of glyceraldehyde-3-phosphate. Glyceraldehyde-3-phosphate dehydrogenase then utilizes one phosphate and NAD+ unit per substrate to produce 1,3-bisphosphoglycerate and 2 units of NADH. Phosphoglycerate kinase then converts one unit of ADP to ATP for each conversion of 1,3-bisphosphoglycerate to 3-phosphoglycerate, offsetting energy needs for producing glyceraldehyde-3-phosphate. Phosphoglycerate mutase and enolase then produce 2-phosphoglycerate and phosphoenolpyruvate in sequential steps, producing one water molecule per 3-carbon substrate. Finally, pyruvate kinase converts phosphoenolpyruvate to pyruvate and produces a summed 2 units of ATP from ADP. Pyruvate is converted by lactate dehydrogenase to lactate, resulting in 2 summed units of NAD+ which can be recycled for 1,3-bisphosphoglycerate production. The entirety of anaerobic glycolysis then produces 2 units of ATP per unit of glucose: substantially less efficient than aerobic glycolysis, which produces 30-32 units of ATP per glucose precursor (Melkonian & Schury, 2022).

The second pathway for consumption of glucose-6-phosphate is the hexose monophosphate pathway. One substrate unit is first converted to 6-phosphogluconolactone by glucose-6-phosphate dehydrogenase and generation of NADPH from NADP+. Gluconolactonase and water then generate 6-phosphogluconate which is converted to ribulose-5-phosphate by 6-phosphogluconate dehydrogenase and consumption of NADP+ to yield NADPH and CO_2. Ribulose-5-phosphate is then isomerized by either ribulose-5-phosphate isomerase or ribulose-5-phosphate-3-epimerase before transketolase conversion to glyceraldehyde-3-phosphate and sedoheptulose-7-phosphate. Transaldolase then converts products to ethyrose-4-phosphate and fructose-6-phosphate. Etyrose-5-phosphate and xylulose-5-phosphate, which is generated by Ribulose-5-phosphate 3-epimerase from ribulose-5-phosphate, can also be converted by transketolase to yield glyceraldehyde-3-phosphate and fructose-6-phosphate. The net reaction is then 3 glucose-6-phosphate + 6 $NADP^+$ + 3 H_2O $\rightarrow$ 2 fructose-6-phosphate + 1 glyceraldehyde-3-phosphate + 6 NADPH + 3 CO_2 + 3 H^+. One of the key uses of NADPH is reduction of oxidized glutathione (GSH) via glutathione reductase. Glyceraldehyde-3-phosphate may be converted to pyruvate through identical pathways described for anaerobic glycolysis, resulting in 2 additional ATP unit generations. Fructose-6-phosphate may also proceed through anaerobic glycolysis to yield 2 additional ATP units per precursor. The summed outcome of ATP through the hexose monophosphate pathway is then 2 ATP units per glucose-6-phophate precursor and 2 NADPH molecules.

For both anaerobic glycolysis and the hexose monophosphate pathway, the common precursor is glucose-6-phosphate via glucose. Glucose is present in the aqueous humor at 3.2 mM in healthy lenses and 7.8 mM in diabetic lenses, so passive diffusion towards the lens is expected to occur (Davies et al., 1984). Two sodium-dependent transporters of glucose, GLUT1 and GLUT3, have been identified in the rat lens by northern blot and immunohistochemistry (Merriman-Smith et al., 2003). GLUT3 displays differential localization depending on fiber maturation: in young fibers, it is found in the cytoplasm, but is inserted along the entire length of the fiber cell plasma membrane with maturation. Additionally, GLUT3 expression responds to glucose abundance in the humor and may be related to diabetic cataract. Contrasting GLUT3, northern blot analysis does not show enrichment of GLUT1 expression in fibers relative to epithelial cells. It is also known that GLUT1 is the only sodium-dependent glucose transporter measured in the bovine and human lens, though undergoing N-terminus modification in the epithelium and cortex of human lenses, but not in bovine lenses (J. C. Lim et al., 2017). A third method for the transport of glucose is through gap junction hemichannels (J. Liu et al., 2020). Using a fluorescent glucose analog, GJA3 and GJA8 hemichannel permeabilities were assessed with wild type and in dominant negative forms. Hemichannels with wild type connexin 50 are permeable to glucose but become impermeable in 368T and 379T truncation mutants. It is then expected that connexin transport of glucose is active in the youngest fiber cells where C-terminus truncation may not have occurred but is inhibited or prohibited with truncation.

The evaluation of connexin gap junction proteins as functional transporters of glucose leads to the next major section (1.6). The lens lacks vasculature and gap junction proteins are passive transporters, yet small molecules traverse multiple cells at a rate higher than expected by passive diffusion alone and are thought to be directed by an intercellular current described as the lens microcirculation system (MCS) (Beebe & Truscott, 2010; Vaghefi & Donaldson, 2018).

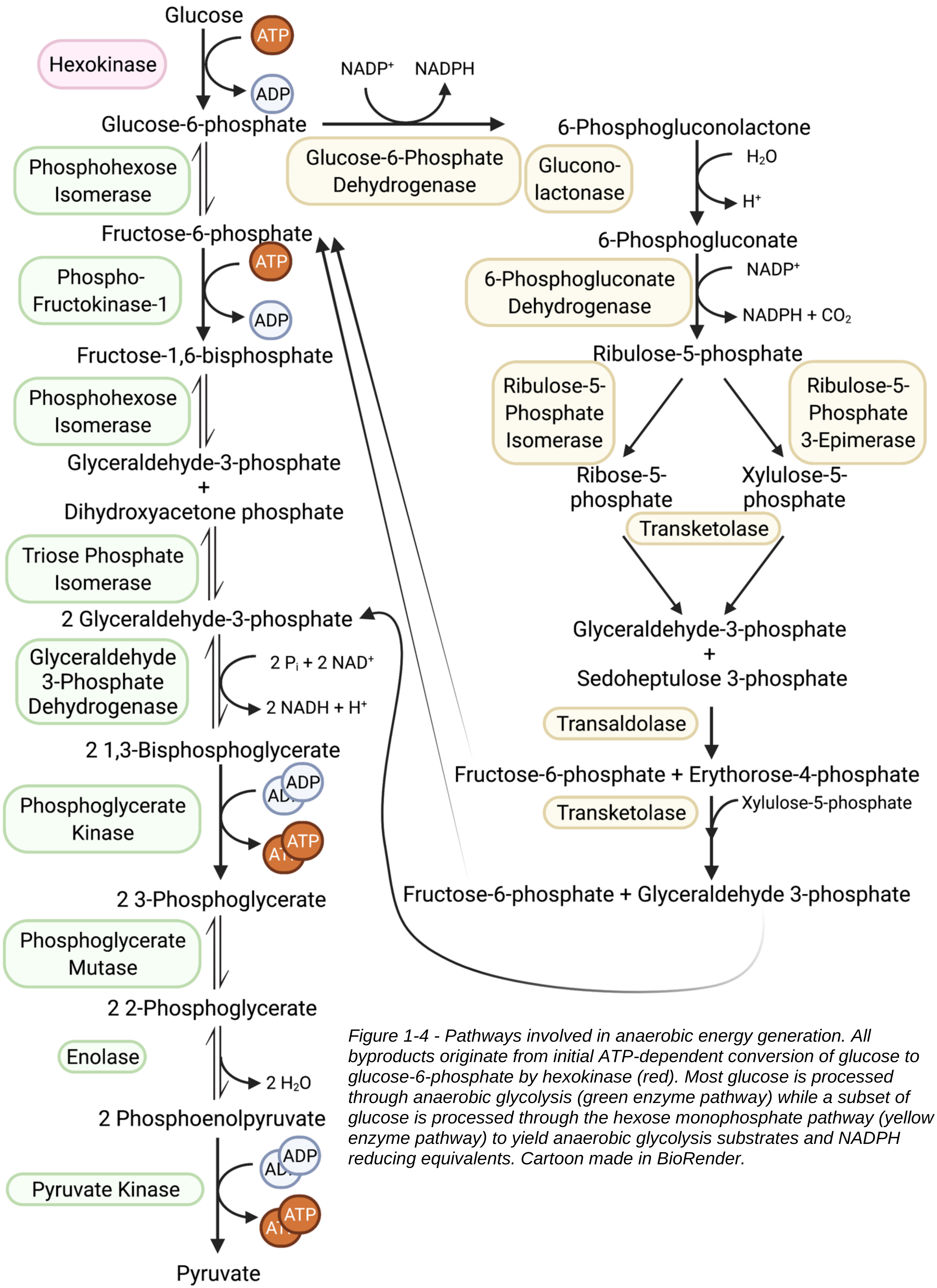

Figure 1-4 - Pathways involved in anaerobic energy generation. All byproducts originate from initial ATP-dependent conversion of glucose to glucose-6-phosphate by hexokinase (red). Most glucose is processed through anaerobic glycolysis (green enzyme pathway) while a subset of glucose is processed through the hexose monophosphate pathway (yellow enzyme pathway) to yield anaerobic glycolysis substrates and NADPH reducing equivalents. Cartoon made in BioRender.

1.5.3. Glucose uptake

As introduced, anaerobic glycolysis is essential in fiber cells and so the uptake of glucose to lens fibers is of particular interest. GLUT1 and GLUT3 are each suggested to be responsible for glucose uptake into lens fiber cells, each acting as ATP-independent transporters (Merriman-Smith et al., 2003). Alternatives to the GLUT family transporters include SGLT1 and SGLT2, each measured at the transcript level and with immunohistochemistry in the rat lens (J. C. Lim et al., 2017; Smith et al., 2002). In addition to glucose substrate selectivity, GLUT1/3 show some transport activity for dehydroascorbic acid, the oxidized product of the antioxidant ascorbic acid (Umapathy et al., 2013). Immunohistochemistry and isotope labeled imaging mass spectrometry (IMS) demonstrates that GLUT1 and GLUT3 are present throughout the lens, but after uptake, glucose accumulates in the lens equator prior to accumulatng in the anterior or posterior pole (Zahraei et al., 2022). This trend was best observed by Zahraei et al. at 15-minutes post glucose isotope spike to artificial aqueous humor (Zahraei et al., 2022). Further incubation with isotopic heavy glucose leads to accumulation of glucose throughout the lens cortex. Measurement of anaerobic glycolysis metabolites (Figure 1-4) further demonstrated time-resolved product accumulation throughout lens fibers, spatially defining localization of metabolism processes downstream of glucose uptake. Of great interest, glucose accumulation occurred first in the epithelium. While GLUT1 and GLUT3 are ubiquitous in the equatorial region of the lens, it is hypothesized that nutrients enter the lens through the anterior and posterior suture space. Interestingly, GLUT1 and GLUT3 are cytoplasmic in immature rat fiber cells, and as fibers mature, the entire transporter population is relocated to the narrow side of the plasma membrane (Merriman-Smith et al., 2003, p. 1). It was also suggested by Merriam-Smith et al. that GLUT3 localization responds to glucose concentration in extracellular space, where *in vivo* and *ex vivo* glucose supplemented humor resulted in cataract and increased membrane localization and concentration of rat GLUT3 relative to the untreated lens. GLUT1 knock out mice also develop cataract, further supporting the GLUT transporter family role in lens homeostasis (Swarup et al., 2018). Prior to results in later chapters, proteomic measurements have not been done to identify the relative abundances of glucose transporters throughout the lens, especially adjacent to the suture with respect to the equator of the lens.

1.5.4. Glutathione-mediated redox

Glutathione (GSH) is a critical component of the lens oxidative stress response (V. N. Reddy, 1990; Venkatn. Reddy & Giblin, 2008; Sweeney & Truscott, 1998). As proteins become oxidized by passive diffusion of oxygen to the lens nucleus and reactive oxygen species are induced by uv transmission, so too must reducing equivalents be present for appropriate mitigation of oxidative stress (Lou, 2003). GSH is the most abundant antioxidant in the lens and is abundant at approximately 3.7 µmol/g tissue in cortical fiber cells of young lenses and decreases in an age and fiber-position specific manner to approximately 0.8 µmol/g tissue in nuclear fiber cells of older lenses (A. C. Grey et al., 2019). Unlike much of the other introduced lens biochemistry, GSH-mediated substrate reduction is similar in the lens to other tissues and cell systems. These functions are described briefly.

Glutathione is a tripeptide of glutamate attached via a gamma peptide linkage to cysteine, which is attached by normal peptide linkage to glycine (Lou, 2003; V. N. Reddy, 1990). Biosynthesis of GSH occurs by gamma-conjugation of glutamate and cysteine by glutamate cysteine ligase catalytic subunit (GCLC), followed by conjugation of glycine to the N-terminus by glutathione synthetase. Synthesis of GSH is rate-limited by GCLC, which is in complex with glutamate cysteine ligase modifier subunit. Two common states exist for glutathione, the reduced form (GSH) and the oxidized form (GSSG). The oxidized form is a conjugation product of two glutathione species and reduction is catalyzed by glutathione reductase: $\text{NADPH} + \text{GSSG} + H_2O \rightarrow \text{NADP}^+ + 2\ \text{GSH} + \text{OH}^-$. The use of NADPH here supports the need of the pentose phosphate pathway, mentioned previously, to generate NADPH *in vivo*.

Glutathione in its reduced form may regulate the redox state of several different substrates (Lou, 2003). Peroxide species may be generated in the lens core by uv light initiation of reactive oxygen species to form hydrogen radicals and hydrogen peroxide. Glutathione may then react with peroxides by the schema, $2\ \text{GSH} + R_2O_2 \rightarrow \text{GSSG} + 2\ \text{ROH}$, where R is H or an alkyl to reduce the peroxide to an alcohol. Alternatively, free reactive oxygen radicals may be reduced by $2\ \text{GSH} + 2\ R^{\cdot} \rightarrow \text{GSSG} + \text{RH}$. These reactions are catalyzed by the glutathione peroxidase family of enzymes. GSH also participates in thiol redox regulation by S-glutathionylation, a post-translational modification (PTM). A cysteine side group in its reduced form is conjugated to GSH, resulting in an GSSR product and water in the presence of free oxygen. Protection of the cysteine side group is catalyzed by glutathione-S-transferase or glutaredoxin and may also be non-enzymatic. Removal of the glutathione group from the cysteine side chain is catalyzed by glutaredoxin or sulfiredoxin.

Glutathione itself is known to decrease in abundance following treatment with hyperbaric oxygen, which is the best treatment to model age-related nuclear cataract (Giblin et al., 1995; Padgaonkar et al., 2000). Further knockout of glutaredoxin-2 (H. Wu et al., 2011) or GSH synthesis by GCLC knockout in the LEGSKO mouse model is shown to increase lens sensitivity to oxidative stress and increase cataract risk.

An additional use for GSH is in the glyoxylate pathway, where GSH conjugates to methylglyoxal, and in a two-step process, returns methylglyoxal to lactate via catalysis by glyoxalase I and II (Haik et al., 1994). The lens possesses both enzymes in a functional state, and the decrease in GSH abundance with age suggests that there is an age-related accumulation of methylglyoxal. The accumulation of methylglyoxal is expected in the aging diabetic lens especially, as shown by Riley and Harding who further support the adduct formation and aggregation of γ-crystallin with methylglyoxal (Haik et al., 1994; Riley & Harding, 1995). Accumulation of methylglyoxal in the lens also results in the formation of advanced glycation end products, which are themselves oxidizing species (Aragonès et al., 2020). The accumulation of methylglyoxal in the limiting presence of GSH then may create a positive feedback loop that further enhances the oxidizing environment in the lens nucleus. While thought to contribute to age-related cataract, advanced glycation end products are primarily studied in their role towards diabetic cataract (J. C. Lim, Grey, et al., 2020; Linetsky et al., 2008; Nahomi et al., 2013).

1.5.5. Glutathione transport

Glutathione delivery to the lens nucleus is thought to proceed through the extracellular suture space, however the diffusion of metabolites into the lens nucleus occurs at a rate faster than expected by passive diffusion alone, suggesting accelerated transfer by suture localized proteins (Vaghefi et al., 2012; Vaghefi & Donaldson, 2018). Additionally, precursor amino acids are anticipated to traffic to the core of the lens and be combined to form GSH *in situ* – if enzymes are present.

Glutathione and its precursors are delivered to the lens through space outside of the capsule, predominantly the aqueous humor. Evaluation of human aqueous humor shows that GSH is present therein at 1.2 µmol +/- 0.16 µmol and that approximately 30% of that GSH store is in the oxidized GSSG form (Stahl et al., 1996). Evaluation of LEGSKO mouse model (GSH synthesis deficient *in situ*) shows that GSH accumulates in the aqueous and vitreous humor suggesting GSH synthesis may be both endogenous and exogenous to the lens (Whitson et al., 2016). Whitson et al. also demonstrated that uptake of GSH through the aqueous humor is likely to proceed through a transporter with low specificity for GSH, but some specificity for broadly defined peptide analogs. Transport of GSH is also demonstrated to proceed inwards from the vitreous in an energy-independent process, but not outwards. The transferability of vitreous humor transport to human lens is in question still, as the abundance of vitreous GSH is much higher in mice than in other organisms, suggesting that Le Chatelier's principal for passive diffusion may not be valid in other organisms as it is putatively in mice.

Several molecular identities are hypothesized for the uptake of GSH and its precursors. For GSH these include two members of the organic anion transporter family (OAT1 and OAT3) and sodium-dicarboxylate transporter 3 (NaDC3). Each of these identities are inferred in the lens based on renal and hepatic GSH uptake (Ballatori et al., 2009; Breljak et al., 2016). Recent work suggests the contribution of OAT1 to full-length GSH transport is suspect, and may instead be responsible for transport of cysteinyl glycine (Hagos et al., 2013). Functionally, NaDC3 is a secondary active transporter coupled to sodium transport making putative influx or efflux dependent on the sodium ion gradient *in situ* and protein orientation in the membrane (Umapathy et al., 2013). Organic ion transporters 1 and 3 are coupled to 2-oxoglutarate anti-transport when transporting GSH (Lash et al., 2007). As a byproduct of oxidative phosphorylation, the distribution of 2-oxoglutarate in the lens is unclear. More promiscuous substrate specificity is shown for OAT1 and OAT3 by KO and subsequent metabolomic assay, suggesting that tryptophan metabolism efflux is mediated by these transporters (Bush et al., 2017). Included in the list of accumulated metabolites to an OAT3 KO human kidney cell line was kynurenine, an oxidized form of tryptophan. Efflux of GSH and GSSG is more likely to be facilitated in the human lens by multidrug resistance proteins (MRP) 1,2, 4, and 5 (Ballatori et al., 2009). Prior to work presented in later chapters, none of the GSH influx or efflux proteins mentioned here (OAT1/3, NaDC3, MRP 1/2/4/5) had been measured in the human lens.

Transport of amino acid precursors to GSH (glutamate, cysteine, glycine) into fiber cells, with assembly by GSH synthesis complexes GCLC/M and GSH synthetase provides an alternate route for the bioavailability of GSH in the lens. The synthesis of GSH is not expected to occur at high frequency in the relatively metabolically inert lens core where only anaerobic glycolysis may provide ATP for enzyme activation. This produces a gradient of GSH, measured previously with IMS where the concentration of GSH decreases in progressively older fiber cells (A. C. Grey et al., 2019). Glycine uptake is facilitated in the lens by glycine transporters (GLYT1/2) and while GLYT1 is located in cortical fiber cells, GLYT2 is present throughout the lens, supporting its role as a potential anti-glycation agent for cataract prevention (J. Lim et al., 2006, p. 1, 2007, p. 2). Uptake of cysteine is putatively facilitated by excitatory amino acid transporters 4 and 5 (EAAT 4/5) and system X_c^-, a glutamate/cysteine antiporter complex of a heavy chain (4F2hc) linked by a disulfide bond to one of several light chains from the solute carrier protein 7 family (SLC7) (Bridges et al., 2012; J. C. Lim et al., 2013). Each of these proteins colocalize in the human epithelium and cortex, but system X_c^- may swap its colocalizing exchange partner for alanine-serine-cysteine transporter 2 (ASCT2) in the lens nucleus where pH is decreased. In anucleate nuclear fiber cells of the rat lens, it is suggested that X_c^- and ASCT2 facilitate cysteine accumulation as an alternative route for thiol protection (J. Lim et al., 2006, p. 1). Finally, uptake of glutamate is putatively facilitated by system X_c^- as described (Bridges et al., 2012).

1.5.6. Calcium transport

Calcium is a second messenger that is responsible for signaling functions including muscle contraction, fertilization, and neurotransmitter release (Cioffi et al., 2011). Calcium may be stored in the endoplasmic reticulum or other organelles and is released upon signal transduction stimulus. Once released to the cytoplasm, calcium may bind receptor proteins, activating cascades of enzymatic activity. In mature lens fibers, calcium is not stored in organelles and is instead present only in cytoplasmic space (Tang et al., 2003). In the cytoplasm, it may activate proteins including calmodulin (CaM), calcium-dependent calpain proteases, and components of the ubiquitin proteasome system (UPS) among other targets (Dargelos et al., 2008; Deniaud et al., 2008; R. Mukherjee et al., 2017; Park et al., 2013). The physiological result of calcium accumulation in endothelial cells results in disruption of cytoskeletal organization, degradation of cell-cell adhesions and intercellular gap formation. In the lens, calcium may activate CaM to inhibit Aquaporin-0 by binding at its CaM binding site, decreasing water permeability (Lindsey Rose et al., 2008). Calcium may also play a role in activating UPS in fiber cells which are shown to have intact an intact and putatively functional UPS in all fiber cells, including the anucleate cells in the lens nucleus (Pereira et al., 2003).

Transport of calcium in the lens is functionally significant and accumulation of calcium has both age and cataract formation correlation in humans (Duncan & Jacob, 2008; Tang et al., 2003). In young lenses, the bulk concentration of calcium is approximately 3 nmol/mg dry weight of tissue and decreases parabolically to 1 nmol/mg dry weight at 50 years before parabolic increase in abundance for the rest of human life, and in human cataract lenses is measured at 10+ nmol/mg dry weight suggesting a physiological correlation with cataract (Tang et al., 2003). Calcium is largely proposed to move inward to fiber cells by passive transport through the lipid bilayer and membrane channels and exported by plasma membrane calcium ATPases and Na/Ca exchangers (Rhodes & Sanderson, 2009). Calcium may also be sequestered in the sarcoplasmic reticulum of immature fiber cells by sarcoplasmic reticular calcium ATPases. Additionally, passive transport of calcium is expected to occur intercellularly by connexin gap junctions (Gao et al., 2004; Pinto et al., 2017, p. 46). Transcriptomic experiments only detect plasma membrane calcium ATPases in the epithelium (Marian et al., 2005), and there is no differential expression of the majority of these proteins when cataract is induced. However, plasma membrane calcium ATPase 2 transcript is approximately 2-fold more abundant in cataract lens than in age-matched transparent lenses, suggesting that there is a transcript-level response to the cataract-related intracellular calcium accumulation (Marian et al., 2008).

1.6. Lens microcirculation system

After establishment of the lens GRIN, maintenance of proteostatic state and net protein concentration is required to prevent light scattering (Vaghefi et al., 2015). The abundant α-crystallin acts as a small heat shock protein, capable of preventing further unfolding of partially misfolded proteins (Horwitz, 1992). However, transparency maintenance in the lens requires homeostasis of oxidative state in addition to proteostatic stress response by α-crystallin and other ATP-independent heat shock proteins (Berthoud & Beyer, 2009; Truscott, 2005). To mediate the lens redox environment, antioxidants and metabolic reducing equivalents must be delivered to all primary and secondary fiber cells in the lens.

To this point, transport of small molecules in the lens has been introduced as a byproduct of protein channels, transporters, exchangers, gap junctions, or by passive diffusion (Berthoud et al., 2014; Lash et al., 2007; J. C. Lim et al., 2013, 2017; J. Liu et al., 2020; Mathias & Rae, 1985; Shahidullah et al., 2018). However, the lens as an organ lacks vasculature to effectively transport small molecules to and from the lens nucleus where fiber cell extracellular space is limited, and passive diffusion of metabolites alone is not expected to be sufficient for the introduction of molecules to metabolically active and less active fiber cells (Vaghefi & Donaldson, 2018). The absence of a concerted network of proteins that influence metabolite transport through the lens would result in accumulation of oxidized species in the lens nucleus and in other fiber cells, eventually leading to disruption of protein stability, causing disruption of protein folded state, and cataract formation (Truscott, 2005). An accumulation of biophysical and biochemical measurements have been made that support the hypothesis that a lens microcirculation system (MCS) facilitates transport throughout the lens (Mathias et al., 1997). The MCS hypothesis proposes that small molecules and metabolites convect through the lens with influx at the anterior and posterior sutures, transport of those molecules to mature fiber cells including the innermost primary fibers where they may be consumed, and export of the small molecules or product metabolic waste through the equatorial epithelium (Figure 1-5A) (Beebe & Truscott, 2010; Donaldson et al., 2010; Vaghefi & Donaldson, 2018). In this section, the biophysical and biological evidence that supports the MCS hypothesis is presented in addition to previously understood perturbations that occur to MCS with age and fiber cell maturation.

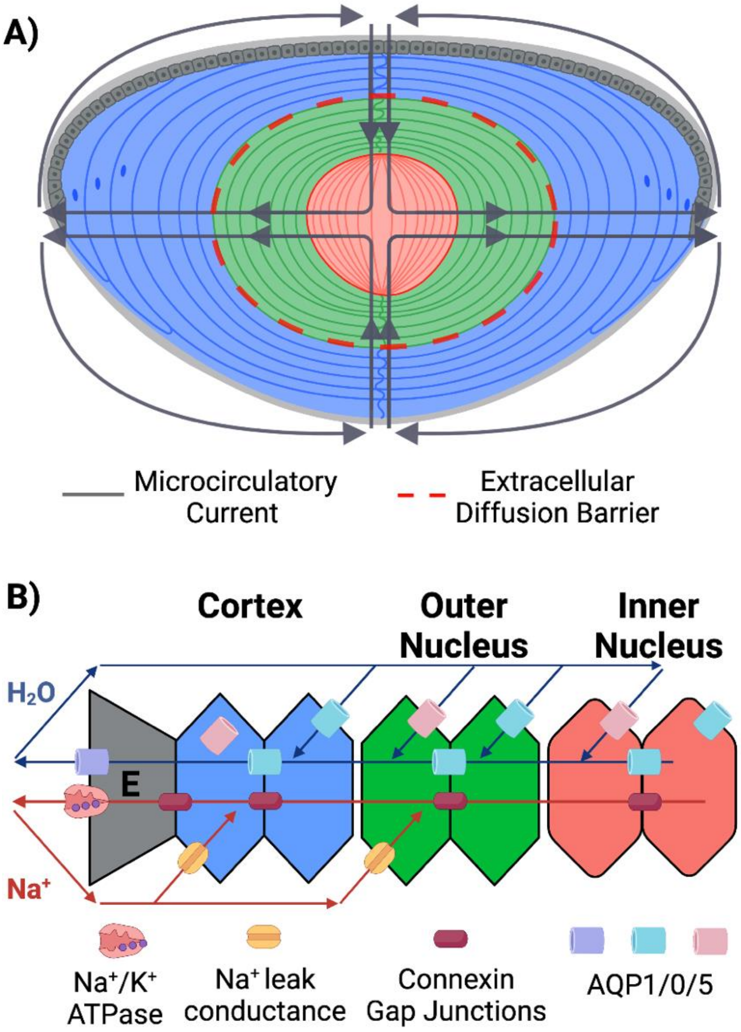

Figure 1-5 - Cartoons of (A) lens microcirculation current with marked extracellular diffusion barrier protein localization and (B) cartoon of MCS cellular organization for known efflux protein networks. Cartoon made with BioRender.

1.6.1. Biochemical measurement of MCS

The lens MCS is dependent on the circulation of water from the anterior and posterior poles and out through the equatorial epithelium into the surrounding humor. Water and solute putatively enters the lens through extracellular space as demonstrated by biophysical measurements, but export cannot proceed through extracellular space of tightly packed fiber cells equatorial length (Schey et al., 2017). Thus, a concerted network of proteins is needed to facilitate export current of water and small molecules from the lens core to the equatorial periphery. It is unclear how small molecules enter fiber cells in the centermost region of the lens, but an accumulation of experiments have developed the following model for intracellular transport thereafter. In the epithelium, Na/K ATPases are positioned near the equator to exchange intercellular sodium for extracellular potassium. To establish a sodium ion electromotive potential gradient, sodium may re-enter the lens through extracellular space near the cortical equator and be taken up by a passive leak channel along the fiber cell membrane. As sodium accumulates in these cells, intercellular sodium currents are directed through passive connexin gap junction channels. Finally, a net water current in the lens is established by permeability of Aquaporin family proteins that direct water from the extracellular space in the lens nucleus through the body of the fiber cell and eventually out of the epithelial layer (Figure 1-5B). In the following sections, the molecular identities and functional regulation of these proteins is discussed.

Na/K ATPases

MCS function is derived from a sodium ion electromotive potential gradient in the lens, established in equatorial epithelial cells by Na/K ATPases (Delamere & Tamiya, 2004). For these pumps, 3 sodium ions are exported in exchange for 2 potassium ions, consuming 1 ATP equivalent. Na/K ATPase is a member of the P-type ATPase family calcium ATPases and sarcoplasmic reticulum calcium ATPases introduced previously (Scarborough, 2002). Each member of the P-type ATPase family has a catalytic α- and non-catalytic β-subunit. The expression of various isoforms of these ATPases is moderately species dependent. The most complete understanding of ATPase expression is in bovine lens epithelium where α1 and α3 are measured in the anterior region and α1-3 in the equator (Ong et al., 2003). Evaluation of frog, pig, rabbit, and rat lenses suggests ubiquitous presence of α1 in the anterior, with less precise molecular designation in the equator and in either anterior or equator of the human epithelium (Dean et al., 1996; Delamere et al., 1996; Gao et al., 2000; A. E. Moseley et al., 1996; Tamiya et al., 2003). There is no clear epithelial cell inwards channel, however passive leak channels are presented in the MCS model as a route for sodium uptake into fiber cells (Ebihara et al., 2014).

Intracellular concentrations of sodium and potassium are 10-15 mM and 130 mM respectively, while at 145 mM and 130 mM respectively in the extracellular humor (Paterson, 1969). In human cortical cataract, there is a greater accumulation of sodium in cortical fiber cells than in the healthy lens, indicating importance for sodium export. While functionally active in the epithelium, it is not expected that Na/K ATPases are active in fiber cells as accumulation of oxidation and glycation PTMs inhibit transporter function (W. H. Huang et al., 1992; Katori et al., 1999). Delamere et al. showed that approximately half of all rabbit Na/K ATPase function occurs in the monolayer of epithelial cells and that the equatorial region of elongating fiber cells constitutes 60% of the fiber cell function (Delamere & Dean, 1993). Thus, the distribution and molecular identity of Na/K ATPases is most relevant in the epithelium where protein turnover and metabolic activation is most prevalent (Sen et al., 1986). Finally, it has been shown that pre-incubation of lenses in Na/K ATPase ouabain or in Na+ deficient media results in loss of microcirculation current, further supporting its necessity in MCS establishment (Candia & Zamudio, 2002).

Aquaporins

The lens MCS model proposes that fluid is transported through the extracellular space at the sutures, but intercellularly through the equator of the lens for export. Thus, fiber cells must maintain water permeability to facilitate water transport and establishment of fluid current in the lens (Schey et al., 2017). Water permeability is facilitated in the lens by the Aquaporin family of proteins. Three proteins have been detected in the bovine, human and rat lenses: AQP1, AQP5, and AQP0. Conventional aquaporin channel permeability is achieved by plasma membrane insertion of AQP1 in epithelial cells and AQP0 in fiber cells. However, AQP5 has unconventional cellular localization and is transported from cytoplasmic space to the plasma membrane of fiber cells in response to physical and biochemical stimuli (Gletten et al., 2022b; Petrova et al., 2020).

As is true for each of the 13 identified human aquaporin channel proteins, AQP1 is a small, membrane channel with four protomeric polypeptides making up a water-conducting pore (Finn & Cerdà, 2015). AQP1 is localized to the epithelium where it exports water from the epithelial cell layer to the humor and is not expressed in differentiating or mature fiber cells (Schey et al., 2017). Expression of AQP1 in the mouse lens begins at E17.5, greatly improving transparency of the embryonic lens, which to that point is only known to express AQP0 in fiber cells (Varadaraj et al., 2007). To demonstrate the physiological significance of cell-type specific differentiation, Varadaraj et al. compared the water permeability and physiology of mouse lenses in wild type, AQP0$^{-/-}$ lens, and a transgenic AQP1$^{+/+}$ crossed with AQP0$^{-/-}$ line where AQP1 translation was induced in fiber cells (Varadaraj et al., 2010). The fiber cells from the crossed model showed a 2.6-fold increase in water permeability compared to wild type, reducing the cataract formed with AQP0 absence, however, fiber cells were morphologically incongruent with normal lens fiber cells. The observed decrease in compact cellular packing may be due to the loss of cell-cell adhesion properties provided by AQP0 presence in the membrane. Mutations to the AQP1 gene do not cause cataract formation (Preston et al., 1994), further supporting the claim of Varadaraj et al. that AQP1 does not contribute to age-related cataract.

Aquaporin-0 is the most abundant protein in the membrane of fiber cells (Varadaraj et al., 1999). While not initially thought to be a member of the aquaporin family, AQP0 was shown to have significant sequence and functional homology to other aquaporins (Chepelinsky, 2009). Though highly abundant in the plasma membrane, the permeability of AQP0 is significantly lower than other aquaporins. With injection of aquaporin cRNA to xenopus oocytes, AQP0 showed approximately 1/20th the permeability of AQP1 and 1/100th the permeability of AQP5 (B. Yang & Verkman, 1997). The abundance of AQP0 in the membrane is suggested to offset this deficiency in its permeability. The *in vivo* permeability of AQP0 is reported to be modulated by lipid membrane environment, local pH, and intercellular calcium concentration (Tong et al., 2013; Varadaraj et al., 2005). Additionally, AQP0 is inhibited by CaM after calcium-induced activation of CaM and subsequent binding to a C-terminal site (Fields et al., 2017; Lindsey Rose et al., 2008). Sensitivity of AQP0 to calcium is deleted by S231 or S235 phosphorylation in the putative CaM binding site, each conferring a 20-50-fold decrease in AQP0 affinity for CaM (Lindsey Rose et al., 2008). While phosphorylation is primarily expected to occur in metabolically active fiber cells, inactive cells possess an alternative route to CaM binding inhibition by truncation of the C-terminus predominately at N246 or D243 in the human lens (Korlimbinis et al., 2009; L. J. Takemoto, 1995). AQP0 truncation is a continuous process, eventually resulting in near-complete incorporation of the modified protein throughout the lens (Korlimbinis et al., 2009; Wenke et al., 2015). Truncation of AQP0 to a 1-243 product is not expected to decrease its permeability (Ball et al., 2003), suggesting that continuous truncation of AQP0 prepares the lens for long term transparency homeostasis in metabolically inert fiber cells.

Unlike other aquaporins, AQP0 shows unique cell-cell adhesion properties. By evaluating adhesion-deficient fibroblasts, Varadaraj et al. showed that AQP0 expressing cells had greater cell-cell adhesion property than AQP1 expressing fibroblasts, but less than E-cadherin expressing fibroblasts (S. S. Kumari & Varadaraj, 2009, p. 0). In addition to interactions with CaM, AQP0 is shown to have PPIs with filensin, phakinin, a chloride channel, and crystallins indirectly (Lindsey et al., 2004). The functional significance of these interactions is not empirically known, but it is suggested that AQP0 plays a role in organizing intracellular contacts and the cytoskeleton, especially after the intermediate filament switching event occurs in the maturing fiber cell (Z. Wang et al., 2020; Wenke et al., 2016).

Aquaporin-5 is the third, and most recently measured aquaporin in the lens. An mRNA screen of AQP1-5 detected both AQP4 and AQP5 in the rat lens at concentrations 1000-fold lower than AQP1 (Patil et al., 1997). To date, AQP4 has not been measured in the lens at the protein level and it is anticipated that it would be measured by tryptic shotgun proteomics if present. AQP5 was first measured in 2013 by Grey et al. by shotgun proteomics and western blotting (A. C. Grey et al., 2013). Immunohistochemistry experiments have localized AQP5 to the cytosol in the epithelium and in both the cytosol and plasma membrane of fiber cells (Petrova et al., 2018). As true for AQP0, it is anticipated that AQP5 is truncated in the inner nucleus, but it is unclear if this influences permeability (A. C. Grey et al., 2013). Unlike AQP1 and AQP0, AQP5 appears to undergo translocation from the cytosol to the plasma membrane in response to P_{H2O} stress and cellular maturation (Petrova et al., 2018; Sindhu Kumari & Varadaraj, 2013). In other tissues, translocation of AQP5 form the cytosol to the membrane occurs following phosphorylation through the cAMP-dependent PKA pathway (F. Yang et al., 2003) indicating a role for phosphorylation in AQP5-mediated water permeability. Recent studies in the lens show that AQP5 is localized to autophagosome-like vesicles which merge with lysosomal vesicles to become autolysosomal vesicles trafficked to the plasma membrane by lysosome secretion (Gletten et al., 2022b). Finally, it was shown that *ex vivo* severance of zonular fibers induces translocation of AQP5 from the plasma membrane to the cytosol, decreasing water permeability in absence of lens tensioning (Petrova et al., 2020). Taken together, it is unclear the extent to which AQP5 contributes to cumulative water permeability in the lens, however, the switch like mechanism for insertion in the plasma membrane in response to stress is an exciting future point of study in lens biochemistry and cataract physiology.

Connexin gap junctions

Fiber cells throughout the lens are connected to each other by gap junctions positioned on the broad side of fiber cells (Mathias et al., 2010). Radial organization allows the transport of small molecules, >1 kDa, through the lens as facilitated by the sodium ion gradient and aquaporin water current generation (J. Liu et al., 2020). Two members of the gap junction alpha family, connexin 46 (GJA3) and connexin 50 (GJA8) have been identified as the predominant fiber cell gap junction constituents (Berthoud et al., 2014; Berthoud & Beyer, 2009). GJA3 and GJA8 each form hexameric gap junctions to enable MCS intercellular transport. Connexin 43 is also present in the lens epithelium but is not in fiber cells and its transcriptional regulation occurs as a part of fiber cell differentiation (Berthoud et al., 2014). In addition to gap junction formation, recent studies suggest that GJA3 contributes to passive leak conductance of sodium in fiber cells (Ebihara et al., 2014).

Gap junction conductivity is sensitive to voltage and pH selective gating by activity of C- and N-terminal disordered region conformational changes (J. Liu et al., 2020; Slavi et al., 2016). Phosphorylation also appears to decrease gap junction permeability, demonstrated by conductivity increase in protein kinase C gamma knockout mouse lenses where wildtype lenses showed greater abundance of phosphorylated GJA8 serine and threonine residues (J. Liu et al., 2011). Additionally, C- and N-terminal truncation PTMs occur alongside cleavage in disordered cytoplasmic loop region in both GJA3 and GJA8 (Slavi et al., 2016). Cytoplasmic loop cleavage was shown by electrophysiology studies to impair intercellular conductivity of fiber cells. However, terminus truncation eliminates connexin pH sensitivity and does not have a statistically significant impact on junctional conductance. This is especially important as the lens nucleus is more acidic than the cortex suggesting that terminus truncation of GJA3 and GJA8 may be essential for maintenance of conductivity in the lens nucleus lens (Baldo & Mathias, 1992).

TRPV 1/4

To this point, water permeability and microcirculation current has been introduced largely without mention of regulation. To maintain the GRIN, specific ratios of water:protein must be maintained in spatially distinct regions (Vaghefi et al., 2015). It is proposed that transient receptor potential cation channel subfamily V proteins TRPV1 and TRPV4 respond to changes in mechanical and hydrostatic pressure changes to activate signaling pathways in epithelial cells (Gao et al., 2015; Shahidullah et al., 2012, p. 4, 2018, p. 1). TRPV1 and TRPV4 have been spatially characterized in mouse, pig and cow lens (Y. Chen et al., 2022; Mandal et al., 2018; Nakazawa et al., 2021; Shahidullah et al., 2012). Insufficient evidence supports the presence of either TRPV channel at the protein level in the human lens (Martínez-García et al., 2013). In the hyperosmotic challenged lens, TRPV1 activation leads to calcium accumulation, protein kinase C dependent ERK1/2 signaling activating WNK kinase (Shahidullah et al., 2018). This results in phosphorylation and activation of the sodium-potassium-chloride cotransporter 1 in the lens epithelium. Activation of the cation cotransporter ultimately inhibits Na/K ATPase activity, resulting in ion accumulation, eventually allowing lens fiber cells to reach osmotic equilibrium (Mandal et al., 2018, p. 1; Schey et al., 2017). Cation cotransport is energetically dependent on Na/K ATPase activity, providing a negative feedback loop for cation cotransport activity (Mandal et al., 2018, p. 1). In the hypoosmotic challenged lens, TRPV4 is activated resulting in Src family kinase activation and Na/K ATPase activation, which decreases hypoosmotic stress. In addition to osmotic-sensitive response, TRPV1/4 are mechanosensitive, responding changing zonular tension (Nakazawa et al., 2021). Decreases in zonular tension removes TRPV4 from the membrane of peripheral fiber cells, which accompanies AQP5 relocation to the cytoplasm (Nakazawa et al., 2021; Petrova et al., 2020). Decreases in zonular tension by contrast do not relocate cytoplasmic TRPV1 to the plasma membrane (Nakazawa et al., 2021).

1.6.2. Biophysical measurements of MCS

Biophysical measurements of the MCS are largely predicated on the hypothesis that water and solutes convect throughout the lens and surrounding extracellular space as demonstrated in Figure 1-5A. Each of the three annotated regions, the cortex, outer nucleus, and inner nucleus are representative of stages in fiber cell maturation and are composed of distinct cell populations described by Augusteyn et al. (Augusteyn, 2007). The metabolic and antioxidant requirements for each anucleate nuclear fiber cell growth region are similar. To measure fluid and solute circulation, two techniques are most used: measurement of liquid circulation by Ussing-type chamber experiments and measurement of molecular transport by magnetic resonance imaging (MRI) experiments. IMS has also been used for the measurement of small molecule distribution throughout the lens.

Fluid circulation in the lens is proposed to originate at the anterior and posterior poles, with water directed through extracellular space at the sutures, and exported through the equator of the lens at the epithelial cell layer. To measure fluid circulation currents and directionality, an Ussing-type chamber has been used by several investigators including the Matthias, Zamudio, and Koniarek (Fischbarg et al., 1999; Candia & Zamudio, 2002; Candia et al., 2012). In Ussing chamber experiments, the lens anterior or posterior is connected to a mechanical or gravity powered water pump reservoir separated from the equatorial region of the lens by rubber O-rings fixed at the anterior and posterior. Fluid then flows from the pumps, entering the lens from the anterior and posterior. Fluid then travels through the lens, eventually exiting via the equatorial epithelial cells. The volume of water exiting the lens is measured. In a passive system as presented by Mathias and Gerometta, each reservoir is a passive microsyringes without plungers (Candia et al., 2012). Each of the three pumps starts at equal measured volume and MCS fluid direction was assessed by the accumulation of fluid in the pump connected to the lens equator. Alternatives to passive pump measurement of fluid transport have also been measured by salt accumulation and conductivity (Candia & Zamudio, 2002). For each model of Ussing-type chamber, it was shown that fluid enters from the anterior and posterior pole and is exported from the equator and that this process is conserved in bovine and rabbit lenses with putative transferability to human lens physiology (Fischbarg et al., 1999; Candia & Zamudio, 2002; Candia et al., 2012). An additional point to the discussion of the protein-basis of MCS establishment: pre-incubation of the lens in Na/K ATPase inhibitor ouabain or Na+ deficient media results in reduced fluid transport through the lens (Candia & Zamudio, 2002).

To evaluate the time-resolved transport of solute and water through the lens, various MRI techniques have been used to support the MCS hypothesis and further elucidate permeability to solute and water throughout the lens (H.-M. Cheng et al., 1987; Vaghefi et al., 2011, 2012; Vaghefi & Donaldson, 2018). Experiments by the Donaldson group demonstrate that water is directed from the cortex to the inner nucleus of the lens, as previously shown by Ussing-type chamber experiments (Vaghefi et al., 2011, 2012; Vaghefi & Donaldson, 2018). In addition to directionality and rate of liquid movement, the localized concentrations of water and protein were determined by MRI, further supporting the organization expected for GRIN establishment (Vaghefi et al., 2015). A key result of MRI studies is that the rate of fluid transport in the bovine lens is not homogenous, but that rate of water transport in the cortex exceeds that of the inner nucleus (Vaghefi et al., 2012). There also appears to be a distinct barrier to the rate of water transport at the interface of the cortex and outer nucleus as shown in Figure 1-5A (Vaghefi et al., 2015). A more recent study by Vaghefi and Donaldson showed that small molecule MRI reagent analogs of physiologically relevant small molecules are transported to the lens core by the MCS at a rate faster than expected by passive diffusion alone (Vaghefi & Donaldson, 2018). Water and small molecule solute is expected to enter the lens through extracellular space and diffuse through the lens in extracellular space, however the accelerated rate of small molecule transport to the inner nucleus suggests that there is a coordinated network of proteins that facilitate transfer of solutes near fiber cell tips at the lens suture. The molecular identity of these transporters or other proteins suture-localized is unknown.

A deficiency in the measurement of solute transport by MRI is that the reagents used are not endogenous substrates and are instead similarly sized molecules which may not be recognized by substrate specific transporters for circulation through the lens. As an alternative approach, the Grey lab used IMS to measure the spatial distribution of key metabolites including GSH and glucose in the lens (A. C. Grey et al., 2019; Nye-Wood et al., 2017; Zahraei et al., 2021). Findings in IMS studies confirmed those presented by MRI and added further evidence that the diffusion of small molecules in the human lens is regulated by the barrier at the interface of the cortex and inner nucleus. This was supported by measurement of GSH distribution in 29- and 66-year-old lenses which demonstrate an age-related depletion of small molecule transport to the inner nucleus, suggesting that the barrier to small molecule diffusion is correlated with fiber cell maturation and subject age. Finally, quantitative immunohistochemistry experiments were performed in rat lens to determine the spatial distribution of GSH and its amino acid precursors (J. Lim et al., 2007). In addition to the findings reported above, it was shown that there is an accumulation of cysteine and glycine in the inner nucleus, but not in the outer nucleus. This finding is consistent with the spatial abundance of GLYT2 and ASCT2 in the rat lens nucleus (J. Lim et al., 2006, 2007). It is possible that both GLYT2 and ASCT2 contribute to accelerated transport as a result of these findings.

1.6.3. Transport Barrier

Maintenance of the MCS and transparency homeostasis is contingent on the functionality of each MCS protein and its spatial positioning. Indeed, for most of the presented MCS proteins, PTMs, inhibitory drug treatment, or sequence mutations result in eventual cataract onset (Ebihara et al., 2014; Francis et al., 2000; W. H. Huang et al., 1992; Nakazawa et al., 2021; Slavi et al., 2016; Varadaraj et al., 2010). A critical role for the MCS as described is osmotic regulation and regulation of water content in the lens (Schey et al., 2017; Shahidullah et al., 2012, p. 4, 2018). In addition to intracellular water content, water content in extracellular spaces plays a role in tight packing of fiber cells and by extension the radial organization of connexin gap junctions (Young et al., 2000). Water composition in the lens is approximately 65% by mass, significantly less than that in other tissues (Paterson, 1970). The extracellular space occupied by water and solutes in the lens represents only 6% of the total volume in the lens and is a critical resource for ATPases and passive transporters which do not participate in intercellular junction formation (Mathias & Rae, 2004; Vaghefi et al., 2012).

In addition to the importance of MCS in transparency homeostasis, it is apparent that a transport barrier to diffusion of molecules is established in the lens with restriction of extracellular space and increasing age (Sweeney & Truscott, 1998; Vaghefi et al., 2012). Confocal imaging, radiography, and MRI have been used to describe onset of the barrier with restricted extracellular space, especially in non-human lenses (Vaghefi et al., 2012). In the bovine lens, extracellular permeability undergoes significant decline between 1.0 and 0.6 normalized radial distance along the axial cross section of the lens (r/a). Note then that the extracellular diffusion barrier depicted in Figure 1-5A is most consistent with modeling of barrier formation by extracellular space restriction. An interesting finding by Donaldson and colleagues was the measurement of increased accumulation of Gd^{3+} in the lens inner nucleus, measured between 0.4 and 0.0 r/a. The restriction of extracellular space was approximately consistent with the decline in space between fiber cell suture tips in the bovine lens, where the most exterior suture tips showed less tight packing than those near the inner nucleus. The accumulation of Gd^{3+} in the inner nucleus was further studied by evaluation of other radiotracers transport in bovine lens (Vaghefi & Donaldson, 2018). Vaghefi and Donaldson showed extracellular diffusion alone is not sufficient for the delivery of water and small molecules to the lens nucleus, but instead that an unknown mechanism for molecule delivery from the extracellular restriction barrier to the innermost nuclear fibers exist. It is hypothesized that this delivery is facilitated by the MCS, as inhibition of Na/K ATPases eliminated the accumulation of small molecules in the bovine lens nucleus. It is also anticipated that several unannotated, substrate-specific transporters are a part of the MCS and play a role in small molecule transport across the barrier.

Age is also thought to play a role in the decline of MCS function and metabolite transport between young cortical and mature nuclear fiber cells (Moffat et al., 1999). MRI visualization of H_2O and D_2O exchange in human lenses demonstrated that the rate of water entry into the lens nucleus is correlated with the subject age and that the most significant changes decline occurs from 40-60 years of age. Moffat and colleagues also demonstrated that the decay of water exchange rate is greater in the nucleus than in the cortex (Moffat et al., 1999). It is then suggested that age-related barrier formation extent is correlated with extracellular space restriction. To support water exchange studies, impediment to GSH transport is measured in the lens nucleus where the 29-year-old lens shows significantly more GSH accumulation than the 66-year-old lens (A. C. Grey et al., 2019). Cortical fibers from these lenses accumulated similar abundances of GSH, albeit still reduced in the older lens. It is expected that the aggregate effect of extracellular restriction and age-related barrier formation plays a role in cataract formation (Sweeney & Truscott, 1998; Vaghefi et al., 2012; Vaghefi & Donaldson, 2018; Z. Wang et al., 2021).

1.7. Lens protein modifications

The following section is adapted from the previously published review: Proteomic Characterization of the Human Lens and Cataractogenesis written by Cantrell and Schey, Expert Review of Proteomics, © 2021, reprinted by permission of Informa UK Limited, trading as Taylor & Taylor & Francis Group, http://www.tandfonline.com. (Cantrell & Schey, 2021a).

1.7.1. Post-translational modifications

In typical human cells, most proteins are maintained for <1-22 hours before they are degraded (Eden et al., 2011). Several tissues such as the heart, lungs and brain are composed of proteins that are retained for months, years, or in the case of lens fiber cells for the duration of life. In mature lens fiber cells, in the absence of organelles, no new proteins are synthesized and metabolic function is decreased in the nucleus after the barrier to extracellular diffusion is established (Garland et al., 1996; Moffat et al., 1999). Lifelong protein retention allows many enzymatic and non-enzymatic PTMs to occur and, as discussed, this complicates comprehensive lens proteome analysis. Reversible enzymatic modifications such as phosphorylation (Gutierrez et al., 2016), ubiquitination (Pereira et al., 2003), methylation (Truscott et al., 2012), lipidation (Schey et al., 2010) and acetylation (Nahomi et al., 2013) occur throughout life, especially during early fiber cell maturation, and are essential for cellular processes including protein-protein interaction (Tanimura & Takeda, 2017), cellular signaling (Betts et al., 2017) and membrane transport (Gutierrez et al., 2016). After fiber cells become less metabolically active, irreversible non-enzymatic PTMs occur including oxidation (Hains & Truscott, 2008), truncation (Korlimbinis et al., 2009), racemization (Fujii et al., 1999), deamidation (Wenke et al., 2015), and cross-linking (Buckingham, 1972). Each of these irreversible modifications are hypothesized to be linked to cataractogenesis due to deleterious or modified protein functionality inherent after modification. Each protein may be singly or multiply modified resulting in a complex network of proteoforms that are difficult to fully characterize in a high-throughput manner. Further, methods for age-related PTM characterization should be resolved to enhance understanding of fiber cell aging and proteoform distribution. Here we discuss several irreversible lens PTMs that are measured as a function of age and the implication of those PTMs towards ARNC formation.

1.7.2. Protein truncation

Fragmentation of proteins by N-terminal or C-terminal truncation to form multiple peptides is typically non-enzymatic and is one of the most common irreversible PTMs in the lens. Each major member of the crystallin super-family (α, β, γ) undergoes truncation at the N- and C-terminus (Srivastava et al., 1992; L. J. Takemoto, 1995). Throughout maturation, α-crystallin undergoes successive c-terminal truncation (L. J. Takemoto, 1995) which is contrasted by N-terminal truncation in β-crystallins (Lampi et al., 1998; Srivastava & Srivastava, 2003). The majority of γ-crystallin proteins undergo proteolytic degradation throughout fiber maturation, but nearly all proteoforms remaining are truncated to various degrees (Lampi et al., 1998). In addition to crystallin proteins, truncation has been detected on most other lens proteins that have been examined including AQP0 (Wenke et al., 2015). C-terminal truncation at N259 and N246 is readily detected in 7-year old human lenses and by 21 years old, full length AQP0 is not detected in the lens nucleus (Figure 1-6) (Gutierrez et al., 2011; Wenke et al., 2015). Other proteins of the lens that are truncated include GJA3, GJA8 (Slavi et al., 2016), and beaded filament proteins filensin and phakinin (Sandilands, Prescott, Hutcheson, et al., 1995; Z. Wang et al., 2010).

The fragmentation of specific regions of lens proteins may confer additional functionality or have negative pathological effects. In GJA8, calpain mediated C-terminal truncation reduces the pH selectivity for gating (Raju et al., 2017). As a byproduct of anaerobic glycolysis, high quantities of lactate from the inner nucleus of the lens must be transported of out of the cortex through gap junction networks (Kinoshita, 1965). The reduced pH selectivity allows for intracellular communication between cortical and nuclear fiber cells. Interestingly, limited c-terminal α-crystallin truncation at S172 was found to increase chaperone function (Aziz et al., 2007), but more extensive truncation has been shown to degrade this function. Truncation products of α-crystallin have also been shown to aggregate, create hydrogen peroxide, and induce apoptosis in cultured cells (Raju et al., 2017). Further, examination of low molecular weight peptides isolated from 3 whole human lenses indicated that peptides from a 72-year-old lens displayed a greater than two-fold increase in ability to produce hydrogen peroxide than peptides from 17 or 43-year-old lenses. Increased oxidation is believed to be a significant agent of ARNC formation and thus, the peroxide byproduct of α-crystallin truncation may be correlated with cataractogenesis (Berthoud & Beyer, 2009; Hains & Truscott, 2008; Truscott, 2005). The transition of potentially problematic α-crystallin over-chaperoning when mildly truncated to deleterious and damaging when more extensively truncated highlights the difficulty of functionally characterizing truncation PTMs.

1.7.3. Non-enzymatic post-translational modification

The most abundant PTM in the lens is racemization of amino acids from their L-forms to D-forms (Truscott et al., 2016). At synthesis, proteins are near completely composed of L-form amino acids, but by age 60, every protein in the lens has an average 2-3 D-form amino acids as determined by HPLC separation of hydrolyzed lens lysates (Hooi & Truscott, 2011). Racemization of amino acids perturbs the tertiary structure of proteins and may change protein solubility and subsequent protein-protein interactions (Luthra et al., 1994; Magami et al., 2020). Thus, it is likely that racemization plays a key role in ARNC formation.

Racemization occurs *in vitro* via an α-proton abstraction followed by re-addition of a proton, and while not validated *in vivo*, kinetic favorability suggests this process occurs in the lens (Bada & Protsch, 1973). For asparagine, a more complex pathway (Figure 1-7) affords the joint racemization and deamidation of L-Asp to D-Asp via a cyclic succinimide intermediate. Racemization and isomerization can both be detected using mass spectrometry (MS) by radical chromophore modification of peptides followed by LC separation in front of serial collision induced dissociation (CID) and Radical Directed Dissociation fragment scans (Tao et al., 2012; Tao & Julian, 2014). This method relies on a ratio calculation and does not allow complete separation of all products, especially in complex mixtures. Multiple Reaction Monitoring has also been used to identify targeted racemates and isomers of asparagine residues in the human lens after LC separation (Fujii et al., 2020). Deamidation modifications are readily identified on high resolution instruments by simple mass shift (+0.98402 Da) in MS1 spectra and localization of the modification conferred in the MS2 spectra (Hains & Truscott, 2010a; N. E. Robinson et al., 2005). *In vivo* measurements have subsequently shown D-isoAsp is the most prevalent product of this racemization/deamidation reaction, especially as humans age (Hooi et al., 2012).

Racemization of L-amino acids to D-amino acids plays a key role in the functional modification of aged fiber cells (Hooi et al., 2012, 2012; Hooi & Truscott, 2011; Luthra et al., 1994). Indeed, racemization has been analyzed in fossils to estimate age (Griffin et al., 2009; Ohtani & Yamamoto, 2010; Yasunaga et al., 2017). Racemization specific to individual amino acids in lenses of different age and pathology revealed a clear correlation of aspartic acid, asparagine and serine with age and pathology, but weaker trends with threonine, phenylalanine, glutamic acid, glutamine, leucine, isoleucine, valine, and alanine (Hooi & Truscott, 2011). This study was expanded to look at α- and γ-crystallin racemization, deamidation, and isomerization in lenses of different age. Unlike the trends in Asx and serine, no linear relationship was detected, but elevations in αA-crystallin D-Asp, deamidation, isoAsp and γs-crystallin deamidation, and isoAsp percent were seen in ARNC lenses, and increased with age (Hooi et al., 2012).

Deamidation and racemization may be correlated with cataractogenesis, as demonstrated by the increased abundance of deamidated residues in the insoluble protein fraction of ARNC lenses as compared to cataract-free controls (Wilmarth et al., 2006). Abundance of insolubilization is of great importance for cataractogenesis because multiple studies have shown increased protein insolubility in cataractous lenses (Forsythe et al., 2019; Kopylova et al., 2011; McFall-Ngai et al., 1985; Schmid et al., 2021; Vetter et al., 2020; Wilmarth et al., 2006). To date, no studies have investigated amino acid-specific isomerization in the whole lens proteome due to methodological challenges associated with MS. Lehmann et al. suggest that the asparagine immonium ion, m/z = 88, decreases in isoAsp and that the intensity of complementary b- and y-ions from the X-(L-Asp/L-isoAsp) phosphodiester bond decreases in the isoAsp isomer species relative to Asp (Lehmann et al., 2000). Alternative fragmentation by electron-capture dissociation (ECD) has also been used to unambiguously delineate isoAsp from Asp (Cournoyer et al., 2006; Sargaeva et al., 2009). Either method cannot separate D-Asp from L-Asp peptide racemates and requires manual interpretation. Alternatively, structure for lossless ion manipulation MS was able to readily separate L-Asp, L-isoAsp, D-Asp and D-isoAsp containing amyloid β peptides (Zheng et al., 2017). Altogether, racemization/deamidation are critical PTMs in lens aging and cataract formation; future work in isomer composition proteomics may reveal age and/or pathology specific dependencies in proteins outside of the crystallin super-family.

Protein aggregation and insolubilization are well-known processes related to lens aging and cataractogenesis (Kopylova et al., 2011; Luthra et al., 1994; Rao et al., 1995; Wilmarth et al., 2006); protein-protein crosslinking plays a critical role in each of these processes (Dilley & Pirie, 1974). Many groups have studied crosslinking by reversible oxidative disulfide formation (Lou et al., 1990; Lou & Dickerson, 1992; L. Takemoto, 1996; B. Wang et al., 2017; Wei et al., 2015; Yu et al., 1985), but irreversible crosslinks have also been detected in lysates treated with denaturing and reducing agents. Several different crosslinking mechanisms have been identified including through advanced glycation end products (Nagaraj et al., 1991), oxidized ascorbate (Linetsky et al., 2008) and dehydroalanine (DHA) formation (Linetsky et al., 2004; Z. Wang et al., 2014).

Among advanced glycation end products, crosslink by pentosidine formation between lysine and arginine residues is a result of a Maillard reaction in oxidized environments (Nagaraj et al., 1991). In the presence of a cellular diffusion barrier, reactive oxygen species are not reduced, putatively allowing pentosidine crosslinks to form (Hains & Truscott, 2008; Nagaraj et al., 1991; Truscott, 2005). Pentosidine crosslinks have only been studied by amino acid hydrolysis, but there is a positive correlation between age and the abundance of crosslinked pentosidine (Nagaraj et al., 1991). In both soluble and insoluble protein fractions, a significantly greater abundance of pentosidine was detected in ARNC lenses as compared to healthy and diabetic cataract lenses.

More recent efforts have identified significant crosslinking through DHA or dehydrobutyrine (DHB) intermediates (Figure 1-8)(Friedrich et al., 2018; Z. Wang et al., 2014). An intermediate formed by β-elimination of 1) a phosphate group from phosphoserine to DHA or phosphothreonine to DHB, 2) water from serine to DHA and threonine to DHB and 3) hydrogen sulfide or disulfide from cysteine or cystine for DHA. DHA and DHB then react with nucleophilic amine or thiol side chains and metabolites, including GSH, to form irreversible crosslinks. At least 90 sites on 18 lens proteins are covalently modified by GSH (Schey et al., 2020), yet protein-protein crosslinks may still be formed. It is suggested that GSH forms a covalent bond as a preventative measure against protein-protein crosslinks which have increased abundance in cataractous lenses (Linetsky et al., 2004). Quantitation of protein crosslinks from crystallin proteins do not show specific cataractous trends, but this may be due to many distinct proteoforms not considered in the analysis. A table of crosslinked peptides identified can be found in a recent review from Schey et al. (Schey et al., 2020).

Identification of lens protein crosslinking sites has been largely facilitated by manual interpretation of tandem MS (Friedrich et al., 2018; Z. Wang et al., 2014, 2019). Recent methodological and algorithmic advances in crosslinked peptide identification may facilitate a more extensive identification of cross-linked peptides (Hägglund et al., 2018). To identify endogenous modification sites, bottom-up approaches have been used most frequently, and recent improvements to experimental preparation include strong cation exchange (SCX) enrichment of cross-linked peptides (Fritzsche et al., 2012), O^{18} enrichment of cross-linked peptides facilitated by tryptic digest (M. Liu et al., 2013), and ultraviolet photodissociation assisted identification of dityrosine crosslinks after GC fractionation (S. Mukherjee et al., 2019). Mixed N^{14}/N^{15} isotope labeling has also been used *in vitro* to differentiate intermolecular crosslinks from intramolecular (Taverner et al., 2002). Automated identification of cross-links has proven more difficult with multiple groups providing rapidly improving algorithms capable of identifying non-cleavable cross-links (Z.-L. Chen et al., 2019; Götze et al., 2012; Hoopmann et al., 2015; Rinner et al., 2008; B. Yang et al., 2012). Altogether, there is a promising future for the identification of high-throughput, site-specific cross-linking sites in the lens with MS technologies. Future improvements in gas-phase separations by ion mobility mass spectrometry and data searching improvements are promising directions for the future of cross-linking MS.

So far, we have discussed several of the most important irreversible cataract-linked modifications in the lens. However, many other important modifications exist including lipidation, acetylation, carbamylation, oxidation, methylation, glycation and phosphorylation. Lipidation, a PTM process that covalently attaches lipids to proteins and may regulate specific targeting to membranes, was identified on AQP0 by LC-MS/MS and spatially characterized by IMS (Schey et al., 2010). Lipidation by oleic acid and palmitic acid was especially prevalent at K238 and the n-terminus in the cortical region after organelle degradation (Figure 1-9) suggesting membrane remodeling as fiber cells mature in adolescence and adulthood. It is likely that AQP0 lipidation is a non-enzymatic process, however enzymatic lipidation by lipid transferases cannot be ruled out (Ismail et al., 2016; Muszbek et al., 1999). Myristoylation and palmitoylation have also been detected in lens fiber cells in global lens proteome analysis (Thinon et al., 2014; Z. Wang et al., 2020; Z. Wang & Schey, 2018).

Acetylation has been well studied in other tissues but is not well studied in the lens. However, acetylation studies have shown that a majority of lens proteins including α-crystallins, β-crystallins and beaded filament proteins are acetylated at the N-terminus or at the N-terminus of truncated proteoforms, likely as co-translational and post-translational modifications respectively (Z. Wang et al., 2010). Lens protein carbamylation also occurs on lens proteins at the N-terminus or lysine residues, and effects α-crystallin activity (Nagaraj et al., 2012). Carbamylation appears to be more age-related than acetylation due to age-related distributions of each modification (Schey, unpublished results); however, neither modification has been conclusively linked to ARNC formation. It is clear that oxidation of the lens proteome plays a key role in ARNC formation (Berthoud & Beyer, 2009; Hains & Truscott, 2008; Linetsky et al., 2008; Truscott, 2005; B. Wang et al., 2017), however, proteomic analysis of oxidized residues by either bottom-up or top-down methods may introduce artifacts which hinder oxidative PTM inference (Verrastro et al., 2015). Multiple approaches to identify endogenous oxidized residues are highlighted in the review from Verrastro et al. (Verrastro et al., 2015). Thiol oxidation has been studied in a GSH deficient (LEGSKO) mouse model and human samples to show that intermediate filament proteins and several enzymes in cataract human lenses were similarly oxidized in the aging, GSH deficient lens (B. Wang et al., 2017). The abundance of oxidized thiols in this study were not mirrored in transparent lenses, implying pathological consequence of thiol oxidation. The functional consequence of these pathology-related modifications is not known, but enzymes identified in this study, including glutathione reductase, are known to have reduced function in the aging lens (Wei et al., 2015).

In contrast to the previously discussed modifications, reversible phosphorylation has been studied in depth in the lens with 2-Dimensional Gel Electrophoresis (2DGE), MS and/or orthogonal fractionation techniques (Aquilina et al., 2004; Chiou et al., 2010; Gutierrez et al., 2016; C.-H. Huang et al., 2011; Kamei et al., 2004; Moroni & Garland, 2001; Schaefer et al., 2003; Z. Wang et al., 2013). Proteins in the lens also undergo extensive phosphorylation. At least 271 proteins are phosphorylated at 855 sites and 54 proteins may be phosphorylated at least 5 times (Z. Wang et al., 2013). Reversible enzymatic phosphorylation of αA- and αB-crystallins occurs via a cAMP-dependent pathway, though autophosphorylation has also been reported (Kantorow & Piatigorsky, 1998). Crystallin phosphorylation is pervasive with 35-50% of crystallin modified and phosphorylation identified in the lens shortly after birth (Thornell & Aquilina, 2015). The pathological role of lens phosphorylation has not been exhaustively studied in ARNC, however phosphorylation of αA-crystallin and αB-crystallin subunit proteins increases in ARNC lenses and expression is stimulated by oxidative stress (Kamei et al., 2004; K. Wang et al., 1995). In lenses of different age, Gutierrez et al. showed that AQP0 and MP20 phosphorylation decreases across the barrier when established, but remains constant in lenses where the barrier is not established (Gutierrez et al., 2016). The pathological role of phosphorylated MP20 is not well established, however AQP0 phosphorylation is known to increase channel water permeability due to CaM resistance (Lindsey Rose et al., 2008). Altogether, identification of PTMs and the resulting proteoforms, especially as they relate to lens fiber aging and cataractogenesis remains a significant challenge and opportunity in the lens community.

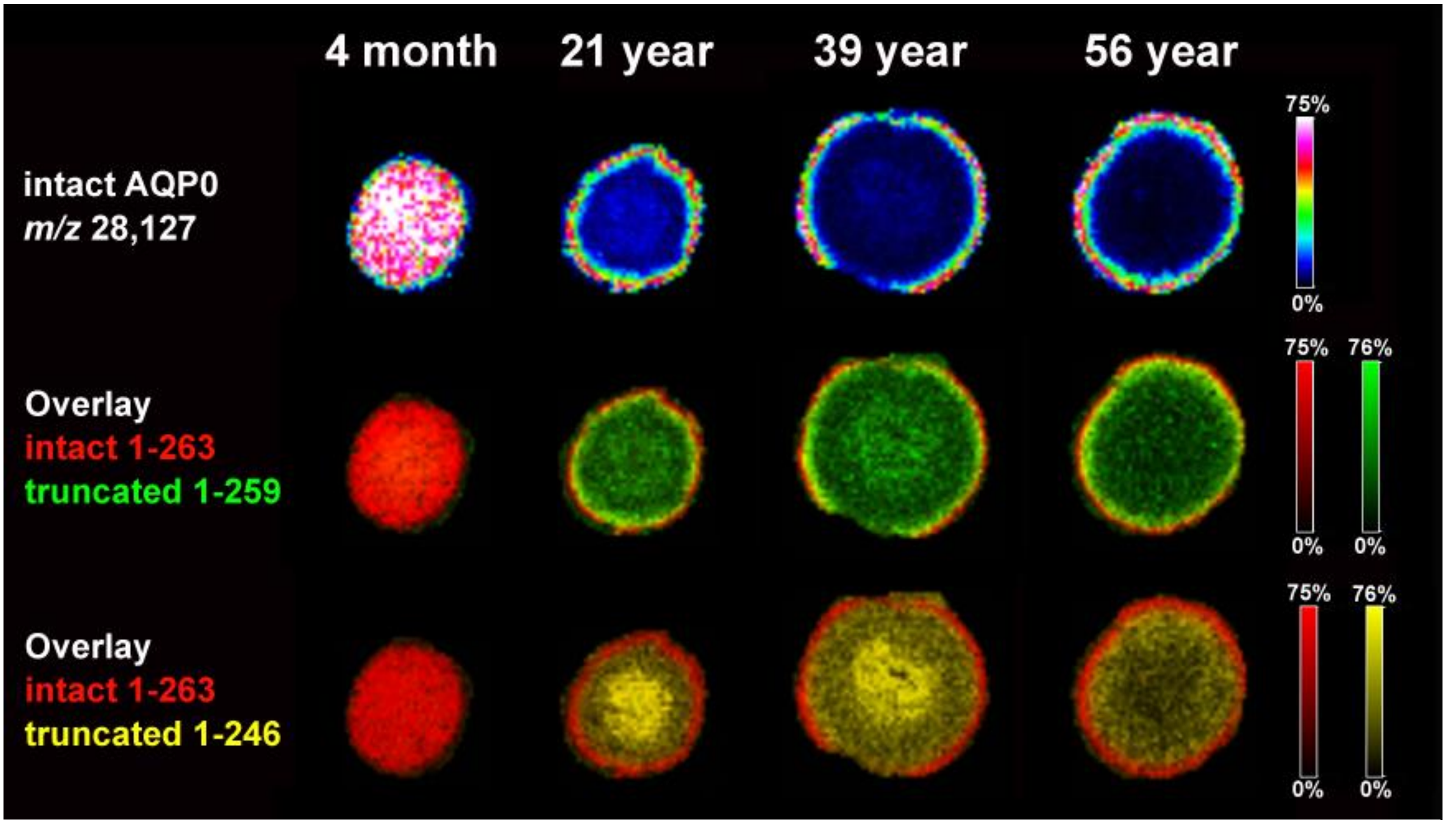

Figure 1-6 - The spatially resolved abundance of intact and C-terminal truncated (N259 and N246) AQP0 in aging human lenses is visualized with MALDI imaging mass spectrometry. Intact AQP0 is not detected in the nucleus by the age of 21. Figure adapted from Wenke et al., 2015.

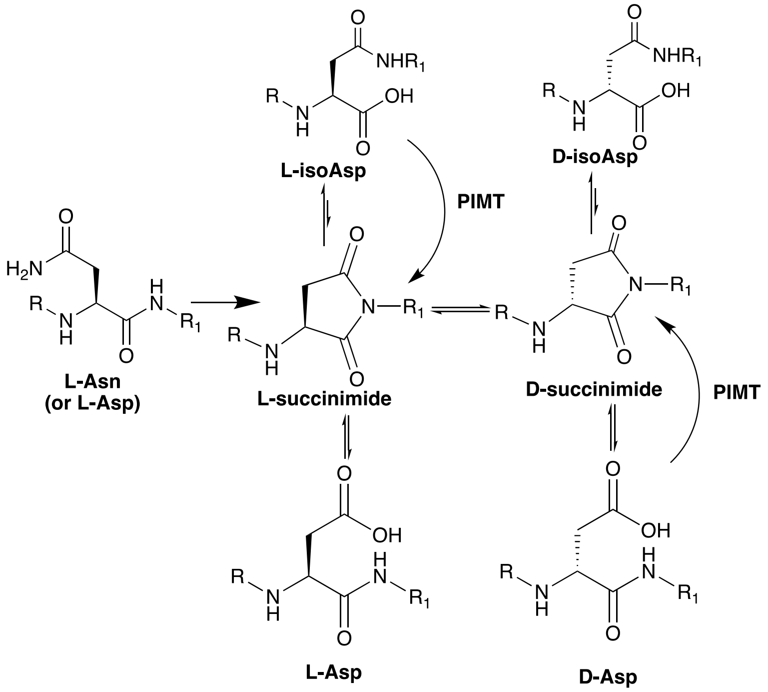

Figure 1-7 - Scheme of L-Asn deamidation and D-Asp formation from either L-Asp or L-Asn. Conversion of L-isoAsp and D-Asp to succinimide intermediates is facilitated by Protein L-isoaspartyl methyltransferase. Figure adapted from Schey et al., 2020.

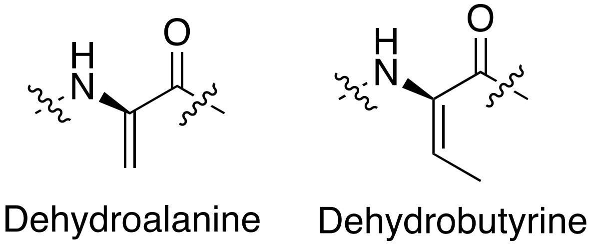

Figure 1-8 - Molecular structure of dehydroalanine (DHA) and dehydrobutyrine (DHB) intermediate residues.

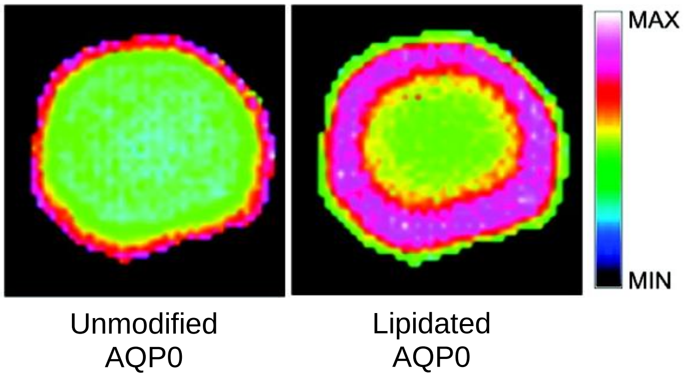

Figure 1-9 - Spatial characterization of full-length, unmodified (m/z 28203) and lipidated (m/z 28377) AQP0 from the equatorial section of an 11-year-old human lens shown by IMS. Figure adapted from Wenke et al., 2016.

1.8. Lens dysfunction: Age related nuclear cataract

The following section is adapted from the previously published review: Proteomic Characterization of the Human Lens and Cataractogenesis written by Cantrell and Schey, Expert Review of Proteomics, © 2021, reprinted by permission of Informa UK Limited, trading as Taylor & Taylor & Francis Group, http://www.tandfonline.com. (Cantrell & Schey, 2021a).

The ocular lens is a transparent tissue suspended behind the cornea and is responsible for transmission and focusing of light to the retina. Gradual opacification of the lens occurs with age and most frequently originates in the nucleus of the lens, classified as an ARNC (Figure 1-10) (Hains & Truscott, 2008). When light passes through the cataractous lens, it is scattered and the degraded signal limits visual acuity and perception. Cataracts were first documented in ancient Egypt as the 'white disease of the eye', and the earliest known descriptions of the lens come from the Roman medical textbook *De Medicina* written AD 30 (Albert & Edwards, 1996). Despite a long history of lens research, cataract causes 51% of global blindness and affects >65% of people over the age of 80 (*2010 Cataract Tables*, 2010; McCarty et al., 1999). As life expectancies increase, so too will the prevalence of ARNC. In 2010, twenty-four million Americans displayed cataract according to a LOCS II grading scale, but this number is expected to grow to more than fifty million by 2050 (*2010 Cataract Tables*, 2010). Cataract surgery costs more than $3.5 billion per year in the US and delay of cataract may subsequently save billions of dollars annually (A. Taylor, 1992). To date, no drug treatment has been developed for human cataract and surgical remediation is most often employed when access is available (Yonova-Doing et al., 2016).

In humans, ARNC occurs over the course of decades, making establishment of aging models difficult. For researchers in fields where model systems are well established for *in vivo* phenotype characterization, this may not be obvious (Truscott & Friedrich, 2019). In contrast to human cataract which develops over several decades, animal models such as the Emory mouse exhibit cataract over a period of 5-8 months (Kuck et al., 1981). A result is that small molecule cofactor abundances are not modified in animal models and protein changes that occur over decades may not occur. This is true for GSH where high abundances are required in the lens nucleus to reduce the levels of reactive oxygen species (V. N. Reddy, 1990). In humans, a barrier to extracellular diffusion and water transport forms by the fifth decade of life at the divide between the outer nucleus and inner cortex region (Moffat et al., 1999). This barrier prevents GSH transport to the inner regions of the lens, leading to GSH depletion in the lens nucleus (Sweeney & Truscott, 1998). The resulting oxidation of lens nucleus proteins appears to be a precursor to a cascade of events for ARNC in humans (Truscott, 2005). In mouse models, this barrier is not reported, and inconsistent analogues to the human barrier are seen in bovine and rat models (A. C. Grey et al., 2003; Vaghefi et al., 2012). For oxidative stress simulation, hyperbaric oxygen (HBO) treated guinea pigs show the greatest similarities to human lens proteome aging and cataractogenesis (Giblin et al., 1995), however, as with other model systems of human ARNC, there are other molecular inconsistencies of aging. We refer readers to the review of Lim et al. (J. C. Lim et al., 2016) for further discussion of cataract models.

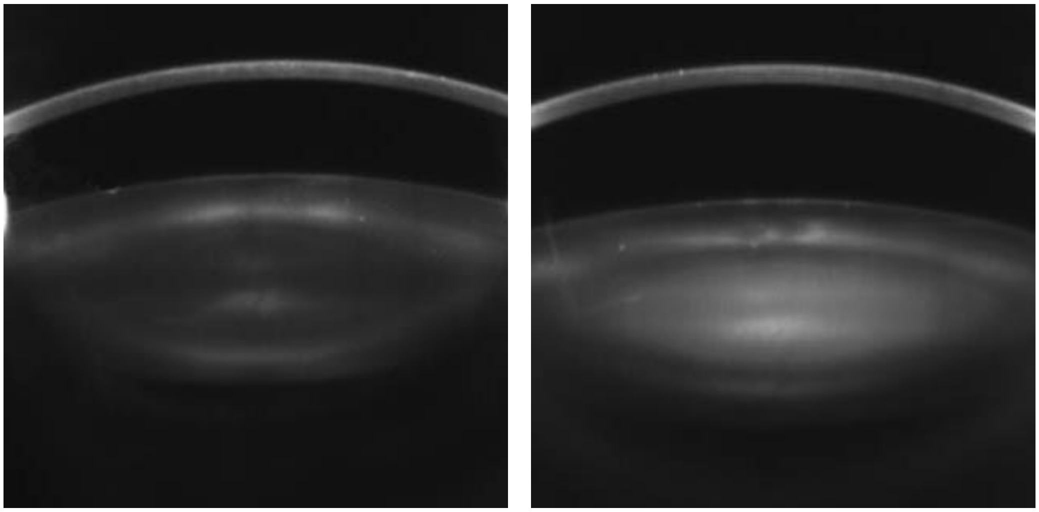

Figure 1-10 - Axial projection of two human lenses: left) a healthy lens with limited light scattering, right) a lens with a developed ARNC. Light is strongly scattered through the lens nucleus. Figure adapted from Yonova-Doing et al., 2016.

1.9. Brief review of lens proteomics methods

The following section is adapted from the previously published review: Proteomic Characterization of the Human Lens and Cataractogenesis written by Cantrell and Schey, Expert Review of Proteomics, © 2021, reprinted by permission of Informa UK Limited, trading as Taylor & Taylor & Francis Group, http://www.tandfonline.com. (Cantrell & Schey, 2021a)*.*

As a consequence of lifelong protein maintenance, lens proteins undergo substantial modification in the form of both enzymatic and non-enzymatic PTMs as well as protein abundance changes (MacCoss et al., 2002; Z. Wang et al., 2013). The compound effect of each modification manifests as ARNC; however, no studies have specifically studied the combined effect of multiple modifications *in vitro* or *in vivo*.

To characterize the lens proteome, HPLC based detection, 2DGE, and various MS approaches have been implemented. However, several outstanding complications of the lens proteome make proteome analysis challenging. Complications include the overwhelming abundance of few crystallin species in the soluble proteome, sampling of the many critical function membrane proteins, the high number of proteoforms caused by compounding PTMs, and transition of proteins from soluble to insoluble due to modification. Each of these complications are significant in ARNC formation and when studied correctly, may uncover biological phenomena in lens aging and ARNC formation.

It stands to reason that functional modification of more than one protein is responsible for ARNC formation due to a complex network of protein-protein interactions. Measurement of such complexity must quantify modified and unmodified proteoforms a measurement that is best executed by LC-MS/MS. Furthermore, in lens proteomics, the spatiotemporal organization of fiber cells allows improved inference by division of tissue into cell age-specific sub-proteomes. These fibers may be collected either by manual, concentric dissection at lens sutures or equatorial sectioning of the frozen lens followed by concentric biopsy punches. To prevent crystallin products from suppressing the signal of low abundance proteins, solubility fractionation has been widely implemented in lens studies. This often results in fractions including water soluble (WSF), aqueous urea soluble (USF), and aqueous urea insoluble (UIF) fractions. The WSF retains the vast majority of crystallins in the lens and is composed of proteins that are less likely to be actively contributing to ARNC. The UIF in contrast is largely composed of membrane and cytoskeletal proteins and the proteins, including many crystallins, that have become insoluble or aggregated in the lens. Proteins in the UIF are most likely to contribute to cataractogenesis due to their insoluble cytoplasmic nature or MCS association. To further complicate data interpretation, lens proteomes naturally change as a function of age e.g., as fibers age, they lose enzymatic and metabolic activity as associated proteins are degraded.

While LC-MS/MS allows extensive coverage of the lens proteome, well-defined spatial analysis is critical for insights into proteome aging. Although the utility of IMS for spatial characterization of the lens has been demonstrated, several new spatially resolved technologies have emerged that may be useful in future lens studies. Here we describe the impact that whole proteome inference has had in identifying moderated protein networks in ARNC formation, spatial methodologies and their impact, and opportunities for enhanced lens proteomic methods in the future.

Unlike PTM specific measurements, measurements of the whole lens proteome seek to identify age-related changes in protein and proteoform abundances. Early whole proteome measurements were done with western blotting or 2DGE (Delamere & Tamiya, 2004; Garland et al., 1996; McFall-Ngai et al., 1985). In the healthy lens of a 42-year-old, 2DGE facilitated the visualization of proteome differences in separated regions of the lens (Figure 1-11). It was clear that as fiber cells age, most proteins are degraded, but the diversity of proteoforms increases as multiply modified proteins increase in abundance (Figure 1-11A). Crystallins were examined and were found to undergo extensive modification after initial fiber maturation. As a limitation of 2DGE, relatively few proteins and proteoforms could be identified. This limitation was partially addressed by the use of Multi-Dimensional Protein Identification Technology (MuDPIT) LC-MS/MS on the UIF of a whole lens proteome of a 4-year-old congenital cataract patient in 2002 (MacCoss et al., 2002). While not from an ARNC lens, this approach allowed identification of 253 proteins and facilitated the identification of 73 PTM sites. Initial investigation to age-related modifications was done in four lenses: a 3-day old, clear 70-year old, cataractous 70-year old, and cataractous 90-year old (Wilmarth et al., 2006). As with similar studies, solubility fractionation was performed, and cation exchange was used as a second dimension of chromatography. With low resolution instruments operated in Data-Dependent Acquisition (DDA) mode, 491 modification sites were identified.

Importantly, deamidated residues were more abundant by spectral counting in the insoluble fractions and in older lenses further emphasizing the importance of PTMs in protein solubility and aging.

By combining solubility fractionation, MuDPIT analysis and improved linear ion trap instrumentation and data analysis, significant improvements in protein and peptide group identifications were reported in 2013 (Z. Wang et al., 2013). In the UIF, 951 proteins were identified across 3 lenses (aged 25, 37 and 58 years). Separate phosphopeptide analysis by TiO_2 enrichment afforded 855 phosphosites on 271 proteins. Finally, this study was among the first to implement Gene Ontology (GO) analysis in the lens (Table 1-1). GO analysis facilitates the identification of protein-network enrichment not easily identified with specific protein analyses often directed towards PTMs (Ashburner et al., 2000). Other ontology networks including KEGG (Kanehisa & Goto, 2000) have since been used for protein-network annotation (Z. Wang et al., 2013; X. Wu et al., 2017a). This early ontology inference was able to identify several key processes in lens development and aging; however, the study did not employ spatial separation of the older nuclear fibers from the youngest fibers in the cortex and ontological implications were limited by non-quantitative overrepresentation analysis of differentially expressed proteins (Lavallée-Adam et al., 2014; Timmons et al., 2015).

Early MS proteome measurements were carried out on low-resolution mass spectrometers. The introduction of high-resolution orbitrap mass analyzers have greatly improved protein quantification for high dynamic range samples such as lens protein lysates (Hu et al., 2005; Krey et al., 2014). To identify proteome differences between whole lenses of different disease state (age related cortical & nuclear cataract, congenital cataract, regenerative lenses with secondary cataract and healthy lenses), one study utilized protein extracts from eight lenses for MS analysis without fractionation or spatial segmentation (X. Wu et al., 2017a). Assisted by orbitrap instrumentation, 1,251 protein groups were identified alongside ontology pathways specific to the nuclear & cortical cataract lens including: endocytosis, salivary secretion, proximal tubule bicarbonate reclamation, vasopressin-regulated water reabsorption, and endocrine and other factor-related calcium reabsorption. Additionally, insignificant abundance differences of αA- and αB-crystallin in cataractous lenses compared to healthy lenses was shown, while γ-crystallins and several β-crystallin subunits displayed near zero abundance in the age-related cataract lenses. These results added to the assumption that WSF and USF are not highly informative for studies of ARNC progression.

As emphasized above, it is of great importance to spatially resolve findings to produce new ARNC directed insights regarding the spatiotemporally organized lens. In measurements of the entire lens, young fiber cells are not separated from metabolically inactive fibers that have sustained optical transparency for several decades which decreases the impact of such measurements. In a similar way, a boundary of fibers with and without organelles lies in the cortical region, adjacent to the barrier to extracellular diffusion that forms in approximately the fifth decade of human life. Thus, even segmentation of the lens into one or a few concentric regions for LC-MS/MS analysis does not effectively capture the continuous fiber-cell aging processes that occur throughout life. Spatially resolved proteomics investigation must effectively coordinate spatial resolution, network coverage, and acquisition time. Here we discuss the impact that IMS, micro liquid extraction surface analysis (microLESA), laser capture microdissection (LCM) coupled to nanodroplet processing in one pot for trace samples (nanoPOTS), and multi-isotope imaging mass spectrometry (MIMS) have had in spatial mapping of the lens and the future opportunities they provide.

Often called a “molecular microscope”, MALDI IMS has been used to detect protein, lipid, and metabolite relative abundances in a spatially resolved, untargeted manner (A. C. Grey & Schey, 2008; Korlimbinis et al., 2009; Z. Wang et al., 2020; Z. Wang & Schey, 2018; Wenke et al., 2015). In MALDI IMS, tissue sections are coated in a matrix that facilitates ionization upon laser ablation. Pulsed sampling in a rastered step allows for assembly of molecular information that correlates to the tissue localization. Heatmap plotting of selected signal abundance results in an image displaying molecular spatial distributions. Typical protein images are compiled at 50 µm step/pixel size but spatial resolution may be reduced to 5 µm with optimized laser ablation (Zavalin et al., 2014). Intact protein IMS with time of flight mass analyzers (TOF) effectively detect low weight proteins in the 5 – 25 kDa range and can discriminate modified from unmodified proteins (Chaurand et al., 2008; Korlimbinis et al., 2009). In the lens, this allows measurement of AQP0 and crystallin family proteins, but prevents detection of large undigested proteins such as connexin and intermediate filament families of proteins (Figure 1-6). To circumvent this limitation, bottom-up approaches can be implemented with on-tissue tryptic digest prior to MALDI ionization. Subsequent products can then be detected by both TOF and Fourier Transform-Ion Cyclotron Resonance (FT-ICR) analyzers. Even with bottom-up approaches, MALDI IMS experiments do not capture as complete of a protein network as LC-MS/MS experiments, resulting in incomplete analysis of low and intermediate abundance products. To improve peptide isolation, tissue washing prior to digestion, increased pixel size and continuous accumulation of selected ion (CASI) in an ion trap have been implemented to improve signal intensity (Fuchser et al., 2014). Finally, MS2 spectra are typically not collected in IMS experiments, so secondary MS/MS experiments are needed for definitive peptide identification (Wenke et al., 2016). MALDI IMS is then capable of multi-cell resolution, may achieve notable proteome depth, and can be performed in reasonable acquisition times.

To demonstrate the success of MALDI IMS in lens studies, Wang et al. confirmed LCM-LC-MS/MS findings from Wenke et al. that there is a transition of ubiquitous vimentin in the outer cortical fibers to lens specific beaded filament proteins filensin and phakinin in the inner cortex of the lens (Figure 1-12) (Z. Wang et al., 2020; Wenke et al., 2016). In this study of moderately abundant, larger molecular weight cytoskeletal proteins, successive washes were performed prior to on-tissue digest. A 50-um ablation spot was used with a 150-um raster to optimize signal intensity on a 15T FT-ICR instrument. Additionally, CASI was employed to enhance the signal of pre-selected modified peptides with validation by LC-MS/MS. While this study of a bovine lens was not targeted for detection of ARNC formation, it highlights the value of spatial mapping of the lens for detection of cell-age specific changes. IMS has also been used to indicate where crystallin truncations and AQP0 modification occur in human lenses as a function of age (Anderson et al., 2020; A. Grey & Schey, 2009; Wenke et al., 2015).

Though low abundance proteins can be detected in IMS experiments with the assistance of CASI, network coverage is not comparable to the proteome identified by LC-MS/MS studies. MicroLESA (Ryan et al., 2019) has been used in previous lens analyses to capture on-tissue digested lysates at >100 µm radius (Z. Wang et al., 2020). In serial sections of bovine lenses, the microLESA method allowed identification and relative quantitation of intermediate filament proteins and each truncation product. MicroLESA results enhanced the hypothesis of lipidation shortly after filament switch to lens specific proteins but was not used for analysis of the lens proteome at large. Since microLESA employs LC-MS/MS, it allows in-depth proteome network analysis, but relative to other technologies does so at low spatial resolution and with long acquisition times. Combining microLESA and IMS is a natural technological progression given the identification bottleneck posed by IMS and the spatial targeting desired in microLESA. Consequently, top-down IMS has previously been paired to ETD LC-MS where samples are collected by 1 µL on-tissue extractions to unambiguously identify crystallin proteins including truncated βA3-crystallin which will not be identified in a bottom-up approach (Schey et al., 2013). The combination of electron transfer dissociation LC-MS paired to IMS has been expanded on recently to map β- and γ- crystallin protein spatial distribution in the bovine lens (Anderson et al., 2020). There remains significant space for expansion of top-down MS lens studies – especially those evaluating spatial distribution of PTMs.

In the lens, LCM has been used to collect small, spatially targeted regions of the lens before trace LC-MS/MS sample analysis (Z. Wang et al., 2008; Z. Wang & Schey, 2021). Recently, trace LCM-MS/MS was used to characterize proteins at either side of the extracellular diffusion barrier (Z. Wang & Schey, 2021). Developments in single-cell proteomics have ushered in new low-sample methodologies, such as nanoPOTS, capable of rapidly characterizing >2,000 protein groups on an LC-MS/MS platform (Budnik et al., 2018; Dou et al., 2019; Zhu et al., 2018). Like other single-cell technologies, the nanoPOTS workflow begins with fluorescence-assisted cell cytometry for cell capture (Budnik et al., 2018; Specht et al., 2019; Tsai et al., 2020; Zhu et al., 2018). Subsequent deposition onto a lithographically created microwell plate and automated sub-microliter reagent additions for lysis, reduction, alkylation and digest is performed to isolate peptides in a reproducible fashion (Zhu et al., 2018). To reduce signal-to-noise, isobaric labeling strategies such as iBASIL and SCOPE-MS have been employed to maximize identifications (Budnik et al., 2018; Tsai et al., 2020). A particular strength of the nanoPOTS platform introduced by Kelly et al. is label free trace sample preparations (Zhu et al., 2018). Recently, nanoPOTS was extended to imaging technologies by dissecting tissue with LCM directly onto microwell plate (Piehowski et al., 2020). In mouse uterine tissue, this method facilitated cell-type specific identification of differentiation based on >2,000 identified protein groups at 100 μm^2 voxel area. Such technology applied to the lens may allow expansion of IMS network coverage and subsequent knowledge of fiber differentiation at fine spatial and molecular resolution. Relative to each previously described method, nanoPOTS is capable of moderate spatial resolution that exceeds current capabilities of microLESA and is one of the best methods for proteome network coverage but requires lengthy sample acquisition times.

Each of the previous methods is capable of proteome characterization of separate bundles of concentric fiber cells. However, these methods are incapable of mapping subcellular proteome organization or differentiating single fiber cells. Due to the 0.75 – 14 µm cross section of fiber cells (depending on axis and cell age, older are smaller), the most effective technology for nanometer resolution definition is a microscopy-based approach (V. L. Taylor et al., 1996). Outside of standard immunohistochemistry experiments, CODEX (co-detection by imaging) microscopy offers an exciting method to spatially coordinate >100 proteins on a single tissue section but has not yet been applied to age-related tissue measurements. CODEX functions by conjugating unique nucleotide extenders to primary antibodies allowing simultaneous submicron resolution in a semiquantitative manner (Goltsev et al., 2018). Recent developments to hybridize secondary ion MS (SIMS) with scanning electron microscopy (SEM) yielded MIMS technology capable of proteomic characterization at 50 nm resolution (Arrojo e Drigo et al., 2019). Unlike other methods, MIMS does not allow identification of individual proteins because aged protein signatures are identified by diet supplemented N^{15} isotope. However, MIMS does allow measurement of aged proteins in a pulse chase-format of labeling. The best implementation of MIMS may be achieved with lenses of HBO guinea pigs to study the rate of cellular differentiation and migration towards the lens nucleus (Giblin et al., 1995). MIMS offers the best spatial resolution of any presented method but has the slowest sample collection rate and has the most limited proteome network coverage. Nonetheless, MIMS and similar microscopy techniques have important implications for lens proteome and ARNC characterization. The relative strengths and weaknesses of each discussed method is summarized in Figure 1-13.

The outstanding goal of ARNC proteomics research is to determine the impact that age-related single protein modifications and network-wide perturbations have on ARNC occurrence. Thus, the features in cataractous subjects that have clear abundance separation from the same feature in healthy lenses are of highest interest. Plotting feature intensity alongside subject age and calculating a linear regression is the most common method for identifying age-related changes. Pathological feature classification is presumptively simpler, comparing same age donors at various LOCS II grades to determine feature that are significantly differentiated with cataract intensity. However, limitations in cohort composition (e.g., size of cohort, subject age range, morbidity control, extent, and type of cataract) reduce statistical power in past studies.

Classification of lens age or pathology based on a whole proteome measurement requires sufficient network coverage to minimize unmeasured feature, so-called “missing data”, impact on model development. Surprisingly, there are relatively few studies that correlate age with whole lens proteome changes. In the lens, an ontological protein analysis detected 19 ontologies differentially expressed by increased protein abundance, however this analysis was limited to one age-related cataract that encompassed both cortical fibers and nuclear fibers(X. Wu et al., 2017a). Additionally, quantitative enrichment was not calculated, which is now computationally realistic with GSEA or PSEA-quant algorithms (Lavallée-Adam et al., 2014). In other long lived protein containing tissues, LC-MS/MS has been used for detection of proteins and protein networks which are most influential in aging and pathology by employing machine learning classification (Angelidis et al., 2019; Lei et al., 2020; Ubaida-Mohien et al., 2019). In cartilage, measurement of age-matched subjects revealed significant differences between Kashin-Beck disease and osteoarthritis tissues (Lei et al., 2020). While each disease is similar, 375 proteins were found to be differentially expressed and were significantly associated with cell junctions, and signal transducer activity. In muscle fiber proteomics from 60 healthy patients, differences between patients along a continuous age gradient was readily detected by PCA feature extraction, yielding 361 proteins with reduced representation and 904 with increased representation as a function of age (Ubaida-Mohien et al., 2019). Overexpression analysis of the differentially expressed genes demonstrated that ribosomal proteins and proteins involved in energetic metabolism were downregulated with age, while proteins associated with immunity, proteostasis and alternative splicing were upregulated. Since strictly healthy patients were used in this cohort, no biomarker of disease was analyzed. The successes of biomarker and age-determination studies clearly paves a path for the future of ARNC proteomics research, and continuous improvements in the methods for analysis must be actively considered for effective investigation.

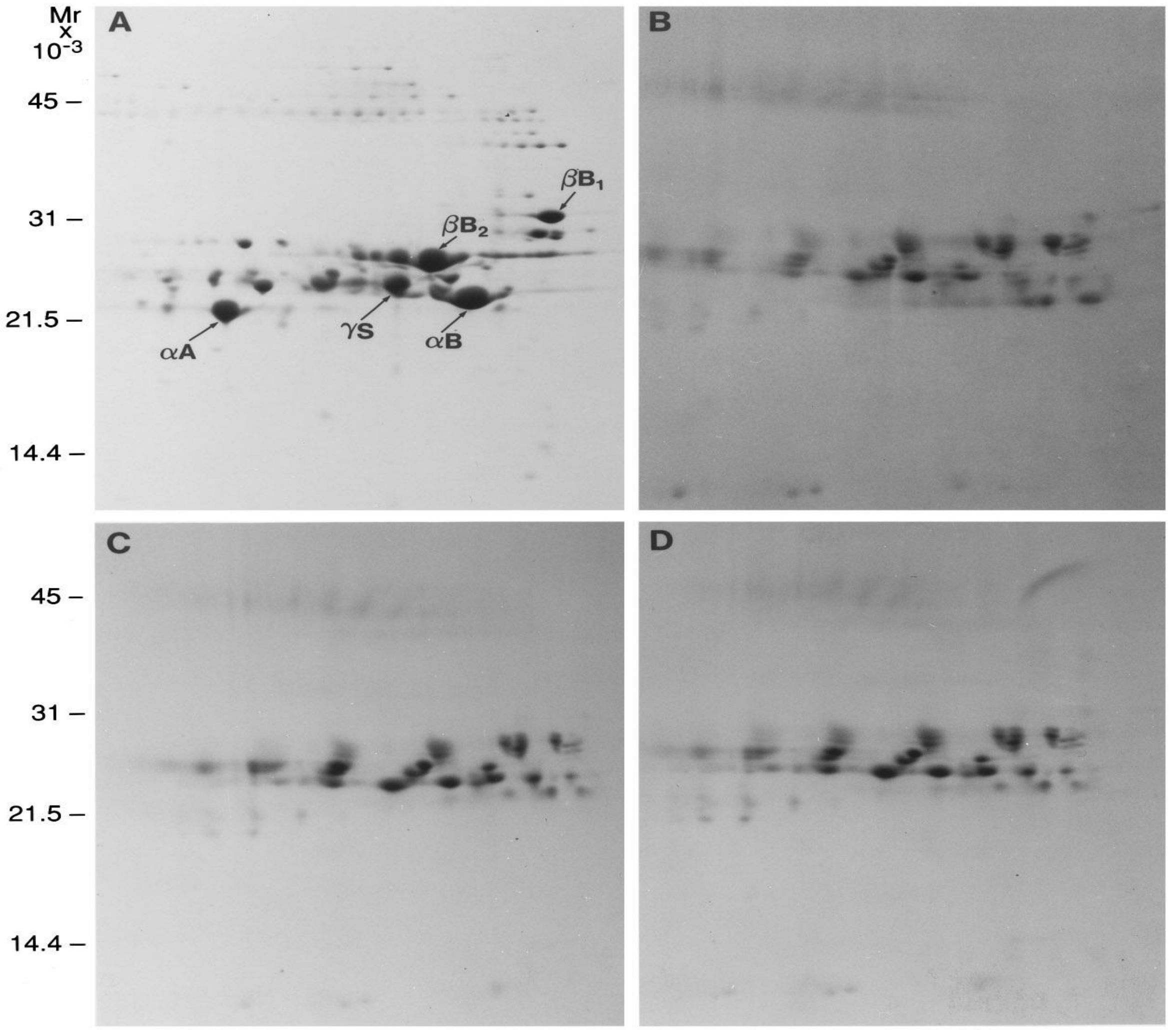

Figure 1-11 - 2DGE of a 42-year-old lens with manual dissection and separate analysis of A) the outer cortex, B) outer nucleus, C) inner nucleus, D) the innermost region of the inner nucleus, formed in embryogenesis. Several α-crystallin, β-crystallin and γ-crystallin species are annotated in A. Second dimension of focusing is from acidic (left) to basic (right). Figure from Garland et al., 1995.

Table 1-1 - Enriched Gene Ontology IDs and KEGG Pathways estimated by DAVID Bioinformatic tools. Sample collected from 3 human lenses. Figure adapted from Wang et al., 2013.

	Terms	**Number of Genes**	***P* Value**
Molecular function	Structural molecular activity	130	5.66E-39
	GTPase activity	58	6.53E-24
	Protein Binding	599	2.62E-22
	Structural constituent of eye lens	17	1.35E-19
	GTP binding	71	2.26E-19
	Guanyl nucleotide binding	72	2.53E-19
	Catalytic activity	414	6.29E-18
	Nucleotide binding	209	7.14E-14
	Structural constituent of cytoskeleton	26	1.28E-13
	Pyrophosphate activity	96	1.43E-13
Biological process	Translational elongation	43	9.63E-26
	Cellular carbohydrate catabolic process	38	1.12E-23
	Alcohol catabolic process	36	2.45E-22
	Glucose catabolic process	30	5.98E-21
	Glucose metabolic process	46	2.63E-20
	Glycolysis	16	4.27E-19
	Small GTPase mediated signal transduction	58	3.05E-15
	Cellular component assembly	110	4.35E-14
	Actin filament-based process	43	1.49E-10
	Cytoskeleton organization	62	1.55E-10
KEGG pathway	Ribosome	40	7.96E-20
	Glycolysis/Gluconeogenesis	29	4.61E-15
	Pentose phosphate pathway	14	2.27E-08
	Proteasome	17	8.07E-07
	Focal adhesion	39	1.83E-06
	Pyruvate metabolism	14	1.58E-05
	Tight junction	28	1.82E-05
	Gap junction	21	4.46E-05
	Glutathione metabolism	15	4.96E-05
	Regulation of actin cytoskeleton	36	1.03E-04

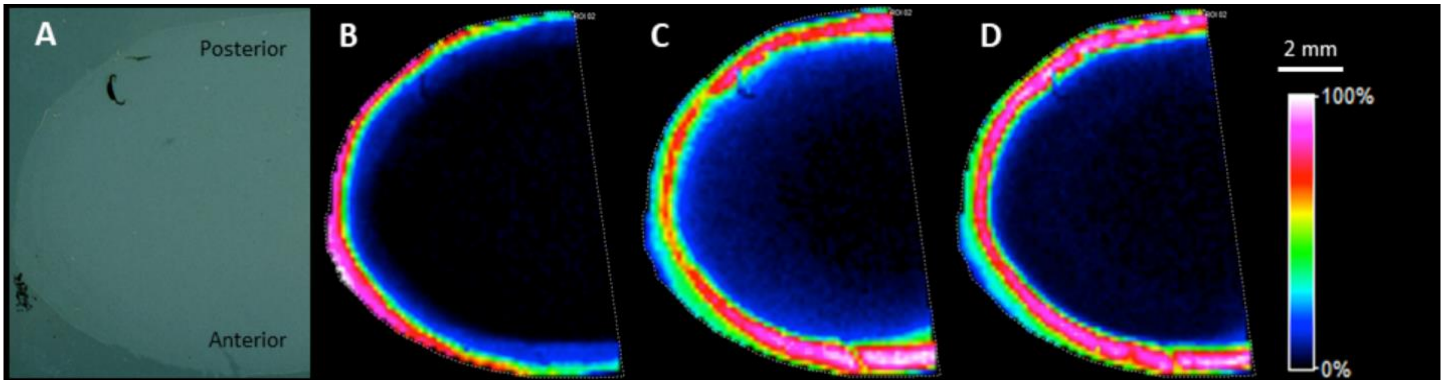

Figure 1-12 - MALDI imaging of lens intermediate filament proteins in an axial lens section after on- tissue digestion. A: optical image; B: image for vimentin 37-50; C: image for filensin 34-48; D: image for CP49 28-42. Figure adapted from Wang et al., 2020.

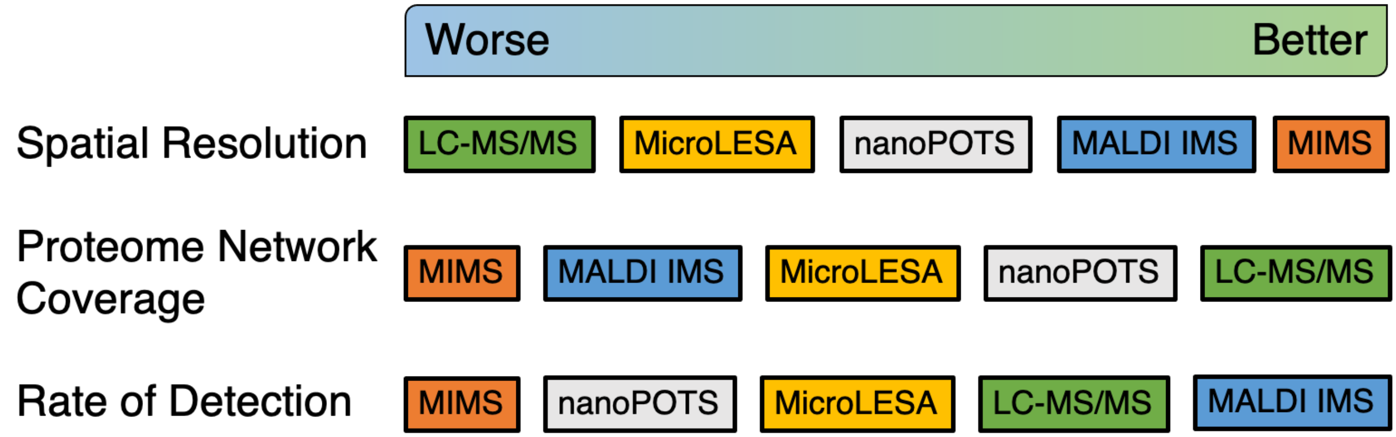

Figure 1-13 - Summary of relative spatial resolution, proteome networks coverage and rate of detection for each of the discussed technologies. Differences are not uniform, especially in comparisons of spatial resolution. Figure adapted from Cantrell and Schey, 2020.

1.10. Data-independent acquisition

1.10.1. Brief introduction

An emerging method in tandem mass spectrometry proteomics is Data-Independent Acquisition (DIA). DDA uses an MS1 scan to define the list of precursors that should be analyzed by an MS2 scan (Figure 1-14). A result of experimental parameterization, only the more abundant precursors are detected in a DDA experiment (Michalski et al., 2011). Precursors may not receive an MS2 experiment for several reasons including: 1) a peptide falls below the signal intensity threshold for MS2 event triggering, 2) a peptide of equal precursor mass to one on the dynamic exclusion list elutes, and 3) too few MS2 scans occur to have an MS2 scan for each eluted peptide. DDA experiments are especially limited when a short chromatography gradient is used, or the sample analyzed has peptides of significantly different abundance (Johnson et al., 2013; Messner et al., 2021). To overcome these limitations, data-independent sampling of each possible peptide has been suggested as an effective method to measure complex samples more accurately.

The first widely recognized DIA experiments were by Venable in 2004 (Venable et al., 2004), but improvements in instrumentation and computational power have allowed more routine implementation of DIA (Amodei et al., 2019; Bekker-Jensen, Bernhardt, et al., 2020; Cantrell & Schey, 2021b; Searle et al., 2018). Several different DIA approaches have been proposed, but sequential window acquisition of all theoretical mass spectra (SWATH-MS) is the most commonly employed for measurement of complex samples (Rosenberger et al., 2014). In a SWATH-MS experiment, like in DDA, an initial MS1 survey scan of all intact peptides is taken. Unlike DDA that isolates all precursors within 0.35 - 0.7 m/z tolerance of the observed precursor mass in MS1, SWATH-MS uses wider windows that can rapidly survey all theoretically possible precursors (Pino et al., 2020; Searle et al., 2018). All peptides within the wider window are isolated prior to fragmentation and detected in a MS2 scan. After MS2 scanning of the first wide isolation window, the next sequential window, offset from the first, is used for precursor isolation and fragmentation. Sequential windows are cycled to a pre-determined loop count, not necessarily spanning the entire mass range, before performing another MS1 scan. In this way, MS1 scans are interspersed between windowed wide window MS2 scans (Reubsaet et al., 2019).

As in DDA, SWATH-MS (further referred to as DIA) has a significant number of parameters that must be defined. As all peptide precursors within the window are co-fragmented and measured, window size must be modest to retain specificity for precursor identification (Pino et al., 2020). Effective windowing uses widths of 10-24 m/z. While DIA is intended to identify all theoretically possible peptides, most peptides fall within a smaller range. The distribution may be calculated within a database, but empirical observation suggests that a range from 400-1000 m/z captures >90% peptides that can be identified in an experiment. Thus, 25-60 windows can be used to access the mass range from 400-1000 m/z (Figure 1-14). Extension of this range to 1100 m/z may be necessary to capture peptides with heavy PTMs, including phosphorylation. Since peptides are simultaneously measured, high mass resolving power is required to unambiguously assign b- and y- ions in MS2. To accomplish this, a resolving power of 30,000 is suggested for each MS2 scan on orbitrap platforms. Similarly, MS1 scans of high resolution improve the determination of which precursors are potentially present in wide isolation windows. For this parameter, a resolving power of 60,000 is reasonable. A limitation of these high resolving powers is long transient times on orbitrap instruments. As resolving power scales linearly by transient length on orbitrap instruments, (~60 ms for 30,000 resolving power in a high field orbitrap Exploris 480 instrument), the maximum ion injection time (IIT) can be increased to just below the transient length to maximize the accumulation of low abundance precursors. To enable this, the automatic gain control (AGC) is set to a higher value than suitable for a DDA experiment. In a well-designed DIA experiment, ~72,000 peptides can be detected from a HeLa lysate, far exceeding the ~34,000 peptides accessed by DDA methods of comparable quality (Searle et al., 2018).

Several improvements to the SWATH-MS DIA workflow have been presented, but the most practical improvement is offset MS2 windowing (Amodei et al., 2019). A limitation to DIA in its basic implementation is the complexity of spectra that may be measured in a >10 m/z wide window. Without some degree of specificity for which fragment ions are attributed to the potential precursor ions, it may become impossible to assign fragments to precursors and vice versa. To overcome this obstacle, Amodei et al. suggested the use of offset windows in such a way that sequential windows acquisition across the entire precursor mass range is done followed by a second series of sequential windows that are offset by half the window width (e.g., the first window in series one may be from 400 – 420 m/z and the first window in series two may be from 390-410 m/z). After collecting raw instrument files, the ProteoWizard msconvert tool is used to convert vendor specific files to unencrypted, community accessible mzML files (Adusumilli & Mallick, 2017). During conversion, msconvert deconvolutes MS2 spectra in such a way that signals are assigned to a smaller mass range that they are detected in within scan series one and two. Thus, the specificity of which precursors and fragment ions are associated is multiplied by 2x (Amodei et al., 2019). This windowing modification has demonstrated meaningful improvements in the assignment of peptides without sacrificing scan cycle time.

Several search paradigms exist for DIA, these algorithms are divergent from DDA algorithms where peptide sequence alone is sufficient to identify analytes and control for type-one error (Doerr, 2015). Because many peptides may elute in a single precursor isolation window, the complexity of DIA MS2 spectra exceeds that of DDA spectra and cannot be readily evaluated by humans. To circumvent this limitation, experimentally collected DDA spectral libraries have been proposed as a method for rapid matching and peak fitting of b- and y-ions in complex spectra. This method requires extensive sample fractionation and effective DDA search to produce a spectral library that fully equips evaluation of DIA spectra. A weakness of a spectral library is that only b- and y- ion masses and their intensities are measured. To improve on this, Searle and colleagues suggested the use of chromatogram libraries, where orthogonal separations are performed prior to DDA or DIA analysis using the exact chromatography that will be used in the DIA experiment (Searle et al., 2018, 2020). By using spike-in standard peptides, retention time is added as an additional dimension of peptide spectral matching, decreasing the probability of type-one error in spectral assignment. A key limitation of each of these methods is the expense of operating enough DDA sample acquisitions prior to injecting experimentally evaluated samples. To circumvent this, community-generated libraries have been produced and may be used to evaluate common tissues for quantitative changes if the protein of interest has been evaluated by other researchers (Rosenberger et al., 2014). In human and mice cell culture and tissues, this method is especially powerful due to the prevalence of these cell types in classic basic science experiments. Finally, it was desirable to limit the influence of other users acquisition on new user acquisition, so artificial intelligence frameworks such as Prosit have been developed to evaluate hypothesized b- and y-ion intensities given a standard collision energy and to estimate the chromatographic elution time of ions relative to one another in a complex lysate (Gessulat et al., 2019). Similar statistical frameworks are now implemented into various search algorithms for offline *de novo* calculation of spectral libraries from a provided fasta database file (Demichev et al., 2020).

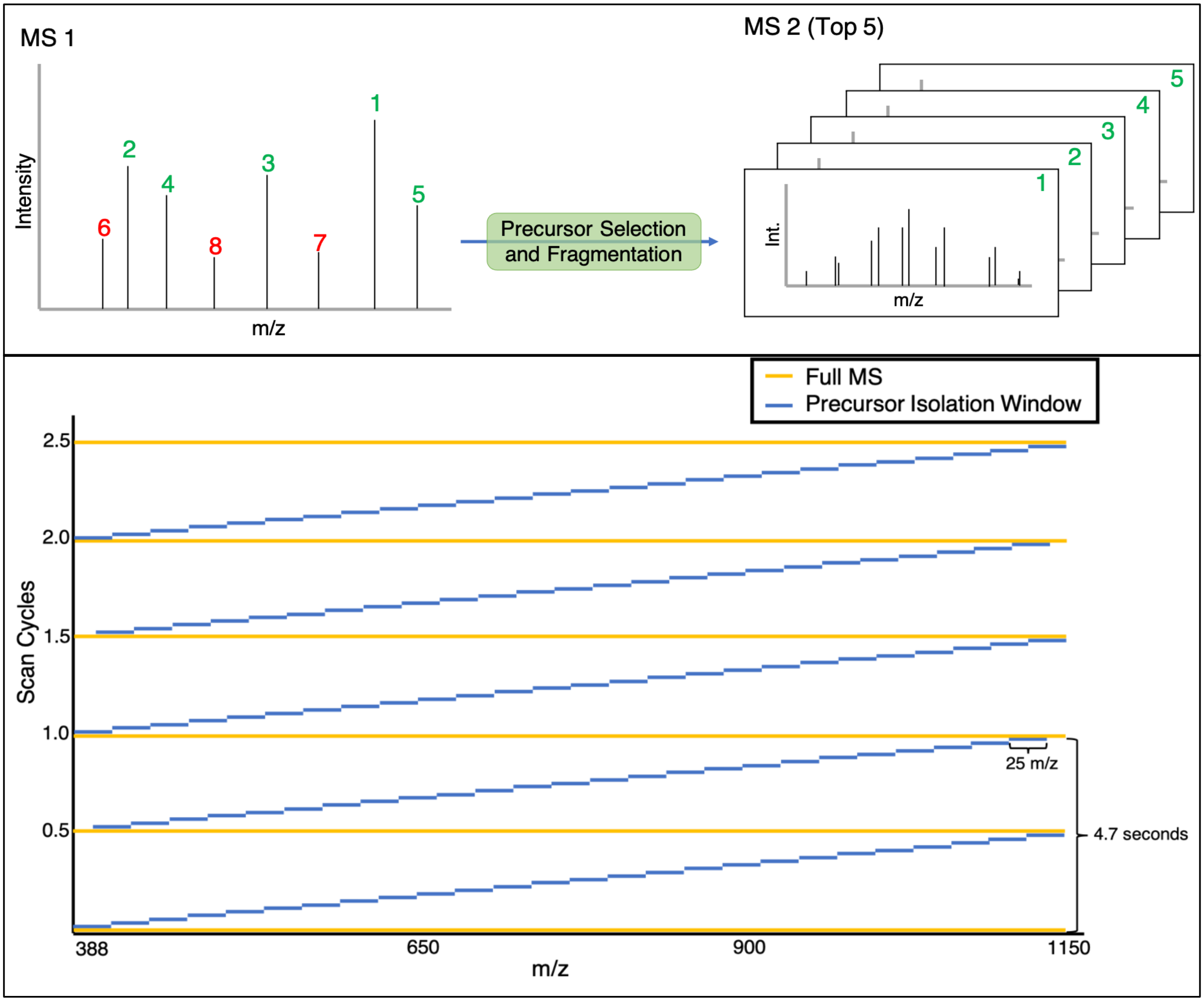

Figure 1-14 - Comparison of DDA (top) and DIA (bottom) windowing schematics. DDA selects only the most abundant ions for MS2 while SWATH MS DIA selects all precursors in mass windows where peptides are anticipated to be measured. Figure adapted from Cantrell and Schey, 2020.

1.10.2. Instrumentation

While any MS/MS-capable instrument may complete the steps needed for DIA data collection, several practical limitations reduce the instruments which may be used for reproducible and highly sensitive DIA measurements (Gillet et al., 2012). Perhaps the simplest of the usable instruments is the triple quadrupole mass spectrometer (QqQ). A key to DIA analysis is rapid scanning through the mass range, allowing frequent peak sampling of peptides for quantitation as in single reaction monitoring or similar quantitative experiment approaches. The limitation to most quadrupole instruments, including the QqQ instrument, is the low mass resolving power. As a result, the QqQ is not ordinarily considered for DIA proteomics, however it is suited to the generation of DDA spectral libraries. Likewise, ion trap instruments can be practically used for the generation of spectral libraries, but not for DIA spectral analysis. For the greatest sensitivity, it is suggested that high resolution instruments be used for library generation (Searle et al., 2020).

Two modern platforms are most conventional for DIA proteomic analysis. These are the quadrupole orbitrap hybrid instruments commercialized by ThermoFisher (e.g., Q-Exactive (QE) HF, QE HF-X, Exploris 240/480, Fusion, Lumos, Eclipse), and QTOF or Triple TOF instruments commercialized vendors including Bruker, Waters, Agilent, and Sciex. Practical differences between different TOF instruments exist, but presentation here is directed towards DIA with the Bruker TIMS TOF Pro. Differences between TOF instruments of different configuration exist, but are beyond the scope of this introduction (Aballo et al., 2021; Lewandowska et al., 2021).

Thermo quadrupole orbitrap hybrid instruments and tribrid instruments function identically in SWATH MS experiments, so discussion here is limited to the collection of data on the Exploris 480 platform (Bekker-Jensen, Martínez-Val, et al., 2020). Conventional ionization for the orbitrap platform is done via electrospray ionization (ESI) where a continuous plume of charged peptides are directed to the capillary inlet at the front of the instrument. Ions are then routed through ion optical elements and a quadrupole before accumulating in the C-trap, a bent linear ion trap. Once an AGC target or maximum IIT is reached, intact peptides are directed to the orbitrap mass analyzer. Before accumulation in the C-trap, the quadrupole serves as a filter for precursor ions in a desired m/z range. While the orbitrap resolves ion signals, a new packet of ions accumulate from the ESI source, this time being filtered into an ion window approximately 20 m/z units wide. Ions accumulate in the C-trap before reaching their AGC target or maximum IIT, are directed to the HCD collision cell before fragment ions are redirected to the C-trap and into the mass analyzer. The movement of ions through the Exploris 480 resembles that of other QE platforms but is distinct in that it has a smaller, high field orbitrap. This analyzer requires shorter transients to reach a given resolving power than other QEs (e.g., two times faster than the Exploris 120). This high field orbitrap is critical to allow rapid cycling of scan windows to enable coverage of all windows in the mass range and maximize the quantity of MS2 scans per ion to improve the quantitative accuracy of each peptide (Pino et al., 2020). Finally, the efficiency of ion transfer to the instrument can be improved by separation of peptides prior to mass analysis in a Field Asymmetric Ion Mobility Spectrometry (FAIMS) source (Swearingen & Moritz, 2012). FAIMS is an atmospheric pressure ion mobility interface that can selectively filter for ions of specified charge or to exclude ions of a specified charge. In DIA experiments, this is best used to filter out uncharged and singly charged ions which are not likely to be assigned as peptides (Bekker-Jensen, Martínez-Val, et al., 2020). Thus, FAIMS acts as a filtering source to reduce background signal which may otherwise complicate peptide assignment.

The most modern TOF platform for DIA proteomics is the qTOF platform on the Bruker tims TOF Pro (Trapped Ion Mobility Spectrometry Time of Flight)(Meier et al., 2020). Unlike orbitrap DIA acquisition, the tims TOF uses ion mobility via PASEF (parallel-accumulation serial fragmentation) for peptide separation at the front end of the instrument. In the conventional tims TOF DIA acquisition scheme, termed diaPASEF, the dual tims device separates ions by counteracting gas flow from the source with a variable electric field. Ions of different mobility (e.g., ions of low mass generally have higher mobility than those of high mass) are pulsed into the qTOF instrument. In the qTOF, pulses of PASEF ejected ions are directed, not filtered, by the quadrupole and delivered to a collision cell before accumulation in the reflectron TOF system. Each TOF mass analysis event takes approximately 100 us resulting in cycle times limited only by the scan rate of PASEF: approximately 50-100 ms/scan depending on instrument parameters. Thus, diaPASEF achieves significantly greater scan rates than orbitrap and collision-cross-section data adds a level of complexity to the data. Unlike the orbitrap platform which has variable resolution depending on parameterization, the tims TOF has a resolving power of approximately 35,000 R through the mass range, decreasing sensitivity possible for MS1 scans. Finally, because diaPASEF has rapid scanning, shorter chromatography gradients may be used to achieve similar results to those on an orbitrap platform. In settings where higher numbers of samples are to be measured, the TOF instrument is then a preferential instrument to a slower orbitrap platform.

1.10.3. Acquisition schemes

To this point, DIA has been introduced as primarily SWATH-MS and the similar but differentiated by ion mobility method, diaPASEF. Several alternatives to these scan modes have been utilized, including MS^E (Plumb et al., 2006), variable window SWATH-MS (Y. Zhang et al., 2015), GPF-DIA (Gas Phase Fractionated DIA)(Pino et al., 2020), Pulse-DIA (Cai et al., 2021), BoxCar (Meier et al., 2018), MSX (Egertson et al., 2013), SONAR (M. A. Moseley et al., 2018), and scanning SWATH-MS (Messner et al., 2021). A more extensive review of these methods was published by Zhang and colleagues (F. Zhang et al., 2020), so only the most significant changes are discussed here. Broadly, each of these scan modes can be subclassified as DIA methods that rely on quadrupole for precursor selection, those that multiplex precursor selectivity, and those that take advantage of rapid TOF scan rates to add additional layers to data complexity.

A key component of all discussed instruments for DIA is the quadrupole placed ahead of the mass analyzer. Thus, each method which utilizes a quadrupole for precursor selection can be performed on any high-resolution instrument. The most basic DIA method is MS^E, which unlike other methods does not filter ions into smaller selectivity windows (Plumb et al., 2006). In this method, a full MS1 scan is pulsed followed by fragmentation of all ions and simultaneous measurement of all precursors. The complexity of the resulting spectrum is such that MS^E is not well suited for measurement of complex samples and is instead used for analysis of more pure samples, as demonstrated by its use in Hydrogen-Deuterium Exchange mass spectrometry (Cryar et al., 2017). Following MS^E, SWATH-MS is the next most complex method, already introduced, and is well suited for complex sample measurement (Amodei et al., 2019). The addition of overlapping windows to SWATH-MS studies improves precursor identification, but is not a distinct method of DIA. An alternative to overlapping window placement, it is assumed that lower mass-to-charge isolation windows have more rich spectra than those at higher mass-to-charge range (Y. Zhang et al., 2015). To accommodate, variable window SWATH-MS uses more narrow isolation windows (4-8 m/z) between 400-600 m/z and wider windows (10-50 m/z) thereafter. This method has been shown to improve identifications, but its implementation is complicated by the limited quantity of search algorithms suited to search its data. The use of variable window SWATH-MS decreases total cycle time and subsequently increases the quantity of peaks per precursor; however, it does decrease sensitivity to higher mass precursors. To overcome this limitation, GPF-DIA has been used, primarily for library generation (Pino et al., 2020). In this format, a sample is re-injected for DIA analysis at least 6 times with approximately 4 m/z width windows in each scan. Unlike other methods, these windows are not collected over the entire 400-1000 m/z range of SWATH-MS and are instead only collected in 100 m/z width acquisition intervals (e.g., injection 1 is 400-500 m/z, injection 2 is 500-600 m/z, etc.). A clear advantage of this is that there will be more robust coverage of all precursors relative to single injection methods, but requires extended access to instrumentation, thus its use in library generation is most recommended. An additional benefit of GPF-DIA is that with overlapping window schematics as presented for SWATH-MS, effective precursor isolation window width is 2 m/z, closely resembling DDA or targeted acquisition modes. Finally, Pulse-DIA combines the principals of variable window SWATH-MS and GPF-DIA (Cai et al., 2021). The utility of Pulse-DIA is limited by the weaknesses of each method contributing to it, and its prime improvement over GPF-DIA is that only 4 injections are used to cover the whole mass range. In large sample cohorts, these multi-injection schemes must be carefully evaluated to control for instrumental deviation between samples and for the proper quantitative assembly of protein groups. To analyze Pulse-DIA datasets, it is then recommended to compile libraries in Spectronaut and search data against the spectral library in DIA-NN in order to generate a spectral library of highest quality and distinct quantitative evaluation (Cai et al., 2021; Demichev et al., 2020). The most adopted of these methods remains SWATH-MS, with most methods utilizing overlapping windows as acquisition schemes. The methods are transferable, and data can be searched with any search engine that takes the open source mzML input.

A key challenge to orbitrap instrumentation is that the mass analyzer takes extended periods of time to resolve peaks. This limitation has been circumvented by taking advantage of the C-trap (Meier et al., 2018). In BoxCar, an MS1 scan is resolved at high resolving power (R > 50,000). Then, for the duration of the MS1 transient (>100 ms), ESI continues to deliver ions to the instrument, far exceeding the charge capacity of the orbitrap. To better use the transient resolving time, multiple staggered packets of ions are delivered to the C-trap with each ion having an AGC target or Max IIT proportional to the charge capacity of the mass analyzer or its transient (e.g., packets of 400-420, 460-480, 520-540, etc.). The multiple ion packets are then co-fragmented and analyzed at high mass resolving power (R > 50,000), while additional packets are delivered to the C-trap. These packets are both staggered to the mass windows in the first ion packet (e.g., 420-440, 480-500, 540-560, etc.) and to the mass range of prior staggered packet groups (e.g., 580-600, 640-660, 700-720). This dataset is deconvoluted by MaxQuant's search algorithm Andromeda for search. The analysis of BoxCar data is computationally challenging and after the development of improved SWATH-MS methods, is not widely used. An alternative to this is approach is MSX (Egertson et al., 2013). MSX is in principle identical to BoxCar but can be performed on any trapping instrument. In MSX, instead of pre-defined window acquisition schemes, the population of possible precursor isolation windows is defined in method development, then during acquisition, multiple isolation windows are co-trapped and fragmented at random until all windows have been slected between MS1 scans. A limitation of MSX is that as with BoxCar, few search algorithms can evaluate its data. It is anticipated that more windows can be selected at once in MSX and can be of narrow mass range, but computational stringency to deconvolute, using multiple scan cycles to do so is not highly feasible. Unfortunately, the orbitrap specific methods have not yielded great improvements over SWATH-MS methods and are not suggested for robust use in a translational or clinical setting.

Finally, several methods have been developed with the TOF mass analyzer in mind. Unlike the Orbitrap, TOF analyzers are capable of rapid analysis of pulsed sets of ions at sufficient resolving power for DIA analysis. As introduced, diaPASEF is a clear implementation of a TOF instrument with data complexity enhanced by PASEF separation of ions. It should be noted again that diaPASEF does not select windows as in SWATH-MS and instead separates ions based on ion mobility, which is correlated with precursor mass, and thus not entirely orthogonal to m/z as a dimension for spectral matching (Gessulat et al., 2019; Messner et al., 2021). Another TOF approach is the proprietary SONAR method produced by Waters (M. A. Moseley et al., 2018). Marketed as an alternative to MS^E, SONAR is like SWATH-MS where MS1 scans are taken followed by isolation window scans as in SWATH-MS. However, SONAR varies collision energy with scan cycle. In the first scan cycle, a low collision energy is used for the entire mass range and then in the second cycle, collision energy is increased in correlation with precursor mass range, with all ions receiving a greater collision energy for fragmentation than in the first scan cycle. The practical value of this is that the TOF analyzer rapidly proceeds through the entire mass range and the cycled collision energy allows greater search algorithm sensitivity towards precursor assignment. Finally, scanning SWATH DIA was developed as a variant of SONAR, where the original low collision energy scan used in SONAR is omitted (Messner et al., 2021). The assumption employed is that high mass ions fragment best with higher energies and thus more complete fragmentation is achieved with variable, higher collision energy data acquisition. Both SONAR and scanning SWATH DIA are currently developed to enable short and high flow (e.g., <40 minutes and µL/min) chromatographic separations, greatly accelerating acquisition times for large sample cohorts.

1.11. Perspective of statistical analysis and considerations

With iterative improvements in methods, instrumentation, and computational power, the workflows for searching DIA data have started to more resemble those of DDA data relative to early DIA search schemes. DIA search results also take advantage of statistical analysis paradigms more commonly resembling transcriptomic data analysis. Several important caveats are important to realize, however. The majority of analytical mass spectrometry proteomics data interpretation is predicated on the fact that single peptides are isolated in a MS2 spectrum and that while less desirable, missing values occur partially at random.

A key advantage of DDA is that single peptides are isolated for MS2 analysis, allowing definite assignment of precursor identity and any proteoform modifications that occur on that sequence (i.e., PTMs). A challenge of DDA data analysis arises when a second peptide is isolated within the narrow mass isolation window for DDA MS2. It then becomes unclear to many algorithms whether that putatively low abundance ion is background signal, contaminant, or a separate proteoform of the predominant isolated precursor. Search algorithms such as Andromeda (Cox et al., 2011) and Proteome Discoverer (Orsburn, 2021) correct this by matching putative b- and y-ions to spectral ions, removing the background signal intensity of other ions for peptide spectral match (PSM) assignment, and then search only the background ions for potential second PSMs in a single spectra. In principal, this is how most DIA search algorithms operate where many peptides of similar abundance may be co-isolated (Demichev et al., 2020; Kong et al., 2017; Tsou et al., 2015). The challenge of these spectral assignments then comes from the effect of PTMs on PSM assignment. Indeed, only MSFragger allows *de novo* assignment of user defined modifications in library-free spectral library DIA search (DIA-NN currently allows N-terminal acetylation, methionine oxidation, phosphorylation, and deamidation). Even so, library-free assignment of PTMs retains a high degree of uncertainty as the probability in PSM validation prefers unmodified peptides to modified peptides for assignment under the assumption that most peptides are not modified. The logical approach to circumvent this limitation is to build a spectral library from DDA data searched against user specified PTMs. An additional challenge of DIA data analysis relative to DDA analysis is that the spectra are not interpretable, and while a skilled mass spectrometry scientist can *post-hoc* assign peaks as done in the DIA search algorithm, humans cannot assign a peptide *de novo* (Venable et al., 2004). Thus, in studies where high degrees of quantitative and identification precision are necessary (e.g., biomarker assignment), it may be necessary to perform targeted analysis after DIA data collection. As search algorithms get more computationally efficient, now routinely searching datasets faster than possible for DDA data, it is important that DIA data be interpreted with these caveats in mind.

A final point to make about DIA results analysis, the outputs of DIA data files are much richer than those in DDA. This may equate to proteins never measured before in the studied cell type or measurement of proteins only thought to exist under one treatment condition (Meier et al., 2018). Indeed, the improved completeness has made the data outputs more resemble those of transcriptomic microarray data structures (Pavelka et al., 2008). The statistical tools relevant for use in analysis of DIA data versus transcriptomic data is beyond the scope of this introduction, however several points will be made. First, unlike transcriptomic screens where all present transcripts can be measured in a well-executed experiment, not all peptides are measured by any mode of ESI MS/MS (Kiontke et al., 2016; Rappsilber et al., 2003). This may be due to ionization efficiency, peptide m/z, protease accessibility, or some other factor. Thus, some peptide data features will not be measured. Second, while DDA has a semi-stochastic algorithm for selecting ions to sequence, DIA is unbiased in the selection of ions and it is assumed that if an ion is measured in one sample and not in another, it is not an artifact of the search algorithm but instead of the experiment itself (whether biological or technical) (Demichev et al., 2020). Therefore, imputation should not be done on a well-executed DIA experiment. Third, DDA data does not have Gaussian normal distributed peptide assignments resulting in heteroscedastic data structures which require non-parametric statistical analysis (Cantrell & Schey, 2021b). DIA results are more representative of population assignments than DDA and have approximately Gaussian normal abundance distributions, resulting in the choice of parametric statistics as appropriate for evaluation of results depending on the experiment. Finally, it is anticipated that samples in most experiments are approximately comparable, with variables modulating a small subset of measured protein networks (Searle et al., 2018). In such a case, it is suitable to use peptide-centric approaches, where the quantitation of a single peptide is evaluated simultaneously for all samples (Ting et al., 2017). For unmeasured peptides, this results in 0 quantitative values in the results matrix. In cases of high heterogeneity, like in the lens, it is anticipated that comparability is more limited with treatment of age. In these cases, peptides should be quantified within each sample, termed spectrum-centric approach, and normalization performed between samples for those peptides that are consistently measured. Of conventional search algorithms, EncyclopeDIA and Spectronaut are the predominant peptide-centric search and quantitation algorithms . In contrast, DIA-NN is the predominant spectrum-centric approach (Demichev et al., 2020). To limit experimental variability, DIA-NN implements a match between runs data search mode where a spectral library with PSMs from all files is created prior to re-search and quantitation of data.

2. CHAPTER 2

ABSTRACT AND SPECIFIC AIMS

2.1. Abstract

The ocular lens is responsible for focusing of light onto the retina and must maintain transparency to effectively transmit light. Age related nuclear cataract is the most common cause of blindness worldwide, and cataract opacification of the lens is a currently unavoidable consequence of human and mammalian aging. To prevent accumulation of oxidative stress and subsequent aggregation, the lens proteome is densely populated by small heat-shock protein α-crystallin, but it is hypothesized that antioxidants and other nutrients are delivered to the lens core through a microcirculation system comprised of lower abundance lens proteins that support influx to the lens nucleus through sutures on the polar axis, and efflux through the lens equator. Since human lenses unavoidably experience cataract formation with age, it is critical to measure which protein networks contribute to and are affected by process of aging in an effort to molecularly characterize age-related cataract formation. This research approach pairs high-sensitivity proteomics methods to characterize how lens protein networks are changed as a function of cellular age and human age in addition to a sensitive measurement of influx networks along the suture with respect to cellular age. This work resulted in the identification of proteins and protein networks that are disrupted by the aging process, particularly as it is related to calcium accumulation, and the transport of antioxidants, metabolites, and their waste products.

2.2. Specific Aims

The ocular lens is responsible for focusing and transmission of light to the retina. To effectively transmit light, the lens must remain clear; however, opacification of the lens naturally occurs with age, resulting in cataract. It is hypothesized that oxidative modification of lens proteins results in aggregate species responsible for light scattering in cataract. As the leading cause of blindness worldwide, cataract treatment is a significant burden to human health and surgical intervention is the only current treatment (Brian & Taylor, 2001). Previous efforts to treat lens oxidative stress are limited by our understanding of how metabolites are transported within the lens.

Glutathione (GSH) is a significant contributor to the oxidative stress response, but transporters of GSH and its precursor amino acids have not been well studied in human lenses (J. C. Lim, Grey, et al., 2020; Sweeney & Truscott, 1998). **It is critical to improve our understanding of how the abundance and localization of antioxidant transporters change with age; specifically with the goal of identifying protein networks that are used for GSH and other antioxidant transport in the lens.**

Unlike most other cells, fiber cells in the lens are retained throughout life and are not degraded. These cells degrade organelles in maturation, causing loss of *de novo* protein synthesis. Therefore, the lens maintains a spatiotemporal gradient of cell age wherein the centermost fiber cells and the retained proteins are as old as the subject (Bassnett & Costello, 2017). In the absence of protein synthesis and a vascular transport system, transport of antioxidants and metabolism cofactors to interior fiber cells must be sustained. It is hypothesized that the transport of these metabolites is achieved by a microcirculation system (MCS) between lens fiber cells, driven by an ion gradient established at the cortical equator of the lens (Donaldson et al., 2010). After the fifth decade of life, metabolite delivery is significantly inhibited, but the protein-network level mechanism of this effect is unclear. It is also known that metabolites are transported to the inner nucleus of the lens through the anterior and posterior poles (J. C. Lim, Grey, et al., 2020) and hypothesized that metabolite delivery occurs along fiber cell sutures at a rate higher than expected by passive diffusion (Vaghefi & Donaldson, 2018). The identity of proteins that contribute to MCS transport along the sutures is not known.

To address limitations in the molecular characterization of lens aging and subcellular localization of MCS transporters, we propose to use mass spectrometry proteomics to identify and quantify the changes that occur in fiber cells as a function of age and subcellular localization. This work will improve characterization of the lens proteome and increase our understanding of how transporters deliver GSH and other antioxidants to the lens nucleus to better enable antioxidant delivery therapies for cataract. With data-independent acquisition (DIA) mass spectrometry methods we propose, we preliminarily identified 5,161 protein groups, 50,376 peptides and 4,960 deamidation sites in a human single lens: enhancing qualitative measurement of the lens proteome by >300% relative to previous approaches. Bioinformatic strategies on single-protein and protein-network levels have also been validated for use in other lens proteomics experiments.

Specific Aim 1. Detect age-related changes in the lens membrane proteome using higher sensitivity quantitative proteomics and to measure aging and antioxidant transport. Aim 1A: We will develop DIA mass spectrometry methods and bioinformatics workflows for analysis of the lens proteome. This preliminary strategy will enable greater quantitative sensitivity and improved qualitative depth of measurement relative to alternative approaches (Cantrell & Schey, 2021b). Aim 1B: Using the platform developed in Aim 1A, we will characterize protein-network level changes that occur in the human lens with age. The lens fiber cell proteome will be measured in three spatiotemporally defined regions among healthy subject donors of various age with a pilot cohort of 16 subject donors. *We hypothesize that this improved method of measurement would enable quantitative comparisons of low-abundance proteins that are critical in MCS establishment and metabolite efflux. More specifically, we hypothesize that cell-to-cell contact proteins will become less abundant or more highly modified and leading to putative functional decrease with subject donor aging.*

Specific Aim 2. Determine the proteomic composition of aging lens fiber cell sutures and identify protein networks putatively functional in MCS metabolite influx transport. Prior work demonstrates that antioxidants are delivered to the lens at a greater rate than expected by passive diffusion alone. Consistent with the MCS model, facilitated transport of antioxidants may occur at lens suture tips. The proteins implicated in transport have not been assigned due to limits in sensitivity in spatially targeted methods. To identify these protein networks, we will use laser capture microdissection to isolate fiber cell suture tips and age-matched equators at two depths of the lens. The bovine lens will be used as a model organism, enabling more controlled comparisons of MCS development with fiber cell age. Modifying methods established in Aim 1A, we will evaluate suture tip proteome composition and quantitative modifications to proteins localized to the suture. We will also compare anterior and posterior suture tips to evaluate if the anterior epithelium impacts the quantitative expression of proteins anterior and posterior fiber cells. *We hypothesize that this method would measure enhanced expression of GSH and GSH-precursor transporters in the suture tips with less adjacent extracellular space.*

3. CHAPTER 3

IMPROVING DEPTH OF LENS PROTEOME MEASUREMENT

The following section is adapted from the previously published article: Data Independent Acquisition Mass Spectrometry of the Human Lens Enhances Spatiotemporal Measurement of Fiber Cell Aging written by Cantrell and Schey, Journal for the American Society of Mass Spectrometry © 2021, American Chemical Society (Cantrell & Schey, 2021b). Additional information has been added towards the development of Basic Reverse Phase Fractionation methods and low-resolution data analysis with MSFragger.

3.1. Abstract

The ocular lens proteome undergoes post-translational modification and progressive degradation as fiber cells age. The oldest fiber cells and the proteins therein are present at birth and are retained through death. Transparency of the lens is maintained in part by the high abundance crystallin family proteins (up to 300 mg/mL), which establishes a high dynamic range of protein abundance. As a result, previous DDA measurements of the lens proteome are less equipped to identify the lowest abundance proteins. To probe more deeply into the lens proteome, we measured the insoluble lens proteome of an 18-year-old human with DDA and DIA methods. By applying more recent library-free DIA search methods, 5,161 protein groups, 50,386 peptides, and 4,960 deamidation sites were detected: significantly outperforming the quantity of identifications using DDA and Pan-Human DIA library searches. Finally, by segmenting the lens into multiple fiber cell-age-related regions, we uncovered cell-age-related changes in proteome composition and putative function.

3.2. Introduction

The ocular lens is a transparent tissue responsible for transmission and focusing of light to the retina. Unlike most tissue cell types, lens fiber cells are not degraded after formation and organelles degrade in early cellular maturation, leading to cessation of protein synthesis. Since genetic material is degraded, proteomic measurement is exclusively capable of characterizing each stage of cellular maturation. Age-related measurements of lens fiber cell proteomes are facilitated by the inherent spatiotemporal gradient of the lens, wherein fibers of the innermost nucleus of the lens are as old as the subject and surrounding concentric layers of fibers are progressively younger. Here, we divide the lens into three age-related regions: the inner nucleus that is composed of fiber cells formed *in utero* and infancy, the outer nucleus that contains fibers differentiated in early childhood, and the cortex that corresponds to fibers differentiated in early and throughout adulthood (Figure 3-1).

Throughout life, transparency of the lens must be maintained to prevent cataract (Schmid et al., 2021). In the absence of vasculature, metabolites are hypothesized to convect through the lens by a microcirculation system (MCS) where metabolite influx at the poles proceeds towards the inner nucleus and outflow proceeds through the equatorial region of the lens. In the proposed system, flux is established at the equatorial epithelium by a sodium ion electromotive potential gradient and water is transported through membranes by aquaporin and gap junction proteins. The MCS is critical for the delivery of GSH to the inner nucleus of the lens, where oxidative stress may otherwise induce PTMs that modify protein structure, function, and induce light scattering by protein aggregation. In addition to GSH conjugation to oxidized species, α-crystallin contributes to aggregation prevention by binding to partially unfolded substrates as a small heat shock protein (Horwitz, 1992; S.-Y. Wu et al., 2016). After the fifth decade of life, a barrier to extracellular metabolite transport is established, further challenging maintenance of lens transparency (Moffat et al., 1999; Sweeney & Truscott, 1998).

Historically, measurement of the lens proteome and its post-translational modifications have centered on the crystallin protein family due to their overwhelming abundance in the lens: estimated as high as 90% of protein dry mass, or 300 mg/mL (Aquilina et al., 2004; Schaefer et al., 2003; Ueda et al., 2002; Wilmarth et al., 2006). The high concentration of lens crystallins reduces the technical ability to measure low abundance proteins in the lens, especially with intensity biased methods such as DDA MS (Gillet et al., 2012), making the lens an excellent test tissue for DIA methodology. Further, biological insights may be gained by solubility-fractionation to deplete soluble crystallin proteins, isolating insolubilized proteins, cytoskeletal components, or proteins localized to the plasma membrane – like those in the MCS (Cantrell & Schey, 2021a; Z. Wang et al., 2013). Using a 13-pulse MuDPIT separation coupled to a LTQ Velos linear ion trap mass spectrometer, solubility fractionation provided previous identification of 951 human lens protein groups (Z. Wang et al., 2013). More recently, 5,466 protein groups from young mouse lenses have been identified with a BRP pre-separation and acquisition on a newer orbitrap instrument. For either mass analyzer, MuDPIT/BRP improves the quantity of protein and peptide identifications by approximately 400% over single-dimension analyses (MacCoss et al., 2002; X. Wu et al., 2017a). While 2D separation is effective in increasing protein identifications, it is less quantitatively reproducible and acquisition times are significantly greater per sample (Lee et al., 2016). Further, if the lens is to be spatially segmented into multiple fiber cell-age-related regions for measurement, 2D separations become significantly more instrument intensive than single-dimension analyses. To overcome limitations in quantitative reproducibility for BRP, MuDPIT, or other orthogonal separation strategies, isobaric tag multiplexing can be performed to reduce the quantity of samples injected in addition to limiting random error in quantitative comparisons. Isobaric tagging is most effective when all samples multiplexed are similar, a case not satisfied in the lens proteome.

Arguably the greatest limitation of DDA is its weakness for measuring low abundance peptides due to intensity biased selection of precursors (Doerr, 2015; Michalski et al., 2011, p. 100). Alternatively, DIA methods including SWATH-MS circumvent biased precursor selection by co-isolating all peptides within a small mass window along the LC gradient (Gillet et al., 2012; Venable et al., 2004). The major limitation of DIA is data-processing where a spectral library is typically required to deconvolute individual product spectra which may represent multiple co-eluting precursors (Searle et al., 2018). Conventional spectral libraries are developed by combining a fraction of each sample in the cohort and sampling with DDA. To improve spectral library size, 2D separations and gas-phase fractionation are frequently employed. Constructing a library is a laborious and instrument intensive process, so widely applicable community libraries such as the pan-human SWATH-MS library may be used instead (Rosenberger et al., 2014). Alternatively, recent software developments include *in silico* library preparation (Bekker-Jensen, Bernhardt, et al., 2020; Demichev et al., 2020). Here, we examine the application of DIA to multiple age-related regions of the human lens and discuss the impact that DIA, pre-developed libraries, and *in silico* searches have on annotating age-related changes in lens fiber cells.

A considerable limitation of mass spectrometry is the high cost of acquisition on high-resolution instruments. For studies where method optimization is the prime objective, it is then desirable to use older low-resolution instruments such as those built on the linear trapping quadrupole (LTQ) platform (Krey et al., 2014). These low-resolution instruments require less frequent calibration than high-resolution instruments but have greater uncertainty in mass accuracy. As a result, the quantity of analytes measured on low-resolution instrumentation is typically less than that on a high-resolution instrument, and area under the curve integration of MS1 signals is not typically done. Finally, as a result of lower mass accuracy, modern search algorithms are not developed for low-resolution instruments. In addition to DIA and DDA analyses on high-resolution instruments, we demonstrate how a Velos Pro LTQ platform can be used for method development in lens proteomics and discuss the modification of MSFragger for analysis of low-resolution data. To the best of our knowledge, this is the first time that MSFragger has been modified for a low-resolution instrument where MS1 and MS2 scans are performed at low-resolution.

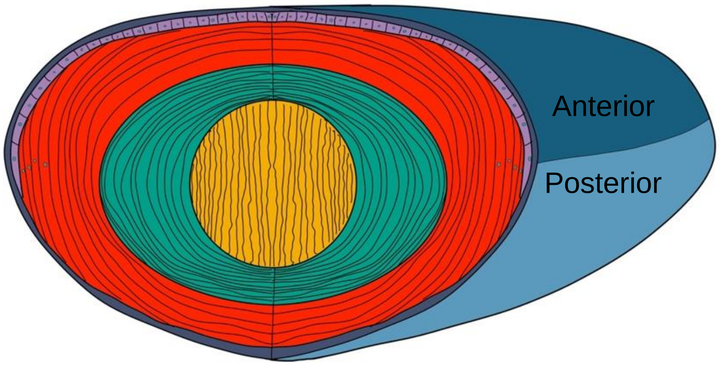

Figure 3-1 - Cartoon of lens with regions annotated. Fiber cells are differentiated from epithelial cells (purple) into the cortex (red) where organelles (teal circles) degrade. After the fifth decade of life, an extracellular diffusion barrier forms between the outer nucleus (green) and cortex, The oldest fibers, formed in utero may be found in the inner nucleus (orange). The entire lens is encompassed by a collagenous capsule (blue).

3.3. Materials and Methods

3.3.1. Materials

An 18-year-old frozen human lens was obtained from NDRI (Philadelphia, PA). Sequence-grade modified trypsin was obtained from Promega (Madison, WI). S-Trap columns were purchased from Protifi (Farmingdale, NY). All other chemicals were purchased from Fisher Scientific (Waltham, MA).

3.3.2. Urea Insoluble Protein Preparation

An 18-year-old, cataract-free human lens (9.2 mm x 7.0 mm) was mounted with its equatorial axis parallel to the cryostat chuck before removal of the anterior and posterior poles of the lens yielding a 1.5 mm thick equatorial lens section. Concentric biopsy centerpunches were taken at 4.5- and 7-mm diameter to yield inner nucleus (0-4.5 mm), outer nucleus (4.5 – 7.0 mm) and cortex (7.0 – 9.2 mm) samples. Tissue was homogenized in buffer containing 25 mM Tris (pH 8), 5 mM EDTA, 1 mM DTT, 150 mM NaCl, 1 mM PMSF. After homogenization, samples were centrifuged at 100,000g for 30 minutes and the supernatant discarded. Pellets were washed twice with the above homogenization buffer followed by washes with 3.5 M and 7 M urea added to the homogenization buffer. Centrifugation at 100,000g was performed to separate the supernatant and pellets for each wash. The remaining urea insoluble pellet was taken up in 50 mM TEAB with 5% SDS and protein concentration was measured with BCA assay.

3.3.3. Tryptic Digest

Membrane pellets of urea insoluble sample (200 µg total protein) were suspended in 5% SDS with 50 mM TEAB and DTT was added to 10 mM before incubation at 56°C for 1 hour to reduce disulfide bonds. Reduced cysteines were alkylated by adding IAA to 20 mM and incubating in the dark at room temperature for 30 minutes. Phosphoric acid was added to 2.5% to insolubilize proteins for efficient trapping. Proteins were taken up in 90% methanol + 100 mM TEAB before transferring 75 µg protein to the S-Trap micro. Trapping solution was centrifuged through the filter at 4,000g for 30 seconds. Trapped proteins were washed three times with 100 mM TEAB in 90% methanol with buffer removed by centrifugation at 4,000g. Proteins were digested by diluting in 50 mM TEAB with 5 µg (1:15) sequencing grade trypsin added and incubated for 1.5 hours at 47°C. To elute digested peptides, four sequential elution solutions of 50 mM TEAB, 0.2% aqueous formic acid, 50% ACN in water and 0.2% aqueous formic acid were added and centrifuged through the filter at 1,000g. Eluted peptides from each sample were pooled and dried with vacuum centrifugation. Peptides were taken up in 0.2% aqueous formic acid and stored at -80°C.

3.3.4. Liquid Chromatography

Peptides were analyzed using a Dionex Ultimate 3000 UHPLC coupled to an Exploris 480 tandem mass spectrometer (Thermo Scientific, San Jose, CA) with sample order randomized. An in-house pulled capillary column was created from 75 µm inner diameter fused silica capillary packed with 1.9 µm ReproSil-Pur C18 beads (Dr. Maisch, Ammerbuch, Germany) to a length of 250 mm. Solvent A was 0.1% aqueous formic acid and solvent B was 0.1% formic acid in acetonitrile. Peptides were loaded (cortex: 200 ng, outer nucleus: 300 ng, inner nucleus: 300 ng) and separated at a flow rate of 200 nL/min on a 95-minute gradient from 2 to 29% B, followed by a 14-minute washing gradient and 35-minute blank injection between runs. The exact gradient was determined by linearized separation of the top 50% most intense cortical peptide signals by Gradient Optimization Analysis Tool (GOAT 1.0.1)(Trudgian et al., 2014). Full details of the chromatographic gradient are provided in Table 3-1 and Figure 3-2.

3.3.5. Mass Spectrometry

For DDA injections, the Thermo Exploris 480 was set to acquire in top-20 configuration with auto dynamic exclusion. Precursor spectra were collected from 400 to 1600 m/z at 60,000 resolution (AGC target 3e6, max IIT of 50 msec). MS/MS spectra were collected on peptidic precursors between charge state +2 and +5 achieving a minimum AGC of 1e4. MS/MS scans were collected at 15,000 resolution (AGC target of 1e5, max IIT of 35 msec) with an isolation width of 1.6m/z. For DIA injections the Exploris 480 instrument was configured to acquire 35x20m/z (400-1100 m/z) precursor isolation window DIA spectra (30,000 resolution, AGC target 1e6, max IIT 55 msec, 27 NCE) using a staggered window pattern with window placements optimized by Skyline (MacLean et al., 2010). Precursor spectra (385-1115 m/z, 60,000 resolution, AGC target 3e6, max IIT 100 msec) were interspersed every 25 MS/MS spectra. In all experiments, default charge state was set to +3, S-Lens RF level set at 40%, NCE set at 27 and data collected in profile mode. See Table 3-2 for complete windowing scheme.

3.3.6. Data Analysis

For analysis of DDA data, RAW files were searched in MaxQuant (1.6.7.0)(Cox & Mann, 2008) with carbamidomethylation set as a static modifications and variable modifications disabled. Identification of second peptides and match between runs were enabled within the Andromeda probabilistic match algorithm. Peptide quantitation was performed with the label free “standard” method. Two missed cleavages were allowed and only peptides greater than 7 residues in length were considered. Shorter DDA peptides (5-6 residues) were not investigated since these peptides are not readily validated in DIA experiments. Peptide spectrum matches and protein groups were filtered at 1% FDR levels. For analysis of DIA data, RAW files were converted to mzML files in MSConvert (Adusumilli & Mallick, 2017), with staggered window deconvolution performed to improve precursor specificity. Processed DIA files were searched in DIA-NN (1.8.0)(Demichev et al., 2020) with an Intel Core i7-7700 CPU at 3.60 GHz utilizing 8 threads. For all searches, up to one missed trypsin cleavage was allowed on peptides 7-30 residues in length with N-terminal M excision and cysteine carbamidomethylation enabled. All fragments between m/z 200 and 1800 and in charge states +1-4 were considered. In each search, the neural network classifier was run in double pass mode with likely interferences removed and retention time dependent normalization initiated between technical replicates from the same region of the lens with high precision quantitation enabled. An initial search of all files produced a library which was used to search the data a second time (termed match between runs). Precursors and protein groups were filtered at 1% FDR and contaminants in the MaxQuant contaminant list were removed. All library-free DIA and DDA analyses were searched against a UniProt SwissProt canonical human fasta database (UP000005640, downloaded 3/12/2021, 20,393 entries) with a predicted trypsin/P protease used. For the library-free search, deep learning-based spectra and retention time prediction was used for library generation. In a separate library-free search, one variable deamidation of glutamine or asparagine was also allowed. For searches against the pan-human SWATH atlas, a consensus speclib file (SAL00035) from Rosenberger et al. (Rosenberger et al., 2014) was downloaded and used for a library-based search in DIA-NN with identical search settings to library-free analysis. Comparisons and analyses were initiated through custom R scripts with peptides having >1% q-value or >1% global protein q-value omitted.

Intraregional peptide abundance measurements were independently normalized by DIA-NN abundance normalization based on the 40% of peptides with the lowest CV (<10% CV). To improve normalization, trimmed means of M-values (TMM) normalization was performed within regions. Interregional peptide abundances were then median normalized. For comparisons of identification efficiency, imputation was not done. When ontology changes were considered in DIA data, the R package DMwR was used for knn-imputation with scaled data pre-processing. Proteins were considered for imputation if detected in 2 of 3 intraregional technical replicates. Protein and peptide abundance was calculated by the diann R package function diann_maxlfq available at https://github.com/vdemichev/diann-rpackage. Proteins were only assembled on peptides considered proteotypic. For DDA comparison, raw intensity peptide abundance values were normalized as above and treated with the diann_maxlfq to retain similarity of protein group quantitation.

Gene association data was downloaded from the Uniprot database (04/06/2021). PSEA-quant (Lavallée-Adam et al., 2014) was initiated through a Java command line interface with R scripts for data preparation. Volcano plots were prepared with limma moderated p-values calculated in the eb.fit function (Ritchie et al., 2015). Quantity of overlapping features were defined by unique razor protein identity or peptides with charge state not considered. For quantitative abundance comparison of DDA and DIA, a linear median normalization factor was determined for proteins identified in both modes and applied to all DDA protein groups. Searches with deamidation enabled were normalized as above, with an additional TMM normalization calculation based on unmodified peptides detected in each search scheme. For all statistical enrichment calculations, PANTHER (Thomas, 2003) was used with the 02/01/2021 GO database applying a Fisher’s exact test with FDR calculated. Significance was set at 0.01 for PANTHER searches. All proteins identified in the modification-free DIA-NN search were included as part of the statistical background.

3.3.7. Bovine lens sample preparation and search

To develop methods for low-resolution measurement of the lens proteome, bovine lenses were used as a model organism for data collection. Intact bovine eyes were received from a local meat processing facility (Light Hill Meats, Lynnville, TN) within 4 hours of butchering. Lenses were enucleated from fresh tissue with collagen capsule not removed. The lens was dried and frozen at -80°C. The lens cortex was then extracted using a 7/16 inch trephine centerpunch. The excised material was collected into multiple sample tubes for separate sample preparations. Urea insoluble fractions were collected, reduced, and alkylated as described for human lenses. For samples that were digested on an S-Trap, digestion was done as described for human lenses. For samples that were digested in-solution, trypsin was added at 1:50 enzyme:protein, calculated by BCA assay. In-solution digest was done overnight at 37°C.

In this study, basic reverse phase (BRP) fractionation was evaluated towards the quantity of peptides and protein groups identified. Two different methods were used for BRP fractionation: a commercial option produced by ThermoFisher, and an in-house stop and go extraction (STAGE) tip-based method. ThermoFisher separation occurred according to manufacturer instructions, with fractions collected at 5, 7.5, 10, 15, 20, 25, 30, and 50% ACN. The STAGE tip method was done by packing two 1.0 mm diameter punches of 3M C18 filter material in a Biotix 250 µL pipette tip. To the packed punches, 2 mg of 5 µm diameter C18 resin (Phenomenex) was suspended in ACN. Tips were loaded on a benchtop centrifuge and placed in 1.5 mL Eppendorf inserts fixed inside a 1.5 mL Eppendorf tube with cap removed. Acetonitrile was then removed by centrifugation and column washed by two additions of 50 µL 80% ACN in 0.1% triethylamine (TEA) with centrifugation between additions. The column was then equilibrated by two additions of 50 µL 0.1% aqueous TEA. Dried down peptides were reconstituted in 50 µL 0.1% aqueous TEA and loaded on the spin column with a clean Eppendorf nesting tube. After the sample was spun through the column, eluted material was reloaded on the column. Samples were washed by two additions of 50 µL aqueous 0.1% TEA. For elution, fractions were collected in clean Eppendorf tube with elution media at either 5, 7.5, 10, 15, 25, 30, 50% ACN or 5, 7.5, 10, 12.5, 15, 17.5, 20, 22.5, 25, 27.5, 30, 50% ACN for 8 and 12 fraction collections, respectively. Technical replicates were not performed. Peptides were dried down on a speedvac and reconstituted in 0.2% formic acid before injection to the Velos instrument.

Approximately 400 ng of each basic reverse phase fraction was separately loaded onto a trap column before separation along a 95-minute gradient from 5% ACN to 37% ACN. Peptides were measured on a ThermoFisher Velos Pro linear ion trap instrument operating in top15 data dependent acquisition mode. RAW files were searched with FragPipe (17.0), modified to accommodate the low-resolution mass analyzer used in this study. Briefly, each sample was selected as part of a single experiment and searched with MSFragger (3.4) with precursor mass tolerance of +/- 500 ppm and fragment mass tolerance of +/- 0.7 Da. Peptides of length 7-50 in mass range 500-5000 with charge 1-4 were included in a database of reviewed and unreviewed proteins (downloaded 12/08/2016, length 32,167). Cysteine carbamidomethylation was included as a default modification. Up to two variable modifications of M oxidation and N-terminal excision were allowed per peptide. Protein level results were filtered at 5% FDR while peptides, PSMs and ions were filtered at 1% FDR. FragPipe outputs were used for protein level data interpretation in R. In addition to searches in FragPipe, a legacy search was performed using a custom framework of TagRecon and IDPicker. Briefly, all search parameters were set as equivalent in TagRecon and output PepXML files were evaluated with IDPicker where parameters were optimized to evaluate peptides at a global FDR of 5% while requiring at least 1 unique peptide and 2 total peptides per protein, to limit protein group misassignment. Final global FDR was evaluated at 4.3% in this legacy search.

Table 3-1 - Full chromatography gradient calculated at 3-minute intervals by GOAT

Time (min)	**%B**
0.0	2.0
1.0	2.0
2.0	2.0
3.0	2.0
6.0	7.1
9.0	8.4
12.0	9.4
15.0	10.1
18.0	11.1
21.0	11.8
24.0	12.3
27.0	12.6
30.0	13.7
33.0	14.4
36.0	14.7
39.0	15.0
42.0	15.5
45.0	16.2
48.0	16.5
51.0	17.0
54.0	17.7
57.0	18.4
60.0	18.7
63.0	19.2
66.0	19.9
69.0	20.6
72.0	21.5
75.0	22.4
78.0	24.1
81.0	90.0
83.0	90.0
84.0	2.0
85.0-95.0	2.0

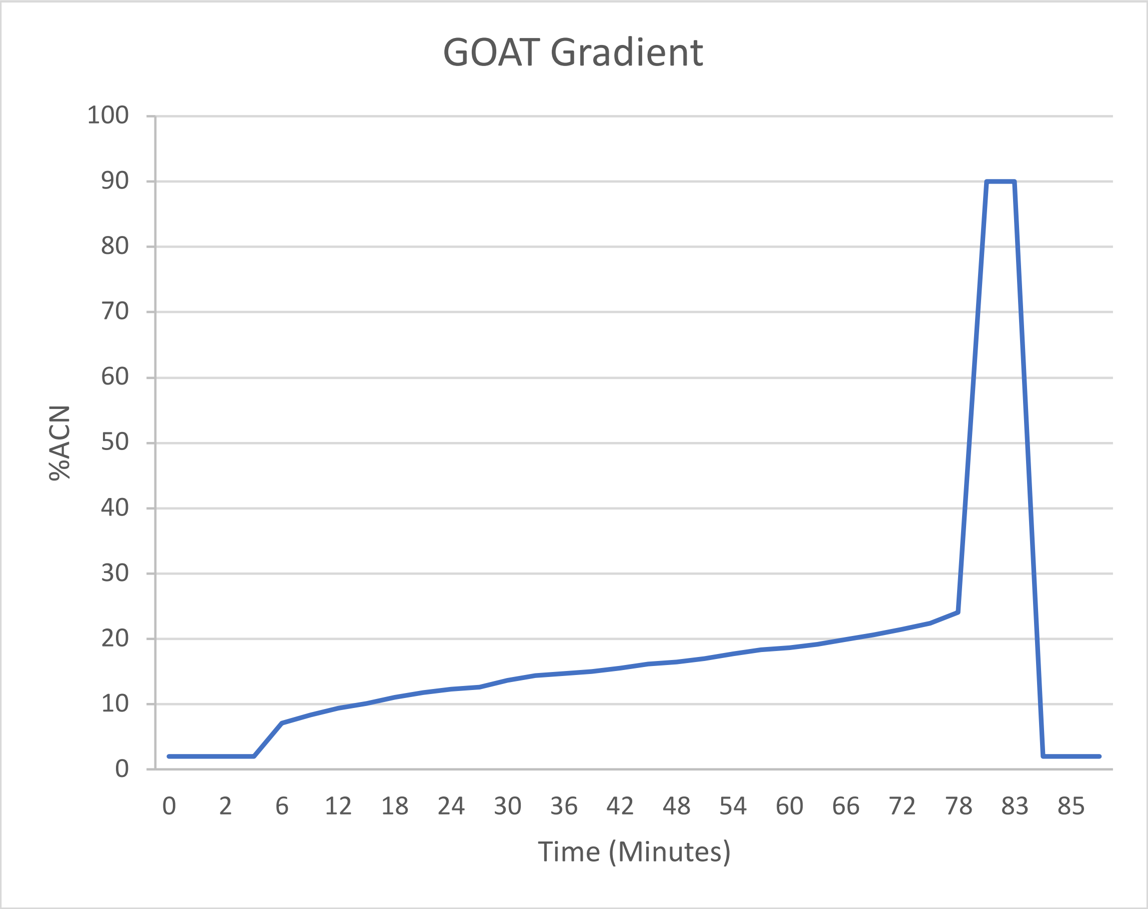

Figure 3-2 - GOAT gradient visual representation

Table 3-2 - Calculated mass windows for DIA experiments. Optimization done in Skyline from 400-1100 m/z with staggered window deconvolution selected. Windows exceeding the specified range were discarded. Table is read top to bottom then left to right.

Calculated m/z Window	
400.4319-420.441	410.4364-430.4455
420.441-440.4501	430.4455-450.4546
440.4501-460.4592	450.4546-470.4637
460.4592-480.4683	470.4637-490.4728
480.4683-500.4774	490.4728-510.4819
500.4774-520.4865	510.4819-530.491
520.4865-540.4956	530.491-550.5001
540.4956-560.5047	550.5001-570.5092
560.5047-580.5138	570.5092-590.5183
580.5138-600.5229	590.5183-610.5274
600.5229-620.5319	610.5274-630.5365
620.5319-640.541	630.5365-650.5456
640.541-660.5501	650.5456-670.5547
660.5501-680.5592	670.5547-690.5638
680.5592-700.5683	690.5638-710.5729
700.5683-720.5774	710.5729-730.582
720.5774-740.5865	730.582-750.5911
740.5865-760.5956	750.5911-770.6002
760.5956-780.6047	770.6002-790.6093
780.6047-800.6138	790.6093-810.6183
800.6138-820.6229	810.6183-830.6274
820.6229-840.632	830.6274-850.6365
840.632-860.6411	850.6365-870.6456
860.6411-880.6502	870.6456-890.6547
880.6502-900.6593	890.6547-910.6638
900.6593-920.6684	910.6638-930.6729
920.6684-940.6775	930.6729-950.682
940.6775-960.6866	950.682-970.6911
960.6866-980.6957	970.6911-990.7002
980.6957-1000.7048	990.7002-1010.7093
1000.7048-1020.7138	1010.7093-1030.7184
1020.7138-1040.7229	1030.7184-1050.7275
1040.7229-1060.732	1050.7275-1070.7366
1060.732-1080.7411	1070.7366-1090.7457
1080.7411-1100.7502	

3.4. Results and Discussion

3.4.1. Benchmarking against DDA

To test the hypothesis that DIA outperforms DDA in lens protein identification and quantitation, we injected three separate regions of the lens in triplicate to the Exploris 480 in both acquisition modes. DDA analysis was performed in MaxQuant and DIA analysis in DIA-NN. For this comparison, a library-free DIA search with no variable modifications was used. In total, 2,161 protein groups and 14,222 peptides were identified in DDA experiments. Previously, as many as 1,251 protein groups had been identified in a cohort of lenses (X. Wu et al., 2017a). The improvement in identifications is facilitated in part by the isolation of insoluble proteins and of the Exploris instrument compared to an older Q-Exactive instrument. Additionally, NaOH washing was not done here, which may otherwise strip proteins interacting with intrinsic membrane proteins. Prior measurements of the lens have shown significant decreases in protein identification quantity within the outer nucleus and inner nucleus regions of the lens due to organelle-associated protein degradation and targeted degradation of proteins that become misfolded with age. In DIA and DDA alike, a trend was observed where approximately 300% more peptides were identified in the cortex than either nuclear fraction in the respective data acquisition mode (Figure 3-3A,B).

Though lens proteomes are less complex than HeLa or other cell culture systems, BRP fractionation established identification of 5,466 proteins in a juvenile mouse lens in ten 100-minute injections (Y. Zhao et al., 2019). With DIA in the current study, as many as 4,482 protein groups and 39,355 peptides were detected in a single 95-minute gradient analysis. Compiled across each region of the lens, a total of 4,980 protein groups and 41,878 peptides were detected when no variable modification was allowed in the search (Figure 3-3A,B). Juvenile lenses do not undergo significant aging and retain more proteins associated with early lens morphogenesis; therefore, it is not expected that the proteome of an 18-year-old human is more complex than especially young mouse lenses. The most similar human dataset presented by Wu et al. identified 1,251 proteins of which 934 could be identified in the DIA experiment. In the remaining 317 proteins, 234 were not present in the SwissProt database used for DIA analysis. The last 83 proteins detected by Wu et al., and not in our DIA results, consist in part of keratins and homologs of other proteins within the dataset (e.g. α-crystallin in identified as CRYAA by Wu et al. and as CRYA2 by DIA-NN). Keratin proteins were removed from the DIA dataset reported here as contaminant proteins in the MaxQuant default contaminant list. Statistical enrichment of these 83 proteins against the human lens genome background showed significance for epidermal growth which is associated with epithelial contaminants and not with lens fiber cell development.

Relative to DDA, DIA facilitated a 211% improvement in protein identifications and 294% improvement in total peptide identifications. As with DDA, there is a significant decrease in total identifiable proteins (Figure 3-3A) as cortical fibers mature to outer nuclear proteins. Unlike DDA results, DIA identification performance of the outer nucleus was nearly matched in the inner nucleus where fibers exceed a decade of age. Our data imply that, although still present, a large subset of the nuclear proteome is not detectable with DDA due to biasing limitations. DIA also facilitated greater coverage of identified proteins, with an approximate 7 associated peptides to every protein in DIA, and 5 in DDA. With maturation of the nucleus, the nuclear peptidome, unlike the proteome becomes less populated by unique peptides (Figure 3-3B). Sequence alignment was not performed on the 1,665 peptides not measured in the inner nucleus; however, the near-complete incorporation of common age-related modifications including deamidation, oxidation, N- and C-terminal truncation may contribute to this difference in searches, like this one, where PTMs are not considered.

To validate the specificity of DIA library-free search relative to DDA search algorithms, overlap analysis of razor proteins (the most probable protein assignment by an Occam's razor approach)(Serang & Noble, 2012) and peptides was done (Figure 3-3C,D). Only unique razor proteins were considered to reduce protein group assembly differences between MaxQuant and DIA-NN peptide assignment algorithms. From the 2,161 DDA proteins identified in total, 62 were not included in the DIA dataset, with 29 being identified in an assembled DIA protein group as non-razor or did not meet FDR filtering criteria. Biological ontology databases including Gene Ontology (GO), Kyoto Encyclopedia of Genes and Genomes (KEGG) and the Reactome pathway database were used to condense high complexity data that emerged from analysis of the lens proteome into biologically meaningful functional annotations. Further discussion of ontologies refers to these biological databases. The remaining 33 unmatched proteins (1.5% DDA IDs) show no ontological enrichment against the lens proteome, leading us to interpret this discrepancy as insignificant towards protein-network insights. A landmark of success for DIA, 29,625 peptides were uniquely measured with DIA. This figure exceeds more than two times the total quantity of peptides identified with DDA, greatly improving the robustness of potential protein quantitation. For proteins detected in both DIA and DDA experiments, there is strong regional agreement that further validates the specificity of the DIA library-free search for peptide assignment. Among peptides, 1,214 from the cortical DDA dataset were not matched to DIA experiments. While not tested, it is expected that the charge detection and appropriate collision energy adjustment resulted in different peptide fragmentation (either precursor ion charge state selection or fragmentation pattern) in DDA whereas DIA employs a static collision energy. It is also possible that ion suppression occurs in wide MS2 DIA windows, preventing the detection of low abundance peptides that co-elute with a small cohort of exceptionally abundant peptides, such as those from α-crystallin. To validate the claim that DIA is more reproducible than DDA, we performed technical replicate overlap analysis (Table 3-3). In both peptide and protein group overlap analysis, DIA shows reduced variability of protein and peptide identifications relative to DDA.

Because of AGC target parameters, chromatographic co-elution of high abundance peptides and the stochastic nature of DDA precursor ion selection, peptides of putatively low abundance are not identified in DDA experiments. To demonstrate the distribution of lens protein abundance, we compared the quantitative distribution of calculated protein abundances in each region of the lens (Figure 3-4A,B,C). Search engine quantitation bias was reduced by protein assembly and normalization with the MaxLFQ algorithm in R. For proteins detected in paired studies, a constant necessary to median normalize DDA data to DIA was calculated and applied to all DDA peptides before protein group assembly. For proteins in both DDA and DIA experiments, a non-significant difference of abundance distribution was associated with each regional comparison (Wilcoxon Test). In all regions, the abundance distribution of proteins detected by DDA and DIA had higher means and medians than proteins exclusive to DIA or in the complete DIA dataset ($p < 2x10^{-16}$). Therefore, we conclude that DIA enables enhanced accessibility to the low abundance lens proteome.

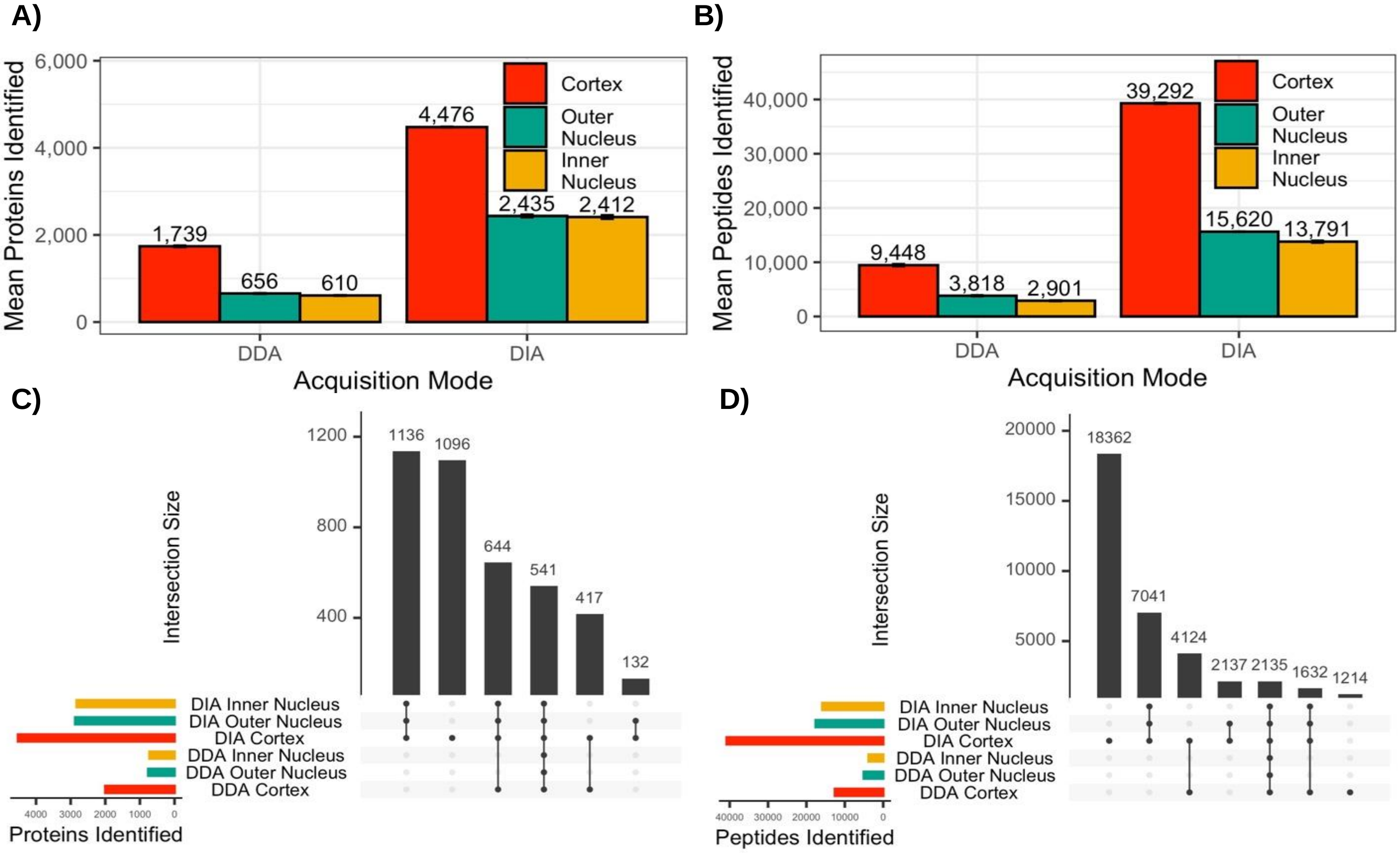

Figure 3-3 - Comparison of Data Dependent (DDA) and Data Independent (DIA) acquisition scan modes for 3 technical replicates of 3 lens regions, PTMs disabled. Only unique razor proteins considered. In total, 4,620 protein groups and 43,847 peptides were detected across all experiments. DIA clearly outperforms DDA for identifications and search provides low CV values in protein (A) and peptide (B) comparisons. Upset plots of proteins (C, 86% represented) and peptides (D, 84% represented) reveals near complete coverage of DIA proteome/peptidomes.

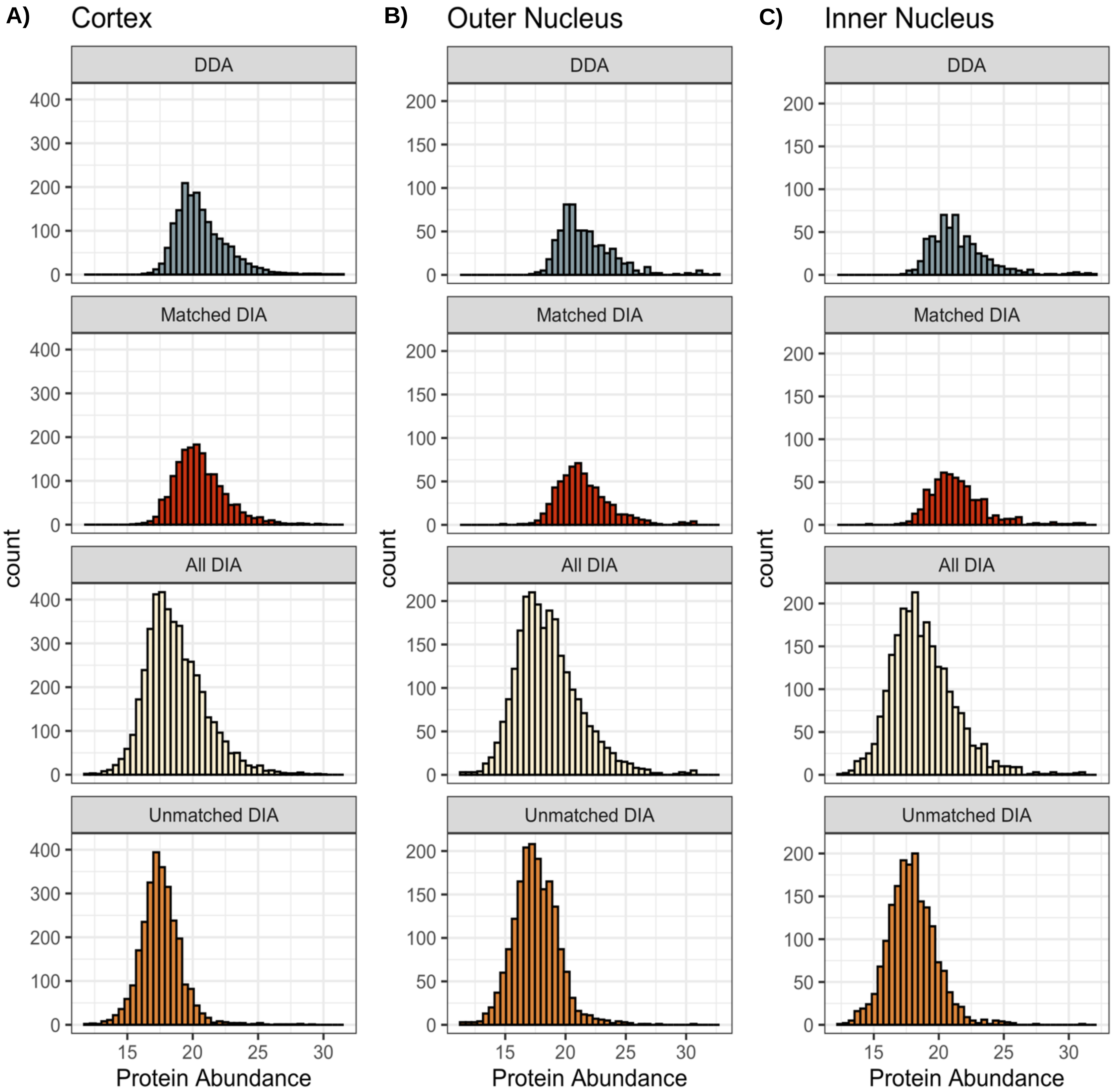

Figure 3-4 - Histogram comparison of Log2 abundances between DDA and DIA, each calculated with the diann R package. For each region of the lens A) Cortex, B) Outer Nucleus, C) Inner Nucleus, quantitative median normalization factors were calculated for matched protein groups between DDA and DIA and applied to all unmatched protein groups. DDA abundances (grey) visually resemble the distribution of matched ID DIA proteins (red). The majority of proteins uniquely identified in DIA (orange) were of lower mean abundance compared to the DDA proteome. The resulting complete DIA experiment (beige) has a moderately decreased median and wider quantitative distribution than DDA.

Table 3-3 - Table of Venn diagrams demonstrating replicate overlap at the protein group and peptide level of identification for DIA and DDA in each lens region. There is a demonstrated increase in reproducibility in DIA relative to DDA. For all demonstrated overlap plots with DIA data, library-free search results with no variable modifications enabled were used.

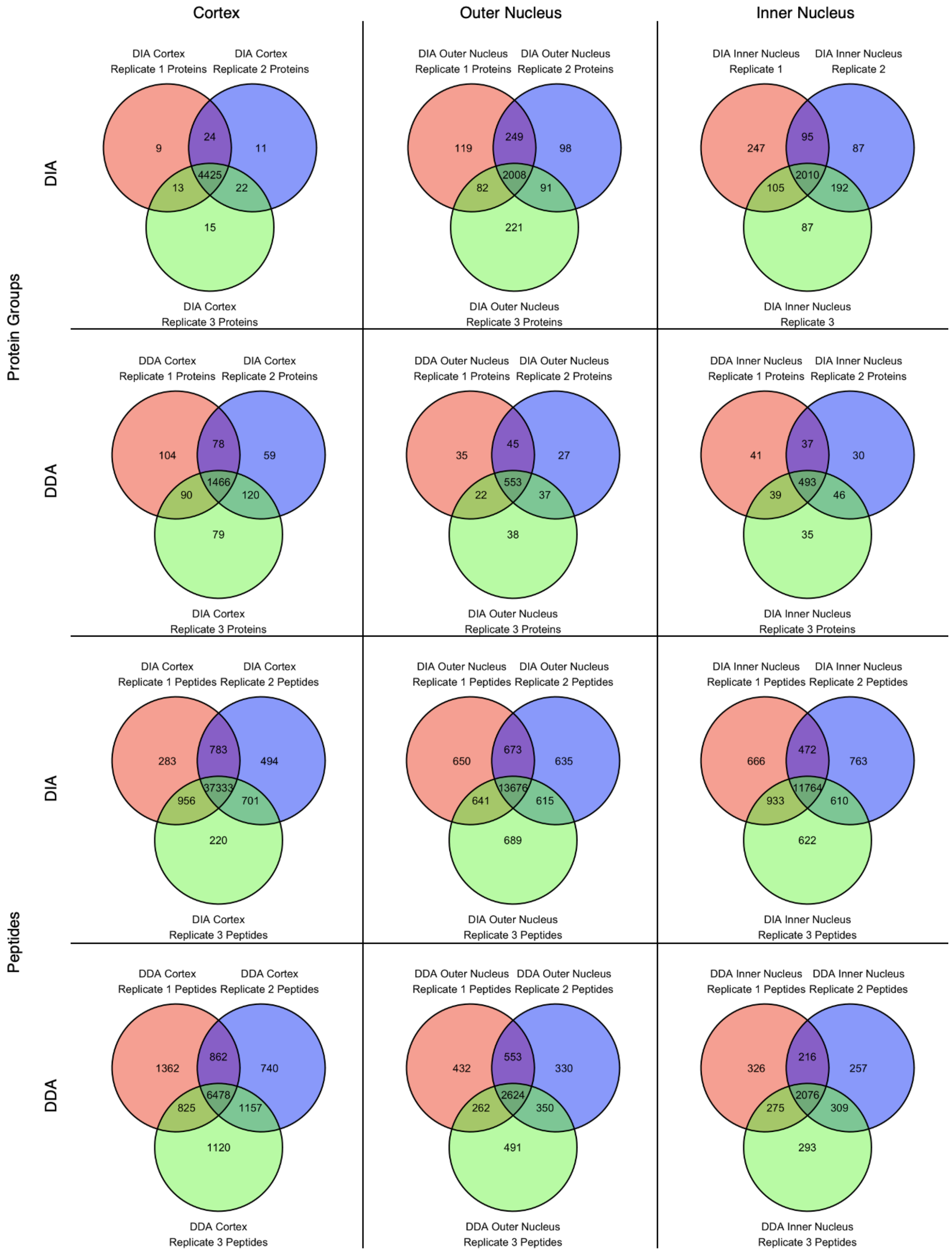

3.4.2. Evaluating the Use of Pan-Human or Library-Free DIA search

Pan-human libraries provide a convenient, sample agnostic approach to DIA assay development. These libraries are highly effective in well-studied tissues or cell lines. Relative to library-free methods, the pan-human library has a significantly decreased search space, decreasing the time needed to process data. To evaluate the utility of pan-human libraries in lens proteomics, we independently searched each sample with and without the pan-human library provided by Rosenberger, Koh, et al. (Rosenberger et al., 2014). Since the pan-human library does not have variable modifications annotated, variable modification remained disabled in the library-free search. As before, we compared regional feature identifications and performed overlap analysis (Figure 3-5). Consistent with library-free DIA search, the pan-human search of cortex samples showed a greater number of protein groups identified relative to the outer and inner nucleus samples. Though much more rapid for data analysis of all 9 replicates (54 minutes for pan-human, 338 minutes for library-free on a personal computer), library-free searching significantly improves the number of protein groups and peptides identified in the nuclear lens regions where low abundance peptides are presumably more prevalent.

In overlap analysis (Figure 3-5C,D), it was clear that both pan-human and library-free DIA analysis methods effectively identify more proteins and peptides than in any prior study of the human lens. However, a significant quantity of proteins (826) and peptides (14,859) were detected in the library-free search and not in the pan-human search. Conversely, 294 proteins and 5,469 peptides were detected in pan-human search and not in the library-free search. The cause of unique identifications is unclear, however, library-free search as initiated from DIA-NN makes best estimates at experimental spectra, but experimentally observed spectra may better enable correlation and q-value reduction. To determine the biological impact of unique proteins to each analysis mode, we performed statistical-enrichment analysis of unique library-free proteins (826) and pan-human proteins (294) against the lens background (Table 3-4). No protein network ontologies were statistically enriched from the pan-human search. However, the large quantity of lens-specific ontologies uniquely identified in the library-free search demonstrate that the pan-human library does not adequately sample lens fiber cells for annotation of lens biology. Of great significance, AQP0, one of the most abundant lens proteins, is not in the pan-human library. For future lens studies and studies where PTMs are desirable to measure, it is then suggested that a library-free search be used in the absence of an exhaustive library.

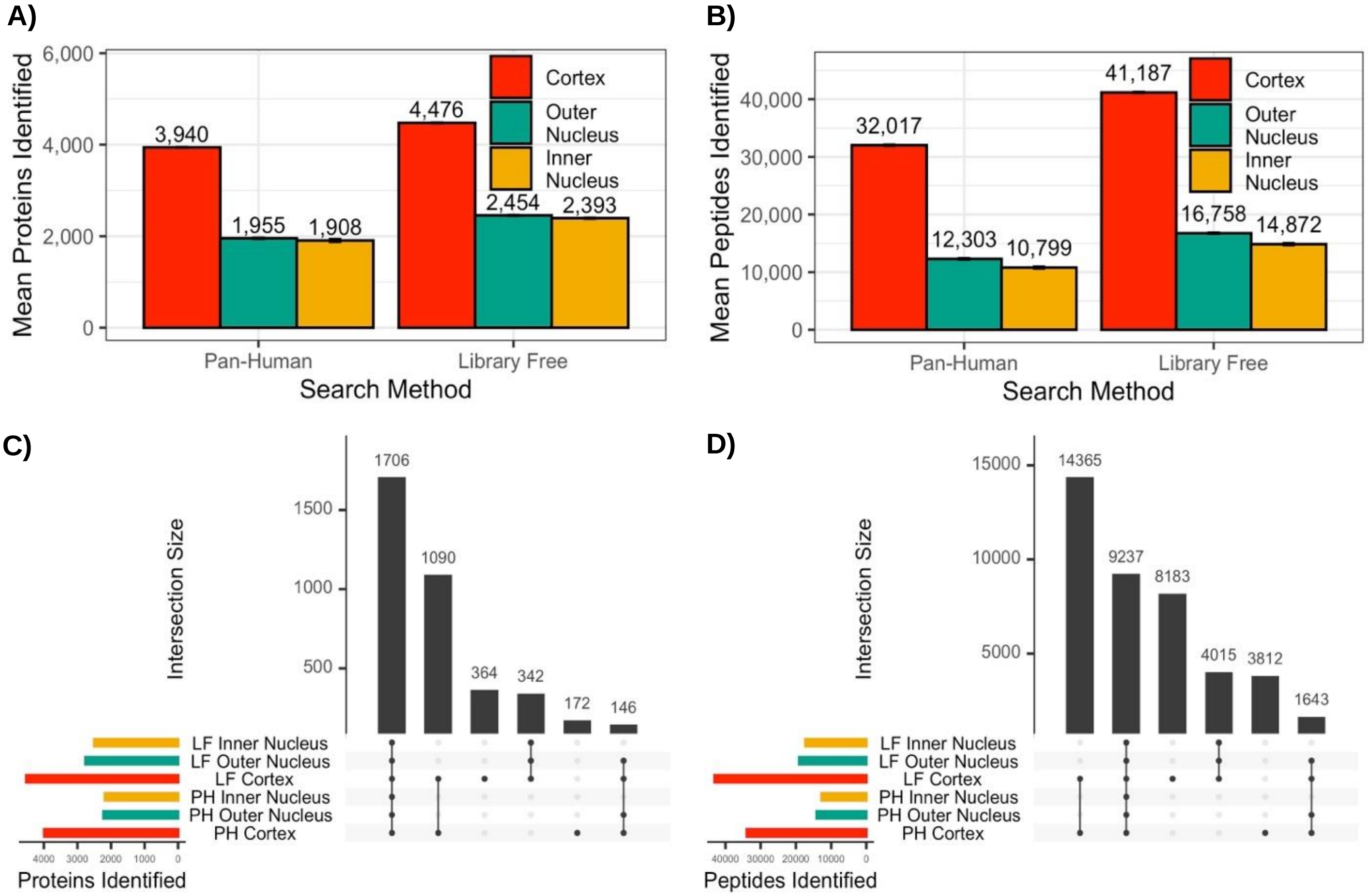

Figure 3-5 - Comparison of Pan-Human (PH) library search with Library-free (LF) DIA-NN Searching, PTMs disabled. Only unique razor proteins considered for identification. A) Protein identifications in each lens region, B) Peptide identifications in each lens region; no modifications were considered. Library-free search produces a greater quantity of IDs filtered at 1% FDR. Upset plots of protein groups (C, 79% represented) and peptides (D, 83% represented) identified in at least one technical replicate of each search method.

Table 3-4 - Ontological enrichment of proteins detected in library-free DIA search and not in Pan-Human DIA search (n = 826). No ontologies were enriched among proteins identified in Pan-Human DIA search and not in library-free DIA search (n = 294). Ontology enrichment and statistical analysis performed by PANTHER, using all identified lens proteins as the statistical background.

GO Term	**Annotation**	**# in Set**	**Fold Enrichment**	**FDR**
	Unique in Library-Free Search			
	GOBP			
GO:0050953	Sensory perception of light stimulus	43	3.11	$<1\text{x}10^{-4}$
GO:0007601	Visual perception	43	3.11	$<1\text{x}10^{-4}$
GO:0007600	Sensory perception	52	2.30	$<1\text{x}10^{-4}$
GO:0048880	Sensory system development	55	2.51	$<1\text{x}10^{-4}$
GO:0150063	Visual system development	55	2.51	$<1\text{x}10^{-4}$
GO:0007423	Sensory organ development	66	2.37	$<1\text{x}10^{-4}$
GO:0002088	Lens development in camera-type eye	26	3.56	0.0003
GO:0001654	Eye development	55	2.56	0.0003
GO:0043010	Camera-type eye development	51	2.66	0.0006
GO:0050877	Nervous system process	69	1.83	0.0024
	GOMF			
GO:0005212	Structural constituent of eye lens	15	4.11	0.0001
GO:0022857	Transmembrane transporter activity	80	1.65	0.0001
GO:0005215	Transporter activity	90	1.57	0.0002
GO:0004888	Transmembrane signaling receptor activity	34	2.13	0.0003
	GOCC			
GO:0005877	Integral component of plasma membrane	93	1.80	$<1\text{x}10^{-4}$
GO:0031226	Intrinsic component of plasma membrane	101	1.78	$<1\text{x}10^{-4}$
GO:0016021	Integral component of membrane	334	1.41	$<1\text{x}10^{-4}$
GO:0031224	Intrinsic component of membrane	345	1.41	$<1\text{x}10^{-4}$
GO:0071944	Cell periphery	351	1.21	0.0024
GO:0005886	Plasma membrane	310	1.22	0.0060

3.4.3. Impact of fiber cell aging on proteome composition

A result of aging, deamidation of asparagine or glutamine is the most prevalent PTM in the lens (Lampi et al., 1998). While deamidation may be initiated by glutaminase-like enzymes, non-enzymatic deamidation is most common in the lens. To investigate changes in the lens proteome as a function of fiber cell age, we included one variable deamidation in the library-free search parameters. Inclusion of a variable deamidation greatly increased the search space over a modification restricted search and may negatively impact FDR calculations. As a result, search time increased from 338 minutes with no modification enabled to 1,531 minutes with one variable deamidation allowed: calculations performed on a personal computer. Here, search time increased linearly with search space. In total, 5,161 protein groups and 50,386 peptides were detected. Among these, 1,480 proteins were partially deamidated at 4,960 unique deamidation sites along 4,662 peptides. Each of these figures exceed the capabilities of previous human lens proteomic measurements.

In the relatively young 18-year-old lens, it is not expected that the lens would undergo significant deamidation. However, significant levels of deamidation has been detected in lenses as young as 4 months old (Wenke et al., 2015). In addition to improvements in DIA-NN PTM algorithms, we validated that there is a gradual fractional accumulation of deamidation. In cortical fibers, 3,741 peptides demonstrated variable deamidation. In outer and inner nuclear fibers, 2,907 and 2,739 peptides respectively were deamidated. This corresponds to a proportional increase from 9% to 17% and 18% of all peptides within progressively older lens regions demonstrating deamidation as the lens ages. A target-decoy approach was also employed to separate PSMs that are true deamidation modifications (+0.984016 Da) from the isotopic peak. The majority of modified peptides are believed to be deamidated non-enzymatically, and prior evidence supports the claim that there will be even more accumulation of deamidated peptides as a function of age (Forsythe et al., 2019; Hains & Truscott, 2010b; Wilmarth et al., 2006).

To evaluate the progressive changes in proteome composition and putative function as a function of fiber cell age, we first evaluated feature overlap between regions (Figure 3-6A,B). Regional segmentation of the lens allows clear comparisons of fiber cell aging whereas whole-lens measurements previously published are most representative of the high protein density cortical fibers. Exceptionally, 2,446 protein groups (47% of all identified) and 16,296 peptides (33%) were detected as common among lens regions. Among proteins uniquely identified in each region, no protein network enrichment was detected by statistical significance testing in Panther. The exceptionally high quantity of overlapping proteins and the non-overlapping proteins low significance in representation of lens biology further highlights the capacity of DIA to measure quantitative and functional differences between fiber cells of different age.

After numeric comparisons of identification, we investigated protein abundance related differences in each region. With the 2,466 proteins identified in all regions, principal component analysis was performed (Figure 3-6C). The majority of variance in the dataset is explained by the transition of fiber cells from more classical cellular function in cortical fibers, to the less metabolically active fibers in nuclear regions of the lens, separating cortical and nuclear fibers along PC1. The 50 most descriptive cortical loadings are associated with nucleosome assembly and proton transmembrane transport activity while the most descriptive nuclear loadings are associated with lens development. Secondarily, proteins in the inner nucleus and outer nucleus separated along axis 2. The top 50 PC2 loadings correlated with the outer nucleus are not biologically statistically overrepresented for any Gene Ontology while the top 50 PC2 loadings of the inner nucleus are correlated with cytoplasmic translation (GO:0002181). Findings in the first principal component are consistent with previous lens biology studies and while cytoplasmic translation does not fit within conventional lens biology thought, the low proportion of variance explained by this component separation may be representative of an artifact rather than biology since protein components of translation are inactive in mature, anucleate fiber cells in the lens nucleus. While valuable, this approach does not take full advantage of the rich DIA dataset. Ontology searches based on a small subset of differentially expressed proteins may be too conservative to identify changes associated with low abundance proteins and analyses considering all identified proteins without considering associated abundance may increase false positive annotations. Therefore, we set out to perform ontology analysis sensitive to each protein and its associated abundance.

It is clear from pairwise comparisons of protein expression (Figure 3-7A,B) that the abundance of most proteins in the cortex exceeds that of either the outer or inner nucleus. As a validation of quantitative comparisons, there is a measured significant increase in γ-crystallin density in each nuclear region respective to the cortex. Unlike the majority of other lens proteins, γ-crystallins are sustained at higher concentration in the lens nucleus due to their role in lens morphogenesis and establishment of the lens gradient of refractive index (Slingsby & Wistow, 2014). As may be expected based on previous discussion, there is limited quantitative change in proteins between the outer nucleus and inner nucleus portion of the lens (Figure 3-7C). We do suspect that in lenses of different age, the relatively younger fibers of the outer nucleus will show significant quantitative differences from the oldest fiber cells in the inner nucleus, especially in age-related nuclear cataract lenses.

To evaluate changes in biology at a protein-network level, abundance-linked ontology analysis was performed. Crystallin proteins make up a disproportionate part of the proteome, so comparisons based on binary expression/non-expression do not represent the dynamic range of the lens proteome. Instead, a rank-based comparison was performed in PSEA-Quant, a modification of the GSEA algorithm (Lavallée-Adam et al., 2014). As may be expected, each region was independently enriched for lens ontologies such as visual perception (GO:0007601) and lens fiber cell development (GO:0070307). Several ontologies were independently enriched in each region but are better delineated in between region calculations.

Between region calculations suffer from the same limitations as previously mentioned; the dramatic dynamic range of the lens proteome abundances does not warrant binary enriched/non-enriched ontology analysis. To quantify changes while between region abundance changes, we again employed PSEA-quant. Briefly, the ratio of protein abundances was computed between each combination of technical replicates of two regions. Only razor proteins that were detected or imputed in all samples were used (n = 2,556, 90 proteins with at least one imputed datapoint). The rank-based enrichment method then identifies changes that are linked to changes between samples, with additional weighting given to proteins with significant changes. PSEA-quant is inherently biased towards defining low quantitative CV proteins, such as ubiquitous extracellular matrix protein networks, as enriched. For our discussion here, we limit ontological enrichment comparisons to those between the cortex and inner nucleus. A result of membrane protein enrichment, it is less likely that the protein networks characterized as enriched are from subcellular localizations not associated with the membrane or insolubilized in the fiber cell aging process.

In total, 110 ontologies were enriched in cortex in relation to the inner nucleus, and 96 of the inverse relationship (Appendix A). While it is to be expected that organelle specific proteins are more abundant in the outer cortex relative to the inner nucleus, several inferences related to MCS function can be made. First, there is clear enrichment of translation and transcription machinery in cortical fibers reflecting activity of protein synthesis in new fiber cells, but not in older fiber cells. Also established in young fiber cells is the machinery to transport cations and establish the MCS ion gradient. In the inner nucleus, there is measured enrichment for proteasome modules. Complimentary enrichment of UCH proteinases which are responsible for negative regulation of ubiquitin-mediated degradation are also measured in the inner nucleus. A final point of interest, positive regulation of purine nucleotide metabolic process (GO:1900544) is enriched in the inner nucleus. The metabolism of purine nucleotides to uric acid is not well studied in the lens, but uric acid production in serum is increased in hypoxic conditions (Baillie et al., 2007) with potential antioxidant capacity. A previous study showed that patients with posterior subcapsular cataract (a less prevalent age-related cataract) had increased quantities of uric acid production in the aqueous humor which resides adjacent to the lens capsule (Qin et al., 2020). It is unclear whether uric acid would act as an antioxidant or pro-oxidative agent in lens fiber cells (Sautin & Johnson, 2008), but the detection of this biological process with DIA highlights the capacity of the presented method to develop testable hypotheses.

A benefit of greater proteome coverage is that a greater proportion of networks may be considered for ontological significance. In PSEA-quant, networks that meet p-value and FDR significance fail to be deemed significant when <3 proteins from the studied ontology are present. For ontology networks enriched in the inner nucleus by DIA measurement (Appendix A), 20 of the significant ontologies are represented by less than 10 proteins in the dataset. Indeed, when DDA data files were processed through the PSEA-quant pipeline with identical treatment, only 59 ontologies were enriched in either the cortex or inner nucleus (Appendix B) – all with functional redundancy to the 206 ontologies from DIA results (Appendix A).

Among cortically enriched DIA ontologies, few are sparsely populated because of the significant improvement in identifications. Thus, the enhanced proteome coverage improves preliminary identification of protein networks that are influential in lens fiber cell aging. Lastly, the enhanced peptidome coverage afforded by DIA provides a more robust quantitative assembly of protein groups in the MaxLFQ ratio-based algorithm, leading to more reproducible and biologically representative protein abundance comparisons.

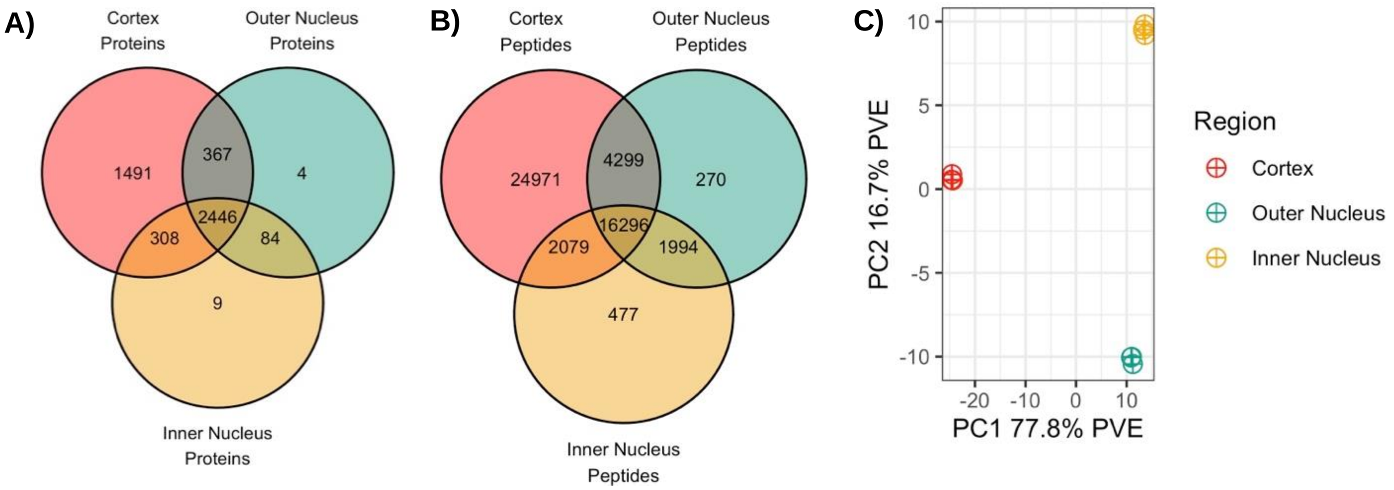

Figure 3-6 - The spatial distribution of peptides and proteins across the lens displays significant differences as a function of fiber cell age. Data with one variable deamidation used for analysis, comparisons were performed without filtering for razor protein uniqueness. A) Lens protein group overlap with one technical replicate required for consideration, B) Lens peptide overlap, charge states combined, one technical replicate required for consideration. C) PCA demonstrated that cortical fiber and nuclear fiber protein abundances show significant differences on PC axis 1, and abundance of nuclear fiber proteins contributes to separation on PC axis 2.

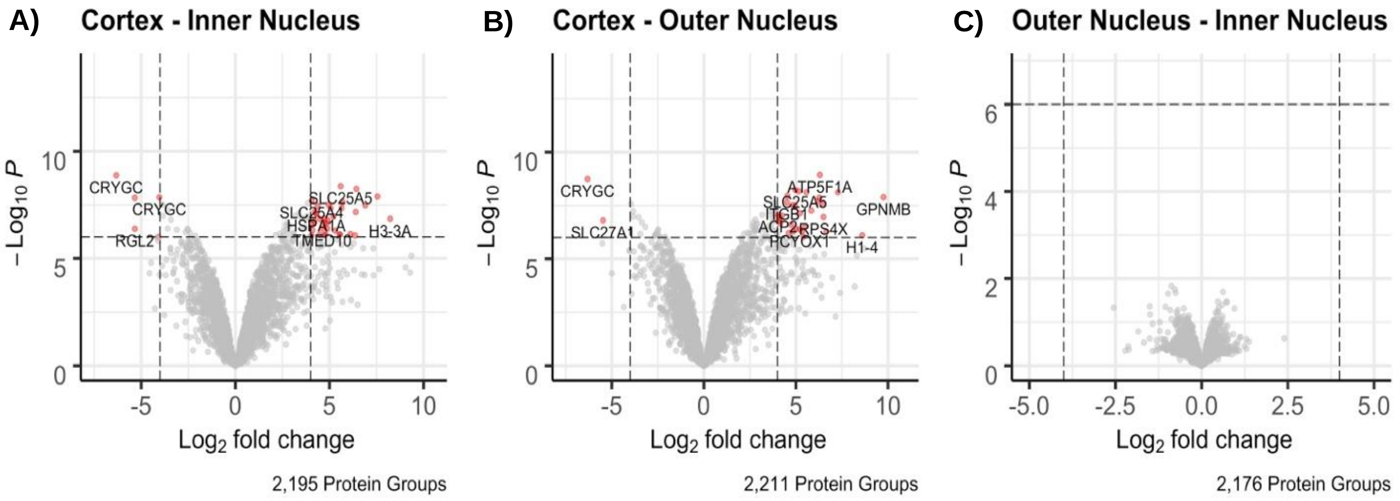

Figure 3-7 – Comparison of protein abundances in the lens. A-C) Regional comparisons of the deamidation enabled search. Limma moderated p-value cutoff was set to $1x10^{-6}$ with a log_2FC significance level of 4. Multiple annotation for the same protein may be present because only the razor protein gene association is shown. Full annotation of protein groups is in supplemental Appendix C. Only values which were detected in all 3 replicates and not imputed were used for comparison. The outer nucleus and inner nucleus show remarkable similarities in protein abundance at young human age.

3.5. Improved sample preparations and low-resolution MS analysis

To develop the protocols demonstrated, optimization of sample preparation was done on a low-resolution Velos Pro LTQ platform. While not used in most discovery-scale quantitative proteomic experiments, LTQ platforms still hold great utility due to their rapid scanning relative to orbitrap platforms, and reduced need for instrument maintenance. Further, these LTQ platforms are significantly less expensive to purchase and operate than a QE instrument, giving utility to the use of low-resolution platforms where precise quantitation is less essential than identification of predominant analytes in the injected sample. To demonstrate the utility of LTQ in a modern research setting, we compared methods for lens sample preparations, evaluating successive improvements with LTQ instrumentation.

As described, fractionation strategies such as BRP provide a convenient way to expand the quantity of peptide and protein group identifications on low-resolution instruments. Whereas DIA has demonstrated utility in identifying low-abundance precursors alongside high-abundance precursors in a single scan, low-resolution instruments and lower field orbitrap instruments are not capable of achieving desired mass resolving power or scan rate for DIA experiments. Thus, demonstration of utility of LTQ for research protocols provides an attractive way to survey preparative method development steps.

Earlier strategies employed by Wang and colleagues demonstrated that the lens can be fractionated to isolate a urea-insoluble fraction where only proteins in the membrane and tightly associated via covalent and non-covalent interactions are measured (Z. Wang et al., 2013). In the shown DIA study, the same protocol was used with exception of NaOH washing of the insoluble fraction used by Wang. It is suggested that the base wash strips the membrane of weak interactions, removing proteins that are not strongly interacting with the membrane. A result of base wash removal, weak protein-protein interactions with the membrane proteome were preserved in the presented DIA study. From this, it was desirable to improve identifications possible in the bovine lens cortex by BRP prior to adapting methods for human lens. Several strategies were evaluated: use of a ThermoFisher commercial BRP kit, an in house stop-and-go-extraction (STAGE) tip-based BRP fractionation with equal and greater separation steps (Lee et al., 2016). Additionally, we evaluated the use of detergent solubilization prior to digest tryptic with S-Traps relative to conventional in-solution tryptic digest.

Four separate sample preparations of the bovine lens cortex were performed by isolating the fibers external to a 7/16" biopsy centerpunch. All lens samples were treated equally prior to digest and separation. The BRP separation was approximately replicated from the ThermoFisher kit instructions, with deviation in column fabrication and mobile phase basic aqueous component (see Methods). Samples were named as follows: Thermo was the ThermoFisher BRP kit, performed with 8 fractionation steps; STAGE 8 was the in-house STAGE BRP method with 8 fractionation steps; STAGE 12 used 12 fractionation steps; and S-Trap which blended S-Trap digest with the STAGE 8 protocol for peptide fractionation. All Raw files were then processed through TagRecon (Dasari et al., 2010) and filtered at 5% FDR by IDPicker (Z.-Q. Ma et al., 2009). Total unique peptides identified in all samples was 12,242, with 4,641 identified by Thermo, 6,562 by STAGE 8, 4,852 by STAGE 12, and 8,290 by S-Trap (Figure 3-8). While it was anticipated for the STAGE 12 to exceed the capabilities of STAGE 8, this discrepancy wasn't evaluated because S-Trap exceeded the capabilities of STAGE 8 by 26% while requiring 33% less instrumentation time relative to STAGE 12. Similarly, protein group identifications totaled 1,772 with 857 identified by the Thermo kit, 1,266 by STAGE 8, 865 by STAGE 12, and 1,455 by S-Trap. Moderate differences in quantity of protein groups identified can be attributed to peptides that constitute the protein group, e.g., a protein group of fewer peptides may correspond to a greater number of candidate protein groups, resulting in a distinct protein group from one where many peptides are measured, narrowing down candidate proteins assembled in the protein group. Thus, S-Trap digest paired to STAGE 8 sample fractionation resulted in the greatest depth of protein and peptide measurements. The quantity of protein groups represented here exceeds that of Wang and colleagues by 504 protein groups.

While effective in the presented study, the use of TagRecon and IDpicker presents a challenge for the MS community at large. TagRecon is available as a legacy search algorithm and IDPicker is accessible through the proteowizard software package, but the utilization of these in the existing literature is infrequent and the workflow is not highly comparable to modern algorithms. Percolator is an open source, modern peptide spectral match (PSM) validation tool that scores client fragment ions to determine PSM q-values from search algorithm defined matches. Unlike IDPicker, Percolator filters appropriate identifications to a global FDR, e.g. 5% as the community standard for LTQ data. Percolator results are then compiled by ProteinProphet to assemble protein groups based on valid PSMs. IDPicker filters search algorithm PSMs by the FDR calculated in search and further filters peptides by their contribution to protein groups. As a filtering tool, IDPicker then relies on specific file input structures to assign PSM confidence in addition to protein group confidence. In contrast to the TagRecon/IDPicker combination approach, many algorithms can be used for PSM identification including Sequest (Eng et al., 1994), TagRecon, and MSFragger (Kong et al., 2017). While TagRecon and Sequest were originally developed for low-resolution data, MSFragger was not written to accommodate LTQ results files. A key advantage of MSFragger however is its pipelined incorporation to FragPipe, where an automated file hand off sequence occurs between MSFragger for search, Percolator (The et al., 2016) for PSM filtering, and ProteinProphet (Nesvizhskii et al., 2003) for protein group assembly. Thus, modifying FragPipe and its constituent software packages to accommodate low-resolution data is important, especially in research situations where advanced knowledge of intermediate data structures in MS search are not available.

To modify FragPipe, we increased the expected precursor and fragment ion tolerances to 500 ppm and 0.7 Da respectively. These values were determined as optimal through iterative changes in identification efficiency on all 36 files evaluated by TagRecon. Instrument true mass accuracy was set to 500 ppm and the number of peaks evaluated in MS2 was limited to 100 in initial search prior to MS2 spectral assignment optimization. Finally, protein group FDR was modified for ProteinProphet to 5%, while leaving ion, PSM, and peptide level FDR at 1% as default in Percolator. When increasing the FDR of fragment and peptide level results, non-specific spectra were identified as true positives and the sensitivity to true positives identified at 1% FDR was decreased (data not shown). Previous work from Krey and colleagues demonstrate that low-resolution quantitation on basis of MS1 is quantitatively similar to results achieved by high-resolution instrumentation, exceeding the accuracy of spectral counts significantly (Krey et al., 2014). Unfortunately, the FragPipe MS1 quant module was not successfully modified in FragPipe for low-resolution data.

To compare the custom framework of TagRecon/IDPicker to the modified pipeline in FragPipe, we evaluated the S-Trap dataset previously shown (Figure 3-8) and matched search parameters including PTMs and fasta database searched against. IDPicker was also operated to best match the FDR estimation of Percolator and ProteinProphet. From this it became clear that MSFragger and its corresponding tools exceed the identification capabilities of TagRecon (Figure 3-9). MSFragger identified 12,242 peptides, while 11,224 were identified by TagRecon. Further substantiating improved identification efficiency, 1,772 unique protein groups were measured with MSFragger, while only 1,349 were evaluated with TagRecon. It is important to note the trade off in identification efficiency of peptide and protein groups measured by TagRecon and IDPicker when modified to match approximate FDR filtering of FragPipe. While this afforded a 35% increase in protein group identifications over default IDPicker filtering parameters, there was an 8% increase in peptide identifications. This is indicative of q-value calculation variance in the TagRecon outputs between search algorithm, but also reflects differences in protein group assembly between the parsimonious and graph theory-based approaches of IDPicker and ProteinProphet, respectively. Finally, while not the original intent of the study, FragPipe was more rapid than TagRecon/IDPicker in the assignment of a greater quantity of unique protein groups and peptides. Whereas the Vanderbilt supercomputing cluster took several hours to produce pepxml results files, which are manually converted to comma separated results files in several minutes by IDPicker, FragPipe completed search and comma separated results files production in 32 minutes without user intervention on a desktop chipset produced in 2018 with 64 GB RAM. Taken together, the adaptation of FragPipe and utilization of the Velos Pro in method development highlight an ongoing use for low resolution instruments as valid tools to the mass spectrometry research community and in research environments.

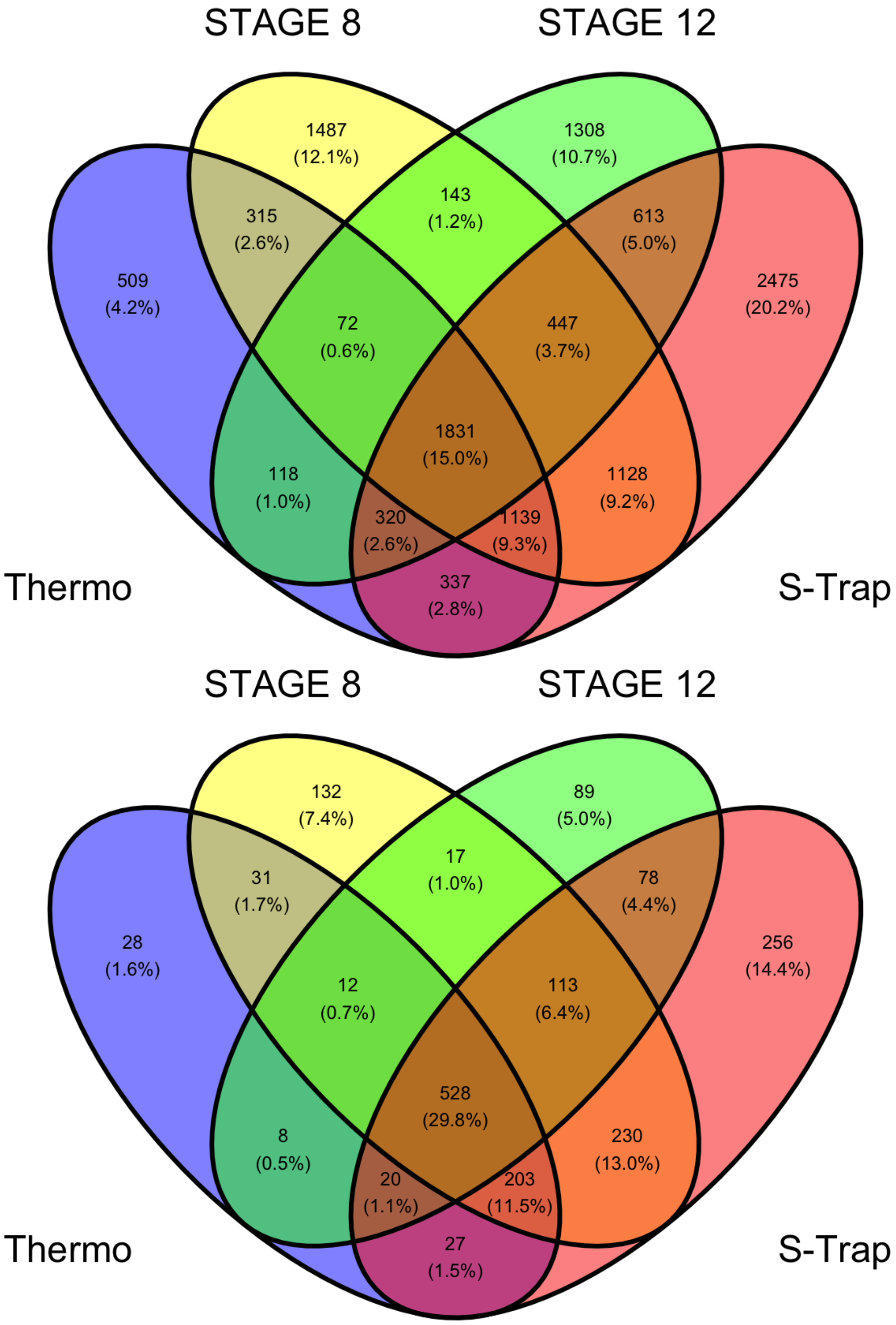

Figure 3-8 - Venn diagram of overlap between Thermo, STAGE 8, STAGE 12, and S-Trap sample preparation methods respective to peptide (top) and protein group (bottom) total identifications.

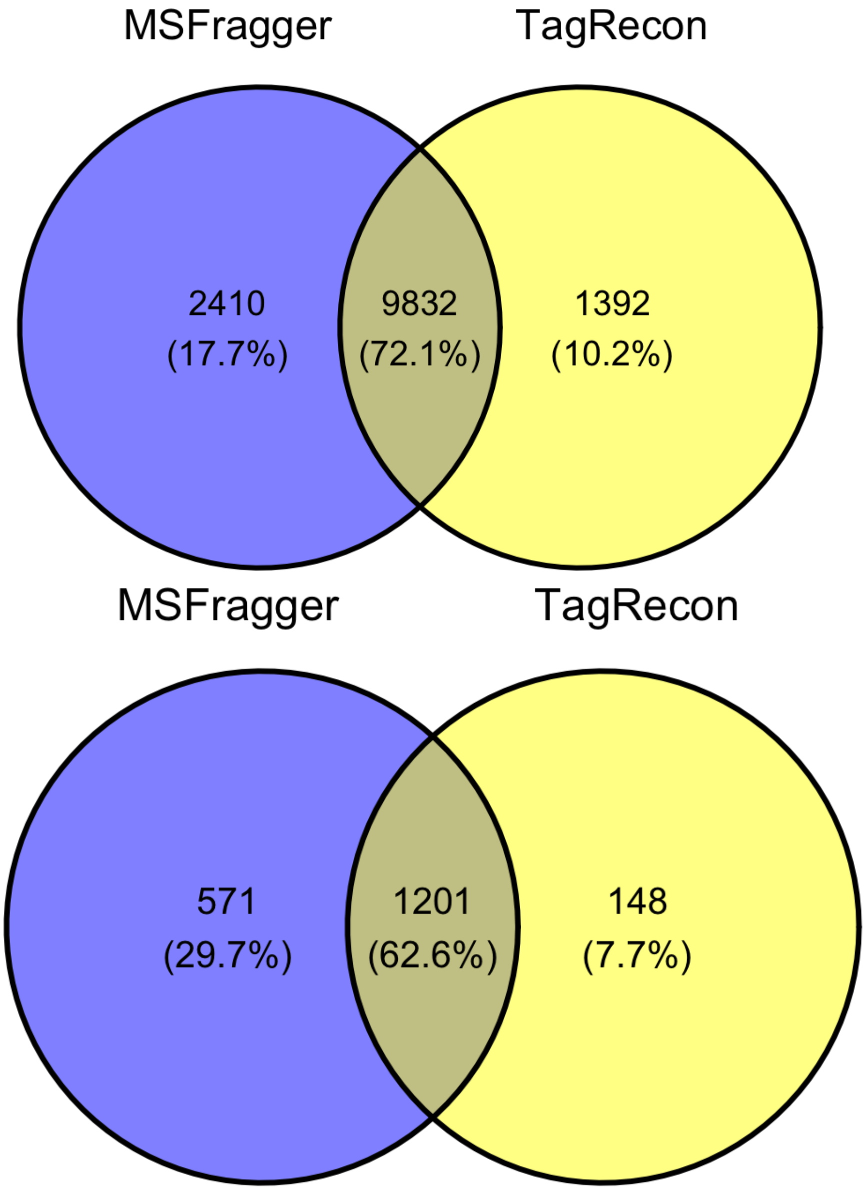

Figure 3-9 - Comparison of search engine identifications between MSFragger (blue) and TagRecon (yellow) with Venn diagrams of unique peptides (top) and unique protein groups (bottom) identified.

3.6. Conclusion

Here, we have shown that DIA methodology greatly improves identification of low abundance proteins in the lens and have demonstrated an effective way to search the data with lens biology in mind. The gradual shift towards protein deamidation and proteome specialization for oxidoreductase activity clearly demonstrates that this method is sensitive to age-related fiber maturation measurements, and the enhanced ability of DIA to measure low abundance peptides improves protein-network level characterization of lens aging. Additionally, the application of PSEA-quant here demonstrates a functional ontology search that is sensitive to protein abundance and is well suited towards assessing lens biology. It is reasonable to suggest that the improved protein network coverage afforded by DIA paired to sensitive analysis pipelines may allow improved insights into human lens aging and cataract formation. Finally, we have demonstrated how low-resolution instruments can be effectively used in method development and have provided a modified pipeline for rapid evaluation of such datasets.

4. CHAPTER 4

PROTEOME REMODELING OF THE EYE LENS AT 50 YEARS IDENTIFIED WITH DATA-INDEPENDENT ACQUISITION

The following chapter is adapted from the previously published article: Proteome Remodeling of the Eye lens at 50 Years Identified with Data-Independent Acquisition written by Schey and Cantrell. Supplementary data is stored under PRIDE accession PXD033722 (ftp://massive.ucsd.edu/MSV000089427/).

4.1. Abstract

The eye lens is responsible for focusing and transmitting light to the retina. The lens does this in the absence of organelles yet maintains transparency for at least five decades before onset of age-related nuclear cataract (ARNC). It is hypothesized that oxidative stress contributes significantly to ARNC formation. It is additionally hypothesized that transparency is maintained by a microcirculation system (MCS) that delivers antioxidants to the lens nucleus and exports small molecule waste. Common data-dependent acquisition (DDA) methods are hindered by the large dynamic range of lens protein expression and provide limited context to age-related changes in the lens. In this study we utilized data-independent acquisition (DIA) mass spectrometry to analyze the urea insoluble, membrane protein fractions of 16 human lenses subdivided into three spatially distinct lens regions to characterize age-related changes, particularly concerning the lens MCS and oxidative stress response. In this pilot cohort, we measured 4,788 distinct protein groups, 46,681 peptides, and 7,592 deamidated sequences, more than in any previous human lens DDA approach. Principally, we demonstrate that a significant proteome remodeling event occurs at approximately 50 years of age, resulting in metabolic preference for anaerobic glycolysis established with organelle degradation, decreased abundance of protein networks involved in calcium-dependent cell-cell contacts while retaining networks related to oxidative stress response. Further, we identified multiple antioxidant transporter proteins not previously detected in the human lens and describe their spatiotemporal and age-related abundance changes. Finally, we demonstrate that aquaporin-5 among other proteins, is modified with age by PTMs including deamidation and truncation. We suggest that the continued accumulation of each of these age-related outcomes in proteome remodeling contribute to decreased fiber cell permeability and result in ARNC formation.

4.2. Introduction

The ocular lens is a transparent tissue lacking vasculature and is responsible for light transmission to the retina for visual perception (Augusteyn, 2007). The lens originates from primary fiber cells that differentiate from epithelial cells *in utero*. Throughout life, concentric growth rings of secondary fiber cells are added to the lens, differentiating at the lens equator from an anterior monolayer of epithelial cells to elongated fiber cells that extend toward the anterior and posterior poles of the lens (Figure 4-1A). Unlike most cell types, lens fiber cells are not degraded throughout life but experience organelle degradation and enter a senescent-like state shortly after elongation as part of cellular maturation (Bassnett, 2002). Thus, proteins in the center of the lens are effectively as old as the subject and proteins are spatially organized, as are fiber cells, in concentric growth rings.

Lens protein oxidation, particularly in the lens inner nucleus is hypothesized to contribute to formation of age-related nuclear cataract (ARNC)(Hains & Truscott, 2008; Truscott, 2005). ARNC is the most common form of blindness and pharmacological options for delaying onset, prevention, or reversal are lacking. In a young lens, the oxidative stress response is primarily mediated by glutathione-requisite proteins (V. N. Reddy, 1990; Sweeney & Truscott, 1998; Lou, 2003; J. Lim et al., 2007; Linetsky et al., 2008; J. C. Lim, Grey, et al., 2020). In the absence of vasculature, small molecules including water and glutathione (GSH) must be delivered to the inner nucleus of the lens through the extracellular space of the lens sutures, established at the anterior and posterior poles of the lens between the tips of fiber cells (J. Lim et al., 2007).

The delivery of antioxidants and efflux of waste products is hypothesized to be established by the lens microcirculation system (MCS)(Vaghefi & Donaldson, 2018). In the MCS, small molecules are delivered through the lens sutures to the inner nucleus, taken up by fiber cells, and are exported through the equator by a concerted network of intercellular junctions (connexins) and water channels (Schey et al., 2017). Exported molecules are then convected throughout the lens humoral exterior towards the anterior and posterior poles before re-entering the lens. Molecular convection is established by an electromotive potential gradient of Na/K ATPases transporting sodium out of the lens at the equator while concurrent export of potassium is mediated by potassium channels on the lens epithelium (Beebe & Truscott, 2010; Donaldson et al., 2010). The resulting potential, coupled to aquaporin water transport and gap junction intercellular contacts leads to a net current of metabolite convection into the lens at the anterior and posterior poles (Berthoud & Beyer, 2009; Mathias et al., 2010)(Figure 4-1B).

In the young lens, and especially in young cortical fiber cells, MCS functionality is sufficient to transport water and metabolites through the lens (A. C. Grey et al., 2019; Moffat et al., 1999). However, convection of small molecules to the lens nucleus and through progressively aged lenses is inhibited by a barrier to diffusion (Moffat et al., 1999; Sweeney & Truscott, 1998). This barrier is formed and becomes kinetically significant by 40-60 years of age (Moffat et al., 1999). After barrier formation, small molecules may enter the lens through the sutures but do not proceed through the restricted extracellular space at the same rate as in the young lens. Thus, as the lens ages and GSH is not delivered to the lens nucleus, proteins incur oxidative damage at an accelerated rate relative to the young lens (A. C. Grey et al., 2019; Hains & Truscott, 2008; Sweeney & Truscott, 1998; Truscott, 2005). Protein byproducts of oxidative damage may ultimately result in protein misfolding, cross-linking, aggregation, and light scattering ARNC (Buckingham, 1972; Truscott, 2005).

Measurement of the lens proteome has previously been achieved by measurement of whole lens lysates, imaging mass spectrometry, and spatially targeted approaches employing manual separation or laser capture microdissection prior to sample analysis (Cantrell & Schey, 2021a; Garland et al., 1996; Truscott et al., 2011; Z. Wang et al., 2021; Wenke et al., 2015, 2016; X. Wu et al., 2017b). A limitation to all lens proteomics experiments is the high abundance of crystallin proteins, reported to constitute up to 90% of the lens proteome (Bloemendal et al., 2004). Although age-related modifications to lens crystallins, such as abundance change, deamidation, and truncation have been identified, a substantial gap in our knowledge exists in understanding how the MCS changes at the molecular level as a function of age. In this study, we use Data-Independent Acquisition (DIA) mass spectrometry coupled to a membrane protein enrichment strategy to measure the membrane proteome of human lenses at different ages. To quantitatively measure spatiotemporal changes, we have divided the lens into three regions with distinct biological functions: the inner nucleus, which contains primary fiber cells formed *in utero* alongside the oldest secondary fiber cells of the lens, the outer nucleus, where fiber cells are fully matured and reside on the interior side of the diffusion barrier (Figure 4-1A); and the cortex, which is composed of the youngest mature secondary fiber cells, differentiating secondary fiber cells with organelles still intact and a monolayer of epithelial cells. Proteome measurement in each of these regions is critical for understanding how age and barrier establishment perturb protein machinery responsible for MCS establishment and delivery of antioxidants to the inner nucleus.

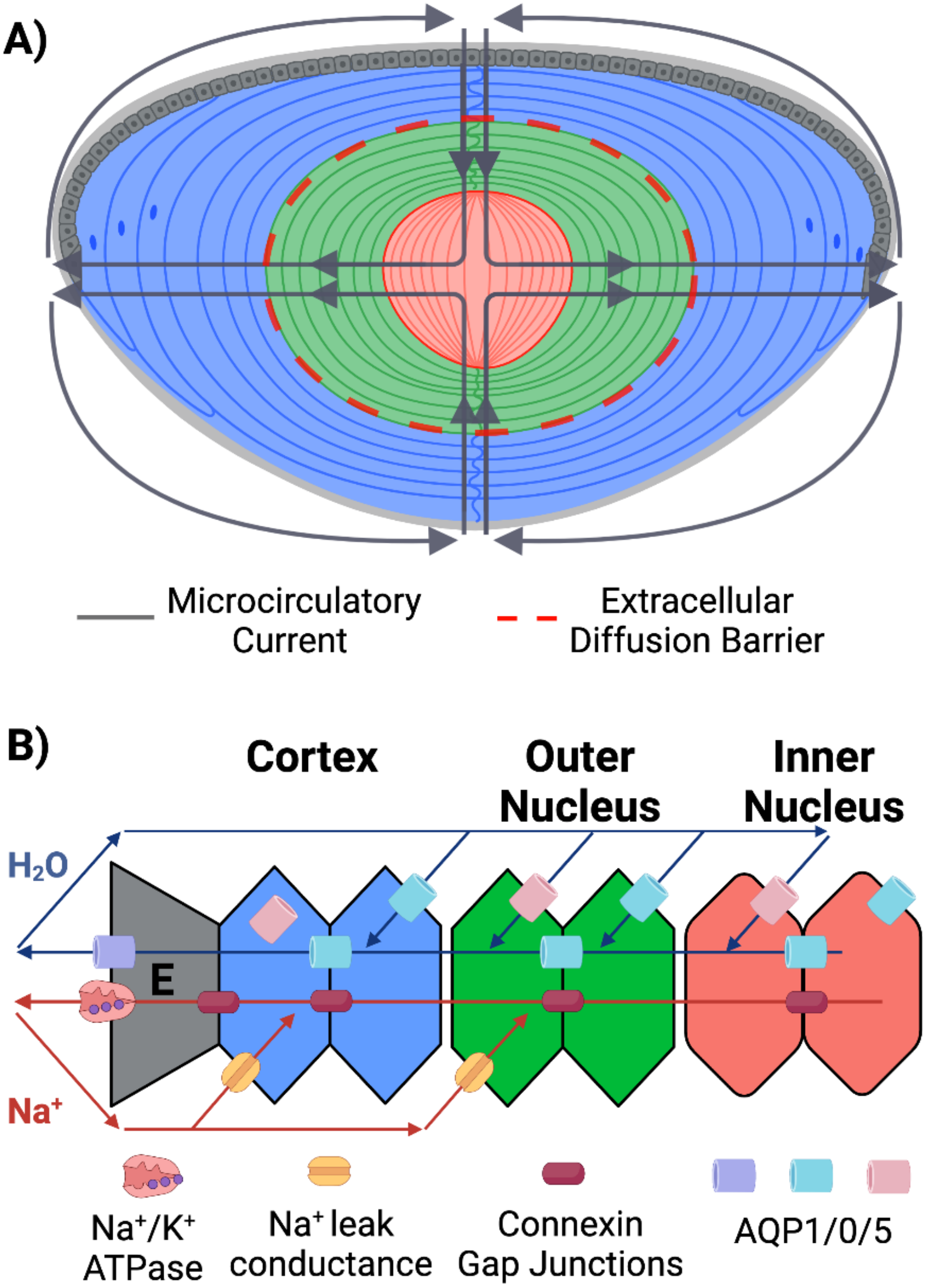

Figure 4-1 - Cartoons of the lens and microcirculation system: A) Cartoon of the lens with fiber cells divided into cortex (blue), outer nucleus (green) and inner nucleus (red) with the net convection of the microcirculation system displayed. The approximate positioning of the extracellular diffusion barrier is noted within the inner nucleus. B) Cartoon of the electromotive potential establishment and net current in the cross section of cells in the microcirculation system. Na/K ATPases at the epithelium (E) transport sodium from the lens, with re-uptake enabled by sodium leak conductance channels in fiber cells. Sodium transport is enabled by aquaporin-0 and -5 in fiber cells and aquaporin-1 in epithelial cells. The current established by microcirculation allows small molecule metabolites to transport intercellularly through connexin gap junctions at the cross section of fiber cells. Figure adapted from Schey et al. 2017.

4.3. Materials and Methods

4.3.1. Experimental Design and Statistical Rationale

Sixteen human lenses from age 15-74 years were analyzed with sample selection guided by known age-related lens physiology. Exclusion criteria included several cataract comorbidities such as diabetes mellitus, nicotine use, and non-age-related cataract. Additionally, no cataract lenses were used in this study. These studies were conducted in accordance with the ethical standards of the institutional research committee and with the 1964 Helsinki declaration and its later amendments. Each of the 16 lenses was divided into 3 regions (cortex, outer nucleus, and inner nucleus) to yield a total of 48 samples in the dataset. For sample quality control, 0.75 µg MassPREP protein standard was added to each approximately 75 µg lysate to monitor digest efficiency between replicates.

Samples were analyzed with DIA without pre-fractionation, with MS1 spectra interspersed every 30-31 scans. Each of the 48 samples analyzed in the study were used to generate a spectral library in DIA-NN (v1.8.0) (Demichev et al., 2020) with an initial *in silico* library predicted by DIA-NN against a UniProt SwissProt canonical human fasta database with 9 MassPREP spike in proteins added (UP000005640, downloaded 10/12/2021, 20,402 entries). From this initial library, a subset of experimentally measured spectra were used to create an experiment specific library. After generation of the experimental spectral library, samples were re-analyzed, and proteins were quantified. No retention time standards were used, instead, endogenous peptide retention times were used for alignment in DIA-NN. Each sample was prepared and analyzed in an order determined by a random number generator and a blank gradient was run between samples to minimize carry over and quantitative bias. Trimmed means of M-Values (TMM) normalization was employed for sample normalization. Sample groups were defined by exploratory data analysis that revealed clustering of lenses before and after 50 years of age. Within the young lens cohort, 9 lenses were analyzed (aged 15, 18, 22, 34, 34, 41, 44, 46, 49 years) and 7 lenses were measured in the old lens cohort (aged 53, 57, 63, 64, 65, 68, 74 years). The sample size of this pilot cohort was set at sixteen to demonstrate changes that occur in human lenses on a protein network level and protein abundance changes that occur over a gradient of human age. Statistical significance of change was assessed with 2-sample t-tests and PSEA-Quant operated in “labeled” analysis mode (Lavallée-Adam et al., 2014).

4.3.2. Urea Insoluble Protein Isolation

The severity of cataract present in each eye was visually evaluated prior to tissue processing to confirm that advanced cataractous lenses were not analyzed. Mild yellowing of the lens was allowed, but each measured lens retained transparency. In addition to sample evaluation, de-identified ophthalmic medical history was reviewed to confirm that no cataract had been diagnosed. Samples were prepared as previously described (Cantrell & Schey, 2021b). Briefly, lenses were mounted with the equatorial axis parallel to a cryostat chuck before removal of the anterior and posterior poles of the lens yielding a 1.0 mm thick equatorial lens section. Concentric biopsy centerpunches were taken at 4.5- and 7-mm diameter to yield inner nucleus (0-4.5 mm), outer nucleus (4.5 – 7.0 mm) and cortex (7.0 – 9.2 mm) samples. Samples were then enriched for membrane proteins by a previously optimized method (Cantrell & Schey, 2021b). Briefly, tissue was hand homogenized in buffer containing 25 mM Tris (pH 8), 5 mM EDTA, 1 mM DTT, 150 mM NaCl, 1 mM PMSF. After homogenization, samples were centrifuged at 100,000g for 30 minutes and the supernatant discarded. Pellets were washed twice with the above homogenization buffer followed by washes with 3.5 M and 7 M urea added to the homogenization buffer. Centrifugation at 100,000g for 30 minutes was performed to separate the supernatant and pellets for each urea wash. The remaining urea insoluble pellet was taken up in 50 mM TEAB with 5% SDS and protein concentration was measured with a BCA assay.

Membrane pellets of urea insoluble sample (75 µg total protein) were suspended in 50 mM TEAB with 5% SDS. Spike-in of 0.75 µg MassPREP protein standard was added before DTT was added to 10 mM before incubation at 56°C for 1 hour to reduce disulfide bonds. Reduced cysteines were alkylated by adding IAA to 20 mM and incubating in the dark at room temperature for 30 minutes. Phosphoric acid was added to 2.5% to acidify proteins. Acidified proteins were precipitated onto the S-Trap (Protifi) membrane bed with 6 working volume equivalents of cold 100 mM TEAB in 90% methanol according to Protifi protocol. Samples were washed on the S-Trap with 100 mM TEAB in 90% methanol four times with centrifugation between steps to remove salts and detergents. Samples were then digested in the S-Trap with a 1:15 trypsin:protein ratio in 20 µL 50mM TEAB, pH 7.5 for 2 hours at 46°C. Digested peptides were eluted in 4 steps of 50 mM TEAB, 0.2%

formic acid, 50 mM TEAB and 50% ACN. Eluted peptides were dried under vacuum centrifugation and taken up in 0.2% formic acid prior to data acquisition.

4.3.3. Instrumentation and Data Analysis

Peptides were analyzed using a Dionex Ultimate 3000 UHPLC coupled to an Exploris 480 tandem mass spectrometer (Thermo Scientific, San Jose, CA). An in-house pulled capillary column was created from 75 µm inner diameter fused silica capillary packed with 1.9 µm ReproSil-Pur C18 beads (Dr. Maisch, Ammerbuch, Germany) to a length of 250 mm. Solvent A was 0.1% aqueous formic acid and solvent B was 0.1% formic acid in acetonitrile. Approximately 200 ng peptide was loaded and separated at a flow rate of 200 nL/min on a 95-minute gradient from 2 to 29% B, followed by a 14-minute washing gradient and 35-minute blank injection between runs. The exact gradient was determined by linearized separation of the top 50% most intense cortical peptide signals by the Gradient Optimization Analysis Tool (GOAT v1.0.1)(Trudgian et al., 2014).

For DIA, the Exploris 480 instrument was configured to acquire 61x20m/z (390-1010 m/z) precursor isolation window DIA spectra (30,000 resolution, AGC target 1e6, max IIT 55 msec, 27 NCE) using a staggered window pattern with window placements optimized by ThermoFisher XCalibur instrument controls. Precursor spectra (385-1015 m/z, 60,000 resolution, AGC target 3e6, max IIT 100 msec) were interspersed after each sequence of 30-31 MS/MS spectra of the mass range. Default charge state was set to +3, S-Lens RF level set at 40%, NCE set at 27 and data collected in profile mode. Each scan cycle of 63 spectra took approximately 4.4 seconds.

For analysis of DIA data, RAW files were converted to mzML files in MSConvert (Adusumilli & Mallick, 2017), with staggered window deconvolution performed to improve precursor specificity to a pseudo 10 m/z window width. Processed DIA files were searched in DIA-NN with an Intel Core i7-7700 CPU at 3.60 GHz utilizing 8 threads. For all searches, up to one missed trypsin cleavage was allowed on peptides 7-30 residues in length with N-terminal M excision and cysteine carbamidomethylation enabled. All fragments between m/z 200 and 1800 and in charge states +1-4 were considered. An initial spectral library was prepared by DIA-NN with deep learning-based spectra and retention time prediction against a UniProt SwissProt canonical human fasta database (UP000005640, downloaded 10/12/2021, 20,402 entries) with a predicted trypsin/P protease used. In each search, the neural network classifier was run in double pass mode with likely interferences removed, quantitation was performed in Robust LC (high accuracy) mode and cross-run normalization was turned off. Two separate searches were performed, one without variable modification and one with up to one variable deamidation on asparagine or glutamine (+0.984016 Da). An initial search of all files produced a spectral library that was used to search the data a second time (termed match between runs). After a search of files against the experimental spectral library (7,504 proteins and 55,875 peptides in the library built without modifications and 5,659 proteins and 27,639 peptides in the deamidation enabled library) precursors and protein groups were filtered at 1% FDR within DIA-NN.

4.3.4. Statistical Analysis

Statistical analysis was initiated through custom R scripts on peptides having <1% q-value and <1% global protein q-value. Prior to protein assembly, all peptides within the MaxQuant contaminant list were removed (Cox & Mann, 2008). Proteins were only assembled on peptides considered proteotypic and abundances for peptides and proteins was calculated by the diann R package function diann_maxlfq (https://github.com/vdemichev/diann-rpackage). Because lens samples were not of high (>90%) quantitative similarity by Pearson correlation of DIA-NN normalized protein abundances, normalization performed in DIA-NN was rejected for quantitation of peptides and proteins. To minimize the assumption employed by most normalization algorithms that all compared samples are congruent, a subset list of peptides and proteins detected in all samples was selected and TMM normalization was applied (M. D. Robinson & Oshlack, 2010). TMM applies a linear multiplier for normalization, which was extracted and uniformly applied to all rows of the peptide and protein matrices, including rows where missing values were present. Subsequent comparisons between lenses of different age are indicative of the representative contribution of a protein to the urea insoluble lens proteome. The distribution of peptides and proteins was qualitatively assessed to ensure that TMM treatment produced similar abundance distributions between samples (Figure 4-2). DIA analysis assumes that all measurable proteins are detected; thus, no missing value imputation was used.

Statistical significance between young and old lenses was calculated with a 2-sample t-test to minimize overfitting of data that had been log2 treated. Significance cutoff was set to a p-value of 0.01 for hierarchical clustering and volcano plot visualizations. Volcano plot significance was further established at 1.5 log2 fold change. Conservative statistical power of 2-sample t-tests was calculated with RnaSeqSampleSize package in R (S. Zhao et al., 2018). PSEA-Quant was used to evaluate significance on an ontology level without arbitrary significance cutoffs (Lavallée-Adam et al., 2014, p.). PSEA-Quant was implemented as recommended by the developers with enrichment between sample groups considered instead of enrichment within a single sample. Default parameters for PSEA-Quant were used, with iterations increased to 1,000,000 to enable empirical p-value assignment as low as 1/1,000,000.

4.3.5. Data Visualization and Presentation

All data visualizations were produced in R with either the ggplot2, heatmap.2, GGally or EnhancedVolcano packages. Principal component analysis (PCA) from the prcomp package was used to separate proteins based on relative protein abundance for all proteins without missing values in the compared dataset (number of proteins used in caption of each PCA figure). PCA processing included scaling of non-log2 transformed data. For hierarchical clustering, a Ward-based approach was used to produce the dendrogram of proteins below the 0.01 p-value threshold (number of proteins in caption). Subsequent visualization was done with the heatmap.2 package. Equivalent statistics were used to plot the volcano plots with the EnhancedVolcano package.

For PSEA-Quant visualizations, the list of significant protein network ontologies exceeds visually interpretable space, so terms returned from PSEA-Quant search were manually filtered based on FDR and p-value to 0.1 and 0.01, respectively. The remaining terms were manually reduced to eliminate unspecific or redundant terms from the visualization. Finally, selected protein abundance was visualized respective to age and lens region with corresponding linear trendlines calculated. For comparison of deamidation accumulation, the results from the DIA search with 1 variable deamidation were prepared as described and the ratio of deamidated peptide accumulation in each sample was calculated as deamidated peptide abundance / (deamidated + undeamidated abundances) to demonstrate the proportional accumulation of deamidation with age. Biological cartoons were drawn at BioRender.com.

4.3.6. Quality Control

Samples were prepared and were ran in random order. A BSA standard was run every 8 samples to verify integrity of retention time, instrument calibration, and chromatographic similarity. Several samples were re-injected to match TIC intensity and subsequently control for variability in quantitation of peaks with different peak shapes. The initial injections of these samples were not used in spectral library development or statistical analysis. The MassPREP protein standard was spiked into protein lysates prior to digestion to monitor digestion efficiency by sequence coverage and Pearson correlation profile of peptide abundances.

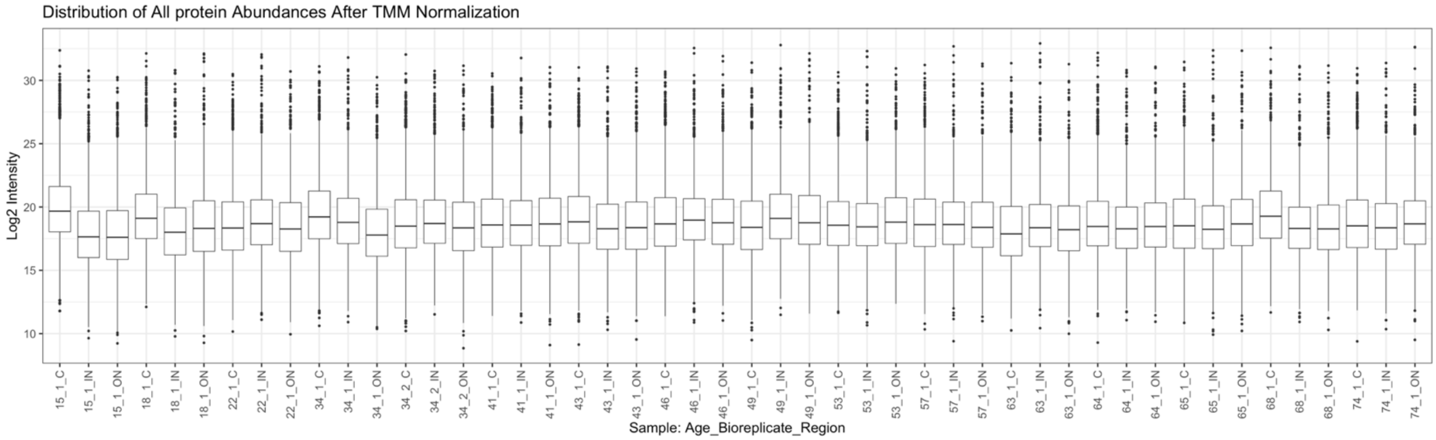

Figure 4-2 - Distribution of protein groups after TMM normalization was performed on all protein groups measured in every sample. Deviation from population distributions is indicative of representative abundance change for protein groups not measured in all samples.

4.4. Results

4.4.1. Data-independent acquisition of the lens proteome

To measure proteins associated with the membrane and intercellular interactions as key components of the lens MCS, we employed DIA on membrane and insoluble protein fractionated lens lysates from human lenses of different age. Fiber cells of increasing age were measured by separating the lens into three age-indexed regions: the cortex (youngest cells), outer nucleus, and inner nucleus (oldest cells). In total, 16 human lenses were measured (15-74 years old) resulting in 48 total samples. Each region described here approximately corresponds to growth regions previously defined by electron microscopy and MRI analysis of lens fiber cell morphology and physiology (V. L. Taylor et al., 1996; Vaghefi & Donaldson, 2018). To evaluate the prevalence of deamidation, a non-enzymatic age-related modification, we performed two distinct DIA data searches. The first was based on a spectral library with no variable modifications and the second was based on a spectral library with up to one variable deamidation. We used deamidation as a proxy for age-related accumulation of post-translational modifications that are less measurable with unenriched DIA approaches utilizing library-free search. In total, 4,788 distinct protein groups and 46,681 distinct peptides, not including modified sequences, were identified at 1% FDR. Additionally, 7,592 deamidated sequences were identified. In this study, DIA facilitated measurement of 2.5-fold more lens proteins than any previous human lens DDA method (Cantrell & Schey, 2021b). The resulting data are evaluated as the representative contribution of each protein within the lens membrane or insoluble proteome. Although lens proteins are not synthesized after fiber cell maturation, the accumulation or positive differential representation of proteins suggests a reduced rate of degradation of a protein relative to its constituent proteome or the accumulation of aggregated or otherwise insolubilized cytosolic proteins.

4.4.2. Determination of sample grouping by age

A primary goal of this study was to identify key subsets of protein networks that are preserved in the aging lens since they may relate to long-term maintenance of transparency. First, we performed PCA on proteins identified in all samples without imputation (n=884) (Figure 4-3A). Relative to conventional cell line model systems (Searle et al., 2019), few proteins were identified in all samples, which is reflective of long-lived protein degradation, modification, and of human biological variability. Separation along principal component axis 1 (PC1) showed a progressive transition of fiber cells from young cortical fiber cells to old inner nucleus fiber cells with some overlap of middle-aged fiber cell populations (e.g., old cortical, young inner nucleus and all outer nucleus fiber cells). Cortical lens region separation on PC1 was explained by cytoskeletal elements periaxin, vimentin, and neurofilament medium polypeptide; cadherin junction proteins cadherin-2 and catenin alpha-2; and brain acid soluble protein 1 (BASP1): each of these proteins were measured as more abundant in young fiber cells relative to old. Consistent with prior lens proteome investigations, older nuclear fiber cells were most associated with crystallins γ-A/B/C/D and β-B1; crystallin species that are known to associate with the membrane with age (Cantrell & Schey, 2021b; McAvoy, 1978; Truscott et al., 2011; Z. Wang et al., 2021). Further supporting the biological integrity of normalization approach employed, intermediate filament proteins were enriched in the young, still maturing cortical fiber cells as previously reported (Wenke et al., 2016). Spearman correlation between samples was also performed, demonstrating similarity between samples of the same region and progressive decrease in correlation between samples of increasing age difference (Figure 4-4).

From PCA analysis of all samples, no clear sample separation of subject age emerges. Age grouping was instead defined using hierarchical clustering of proteins with t-test significance at a 0.01 p-value between lenses below 50 years (young) and above 50 years (old). This preliminary cutoff was established congruent with the hypothesis of barrier formation at 45-50 years old (A. C. Grey et al., 2003). To evaluate consistency of biological changes directly associated with human age, each region of the lens was separately evaluated by hierarchical clustering (Figure 4-3B-D). As demonstrated in the dendrograms of each lens region, there is an appreciable change in the clustering of lenses before and after 50 years of age with single sample deviations for the 64-year-old inner nucleus and 53-year-old outer nucleus. No prior dataset of the lens has demonstrated the clear separation of lenses observed at 50 years as shown here. This suggests a biological event occurs after approximately 50 years of aging that initiates a time-diffuse proteome remodeling event in the lens. As a result of these findings, we considered sample groups in the lens as young or old based on a 50-year cutoff. Note that prescribed changes will gradually occur over time and specific changes depend on the subject, thus there will be a gradient of onset age observed in a larger sample cohort which better represents the population.

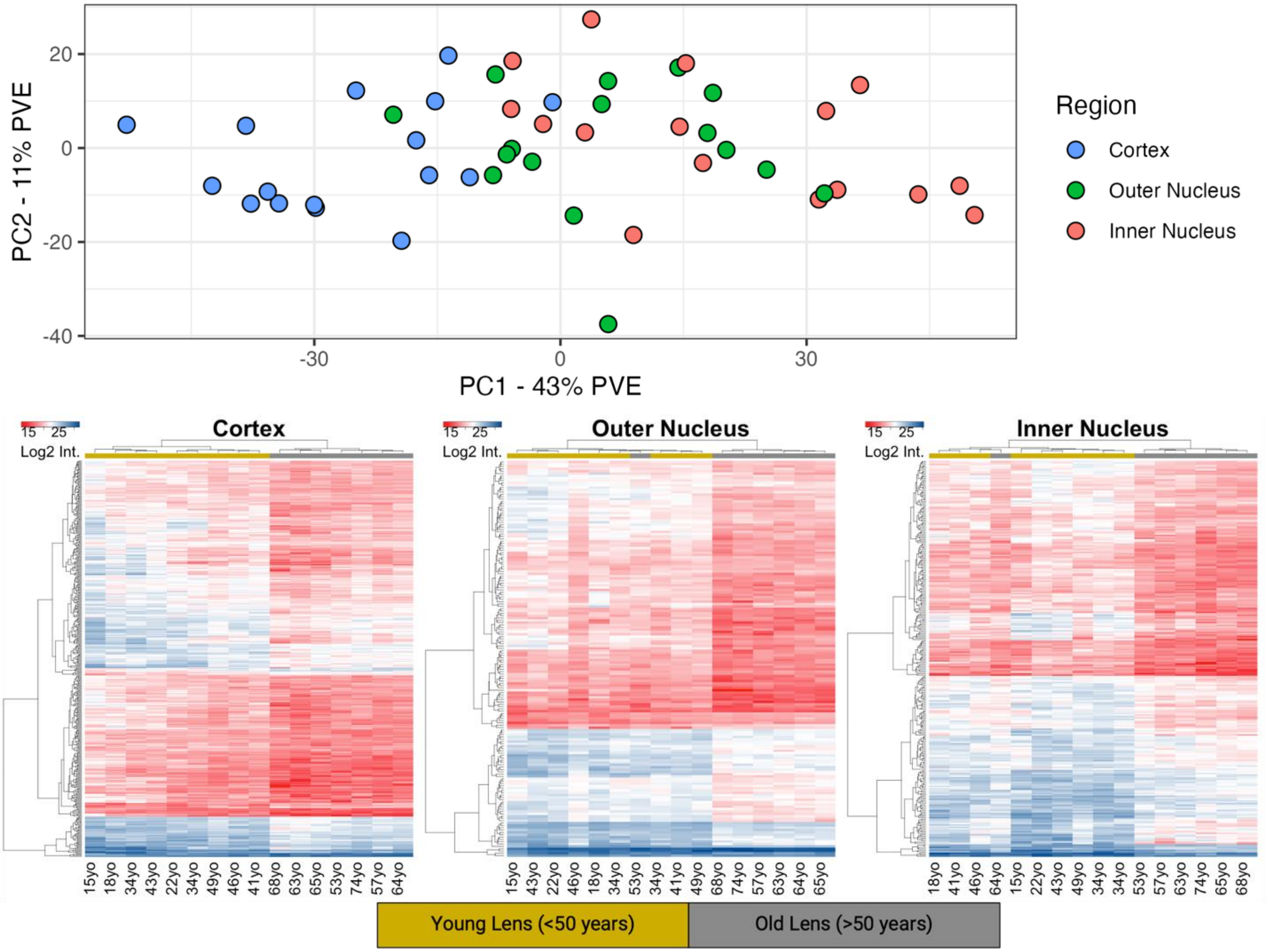

Figure 4-3 - Determination of age groups in the human lens based on fiber cell positioning and age. A) Principal Component Analysis (PCA) on all 48 samples based on only protein groups measured in all samples (n = 884). Each point was colored according to lens region as in Figure 4-1. B) Cortex hierarchical clustering demonstrates clustering of proteins differentially present in samples above and below 50 years. Significance was measured by a t-test with a 0.01 significance cutoff (n=432). Columns colored by t-test sample grouping. Protein group names presented in Appendix D if protein log2 fold change between groups exceeds 1.5. C) Outer Nucleus hierarchical clustering presented as in B (n=170). D) Inner Nucleus hierarchical clustering presented as in B (n=278).

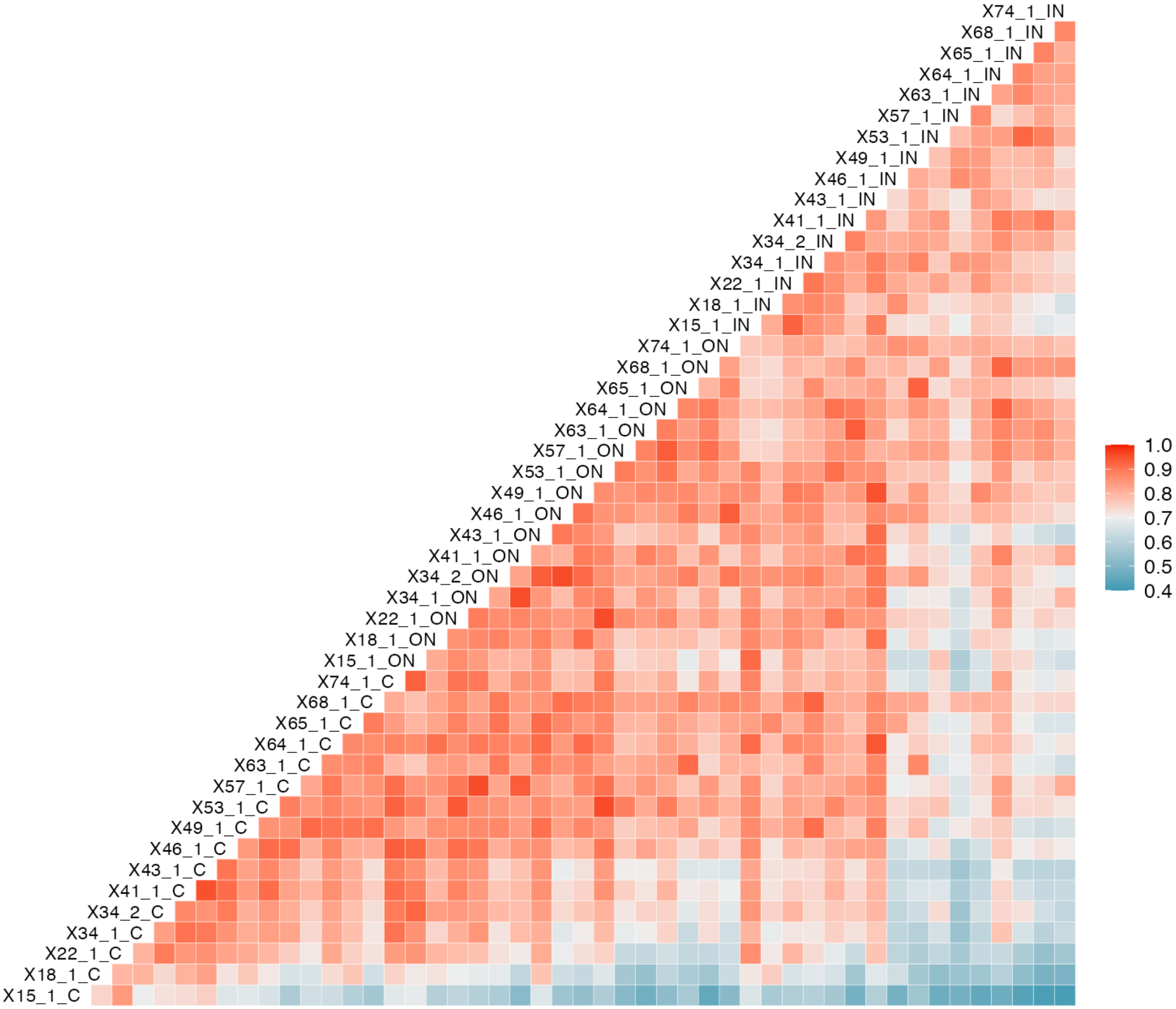

Figure 4-4 - Spearman rank correlation plot of all 48 samples, demonstrating that samples within lens regions are approximately similar and correlation decreases concurrent to increasing difference in age between paired samples. Sample naming scheme is as follows X + subject age + subject age biological replicate + lens region (C = Cortex, ON = Outer Nucleus, IN= Inner Nucleus). Samples are grouped by fiber cell population and ordered by subject age.

4.4.3. Age-related changes in the lens cortex

To demonstrate changes at the single-protein and protein-network level in the aging lens cortex, a three-step approach was taken. First, we performed PCA on all protein groups identified in each cortex sample. While the cortical data approximately clustered in Figure 4-3A, young and old lens fibers are separated on PC1 of the subset samples (Figure 4-5). A volcano plot analysis was done to evaluate all proteins that change between young and older lenses (Figure 4-6, Appendix D), with few proteins measured as increased in the old cortex relative to the young cortex. Few proteins are anticipated to increase with age, as proteins are only synthesized during maturation and an increase in protein abundance may reflect inaccurate data comparisons.

PSEA-Quant was employed to identify protein networks that are most changed with age. Unlike t-tests, PSEA-Quant eliminates arbitrary p-value cutoffs in volcano plots by establishing enrichment scores as done in the Gene Set Enrichment Algorithm (Subramanian et al., 2005). The results file of significant GO terms was filtered consistent with PSEA-Quant developer suggestions (Figure 4-7, Appendix E, Appendix F)(Lavallée-Adam et al., 2014). As expected, young lenses with intact organelle machinery still maintain ribosome, endoplasmic reticulum, Golgi, and other classical organelle structures (GO:0044391, GO:0048200, GO:0005783). While these organelle structures are present in both young and old lenses, the proportion of young and still maturing fiber cells is greater in the young lens than in the old lens. These young fiber cells also demonstrate canonical proteostasis enrichment relative to old fiber cells (GO:0030433, GO:0032469). Proteins involved in proteostasis include hsp70 BIP, hsp90 endoplasmin, wolframin, and DNAJB2. In the older cortical fiber cells, the results suggest that metabolic remodeling occurs as mitochondria are degraded, transitioning from oxidative phosphorylation to anaerobic glycolysis via the hexose monophosphate shunt pathway (GO:0051287, GO:0005911). It was also shown that cell-cell junctions are enriched in the young fiber cells relative to old and that oxidative stress response machinery is enriched in old fiber cells relative to young. Based on this result, we hypothesize that NADH production machinery is established in cortical fiber cells to metabolically support enzymes responsible for GSH-mediated oxidative stress response in aging fiber cells. Note that in-text graphics of PSEA-Quant results are a subset of all significant GO enrichment terms and were manually filtered by eliminating redundant or unspecific terms.

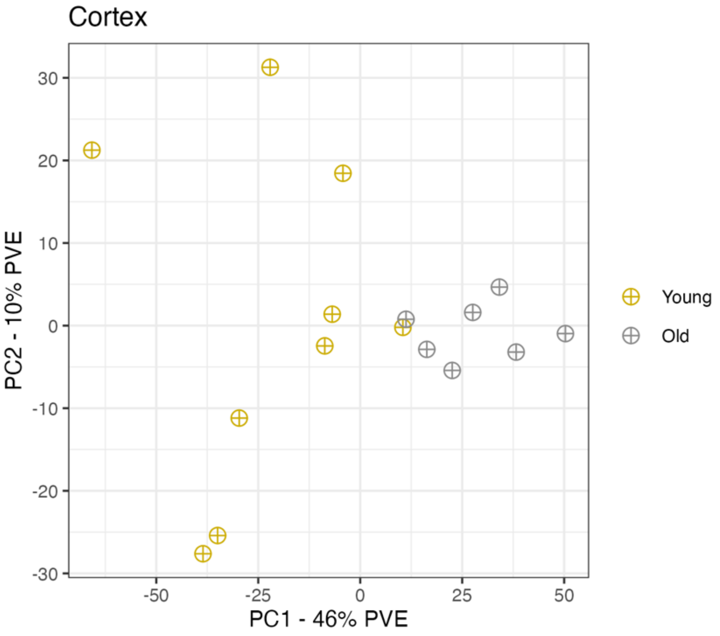

Figure 4-5 - PCA plot colored by age group demonstrates separation of young and old fiber cell populations on PC1 based on protein groups identified in all 16 samples (n=1,429). Proteins that significantly contribute to the negative (younger) loading on PC1 include epoxide hydrolase, fibrillin-1, phosphate carrier protein, cytochrome c oxidase subunit 2, and tubulin beta-4A chain. Loadings that most significantly contribute to the positive (older) loading on PC1 include γB-crystallin, WD repeat-containing protein 25, 4-hydroxyphenylpyruvate dioxygenase, and glutamate synthesis enzyme kynurenine oxoglutarate transaminase.

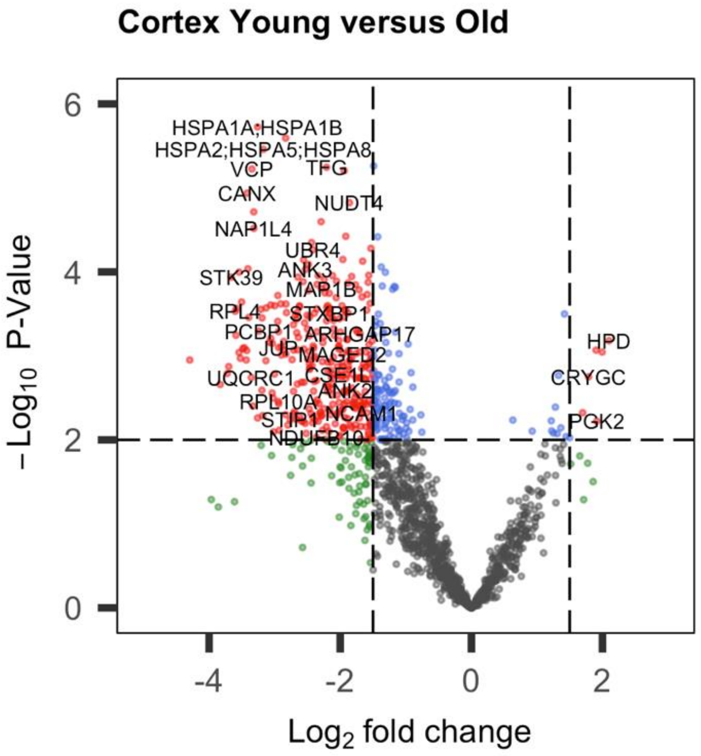

Figure 4-6 - Volcano plot of preferentially retained or degraded proteins with significance cutoffs of 0.01 unmoderated p-value and 1.5 log2 fold change. UniProt identifiers converted to gene names. The statistical power of this test is estimated to be approximately 0.65 with a sample size of 7, the size of the old lens sample group, and at 5% FDR.

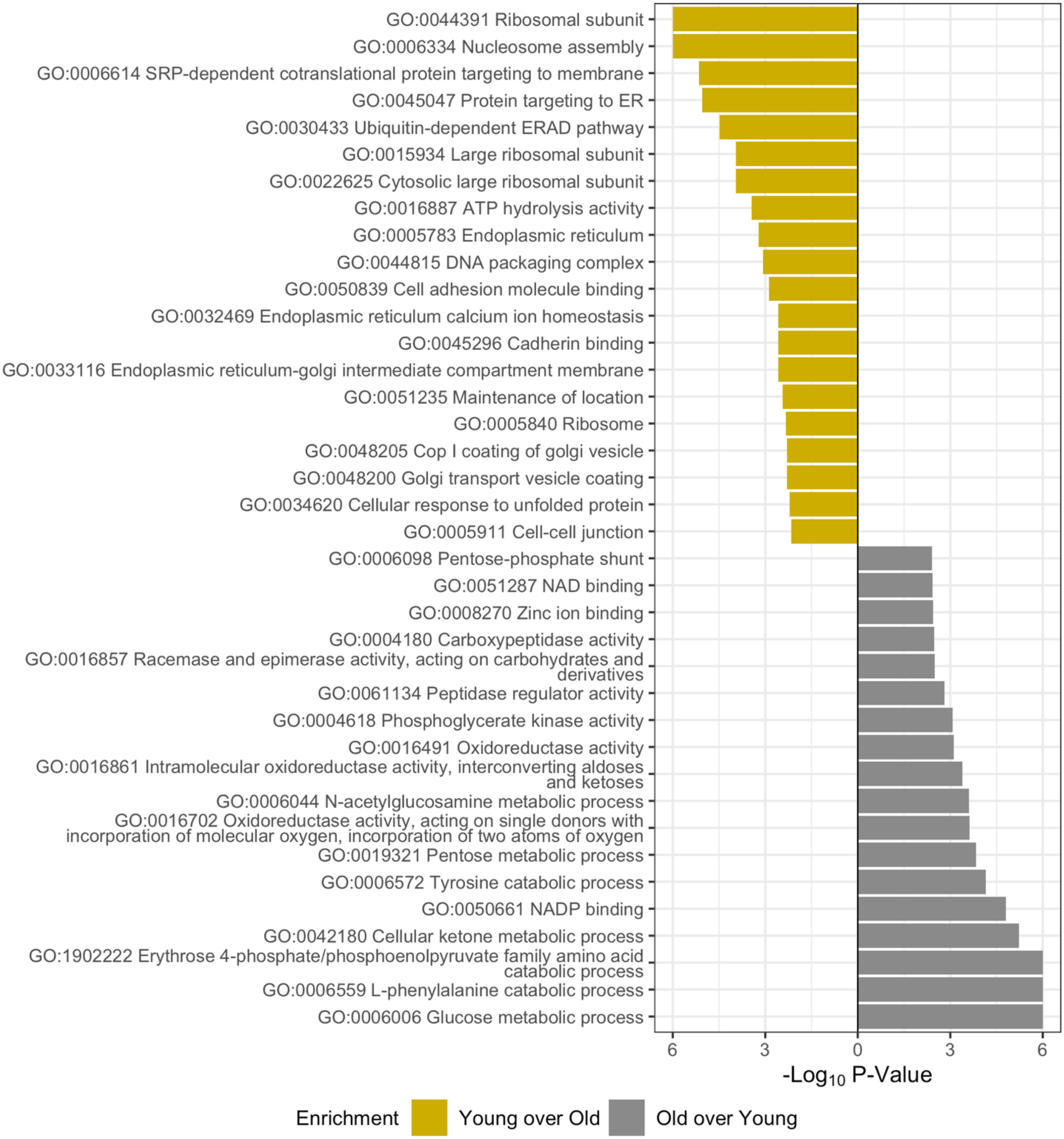

Figure 4-7 - PSEA-Quant pairwise enrichment calculated between young and old lens fiber cell regions. Separate calculations performed to determine each enrichment. Significant Gene Ontology terms were filtered at 0.01 p-value and 0.1 FDR. Ontologies in graphic are a subset of all measured, demonstrating non-redundant daughter terms indicative of the complete enrichment set. Full list of enriched terms included in Appendix E, Appendix F.

4.4.4. Age-related changes in the lens outer nucleus

In the outer nucleus, PCA analysis (Figure 4-8) demonstrates separation of young lenses from old lenses congruent to Figure 4-3C. However, a single sample from the old cohort (53-years-old) did not separate according to the prescribed trend, as also demonstrated in hierarchical clustering (Figure 4-4C). This may be reflected in population measurements as a more diffuse gradient between 45 and 55 years old to delineate "young" and "old" lenses. Two-sample t-testing of young and old lens outer nucleus did not yield as many significantly changed proteins as in the cortex (Figure 4-9, Appendix D). However, PSEA-Quant was successfully used to enrich for ontologies differentiated with age, followed by enriched ontology network analyses (Figure 4-10, Appendix G, Appendix H). In the outer nucleus, the prevailing theory is that anaerobic metabolism established in the cortex is less active and that remodeling of the proteome is exclusively attributed to age-related changes caused by intercellular signaling and oxidative homeostasis, not to transcriptional control. This is demonstrated by the enrichment of GO terms related to gap junction (GO:0034329) and cell-to-cell contacts (GO:0007156) in young lenses and enriched representation of oxidoreductase (GO:0016491, GO:0016655, GO:0016701) protein networks in old lenses relative to young lenses. Each of these trends are expected to be a continuation of the aging process observed in the cortex where transcription is eliminated. Specific analysis of proteins related to respiratory electron transport reveals most of these proteins (UniProt identifiers O96168, O43574, Q86Y39, O95298, Q9P0J0, O43181) are NADH dehydrogenases. It is expected that if these dehydrogenases are functionally active, they are not contributing to mitochondrial respiratory electron chain function because organelles are degraded in the outer nucleus. This study then suggests that proteins resident to degraded organelle structures are not degraded simultaneous to organelle structure disassembly.

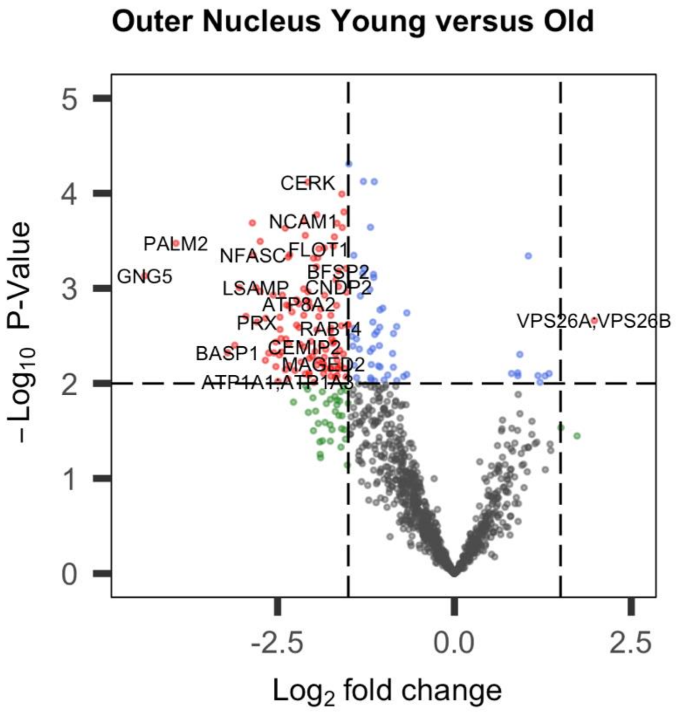

Figure 4-8 - Volcano plot of Outer Nucleus preferentially retained or degraded proteins with significance cutoffs of 0.01 unmoderated p-value and 1.5 log2 fold change. UniProt identifiers converted to gene names. The statistical power of this test is estimated to be approximately 0.6 with a sample size of 7, the size of the old lens sample group, and at 5% FDR.

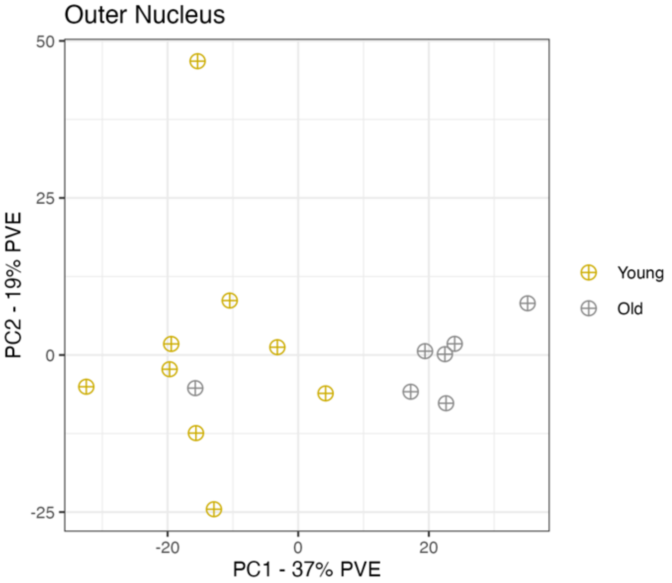

Figure 4-9 - PCA plot colored by age group demonstrates separation of young and old fiber cell populations on PC1 based on protein groups identified in all 16 samples (n=1,114). Cell adhesion molecule 3, guanine nucleotide binding protein, insulin-like growth factor-binding protein 7, and BASP1 are protein groups associated with negative, young PC1 protein loadings. Protein phosphatase-1 regulatory subunit 15a, hspB3, βB1-crystallin and WD repeat-containing protein 25 are associated with positive, old PC1 protein loadings. No clear trends in biology emerge from these results aside from consistent young-lens loading annotation of BASP1 and old-lens βB1-crystallin and WD repeat-containing protein 25.

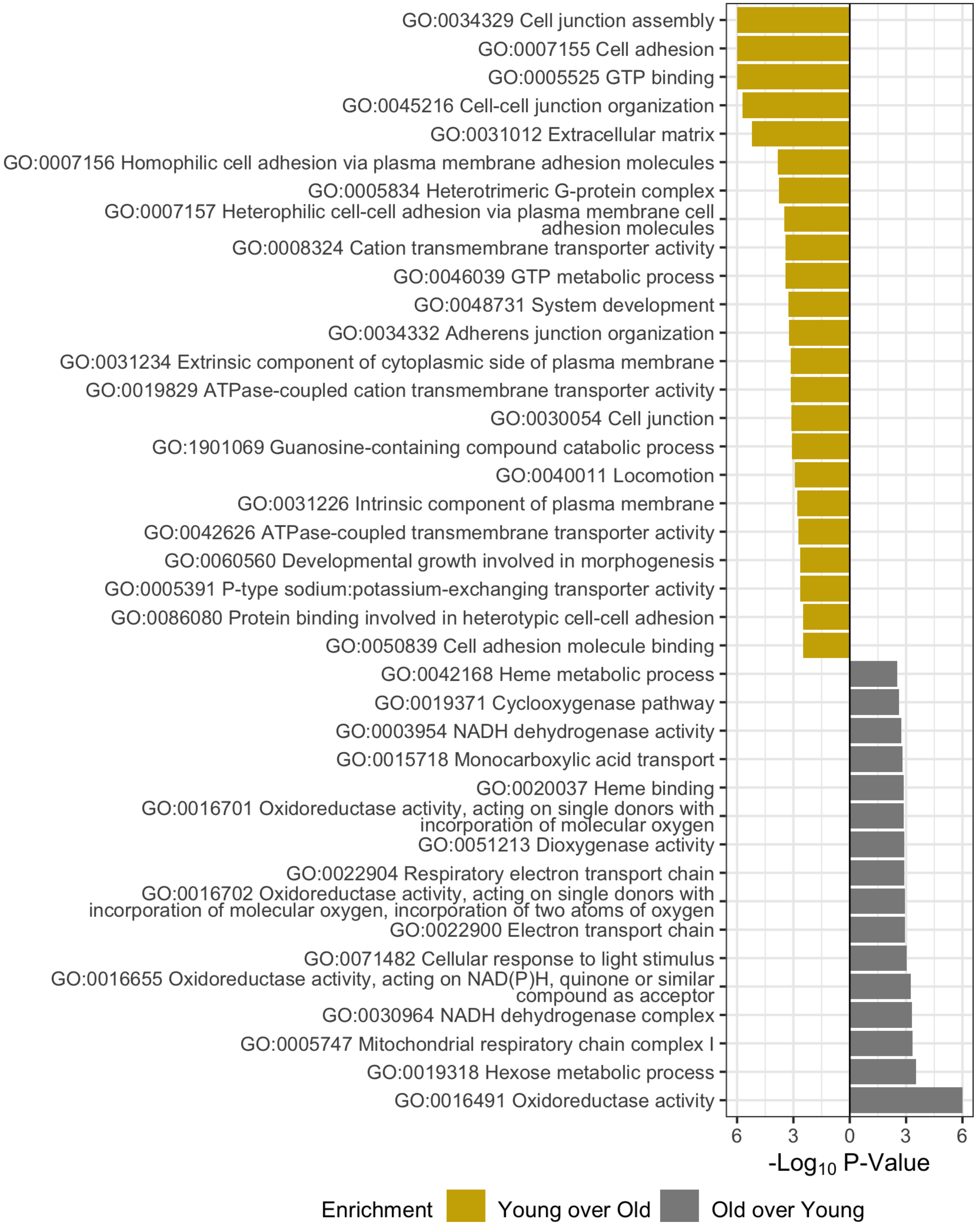

Figure 4-10 - PSEA-Quant pairwise enrichment calculated between young and old lens fiber cells in the Outer Nucleus. Separate calculations performed to determine each enrichment. Significant Gene Ontology terms were filtered at 0.01 p-value and 0.1 FDR. Ontologies in graphic are a subset of all measured, demonstrating non-redundant daughter terms indicative of the complete enrichment set. Full list of enriched terms included in Appendix G, Appendix H.

4.4.5. Age-related changes in the lens inner nucleus

The inner nucleus was evaluated as done for the cortex and outer nucleus regions. In PCA (Figure 4-11), young and old lenses separated on PC1 precisely at the 50-year age cutoff. In volcano plot analysis (Figure 4-12, Appendix D), no proteins were significantly represented in the old lenses relative to young lenses. The low number of statistically enriched old inner nucleus proteins relative to young inner nucleus abundances is likely due to accumulation of age-related modifications including deamidation (Wenke et al., 2015; Hains & Truscott, 2010b; Forsythe et al., 2019; Vetter et al., 2020). Deamidation is the most abundant non-isobaric irreversible PTM in the lens and randomly occurs on disordered region of client proteins, which is the region most likely to be measured in a membrane protein (Cantrell & Schey, 2021a). Therefore, we examined the extent of deamidation as an explanation for decreased protein group abundance with age. We suggest that if the abundance of the unmodified peptide decreases and the deamidated peptide does not increase to a similar extent, that an alternative PTM is occurring, for example, truncation.

To demonstrate the impact of deamidation with age, we plotted the age-related abundance of connexin 46 (GJA3) when no variable modifications were included in the spectral library alongside the abundance of deamidated peptide L10-K23 measured in a separate search where a single deamidation modification was enabled (Figure 4-13). Figure 4-13A demonstrates that there is a modest decrease in the abundance of GJA3 in the inner nucleus with age ($p < 0.05$). This may be partially explained by the accumulation of deamidation on the L10-K23 peptide (Figure 4-13C, proportional deamidation being the measured intensity of deamidated peptide divided by the sum of deamidated and unmodified peptide). When protein abundance change is calculated with deamidated and unmodified peptides combined, the statistical significance of abundance change is not observed (Figure 4-14).

Within inner nucleus PSEA-Quant results and network analysis (Figure 4-15, Appendix I, Appendix J), oxidoreductase related terms (GO:0016491, GO:0016705) and negative regulation of several protein or peptide truncation ontologies (GO:0004867, GO:0010948) were among the few ontologies enriched in the old inner nucleus relative to the young inner nucleus. Peptide truncation ontologies were represented by protease inhibitors (UniProt identifiers P30740, Q92530, P04080, P35237, P50453). The consistent identification of enriched oxidoreductase activity in each old lens region relative to the young lens supports the hypothesis that a primary function in the aging lens is reduction of oxidative stress, and that this functionality is preserved by sustained protein abundances. Likewise, protein truncation ontology enrichment suggests that the lens proteome attempts to preserve intact protein structure and function. A final observation from the PSEA-Quant results is the continued enrichment of cellular adhesion-related terms in young lenses relative to their old counterparts (GO:0045216, GO:0034330, GO:0007155, GO:0034329). The inferred depletion of these terms in old lenses demonstrates that age may be responsible for depletion of cellular adhesion and intercellular metabolite transport. Taken together, we propose that while putatively active, oxidative stress protein networks are inhibited by the decrease of cellular contacts and metabolite transport in the lens that accumulate with age.

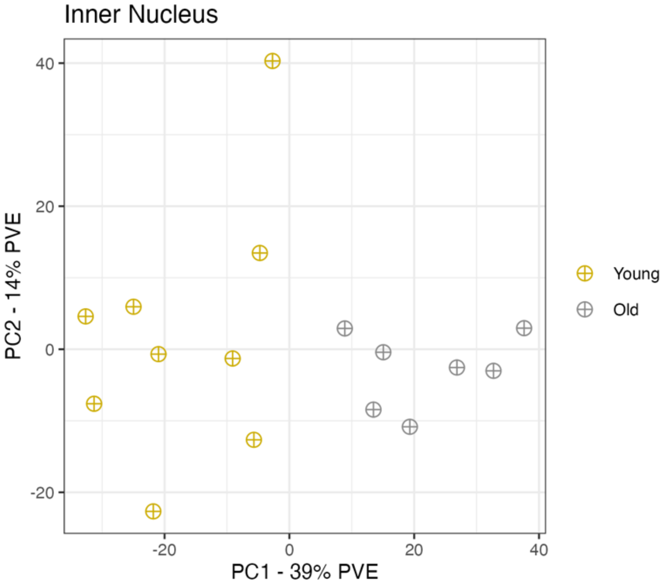

Figure 4-11 - PCA plot colored by age group demonstrates separation of young and old fiber cell populations on PC1 based on protein groups identified in all 16 samples (n=969 PC1 protein loadings with the largest negative value include cell adhesion molecule 3, insulin-like growth factor binding protein 7, A-kinase anchor protein 2-related, and BASP1. Positive PC1 protein loadings included AP-1 complex subunit sigma 1a, protein phosphatase 1 regulatory subunit 15a, hspB3, βB1-crystallin, and vacuolar protein sorting-associated protein 26A.

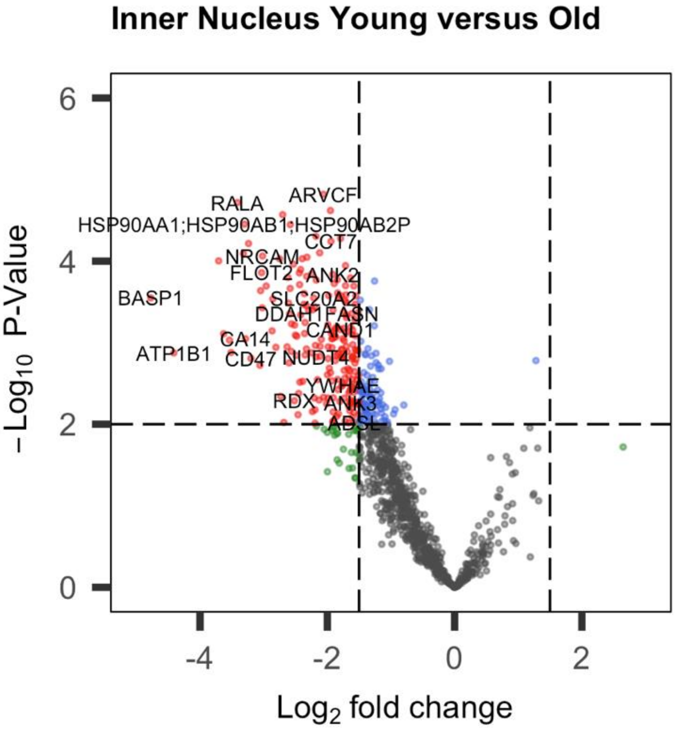

Figure 4-12 - Volcano plot of Inner Nucleus preferentially retained or degraded proteins with significance cutoffs of 0.01 unmoderated p-value and 1.5 log2 fold change. UniProt identifiers converted to gene names. The statistical power of this test is estimated to be approximately 0.6 with a sample size of 7, the size of the old lens sample group, and at 5% FDR.

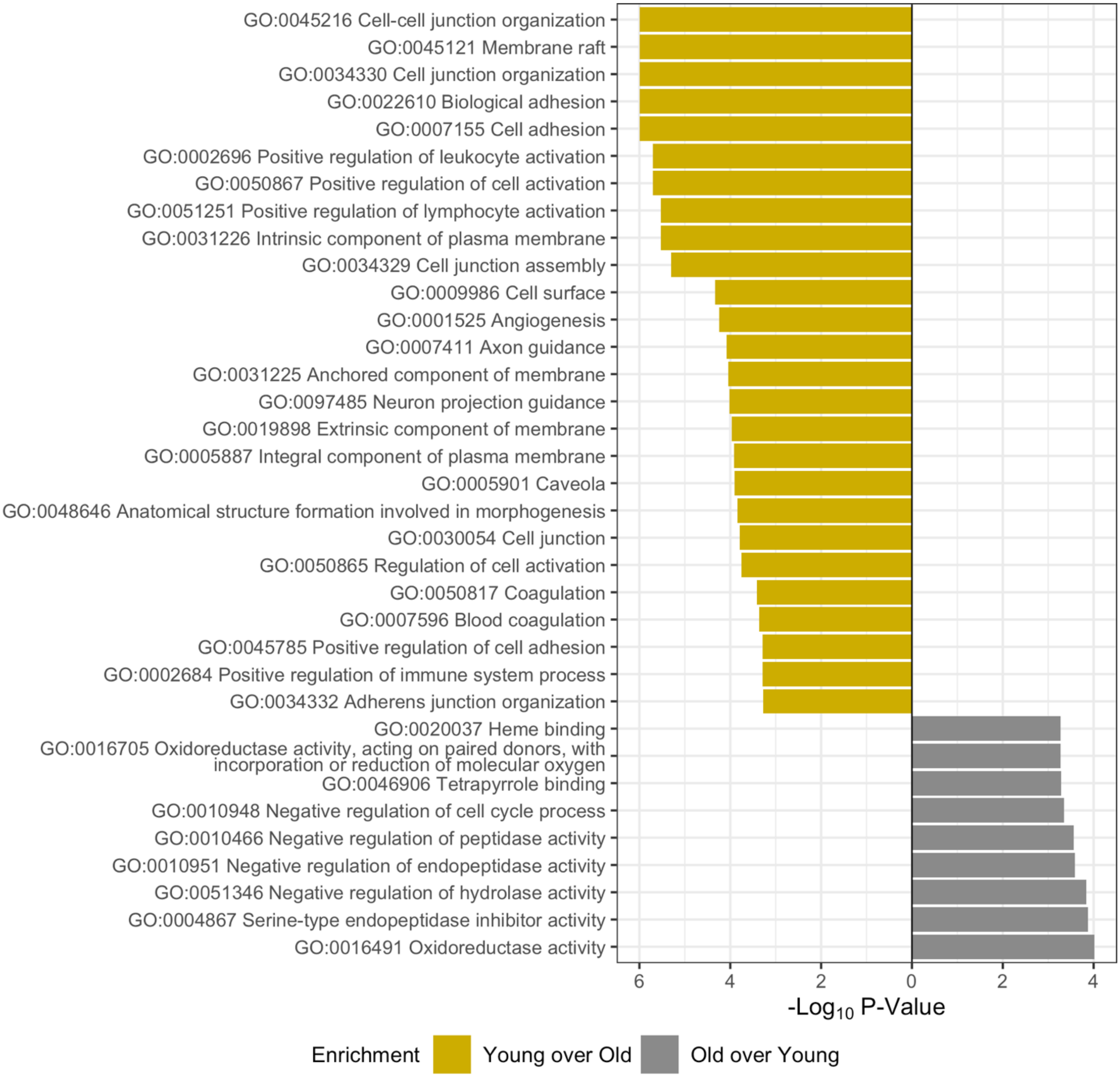

Figure 4-13 - PSEA-Quant pairwise enrichment calculated between young and old lens fiber cell regions. Separate calculations performed to determine each enrichment. Significant Gene Ontology terms were filtered at 0.01 p-value and 0.1 FDR. Ontologies in graphic are a subset of all measured, demonstrating non-redundant daughter terms indicative of the complete enrichment set. Full list of enriched terms included in Appendix I, Appendix J.

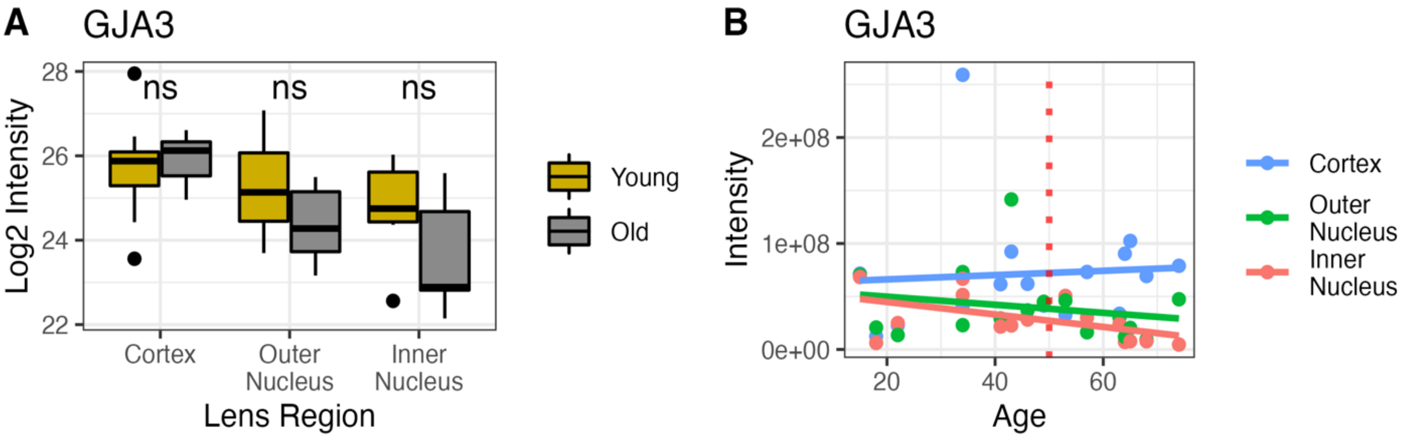

Figure 4-14 - Abundance of Connexin 46 (GJA3) when ***deamidated peptides are considered towards the total abundance of the protein group****. When GJA3 is unmodified (Figure 4-15), a significant change is measured by two-sample t-test. A) When deamidation is included, no significance is established; B) There is a qualitative decline in GJA3 abundance in the outer and inner nucleus with age, but it is not consistent with the proteome remodeling event. T-test significance cutoffs were set at * = <0.05, ** = <0.01, *** = <0.001, **** =<0.0001*

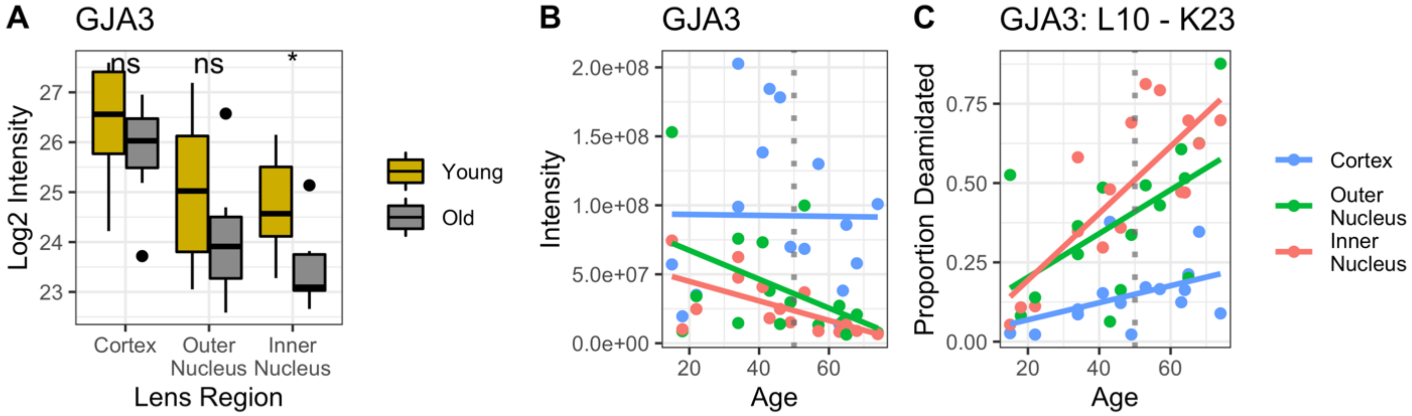

Figure 4-15 - Representative abundance of Connexin 46 (GJA3) in each sample when ***deamidated peptides are not considered towards the total abundance of the protein group****. A) Protein abundance of GJA3 in a search with no variable modifications and t-test significance of distributions (* = <0.05, ** = <0.01, *** = <0.001) between young and old lenses. B) Individual representative intensity of GJA3 signal in unmodified search, linear trendline plotted to demonstrate trend. C) Representative deamidation accumulation of GJA3 L10-K23 calculated on single variable deamidation dataset with linear trendline to show accumulation of modification.*

4.5. Discussion

In this study we have measured more proteins than previously detected in the human lens with DDA, exceeding all prior approaches in total protein groups identified by 2.5-fold (Cantrell & Schey, 2021b). As a label-free analysis in samples with putatively high biological variability, it was important to confirm previously described lens biology in the present analysis. Previous studies comparing progressively aged fiber cells have been performed and are consistent with the results presented here and with the MCS hypothesis (Z. Wang et al., 2021; Wenke et al., 2016). In addition to considering aging fiber cells, Truscott and colleagues previously evaluated human lens aging with isobaric tags (Truscott et al., 2011). While those results are less rich than those afforded by DIA, several similarities can readily be made. In Truscott and the presented work, the measured abundance of β- and γ-crystallin variants was increased in progressively aged lenses (see supplemental data for protein group intensities). Each study showed no significant age-related change in the abundances of α-crystallin A and B subunits or AQP0. Similar distributions of connexin proteins were also observed in each study. Finally, each study demonstrates age-related decline in the abundance of BASP1, paralemmin 1, and vimentin. The single disagreement between these studies is the inner nucleus measurement of GJA3: both studies suggest that the abundance is decreased significantly in older lenses, but we find that this change is insignificant when considering deamidation as a variable modification (Figure 4-14). Deamidation was not considered in the prior study. Taken together, these results suggest that the label-free DIA analysis employed here is sensitive to measurement of known changes in the lens proteome with age.

As presented in the introduction, oxidative stress response must occur in the inner nucleus, where fiber cells are metabolically less active and are not connected to a vascular transport system. Stress response is then thought to be mediated by the lens MCS delivery of reduced GSH and other metabolites to the inner nucleus through extracellular space along fiber cell sutures, and the export of metabolites through intercellular contacts (gap junctions) toward the equator of the lens. As such, this discussion of proteome measurements is primarily focused on the oxidative stress response and the physiology of the MCS before and after 50 years of age.

4.5.1. Antioxidant protein networks

Previous lens proteome studies have identified putative transporters of GSH and its precursors, but not in the human lens (J. Lim et al., 2007; J. C. Lim, Caballero Arredondo, et al., 2020; J. C. Lim, Grey, et al., 2020). GSH uptake from extracellular suture space is putatively mediated by organic anion transporter 3 (OAT3) and sodium-dependent dicarboxylate transporter 3 (NaDC3) and efflux is mediated by multidrug resistance proteins 4 and 5 (MRP4/5) and connexins 46 and 50 (GJA3/8). The transport of GSH-precursor amino acids (glutamate, cysteine, and glycine) is also important for *in vivo* synthesis of GSH. These transport proteins include glycine transporters sodium- and chloride-dependent glycine transporters 1 and 2 (GLYT1/2), glutamine/glutamate transporter neutral amino acid transporter B(0) (ASCT2), glutamate and sodium cotransporters excitatory amino acid transporters 1 and 2 (EAAT1/2) and cysteine/glutamate antiporter complex (System X_c^-) composed of 4F2 cell-surface antigen heavy chain (4F2 or SLC3A2) and light-chain cysteine/glutamate transporter (XCT or SLC7A11). The functionality of GSH synthesis in the lens is beyond the scope of this study, but we note that the rate limiting enzyme of GSH synthesis – glutamate cysteine ligase catalytic subunit (GCLC) is measured in all 48 samples, but its abundance is not changed with age. Finally, while GSH is believed to be the antioxidant most responsible for lens homeostasis, ascorbic acid (vitamin C) is also proposed to be transported through the lens as an antioxidant in its oxidized form via glucose transporter 1 (GLUT1) and its reduced form by sodium-coupled vitamin C transporter 2 (SVCT2) as an alternative route for oxidative stress response.

For each of the proteins described above, the frequency of identification and description of sample distribution is given in Table 4-1 (graphical abundances in Figure 4-16). From these data, several key observations were made. First, the most ubiquitous antioxidant transporter measured in the membrane is OAT3, facilitating uptake of intact GSH. Age does not appear to have an effect on the abundance of OAT3 in the membrane. Next, that NaDC3, MRP4, EAAT1, and SVCT2 are only measured in the youngest cortical samples, indicates little importance in long-lived proteome homeostasis. System X_c^-, a two-protein complex thought to contribute to cysteine accumulation in the lens nucleus for thiol protection, is not likely to be intact in these samples as XCT is not measured in any sample. Concurrently, 4F2 is less abundant in the membrane with increasing fiber cell age and subject age. Finally, GLUT1 is measured in all samples and its abundance does not change with age. The loss of NaDC3, MRP4, EAAT1, and SVCT2 measurement in older fiber cells and the age-related reduction in 4F2 measurement suggests that GSH and vitamin C transport occurs in the lens, but that affinity for transport is reduced with aging. Future experiments should be directed towards specific measurement of missing or otherwise low abundance antioxidant transporters to further support the spatial regulation and absence of these transporter proteins.

Our DIA analysis allowed additional novel observations to be made regarding oxidative stress response in the lens. First, PCA separation of cortical fiber cells showed kynurenine oxoglutarate transaminase, responsible for formation of kynurenic acid from kynurenine and oxoglutarate, is enriched in older subject donors. Interestingly, kynurenic acid is shown to upregulate the activity of the GCLC transcription factor Nrf2, suggesting a role for the transaminase in oxidative stress response in transcriptionally regulated cortical fiber cells (Ferreira et al., 2018). We also identified several key cytosolic proteins involved in GSH-mediated oxidative stress response. These include glutathione-s-transferase (GST) and glutathione reductase (GR) which are ubiquitously measured in each region of the lens (Figure 4-17). Each of these proteins show a slight increase in measured intensity at approximately 50 years, but no age-dependent statistical significance is detected. The consistent measure of GST and GR in all lenses studied suggests that oxidoreductase pathways may be at least partially functional in older lenses.

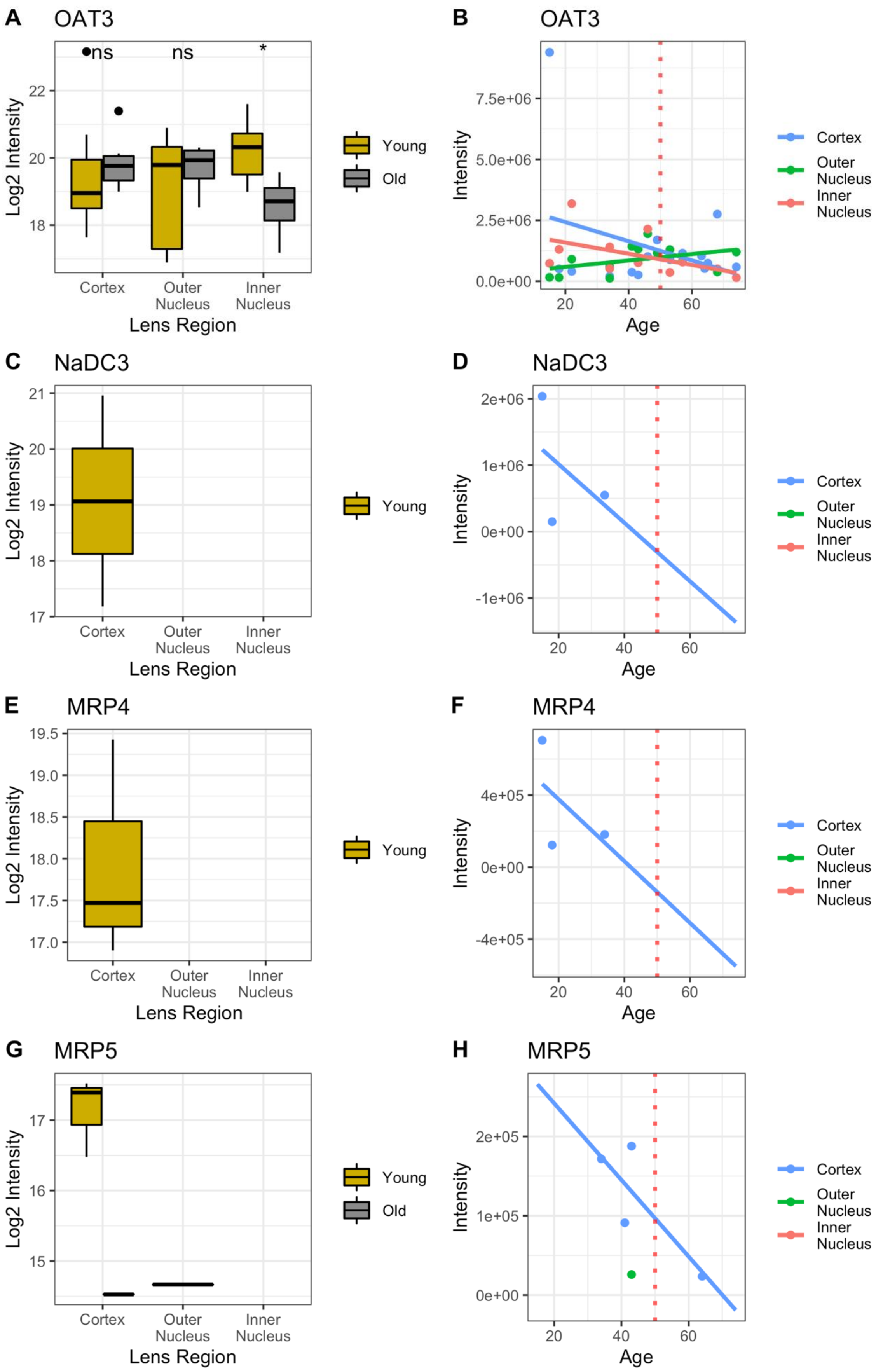
A
OAT3
ns
ns
*
Log2 Intensity
22
20
18
Cortex
Outer Nucleus
Inner Nucleus
Lens Region
Young
Old
B
OAT3
Intensity
7.5e+06
5.0e+06
2.5e+06
0.0e+00
20
40
60
Age
Cortex
Outer Nucleus
Inner Nucleus
C
NaDC3
Log2 Intensity
21
20
19
18
17
Cortex
Outer Nucleus
Inner Nucleus
Lens Region
Young
D
NaDC3
Intensity
2e+06
1e+06
0e+00
-1e+06
20
40
60
Age
Cortex
Outer Nucleus
Inner Nucleus
E
MRP4
Log2 Intensity
19.5
19.0
18.5
18.0
17.5
17.0
Cortex
Outer Nucleus
Inner Nucleus
Lens Region
Young
F
MRP4
Intensity
4e+05
0e+00
-4e+05
20
40
60
Age
Cortex
Outer Nucleus
Inner Nucleus
G
MRP5
Log2 Intensity
17
16
15
Cortex
Outer Nucleus
Inner Nucleus
Lens Region
Young
Old
H
MRP5
Intensity
2e+05
1e+05
0e+00
20
40
60
Age
Cortex
Outer Nucleus
Inner Nucleus

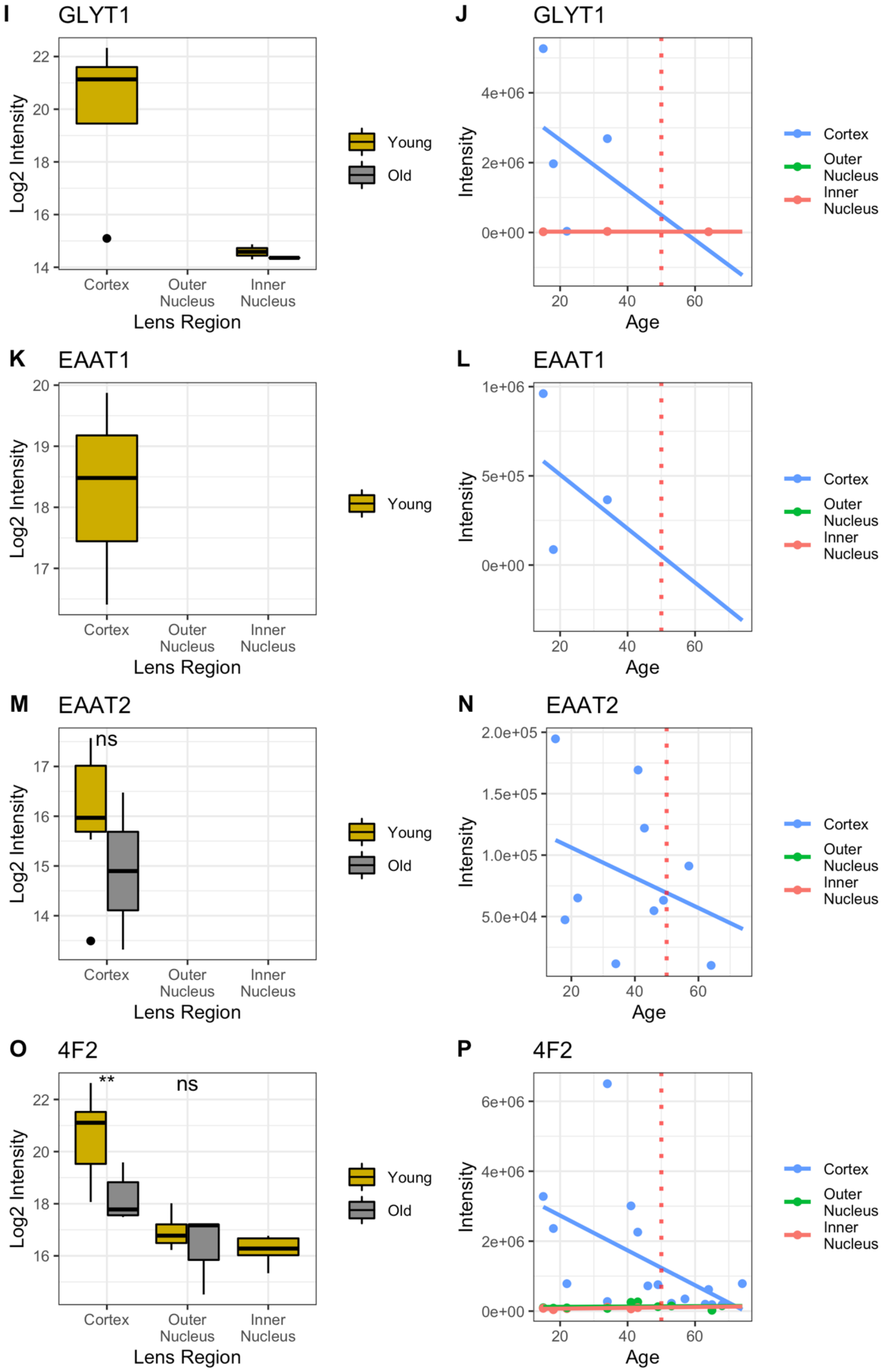
I
GLYT1
Log2 Intensity
22
20
18
16
14
Cortex
Outer Nucleus
Inner Nucleus
Lens Region
Young
Old
J
GLYT1
Intensity
4e+06
2e+06
0e+00
20
40
60
Age
Cortex
Outer Nucleus
Inner Nucleus
K
EAAT1
Log2 Intensity
20
19
18
17
Cortex
Outer Nucleus
Inner Nucleus
Lens Region
Young
L
EAAT1
Intensity
1e+06
5e+05
0e+00
20
40
60
Age
Cortex
Outer Nucleus
Inner Nucleus
M
EAAT2
ns
Log2 Intensity
17
16
15
14
Cortex
Outer Nucleus
Inner Nucleus
Lens Region
Young
Old
N
EAAT2
Intensity
2.0e+05
1.5e+05
1.0e+05
5.0e+04
20
40
60
Age
Cortex
Outer Nucleus
Inner Nucleus
O
4F2
**
ns
Log2 Intensity
22
20
18
16
Cortex
Outer Nucleus
Inner Nucleus
Lens Region
Young
Old
P
4F2
Intensity
6e+06
4e+06
2e+06
0e+00
20
40
60
Age
Cortex
Outer Nucleus
Inner Nucleus

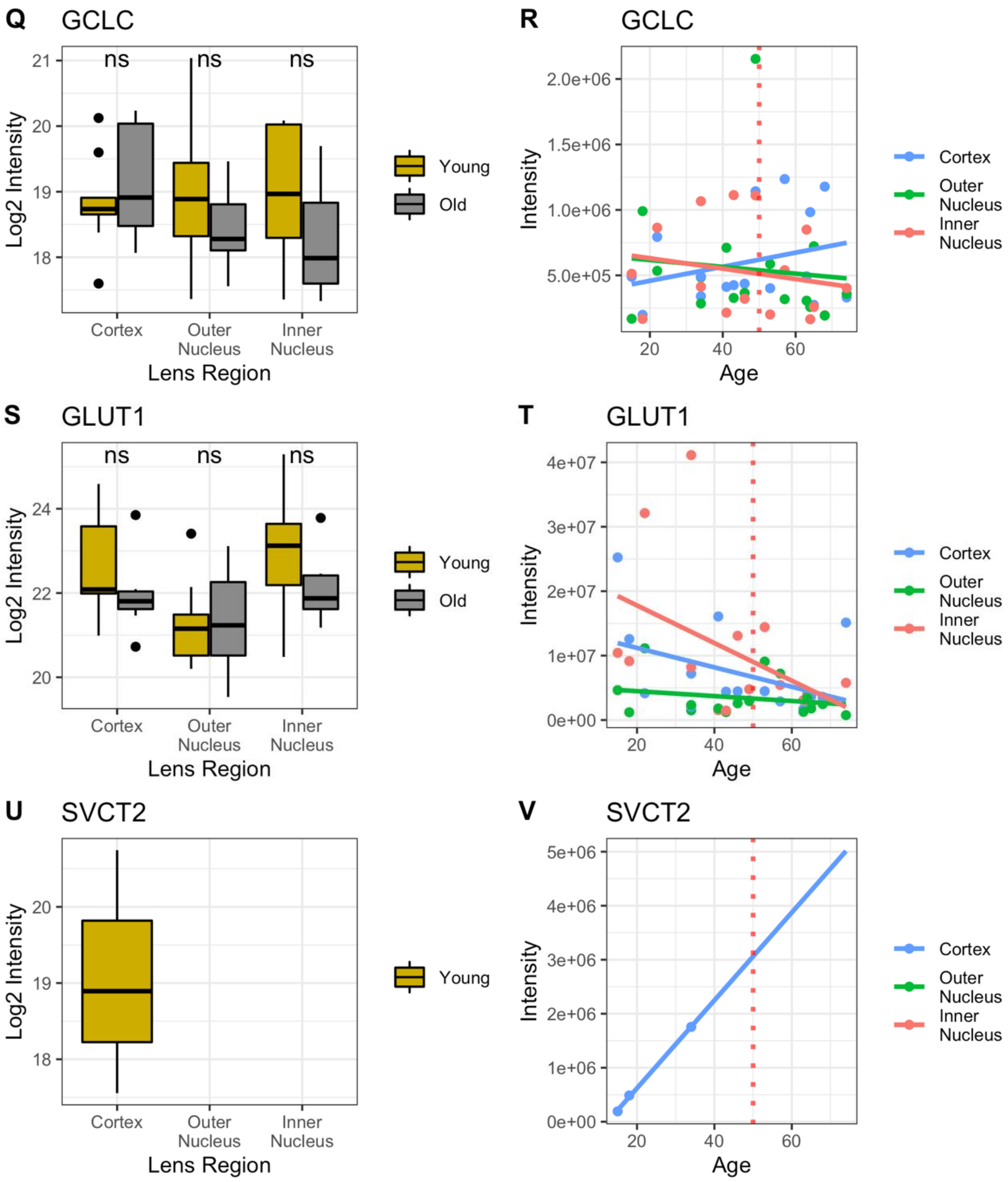

*Figure 4-16 - Age-related expression of each protein mentioned in the discussion as related to glutathione transport, glutathione synthesis or vitamin C transport. Proteins not measured are not plotted. T-test significance cutoffs were set at * = <0.05, ** = <0.01, *** = <0.001, **** =<0.0001*

Table 4-1 - Proteins involved in antioxidant transport in the lens, their putative function, detection in the lens cohort and approximate age-related distributions. Visualized abundances represented in Figure 4-16

Protein	**Function**	**Detection**	**Comments**
OAT3	GSH influx	40/48 samples	Approximate uniform distribution
NaDC3	GSH influx	3/48 samples	Only in young cortex
MRP4	GSH efflux	3/48 samples	Only in young cortex
MRP5	GSH efflux	6/48 samples	Decreasing expression with age; only in middle aged lenses (34-63 years old)
GLYT1	Glycine transport	3/48 samples	Only in young cortex
GLYT2	Glycine transport	0/48 samples	Not measured
ASCT2	Glutamine/Glutamate transport	0/48 samples	Not measured
EAAT1	Glutamate transport	3/48 samples	Only in young cortex
EAAT2	Glutamate transport	10/48 samples	Only in cortex, age-related decrease; not in oldest cortex
4F2/SLC3A2	Cysteine glutamate antiporter	34/48 samples	Most abundant in cortex, age-related decrease; not in old outer/inner nucleus
XCT/SLC7A11	Cysteine glutamate antiporter	0/48 samples	Not measured
GCLC	Rate limiting enzyme in GSH synthesis	48/48 samples	Indistinct trend, approximately uniform
GLUT1	Dehydroascorbic Acid Transporter	48/48	Age-related decrease; high abundance in inner nucleus
SVCT2	Vitamin C transport	3/48	Only in young cortex

4.5.2. Physiology of the lens microcirculation system

Ion gradient establishment

Sodium-potassium ATPases along the epithelium are responsible for the establishment of a sodium cation gradient in the lens. It is not immediately apparent that these ATPases are modified in abundance in young or old lenses, suggesting that there is little change in expression with respect to age. This measurement may be artifactual as fiber cells were not separated from the epithelium, where these ATPases are functionally assigned in the MCS. Coupled to Na/K ATPases, a non-selective sodium leak channel is hypothesized to be responsible for the continuous influx of sodium to mature fiber cells. A suggested protein responsible for this, non-selective sodium leak channel, NALCN, was not measured in any sample. The functional alternative to NALCN as a leak channel is GJA3, which does not decrease in abundance as a result of the proteome remodeling event. Previous biophysical studies have identified GJA3 as critical in maintenance of sodium conductivity in the lens (Ebihara et al., 2014, p. 4) but not as a leak channel explicitly.

Cell-cell junctions

A consistently measured change in PSEA-quant analysis for each region of the lens was age-related depletion of cell-cell adhesion and junctions (e.g., GO:0005911, GO:0034329, GO:0045216). Cell-cell junctions of the lens are largely established by connexin gap junctions, actin-network tight junctions, and AQP0 (Mathias et al., 2010; Sindhu Kumari et al., 2015; Wenke et al., 2016). Connexin proteins play a key part in the transport of metabolites in the lens via formation of GJA3 and GJA8 gap junctions. For GJA3, abundance change is not observed (Figure 4-13), but there are decreases in GJA8 abundance with fiber cell age and proteome remodeling (Figure 4-18). These decreases cannot be explained solely by deamidation, as represented by age-related accumulation of GJA8 G265-K273 proportional deamidation (Figure 4-18) and it instead suggested that a real decrease in protein abundance by truncation occurs. From prior DDA analyses, it is known that connexins are truncated at the N-terminus, C-terminus, or undergo cleavage in a central cytoplasmic loop (Slavi et al., 2016). Neither gap junction is functionally restricted by truncation of the N- or C-terminus, however truncation by cleavage at a mid-sequence, cytoplasmic loop restricts hemi-channel formation (Slavi et al., 2016). Evaluating the cytoplasmic loop peptide E110-K139, we show that this peptide decreases similarly to the whole GJA8 protein group in the cortex but is not detected in inner nucleus samples older than 43 years (Figure 4-18). In the outer nucleus, we measured this peptide in lenses up to 53-years-old. This demonstrates that GJA8 undergoes progressive decreases in abundance, but in mature fiber cells of older lenses, is likely non-functional, decreasing net connexin gap junction permeability.

Non-connexin junctional proteins decreased with the age-related remodeling in the cell-junction or cytoskeleton associated structural protein family of terms include vinculin, cell adhesion molecule 1/2/3, lens fiber membrane intrinsic protein 2, and cadherin-2. Many of the proteins associated with cell-cell and cell-junction ontologies are calcium-dependent for maintenance of adhesion. The functional relevance of the decreased abundance of these proteins in older lenses is unclear, but similar cell junction ontology terms to those measured here have been detected in previous analysis of progressively older fiber cell populations (Cantrell & Schey, 2021b; Z. Wang et al., 2021). Calcium acts as a second messenger, and in addition to calmodulin-dependent inhibition of water permeability through aquaporin-0, regulates actin cytoskeleton integrity and the activity of the ubiquitin proteasome system (UPS), and calpain proteases (Lindsey Rose et al., 2008; K. Liu et al., 2015; R. Mukherjee et al., 2017). Prior measurements of the lens demonstrate that there is a parabolic decrease of calcium concentration in the lens with age, reaching its lowest point around 50 years, and increasing in lenses thereafter, with significantly elevated levels of calcium in cataract lenses (Tang et al., 2003). The accumulation of gene ontology terms presented here led us to evaluate the effect of aging on selective calcium transporters.

Calcium transport

To evaluate age-related changes in calcium transporters, we first selected the subset of broadly defined ATP-independent solute-carrier membrane (SLC) proteins. Of 121 SLC protein groups, only 21 candidates were measured in at least 36/48 samples. This allowed filtering for SLC proteins that may be completely absent in old inner nucleus, but required that they be measured at young age, when calcium export is putatively functional. From this subset list of 21 SLC proteins, we evaluated if age-related changes in abundance, consistent with the proteome remodeling event at 50 years, occurred. Many SLC proteins undergo statistically significant reduction in representation with age in the cortex, but this is anticipated to be a result of decreased organelle concentration and loss of protein synthesis in old fiber cells relative to young fiber cells. Thus, we elected to only identify candidate SLC proteins where statistical reduction occurred in at least two lens regions, reducing the 21 SLC candidate proteins to 2 proteins of interest. The first is SLC30A1, a relatively low abundance zinc transporter not measured in the old inner nucleus and significantly decreased in the outer nucleus. Interestingly, the only other protein which showed consistent, age-related decrease in abundance was SLC24A2, a sodium, potassium, calcium exchange protein which is activated in the retina following light stimulus and subsequent photoreceptor signaling. The abundance profile of SLC24A2 with age (Figure 4-19) demonstrates little change in the cortex, but especially interior to the established diffusion barrier, a remodeling-dependent decrease in abundance occurs. No other members of the sodium, potassium, calcium exchange protein family were detected.

It is unclear whether SLC proteins contribute to intracellular transport after the extracellular space between fiber cells is decreased with fiber cell maturation. However, considering biophysical evidence, we suggest that the age-related proteome remodeling event at 50 years of age is responsible for functional restriction of calcium export from lens fiber cells. Thus, if SLC24A2 contributes to calcium export, it is expected that its degradation is a precursor to calcium accumulation and subsequent signaling events. The functional alternative to SLC24A2 for calcium transport is through non-selective connexin gap junction channels. Recent studies show that GJA8 is permeable to calcium (Valiunas & White, 2020). In contrast, calcium binding to GJA3 decreases channel permeability and age-related accumulation of calcium may lead to inhibition of GJA3 function. In the context of GJA3 and GJA8 age-related abundances (Figure 4-13, 4-18), we suggest that the age-related decrease in GJA8 abundance and function may inhibit net calcium export from the lens resulting in calcium accumulation, which in turn inhibits the permeability of GJA3, for which abundance is not significantly decreased with age. Taken together, it is anticipated that proteome remodeling at 50 years directly contributes to calcium accumulation in the lens and that accumulation may lead to inhibition to MCS as a whole. The physiological significance of this being that a current of metabolic waste in old lenses is less efficient than in young lenses, identifying a potential role of calcium in cataract formation (Figure 4-20).

Aside from MCS functionality, prior studies establish the UPS as functional in mature fiber cells, which lack significant metabolic activity (Pereira et al., 2003). Indeed, components of the proteasome are not age-degraded (Figure 4-21). Our data suggest that calcium accumulation then results in UPS activation as in other cell types, initiating elevated rates of protein degradation and E3 ligase conferred substrate specificity (R. Mukherjee et al., 2017). As a result, UPS activity may contribute to degradation of oxidative stress response proteins leading to further accumulation of reactive oxygen species and oxidized substrate proteins responsible for ARNC. Finally, it is anticipated that calcium accumulation results in activation of calpain proteases, including calpain-2 catalytic subunit (P17655) which is measured in all 48 samples with no age-related change in abundance (K. Liu et al., 2015). In K6W ubiquitin model systems, UPS is inactive and in the presence of accumulated calcium, calpain-associated fragmentation occurs on critical proteins including filensin, vimentin and β-crystallin. These lenses also formed cataract, further supporting a role of calcium accumulation in ARNC formation.

Aquaporins

Previous publications have thoroughly reviewed the importance of aquaporins in the lens MCS (Ball et al., 2003; Gutierrez et al., 2011; Korlimbinis et al., 2009; Schey et al., 2017, 2022; Wenke et al., 2015). Briefly, aquaporins serve as water channels that facilitate water permeability in fiber cells (Sindhu Kumari et al., 2015). AQP0 is the most abundant membrane protein in lens fiber cells, and it undergoes truncation of the C-terminus as an age-related modification throughout the lens (Korlimbinis et al., 2009). Truncation of AQP0 has been visually mapped with imaging mass spectrometry (Wenke et al., 2015). Aquaporin-5 is a second, less abundant aquaporin family member measured in lens fiber cells. Though structurally similar to AQP0, AQP5 has approximately 20-fold higher water permeability than AQP0 (B. Yang & Verkman, 1997). Unlike AQP0, which does not undergo any significant change in abundance with the proteome remodeling event, AQP5 undergoes a significant decrease in abundance with age in the inner nucleus (Figure 4-28). To evaluate if a significant change to AQP5 abundance is derived from deamidation, we evaluated the accumulation of deamidation on AQP5 S189-R198. The change in proportional deamidation on this peptide is incongruent with the magnitude of protein abundance decline, which suggests that deamidation does not account for the decrease in measured AQP5 abundance. Thus, we speculate that AQP5 is further modified in an age-dependent manner, which may include truncation. The functional implication of AQP5 modification may be reduced export of water from the inner nucleus to the epithelium, resulting in decreased cellular permeability.

Because water permeability must first be established in the inner nucleus to transport small molecules towards the epithelium, the decrease in unmodified AQP5 abundance has putative functional consequence on the net current of water and small molecules throughout the lens. The net effect of AQP5- relative to AQP0-mediated water permeability in the inner nucleus has not been established, but AQP5-degradation may result in accumulation of small molecules including calcium and oxidized GSH. Ultimately, this may result in further proteostatic and homeostatic stress, leading to eventual ARNC formation.

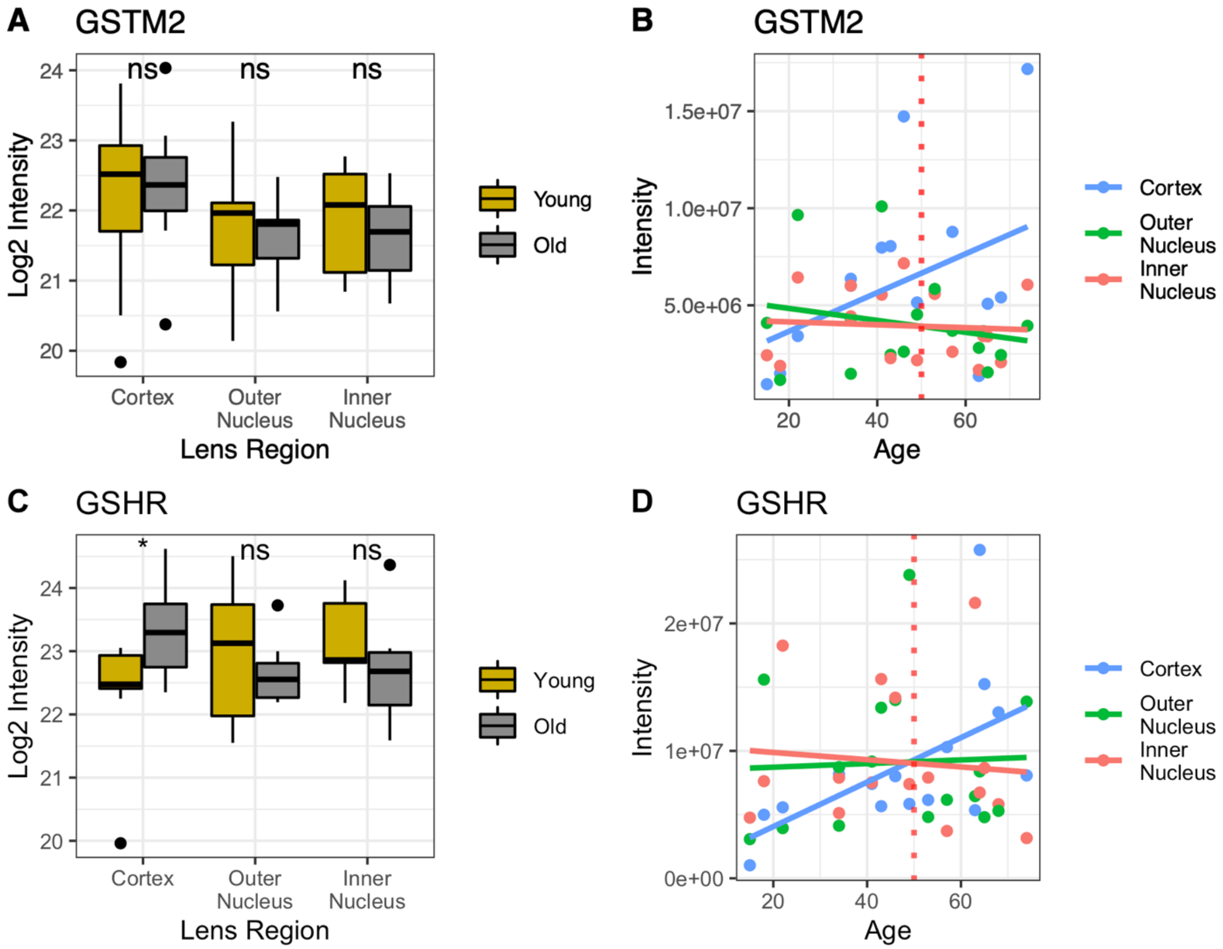

Figure 4-17 - A,C) Age-grouped t-test (= <0.05, ** = <0.01, *** = <0.001, **** =<0.0001) and B,D) age-related expression of A,B) glutathione-s-transferase mu 2 (GSTM2) and C,D) GSH reductase (GSHR). There is not a clear statistical change in the representation of either protein within the dataset and each protein is consistently measured throughout the lens. It is hypothesized that the accumulation of each cytosolic protein represents insolubilization by misfolding.*

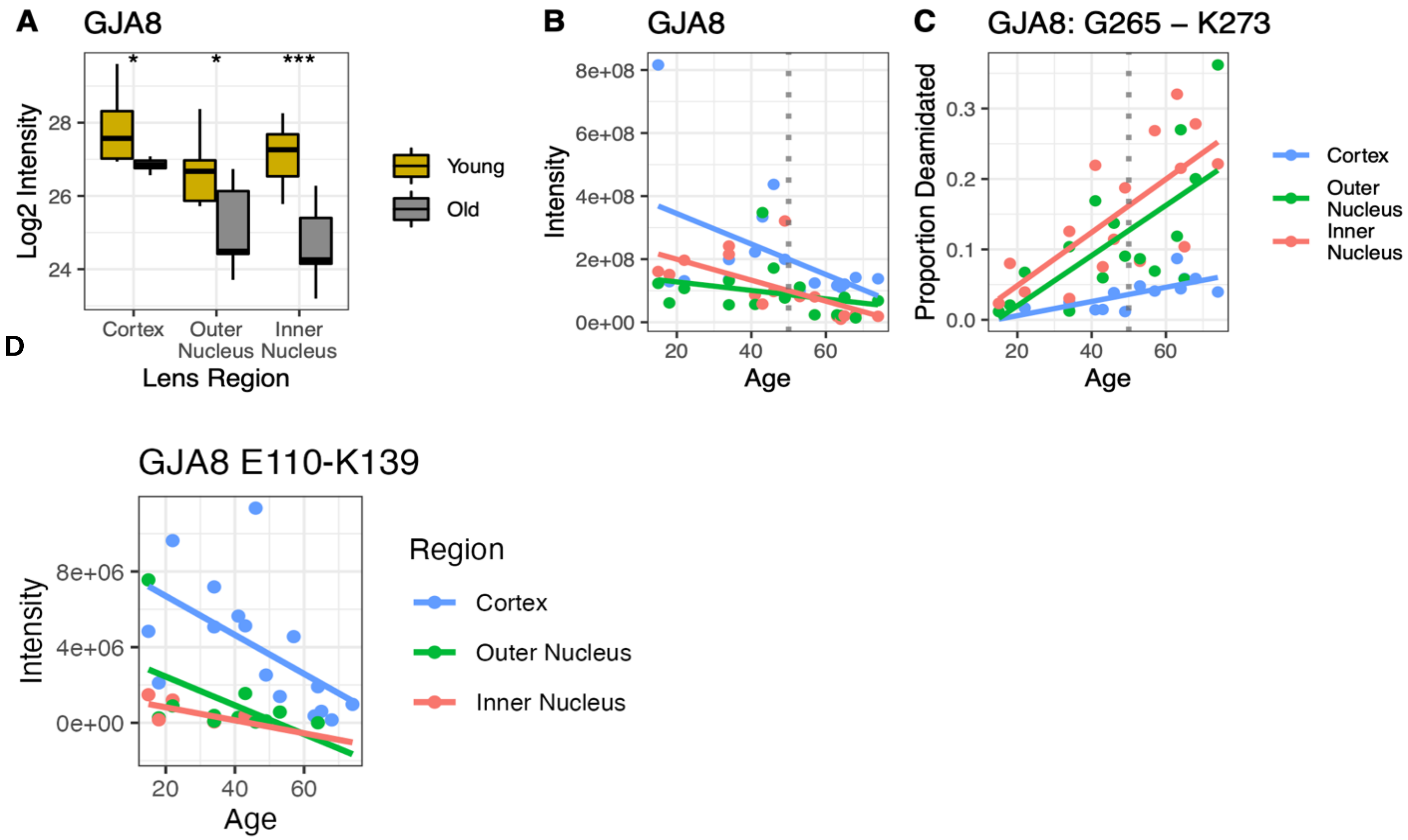

*Figure 4-18 - Demonstration of age-related abundance change of connexin 50 (GJA8) and A) An age-related decrease was appreciable for GJA8, especially in the inner nucleus, and B) decrease in protein expression cannot be solely attributed to PTMs, as shown by C) accumulation of deamidation on the G265-K273 peptide. D) Abundance of a cytoplasmic loop region peptide (E110-K139) for GJA8 demonstrates that cytoplasmic loop cleavage and functional deletion occurs in older nuclear lens regions after 50 years. T-test significances shown as * = <0.05, ** = <0.01, *** = <0.001, **** =<0.0001.*

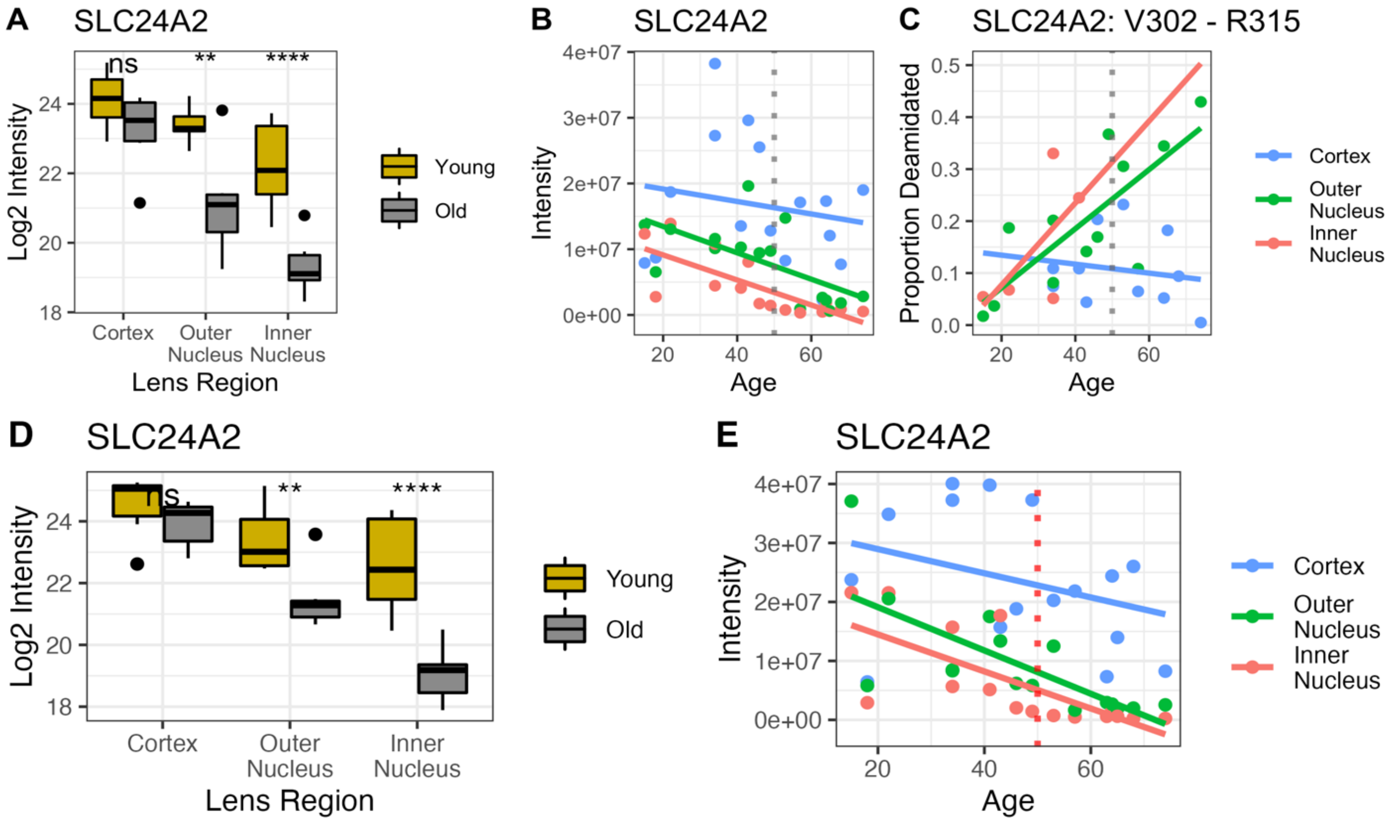

*Figure 4-19 - Demonstration of age-related abundance change of SLC24A2 (Sodium, Potassium, Calcium Exchange Protein 2). A) A proteome-remodeling related decrease in SLC24A2 abundance was appreciable in each nuclear region, especially the inner nucleus, and B) There is a steady linear decline of SCL24A2, however, there is a significant decrease in the abundance of measured SLC24A2 in the inner nucleus young region relative to old region, which is not consistent with linearity. C) Proportional deamidation of V302-R315 on SLC24A2 is demonstrated, showing some accumulation of deamidation with age, but that nuclear samples are less likely to be singly deamidated, suggesting further modification or decrease in abundance below the limit of detection and that PTMs alone are unlikely to explain the decrease in measured abundance. D, E) When t-test significance and linearity of protein abundance change was assessed with deamidation enabled, identical trends to those measured in the unmodified dataset were demonstrated. T-test significances shown as * = <0.05, ** = <0.01, *** = <0.001, **** =<0.0001*

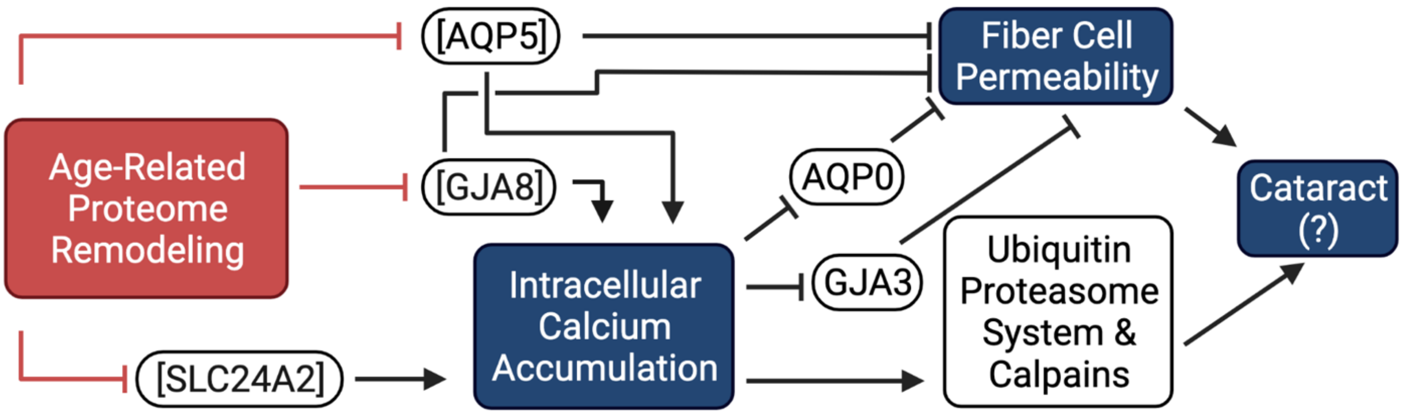

Figure 4-20 - Schematic of suggested effect of age-related proteome remodeling. Remodeling results in decreased abundance of AQP5, decreasing fiber cell permeability and decreases GJA3 and SLC24A2 abundances, resulting in calcium accumulation. Calcium accumulation inhibits GJA8 and AQP0 functionality, further inhibiting fiber cell permeability. Fiber cell permeability inhibition may then result in cataract. Calcium accumulation also results in ubiquitin proteasome and calpain protease activation which may lead to cataract. Activation, →, and inhibition, ⊥, is indicated in reference to proteome remodeling treatment and not necessarily young lens function.

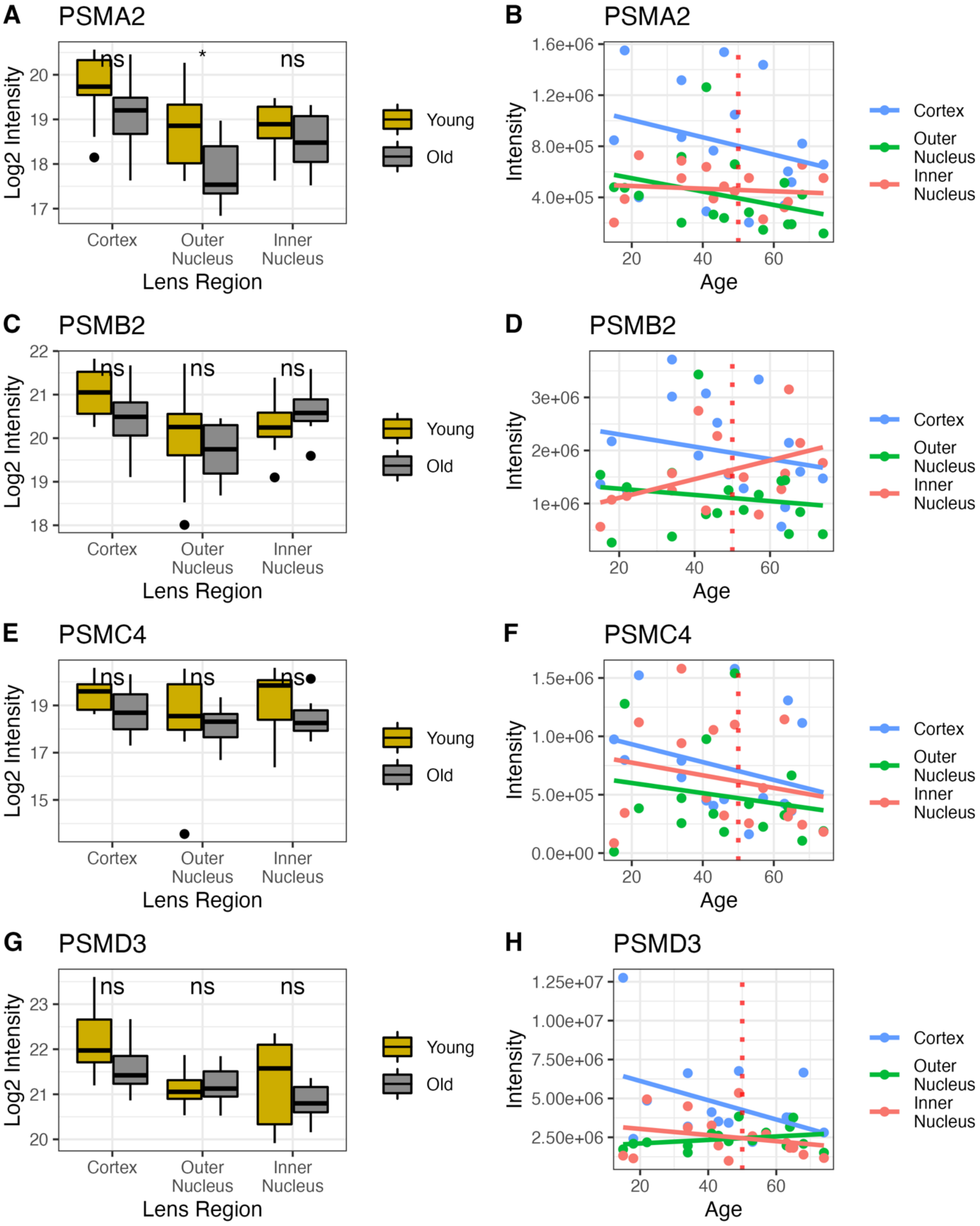
A
PSMA2
Log2 Intensity
ns
*
ns
Cortex
Outer Nucleus
Inner Nucleus
Lens Region
Young
Old
B
PSMA2
Intensity
1.6e+06
1.2e+06
8.0e+05
4.0e+05
20
40
60
Age
Cortex
Outer Nucleus
Inner Nucleus
C
PSMB2
D
PSMB2
3e+06
2e+06
1e+06
E
PSMC4
F
PSMC4
1.5e+06
1.0e+06
5.0e+05
0.0e+00
G
PSMD3
H
PSMD3
1.25e+07
1.00e+07
7.50e+06
5.00e+06
2.50e+06

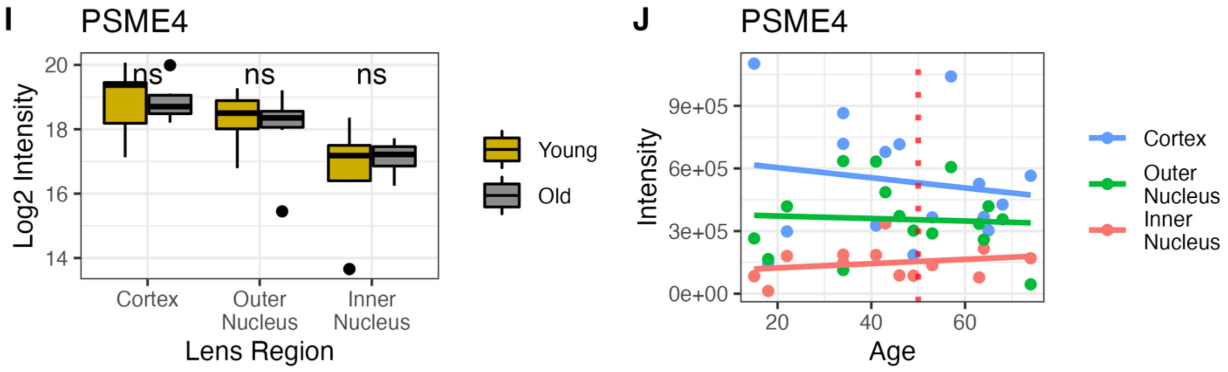

*Figure 4-22 - Evaluation of several proteasome components and their statistical change relative to proteome remodeling event. All samples demonstrate some fiber cell maturation stage related degradation, but there is no significant change in the abundance of each proteasome component with age. T-test significance cutoffs were set at * = <0.05, ** = <0.01, *** = <0.001, **** =<0.0001 for boxplot comparison.*

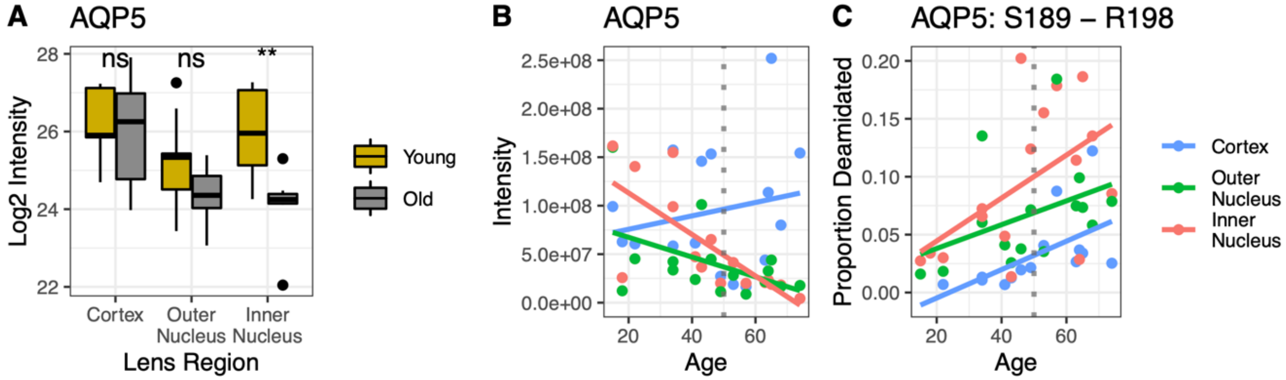

Figure 4-21 - A) T-test comparisons (= <0.05, ** = <0.01, *** = <0.001, **** =<0.0001) and distribution of AQP5 abundance relative to the proteome remodeling event and B) AQP5 distribution with age relation. Increase of cortical AQP5 is not necessarily indicative of increased cortical expression, but instead that AQP5 contributes proportionally to the lens proteome more significantly in several biological replicates. Distribution and t-testing demonstrates that this is statistically insignificant . C) The proportion of deamidation on C-terminal peptide G241-R253 demonstrates that the accumulation of deamidation alone is not responsible for the age-related decrease in AQP5 representation in the lens proteome.*

4.6. Summary

In summary, we demonstrate that DIA identifies more proteins in the lens than previously possible and delineates age-related changes in defined spatiotemporally distinct regions. Novel to this study, we show that a proteome remodeling event occurs at approximately 50 years of aging and that oxidative stress response networks are retained with age, while cell-cell contacts are degraded with age. Expanding on this, we demonstrate the first proteomic identification of multiple GSH and ascorbic acid transport proteins in the human lens. In addition to supporting prior measurements of the aging lens, we identified that calcium transporter SLC24A2 is less abundant after proteome remodeling, leading to its accumulation and potential inhibition of the MCS. Finally, we show that AQP5 is depleted in the inner nucleus of the lens, coincident with proteome remodeling; a finding with important physiological implications for MCS activity changes with age (Figure 4-20). Further functional studies are needed to evaluate these hypotheses, especially related to calcium accumulation in the aging lens. Additionally, it is desirable to further expand this approach to cataract lenses to clearly delineate changes that occur in ARNC lenses relative to old, healthy lenses.

5. CHAPTER 5

PROTEOMIC ANALYSIS OF LENS INFLUX PATHWAYS

5.1. Abstract

Purpose: To measure differential proteome composition at fiber cell suture tips as a function of cell age and relate expression at the sutures to microcirculation influx pathways.

Methods: Fixed bovine lenses were axially sectioned prior to laser capture microdissection of tissue, separating anterior and posterior fiber cell tips from equatorial cell regions in two cell age groups. Data-independent acquisition proteomics was used to quantify each protein. Proteomic results validation was performed by immunohistochemical analysis.

Results: Proteomic measurement of fixed tissue resulted in the quantitation of 700 distinct proteins and 7,323 peptides in 6 lens regions. The most significant changes measured were between outer and inner fiber cells. Adherens junctions, catenin protein networks, CLIC5, TMEM47, and GCLC were among proteins enriched at the outer suture tips relative to the outer equator. Additionally, the inner posterior suture tips showed depleted GJA8 and enriched GLUT1 and GLUT3 expression relative to the inner equator. Each glucose transporter was also more abundant in the inner suture relative to outer suture, suggesting a role for glucose delivery in hydrostatic gradient establishment.

Conclusion: This first study of the suture proteome supports previous reports that adherens junction protein networks are enriched in the suture relative to the equator. Detection of GLUT1 and GLUT3 enrichment in the inner suture suggests a greater propensity for glucose in the lens nucleus relative to cortical fibers. In addition to providing an energy source to the lens, GLUT-mediated influx may be partially responsible for lens osmotic regulation, influx current generation, and oxidative stress response.

5.2. Introduction

The avascular lens retains transparency under oxidative stress for multiple decades in humans before accumulated effects of stress results in cataract formation (Berthoud & Beyer, 2009; Truscott, 2005). To prevent cataract, the lens must deliver antioxidants and other nutrients to the lens nucleus (Beebe & Truscott, 2010; Donaldson et al., 2010). In absence of vasculature, nutrients are delivered from the surrounding eye humors through a lens microcirculation system (MCS)(Beebe & Truscott, 2010; Donaldson et al., 2010). The MCS supports water and nutrient entry to the lens through extracellular space in the lens suture, with eventual export of water and waste products, equatorially and intercellularly, through the cross section of lens fiber cells (Figure 5-1, 5-2)(Beebe & Truscott, 2010; Donaldson et al., 2010; Schey et al., 2017). MCS efflux current is generated by a sodium electromotive potential gradient and hydrostatic gradient where epithelial Na/K ATPases establish a cation gradient with water procession through epithelial aquaporin-1 and fiber-cell localized aquaporin-0 and aquaporin-5 channels (Delamere & Tamiya, 2004; Schey et al., 2017)

As part of lens development after organogenesis, germinative epithelial cells near the lens equator differentiate to form secondary fiber cells (Kuszak, Zoltoski, & Tiedemann, 2004). These fiber cells are added in concentric growth rings, elongating from a cuboid to columnar structure extending from the equator towards the anterior and posterior pole of the lens. To minimize plasma membrane mediated light scattering, fiber cells are tightly packed and have interdigitating processes along their short and broad sides. The apexes of elongating fiber cells meet at the anterior and posterior poles to form the lens sutures. The geometry of sutures are species specific, with bovine lenses having a Y shaped suture when looking on the optical axis. Human suture geometry is a more complexed branched Y shape, resembling a star shape (Kuszak, Zoltoski, & Sivertson, 2004; Kuszak, Zoltoski, & Tiedemann, 2004). While there is limited extracellular space between the broad and narrow sides of hexagonal fiber cells, the sutures provide an opening for extracellular transport between fiber cell tips, with accessibility to the adjacent aqueous and vitreous humors, and a pathway to the lens nucleus (Paterson, 1970; Vaghefi et al., 2012).

While proteomic, immunohistochemical, and functional studies have established the protein networks that establish efflux current from the lens (Cantrell & Schey, 2021b; Nye-Wood et al., 2017; Petrova et al., 2020; Schey et al., 2022; Vaghefi et al., 2012; Vaghefi & Donaldson, 2018), limited measurements exist regarding influx pathways. Entry and influx of metabolites through the suture is supported by Ussing-type chamber experiments (Candia et al., 2012; Candia & Zamudio, 2002; Fischbarg et al., 1999), with further MRI experiments suggesting that water and other small molecules are transported through extracellular space more rapidly than anticipated by passive diffusion alone (H.-M. Cheng et al., 1987; Vaghefi et al., 2011; Vaghefi & Donaldson, 2018). It is then hypothesized that passive diffusion may mediate nutrient uptake in young growth shells, while an alternative mechanism is required for nutrient delivery to the centermost fiber cells in the lens nucleus. Additionally, axial sectioning of the lens demonstrates clear restriction of extracellular space in nuclear sutures relative to cortical and outer nuclear counterparts (Figure 5-1, 5-2)(Vaghefi & Donaldson, 2018). Thus, it is suggested that a non-random mechanism enables enhanced metabolite rate of transport through the sutures, potentially by previously unmeasured protein networks along the extracellular restriction space in the suture.

To date, no study has performed unbiased measurement of proteins that are enriched in fiber cells adjacent to the suture relative to suture-non-adjacent fiber cells. To this end, we used laser capture microdissection (LCM) coupled to state-of-the-art LC-MS/MS technologies to perform unbiased measurement of differential expression between protein networks adjacent to the suture and along the equator of the fiber cell, not adjacent to the suture. We additionally evaluated changes between the anterior and posterior lens regions and performed all comparisons in two growth layers concurrent to the restriction in suture extracellular space (Figure 5-3). Supplemental immunofluorescence approaches support and enhance the spatial definition of our findings.

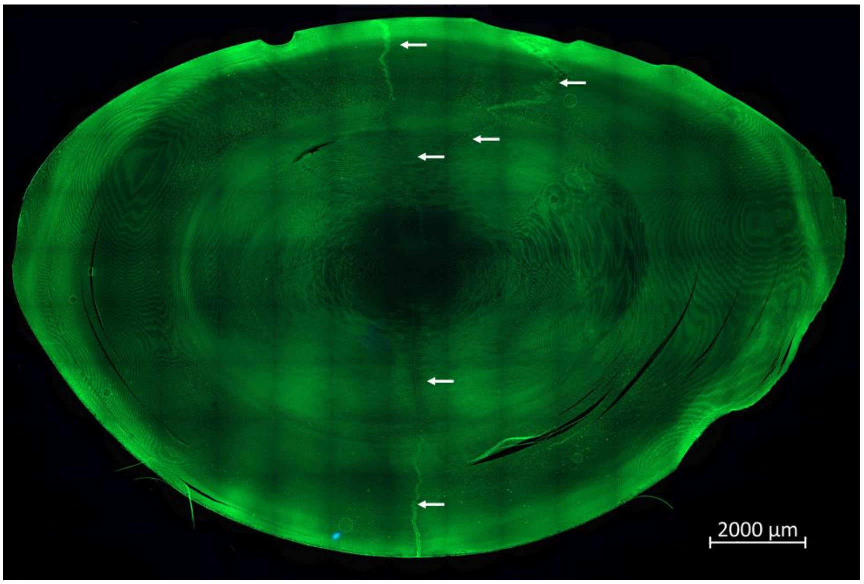

Figure 5-1 - AxioScan image of axially sliced bovine lens. Plasma membrane shown with WGA stain. Arrows delineate approximate location of the outer and inner suture.

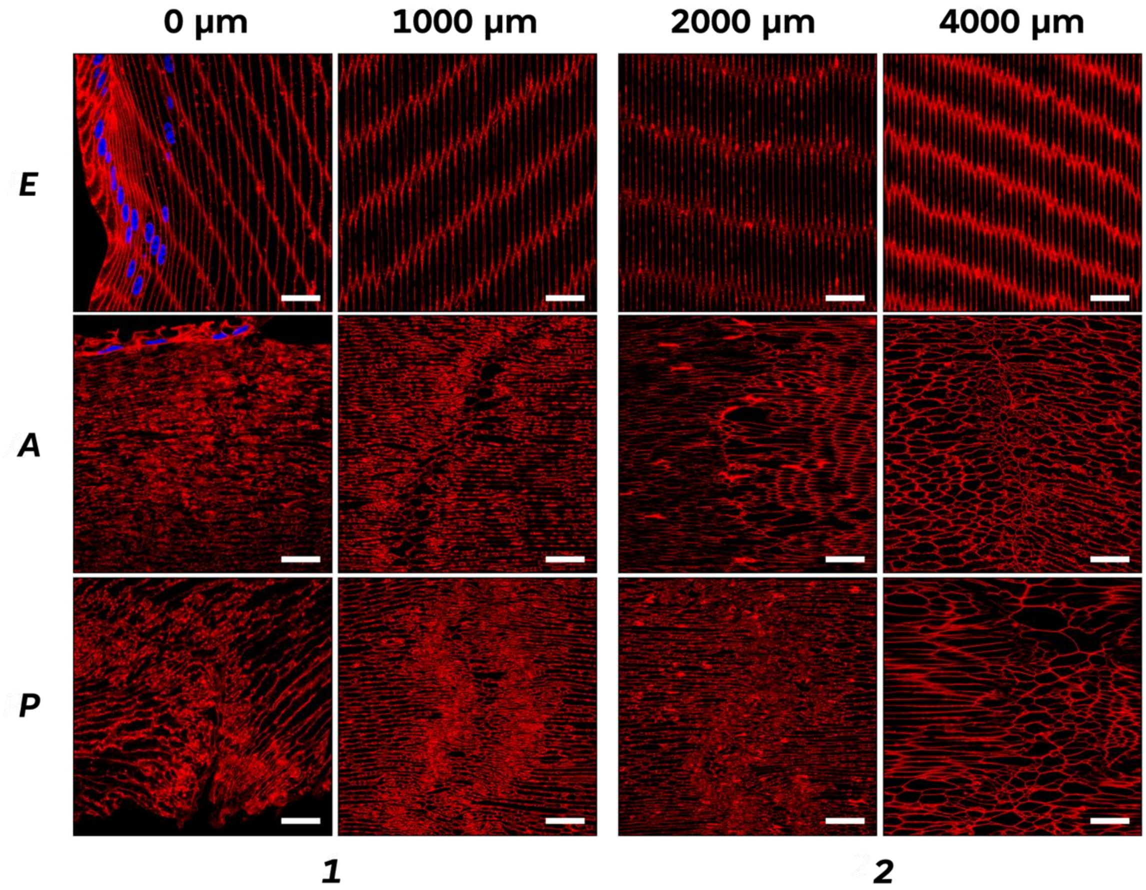

Figure 5-2 - Plasma membrane imaging throughout the lens with WGA stain. Columns are organized by depth (0 and 1000 μm are outer lens, 2000 and 4000 μm are inner lens). Rows are organized by region a (Equatorial, Anterior, and Posterior). Nuclei are shown in blue with DAPI. Sutures in the inner region have more extracellular space between sutures. Scale bars are 10 μm.

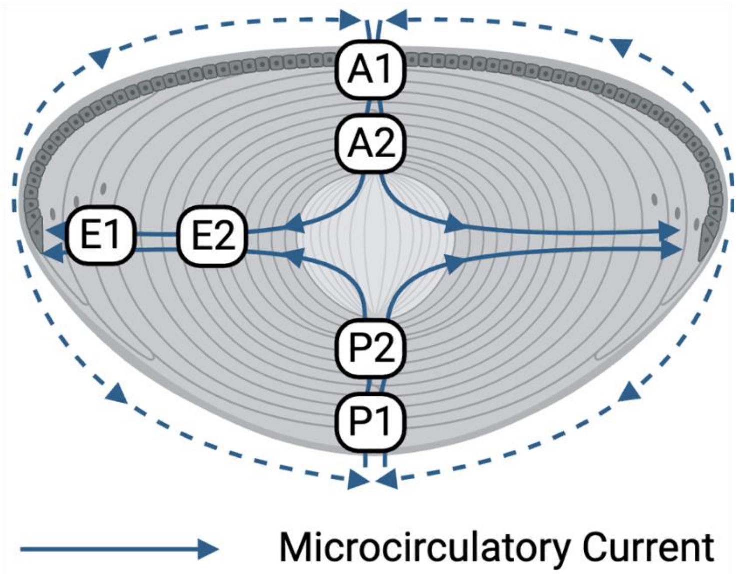

Figure 5-3 - Cartoon schematic of lens showing microcirculation current (blue arrows), with influx along the anterior and posterior sutures and efflux through the equator. Sample groups Anterior, Posterior, Equatorial, 1(outer), 2(inner) fiber cell populations labeled. Dashed lines represent circulation of efflux products to humors, which may be taken up by influx at sutures. Generated with BioRender.

5.3. Experimental Materials and Methods

5.3.1. Materials

Fresh bovine lenses (one to two years old) were received from Light Hill Meats (Lynnville, TN). LCM polyethylene napthalate (PEN) slides were obtained from Thermo Fisher Scientific (Waltham, MA). S-Traps were obtained from Protifi (Farmingdale, NY). Drierite™ anhydrous desiccant was obtained from W.A. Hammond Drierite Company, Ltd. (Xenia, Ohio). All other chemicals and materials were obtained from Fisher Scientific (Waltham, MA).

5.3.2. Antibodies

Rabbit anti-GLUT1 (ab115730) and rabbit anti-GLUT3 (ab234756) IgG were obtained from Abcam (Waltham, MA). Rabbit anti-N-cadherin (CDH2) (PA5-19486) and mouse anti-connexin 50 (33-4300) IgG were purchased from ThermoFisher Scientific (Waltham, MA). Normal rabbit IgG antibody was obtained from Cell Signaling Technology (2729; Danvers, MA). Normal mouse IgG antibody was obtained from Santa Cruz Biotechnology (sc-2025; Dallas, TX). Secondary antibodies (goat anti-rabbit Alexa Fluor 488 and goat anti-mouse Alexa Fluor 647) were obtained from Fisher Scientific (Waltham, MA).

5.3.3. Other biologics

Alexa Fluor 488-conjugated wheat germ agglutinin (WGA) was used to label fiber cell plasma membranes and to visualize lens sutures. Invitrogen™ DAPI (4',6-Diamidino-2-Phenylindole, Dilactate) (D3571) was used to label cellular nuclei.

5.3.4. Bovine lens fixation and fluorescent labeling

Fresh bovine lenses were fixed in 2% paraformaldehyde with 0.01% glutaraldehyde in phosphate buffered saline (PBS; 72 hours at room temperature), cryoprotected in 10% sucrose-PBS (2 days, 4°C), 20% sucrose-PBS (1 hour, room temperature), and 30% sucrose-PBS (> 7 days, 4°C), snap frozen in liquid nitrogen, encased in Scigen Tissue-Plus® O.C.T. Compound (Singapore, Singapore) and cryosectioned parallel (axially) to the optical axis using a Leica CM3050 S cryostat (Leica Biosystems Inc; Buffalo Grove, IL), and finally were transferred into clear 6-well plates in PBS. Lens tissue cryosections ("sections") were acquired at 12 µm thickness for LCM-mass spectrometric analysis and 20 µm thickness for immunofluorescence. For LCM-mass spectrometric analysis, sections were triply washed in PBS, incubated in Alexa488-conjugated WGA (1:100) in combination with DAPI (1:100) in PBS (1 hour at room temperature), triply washed in PBS to remove excess WGA and DAPI-dilactate, and finally transferred onto PEN membrane slides. Sections on PEN membrane slides were dried in a desiccator with anhydrous desiccant for at least 16 hrs.

For immunofluorescence, sections were processed as outlined previously (Gletten et al., 2022b). Briefly, sections were placed in blocking solution (6% bovine serum albumin, 6% normal goat serum, in PBS) for 1.5 hours to reduce nonspecific labelling, and immunolabeled with rabbit anti-GLUT1 (1:200), rabbit anti-N-cadherin (1:200), or mouse anti-connexin-50 (1:100) primary antibody in blocking solution (16 hours, 4OC) followed by Alexa488- or Alexa647-conjugated goat secondary antibodies with DAPI (1:100) in blocking solution (2 hours, room temperature). Finally, sections were labeled with Alexa647- or Alexa488-conjugated WGA in PBS as listed above. Normal rabbit IgG and normal mouse IgG were used as host-specific negative controls to determine nonspecific IgG binding. Finally, sections were coverslipped in ProLong™Glass Antifade Mountant.

5.3.5. Whole lens cryosection imaging

Fluorescently labeled bovine lens tissue sections were imaged using a Zeiss Axio Scan.Z1 slide scanner (Carl Zeiss Inc; White Plains, NY). Images were post-processed by subtraction of background fluorescence using Zen 2.3 slidescan (Carl Zeiss Inc). For immunofluorescence, immunolabeled sections were secondarily imaged using a Zeiss LSM 880 confocal laser scanning microscope (Carl Zeiss Inc). Confocal microscope images were post-processed using Zen Blue (Carl Zeiss Inc) to improve resolution via Airyscan processing and by subtraction of background fluorescence.

5.3.6. Laser Capture Microdissection

Cryosections dried on PEN membrane slides were dissected on a Zeiss PALM MicroBeam microscope (Carl Zeiss Inc). Membranes stained with WGA were visualized in fluorescence mode with excitation at 496 nm and emission at 524 nm to identify suture location and mark regions for sample selection. Using Axioscan images, the normalized distance to the start of the reduced extracellular suture space along the anterior and posterior pole was determined. This normalized radius (r/a) was consistently measured between the interval of r/a (0.68, 0.66). Thus, fiber cells with large extracellular sutures were collected between r/a of 1.0 and 0.68. Similarly, Axioscan images did not consistently show sutures interior to r/a 0.15. Thus, the reduced suture space samples were collected between r/a 0.66 and 0.20. An approximated width of increased extracellular space was calculated on 4 biological replicate lenses using ZEN software measurement of space between plasma membranes on either side of the suture. In the extracellular reduced space, no distance could be reproducibly measured between plasma membranes. Using the normalized radius intervals noted, matched equatorial samples were collected into 25 µL water. In total, 6 samples were collected: cortical equator, anterior suture, posterior suture, and nuclear equatorial, anterior suture, and posterior suture. All suture samples were collected within 100 µm of the fluorescence identified suture. Approximately 2,000,000 µm^2 tissue was pooled per tube from serial sections. LCM caps were then frozen and centrifuged into a 1.5 mL Eppendorf tube. In total, 6-12 serial sections were used per lens and 4 biological replicates were prepared.

5.3.7. Antigen retrieval and tryptic digest

Cryosections were fixed prior to LCM collection, necessitating antigen retrieval prior to tryptic digest. This was done as described previously(Griesser et al., 2020). Briefly, LCM captured tissue was dissolved in 100 µL 2% SDS in 300 mM Tris, pH 8.0. Samples were boiled at 99°C for 25 minutes at 350 rpm rotation to reverse crosslinks. Samples were then sonicated in an ultrasonic bath during 30 second cycles 20 times with 30 second intervals between sonication. Samples were then heated to 80°C for 2 hours at 500 rpm rotation before sonicating 20 additional cycles. Samples were spun down at 21,300xg and supernatant removed. Extraction steps were repeated with the remaining pellet. Free cysteines in the pooled supernatant were reduced with 10 mM DTT incubation for 45 minutes at 50°C at 1000 rpm and alkylated by addition of 20 mM iodoacetamide for 45 minutes at room temperature at 1000 rpm in the dark. Protein sample abundance was estimated by BCA assay.

After reduction and alkylation, 10 µg protein isolates were dried to 25 µL and acidified by 2.2 µL addition of 55% phosphoric acid. To the acidified protein, 2 µg trypsin in 50 mM acetic acid was added before transfer to the S-Trap micro containing 165 µL 100 mM triethylammonium bicarbonate (TEAB) in 90% methanol for protein precipitation. Precipitated protein solution was centrifuged at 4,000g for 30 seconds to remove solvent and non-protein material. Samples were washed by 4 additions of 150 µL 100 mM TEAB in 90% methanol and centrifuged between steps. A digest mixture of 0.5 µg trypsin in 25 µL 50 mM TEAB was then added to the S-Trap bed before overnight incubation at 37°C. Peptides were eluted in 40 µL wash steps of 50 mM TEAB, 0.2% formic acid, and 50% ACN in 0.2% formic acid. Samples were dried by SpeedVac and reconstituted in 0.2% formic acid for mass spectrometry data acquisition.

5.3.8. LC-MS/MS

Peptides were analyzed using a Dionex Ultimate 3000 UHPLC coupled to an Exploris 480 tandem mass spectrometer (Thermo Scientific, San Jose, CA) with sample order randomized. An in-house pulled capillary column was created from 100 µm inner diameter fused silica capillary packed with 3.0 µm Jupiter Phenomenex C18 beads to a length of 220 mm. Solvent A was 0.1% aqueous formic acid and solvent B was 0.1% formic acid in acetonitrile. Approximately 125 ng peptides were separated at a flow rate of 500 nL/min on a 95-minute gradient from 2 to 29% B, followed by a 14-minute washing gradient and 35-minute blank injection between runs.

For data-dependent acquisition (DDA) analyses, the Thermo Exploris 480 was set to acquire using a top-20 method with auto dynamic exclusion. Precursor spectra were collected from m/z 400 to 1600 at 60,000 resolution (AGC target 3e6, max IIT of 55 msec). MS/MS spectra were collected on peptidic precursors between charge state +2 and +5 achieving a minimum AGC of 1e4. MS/MS scans were collected at 15,000 resolution (AGC target of 1e5, max IIT of 35 msec) with an isolation width of 1.6 m/z. The S-Lens RF level was set at 40%, CE set at 27 and data collected in profile mode.

For data-independent acquisition (DIA) analyses, full MS scans were performed at 60,000 resolution (AGC target 3e6, max IIT of 110 msec). Ions isolated for MS/MS scan were fragmented at NCE 27 with default charge state +3 assumed. For quantitative DIA injections, an overlapping window scheme was employed between m/z 400 and 1000. Briefly, full MS spectra were collected followed by sequential isolation of ions in 20 m/z width windows in the mass range. Isolated ions were fragmented and measured with an MS2 scan. After scanning across the whole mass range, another full MS spectra was collected followed by sequential window MS2 acquisition offset by 10 m/z (e.g., windows from m/z 400-420, 420-440, 460-480 in the first scan cycle and m/z 390-410, 410-430, 430-450 in the second scan cycle). For gas-phase fractionated DIA collection, 6 repeat injections of pooled samples representative of the whole dataset were performed. Each injection scanned across a 100 m/z acquisition window (e.g., injection 1 from m/z 400-500, injection 2 from m/z 500-600, etc.) with 4 m/z width fragment isolation windows offset by 2 m/z in sequential scans. In addition to a MS scan of the full mass range prior to windowed collection, a second 100 m/z MS scan of unfragmented ions in the range of the injection was performed prior to MS2 scans.

5.3.9. Mass spectrometry data analysis and bioinformatics

For analysis of DDA data, RAW files were searched in the FragPipe (version 18.0) environment with MSFragger (Kong et al., 2017; Teo et al., 2021)(version 3.5) search, Percolator validation (Käll et al., 2007) and EasyPQP (version 0.1.30) library generation. All searches were performed with fixed cysteine carbamidomethylation modification. Variable modifications were enabled as follows: methionine oxidation, protein N-terminal acetylation, N-terminal pyroglutamic acid formation, N-terminal water loss from glutamic acid, lysine formylation, serine formylation, threonine formylation, and formaldehyde adduct formation on cystine, lysine, arginine, histidine, tyrosine, tryptophan, and phenylalanine. Up to 3 variable modifications were allowed per peptide with up to 3 missed cleavages allowed. Results were searched against a bovine canonical database (downloaded 7/14/2022, 17,096 entries) filtered by homology to human SwissProt proteins with the PAW_BLAST tool from Phil Wilmarth (https://github.com/pwilmart/PAW_BLAST).

For analysis of DIA data, a multi-stepped approach was used for spectral library generation inclusive of sample-preparation induced PTMs. First, all 24 DIA files were searched by DIA-NN (Demichev et al., 2020) (version 1.8.1) against the described fasta database. Separate searches were performed for each modification described in the DDA search settings. Up to 2 missed cleavages were allowed per peptide, with a maximum of 1 variable modification per peptide allowed. Results were filtered to 1% FDR before generation of an experimental spectral library for each PTM. Each spectral library, including the DDA library, were converted to Spectronaut tsv format using custom R scripts and then converted and combined into a master experimental spectral library with blib_build, implemented through the EncyclopeDIA (Searle et al., 2018) GUI (version 1.12.34). The experimental library was empirically corrected against the previously unsearched set of GPF-DIA sample acquisitions to generate a spectral library with chromatographic correction applied and higher statistical match certainty in precursor and fragment identification than that possible in the input experimental library (Searle et al., 2020). Each of the 24 DIA files for quantitative inference were then searched by EncyclopeDIA implemented through command line with filtering at 1% FDR. Peptide level quantitative reports were produced for further inference.

All protein inference and analysis was performed through custom R scripts. Prior to protein quantitation, contaminant peptides and peptides with less than 5 quantitative fragments were filtered out. If a protein was only identified by 1 unique peptide, the protein was filtered out of the dataset unless its quantitative variance was low. Briefly, the variance of all peptides belonging to protein groups with >1 peptide were evaluated with regions (E1, A1, P1, etc.). The median c.v. between the 6 regions was calculated and the 20th percentile of c.v. evaluated (28% on non-log2 transformed data). Finally, peptides belonging to proteins with only one unique peptide were considered as identified if the within region median c.v. was below this conservative variance threshold. Inclusion of low-variance, single-peptide protein groups facilitated the identification of 86 proteins, the majority of which were membrane proteins with limited tryptic accessibility. Protein quantitation was evaluated as the sum of all peptide precursor intensities. In total, 700 proteins and 7,323 peptides were identified. Samples were normalized by global sum normalization prior to quantitative inference (Figure 5-4). Biological replicate effects were evaluated with principal component analysis (PCA) plots. t-Testing of difference between sample regions was performed with Welch’s 2-sample t-tests and significance defined at $p < 0.05$. Panther results were generated at PantherDb.org (version 17.0, 8/31/2022) with the overrepresentation module (Thomas, 2003). Appropriate background proteomes of all 700 measured proteins were used in a Fisher’s Exact test with FDR correction on PANTHER GO-Slim ontology sets. When filtering was done by redundancy and specificity, terms such as “plasma membrane” and “intrinsic component of plasma membrane” were considered to be redundant. A STRING search was initiated on human gene names for protein-protein interaction enrichment analysis (von Mering et al., 2003).

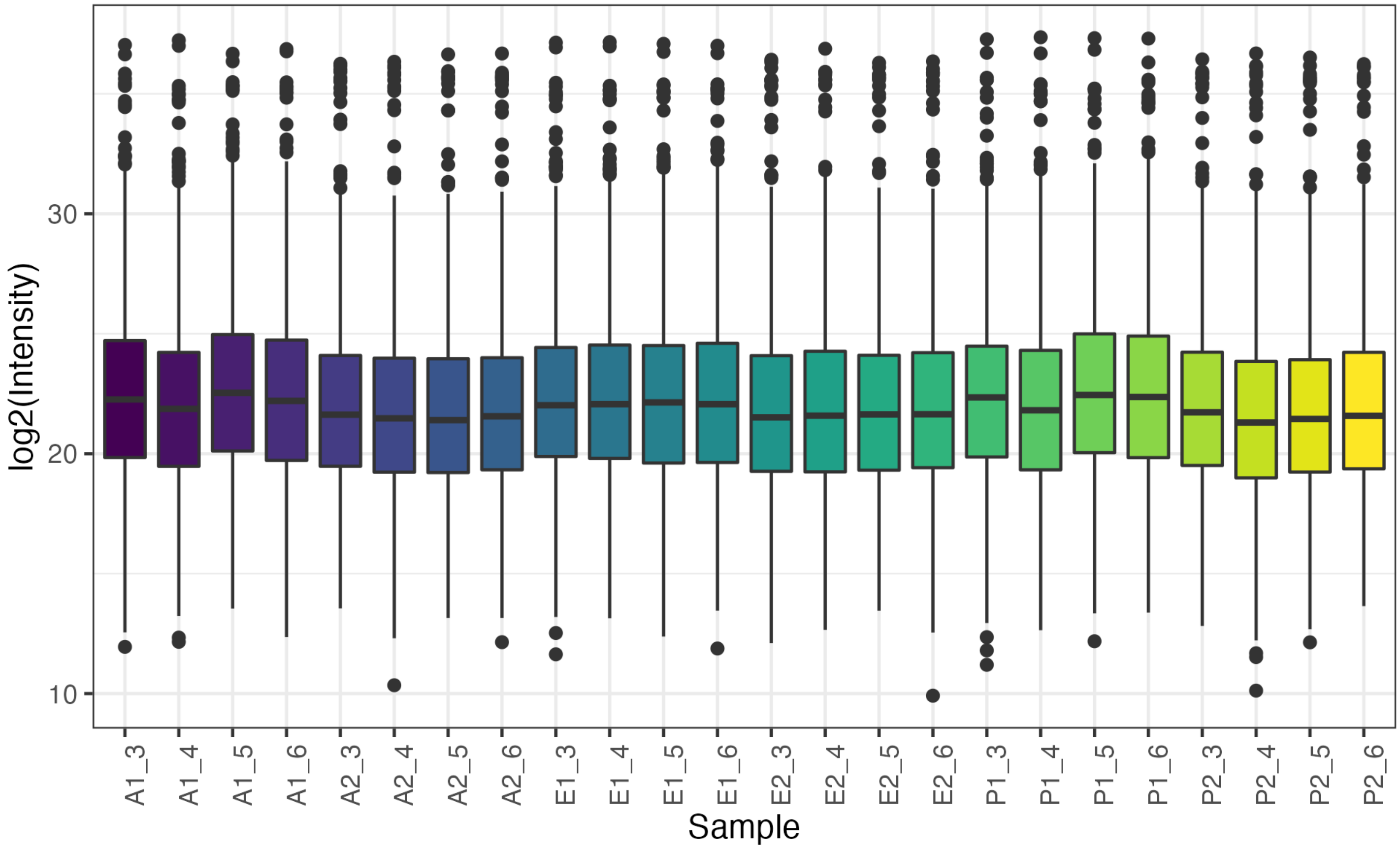

Figure 5-4 - Boxplot of peptide intensities post-normalization with global sum method.

5.4. Results

To evaluate age-related changes of fiber cell tips at lens sutures, further referred to as “suture tips”, we employed data-independent acquisition mass spectrometry proteomics (DIA MS) which has shown prior utility in measuring the aging lens proteome (Cantrell et al., 2023). While desirable, we were unsuccessful in attempts to axially section fresh-frozen or ethanol fixed lenses along the polar axis while maintaining sufficient cell morphology for suture visualization. Therefore, bovine lenses were fixed prior to LCM capture and preparation of tissue-limited samples. Samples were collected at the Equator (E), and Anterior suture tips (A), Posterior suture tips (P). In preliminary lens imaging experiments, an observed narrowing of the extracellular space was observed at approximately r/a 0.68, where the outer sutures had wider gaps between fiber cell tips than the inner suture. Across 4 biological replicates, the width of extracellular space between outer sutures was approximately 8 µm (4 µm minimum, 14 µm maximum without observed spatial trend) throughout the range r/a (1.0, 0.68]. The width of low extracellular suture space was approximately 0 µm along the range r/a [0.66, 0.20). In this range, the suture can be visualized, but space between fiber cell membranes is negligible. Interior to r/a 0.20, the suture is not reproducibly observed. Samples in the outer, high extracellular suture space (1) were collected in addition to inner, low extracellular suture space (2). In total, 6 sample regions (E1, E2, A1, A2, P1, P2) were collected across 4 biological replicates, resulting in 24 total samples (Figure 5-3). To accommodate tissue fixation, a preparation method previously used to evaluate cytosolic and membrane proteins from FFPE tissue was used (Griesser et al., 2020). Finally, compared to conventionally applied shotgun MS proteomics methods, DIA MS enabled greater coverage of the lens proteome than otherwise possible (Cantrell et al., 2023; Cantrell & Schey, 2021b). Unlike conventional methods, DIA MS requires a spectral library for peptide measurement. Here, we prepared a spectral library by combining results from conventional DDA MS experiments of representative samples with results from a pooled sample collected by gas-phase fractionation DIA (see Methods for further description). The combined results were converted to an empirically corrected spectral library (i.e., a spectral library of experimental spectra with retention time indexing) which was used to identify and quantify peptides in each of the 24 samples (Figure 5-5). Protein abundance was based on summation of peptide signal according to software developer recommendations. In total, 7,323 distinct peptides belonging to 700 proteins were quantified in all samples. Ontology overrepresentation analysis of the 700 measured protein groups relative to the bovine genome included lens development in camera-type eye (GO:0002088) among other ontologies anticipated in lens tissue (Supplementary Data)(Cantrell & Schey, 2021b; Z. Wang et al., 2013). Epithelium specific proteins such as aquaporin-1 and connexin 43 were not measured, suggesting that proteome measurement was targeted to fiber cells and did not include epithelial cells in the anterior suture and equator regions (A1 and E1).

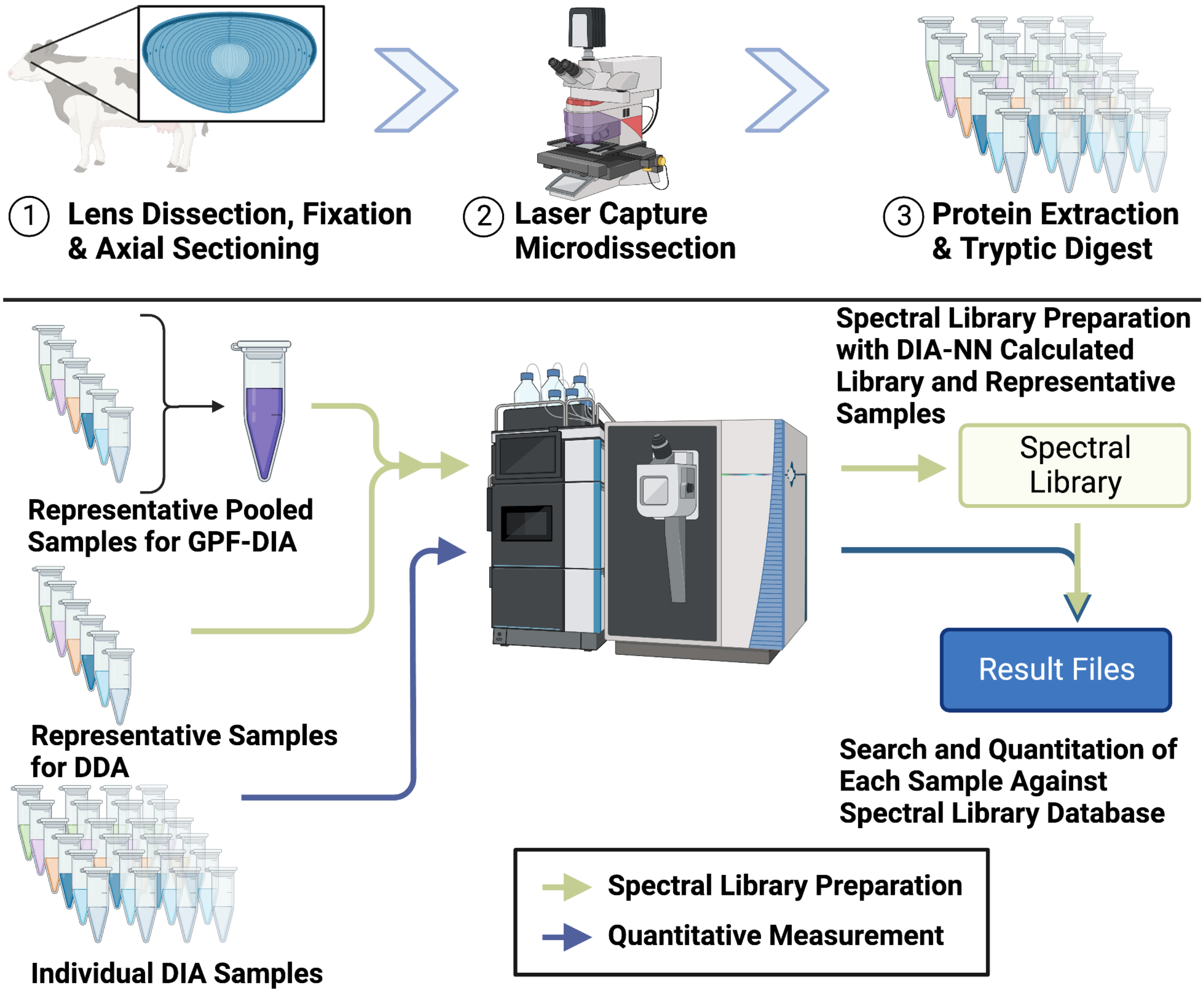

Figure 5-5 - Workflow employed for spatially-resolved mass spectrometry proteomics measurements. Top: enucleated bovine lenses were formalin fixed with glutaraldehyde supplementation and sectioned axially. Selected regions were isolated by laser capture microdissection and samples processed by antigen retrieval and tryptic digest before LC-mass spectrometry injection. Bottom: of the 24 LCM generated tryptic digests, 6 were pooled to create one sample for gas-phase fractionated DIA (GPF-DIA). Six other representative samples were selected for DDA. In total, 12 injections were used to create a spectral library (green arrow path). The spectral library was generated in DIA-NN and FragPipe with compilation and empirical correction in EncyclopeDIA. All 24 digests were then injected in DIA mode and results were generated against the prepared spectral library (blue arrow path). Figure generated in BioRender.

5.4.1. Changes as suture tips age

Preliminary evaluation of all samples by Spearman rank correlation (Figure 5-6) demonstrates that similarity between samples primarily occurs between samples of the same age and not within a given lens region (i.e., young and old anterior suture regions are less similar than old equator and old posterior regions). This is supported by principal component analysis (Figure 5-6) where PC1 precisely separates outer and inner samples, with no clear PC2 separation of cells of different groups. Cumulatively, this suggests that the majority of the suture proteome and equator region proteome are homogenous with each other within the same concentric growth aging regions. Therefore, comparative analysis was not performed between samples of both different age grouping and lens localization (e.g., A1 vs E2 comparisons).

Volcano plot visualization of differential expression was done for individual proteins as a function of fiber cell age (outer/young and inner/old) within subcellular regions (equator or tips) (Figure 5-7). Extensive prior proteomic work has been done to this end to characterize MCS efflux networks in the aging equatorial region of fiber cells (Truscott et al., 2011; Z. Wang et al., 2021; Wenke et al., 2016). Consistent with prior studies, brain acid soluble protein 1 (BASP1) and glutamate-cysteine ligase catalytic subunit (GCLC) were enriched in outer fiber cells relative to inner growth layers (Figure 5-7C). Conversely, two gamma crystallins (CRGA, CRYGN) show enrichment in inner equatorial fibers. Taken together, these results support the ability of this method to measure age-related changes.

Proteins differentially expressed along the aging suture tips (Figure 5-7A, 5-7B) was largely consistent with results in the equator. In addition to continuity of protein differential expression, protein networks at the level of gene ontology showed congruent trends. Few ontologies were identified as differentially expressed with age along the suture tips, but not in the equator (Supplementary Data). Interestingly, we identified facilitated glucose transporters GLUT3 and GLUT1 as enriched in the inner anterior and posterior suture tips respectively, relative to the equator. In addition to GLUT1, calpain-3 (CAPN3), gamma-glutamylcyclotransferase (GGCT), and l-lactate dehydrogenase (LDHAL6B) were identified as enriched in the inner posterior suture (P2) region relative to the outer posterior suture (P1) tips. CAPN3 has a putative role in connexin truncation, eliminating its gap junction function when truncated along the cytoplasmic loop or inducing pH regulatory effects when occurring on the N- or C-termini (K. Liu et al., 2015; Slavi et al., 2016), whereas GGCT is the penultimate enzyme in glutathione (GSH) catabolism. LDHAL6B is a predicted structural upsilon crystallin previously identified in the platypus lens (van Rheede, 2003).

Among proteins with suture specific differential expression between the outer and inner fiber cells, most could be classified as one of three subclasses. First as proteins related to nuclear centrosome function and differentiation (FHL1, PATL1, CEP170, ISOC1, ACTR, SH3GLB2), second to kinase activity (PACSIN3, PRKACB), and third to cytoskeletal structure (PRX, PALM, GSN, ACTB, VIM). Each of these classes were expected since 1) nuclear function and cellular differentiation are enriched in outer fiber cells with organelles, 2) cytoskeletal remodeling occurs with cellular maturation (Wenke et al., 2016), and 3) kinase activity is expected to be downregulated in more enzymatically inert, mature fiber cells (Venkatn. Reddy & Giblin, 2008). The sole outlier to these designations was chloride intracellular transporter CLIC5, which was previously hypothesized to be responsible for chloride influx in mature fiber cells, especially interior to the age-related cellular diffusion barrier (Z. Wang et al., 2021; Webb et al., 2004).

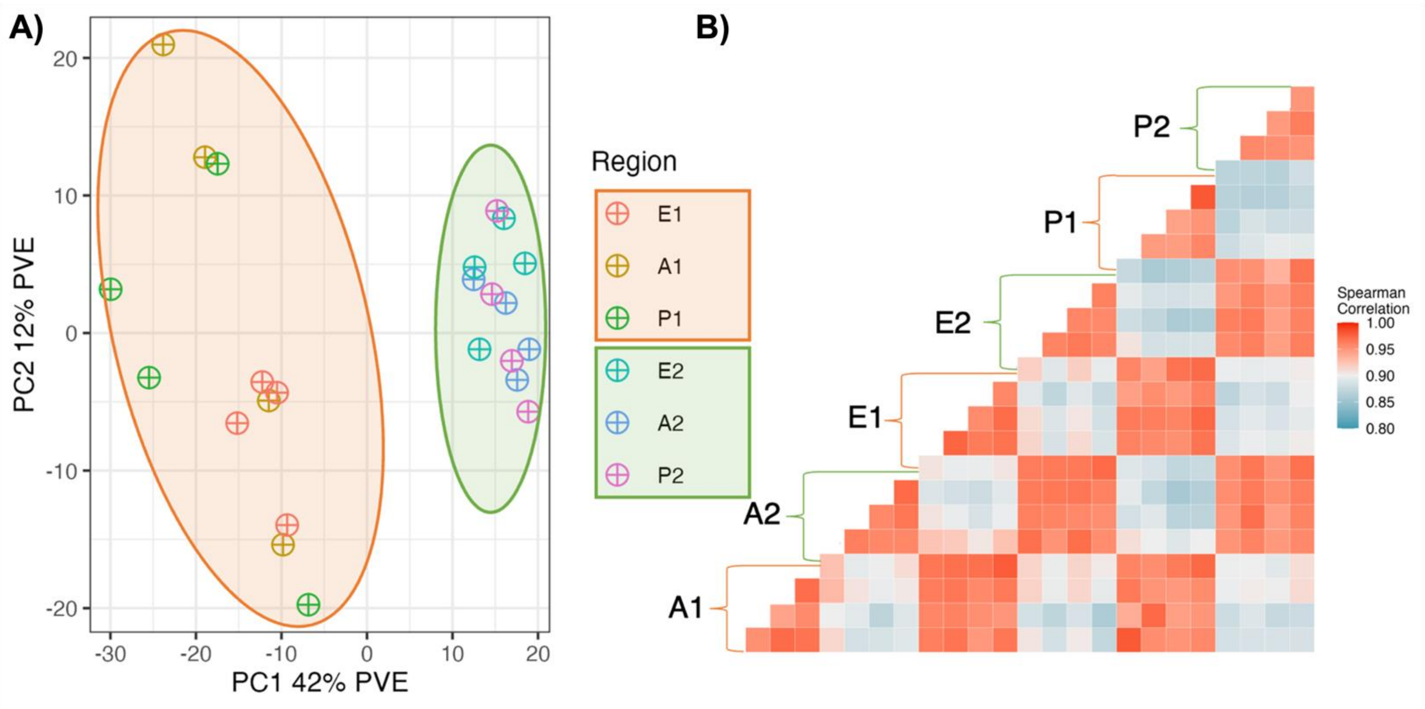

Figure 5-6 - Primary changes between samples occur between the outer and inner fiber cell populations. A) Principal component analysis plot with group coloring by lens region. Axis dimensions approximately correlated with proportion of variance explained (PVE). Outer (orange boxed) and inner (green boxed) fiber cells separate from each other on PC1. No clear trend emerges on PC2. B) Spearman correlation between samples based on relative protein abundance. Biological replicates grouped and annotated. Lower limit of correlation adjusted to best show contrast between young (E/A/P1) and old (E/A/P2) fiber cell populations.

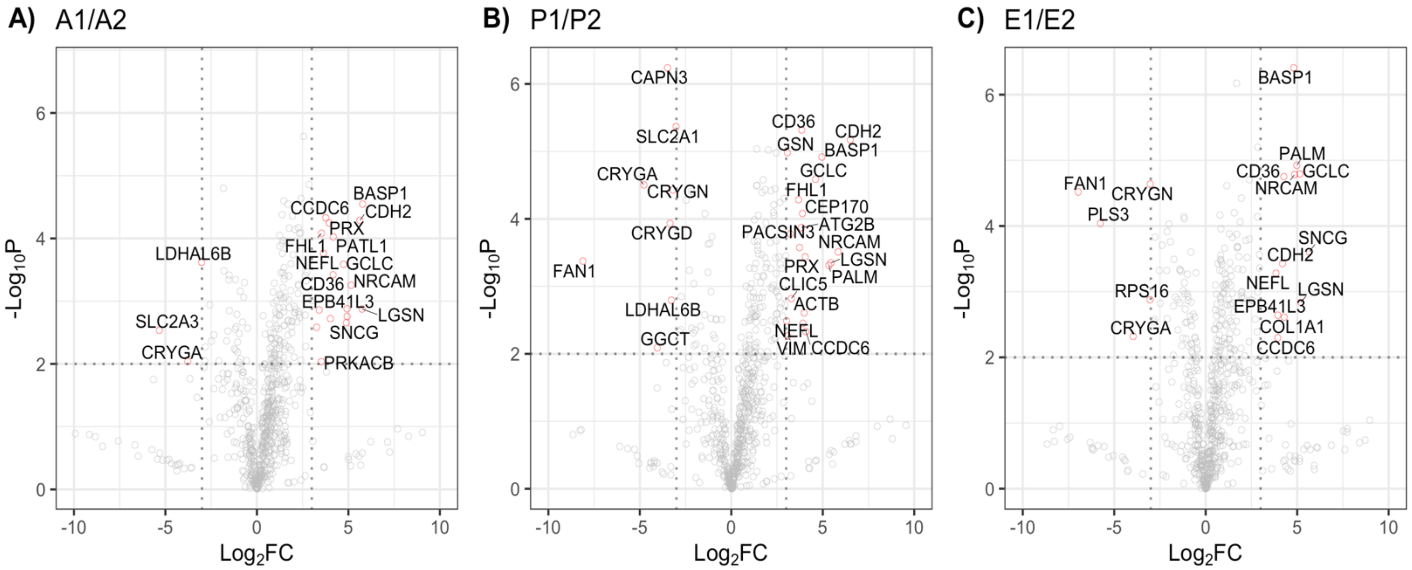

Figure 5-7 - Volcano plots of results to compare protein expression within regions of different ages. 700 proteins were used to compare all samples with significance cutoffs (dotted lines) at 3 Log2FC and p < 0.01. Several insignificant changes are filtered to enhance visualization on the x-axis. A complete list of significant differences are available in Supplementary Table S1. A visually unfiltered volcano plot is available as Supplementary Data.

5.4.2. Differences between suture tips and the equator

To evaluate changes between different subcellular lens regions we performed similar analysis by comparison of suture tips and the equator with control for cellular age. Supporting results of Martin et al. (Martin et al., 2022), we demonstrate that ARVCF and N-cadherin (CDH2) are similarly enriched in the outer anterior and posterior suture relative to the equatorial portion of the fiber cell and may be essential for suture formation. We confirmed this relationship with immunofluorescence experiments for N-cadherin (Figure 5-8, 5-9). High-resolution imaging supports the measured trend towards CDH2 suture enrichment, with the anterior and posterior sutures being particularly bright. We also measured α- and β-catenins (CTNNA1, CTNNB1) as enriched in the suture tips, and proteasome component PSMC6 as enriched in the equator (Figure 5-9A, 5-9B). In agreement with age-related results, the specific enrichment of catenins CTNNA1, CTNNB1, and ARVCF suggest catenin complex proteins and adherens junction protein networks are enriched in the sutures. In support of this finding, overrepresentation analysis of volcano plot significant proteins relative to the measured 700 protein background identified adherens junction (GO:0005912) and cadherin binding (GO:0045296) as anterior and posterior suture enriched relative to the equator (Table 5-1).

Statistical overrepresentation of significant proteins relative to a background of all measured proteins in Panther revealed several clear similarities in the outer anterior and posterior suture relative to the equator (Table 5-1). Particularly, transcription initiation from RNA polymerase II promoter (GO:0006367) and ubiquitin dependent ERAD pathway (GO:0030433) were enriched in the equator, while homophilic cell adhesion via plasma membrane adhesion molecules (GO:0007156) and cadherin binding (GO:0045296) were enriched in the sutures. Combined analyses here depict subcellular organelle localization in the fiber cell equator, but also supports adherens junction localization and catenin complex overrepresentation at the outer suture tip.

Although the anterior and posterior suture tips show consistent patterns of differential expression in the outer suture, we measured several distinct differential expression patterns in the outer posterior suture relative to outer equator (Figure 5-10E). First, we identified GCLC as enriched in the inner posterior suture tip population. Transmembrane protein 47 (TMEM47), a member of the claudin family, is also enriched in the posterior suture, suggesting enrichment of tight junctions therein (Bassnett et al., 2009). Cytoplasmic dynein (DYNC1H1) was also enriched in the inner posterior, potentially interacting with TMEM47. Most interestingly, GLUT1 was measured as enriched in the posterior suture with GLUT3 trending towards significance. Kinesin 1 (KCL1), autophagy-related protein (ATG2B), and LIM domain and actin binding protein (LIMA1) were measured as enriched in the equator relative to posterior suture tips. By STRING protein network analysis, these cytoskeleton-related proteins do not have high confidence predicted protein-protein interactions, suggesting limited cytoskeletal function disruption. Finally, connexin 50 (GJA8) was measured as posterior suture depleted relative to the equator. Equivalent significance was not established in the anterior suture tips, but a trend towards significance was observed ($p = 0.024$, Log2FC = -0.51). This combined result was supported by immunofluorescence (Figure 5-11, 5-12). Low-resolution images show a gap in fluorescence along the suture, especially at the inner posterior suture (Figure 5-12). The same trend is observed in high resolution images; however, we note that fiber cells also lack appreciable GJA8 fluorescence between 2- and 4.4-mm interior to the peripheral equator. This may be a result of antigen specificity for a truncated or modified region of GJA8.

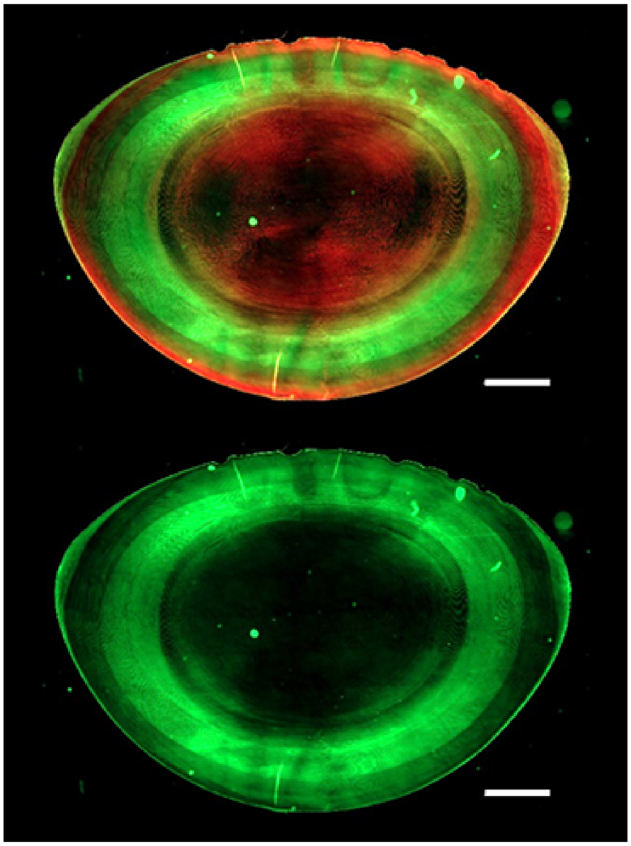

Figure 5-8 - AxioScan images of fixed lens with (top) overlay of N-cadherin (CDH2, green) and WGA stain (red) and (bottom) exclusively CDH2 stain. Scale bars are 10 µm.

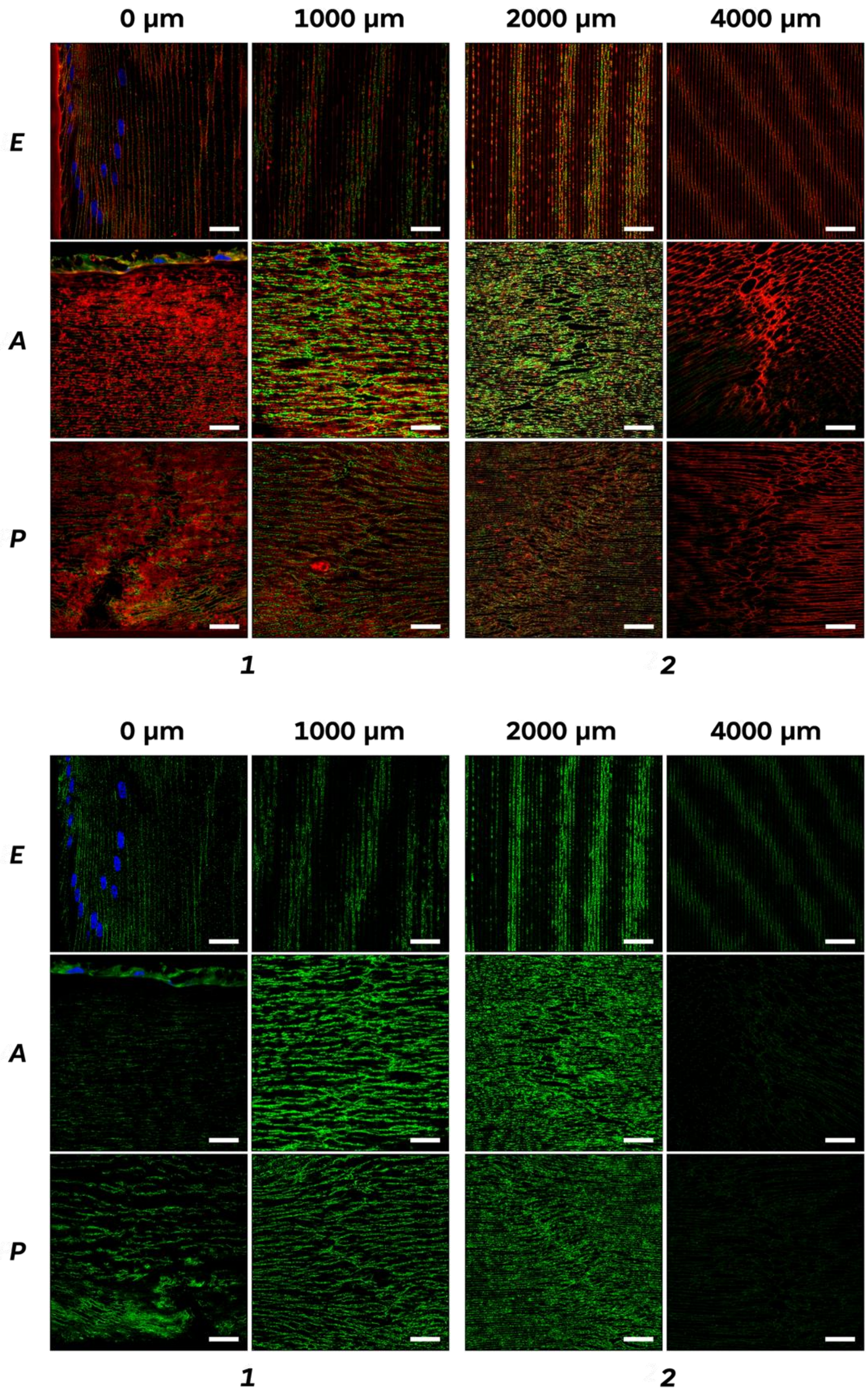

Figure 5-9 - Immunohistochemical imaging of N-cadherin (CDH2, red) throughout the lens. Plasma membranes shown by WGA stain (green). Nuclei shown by DAPI stain (blue). Columns are organized by depth (0 and 1000 µm are outer lens, 2000 and 4000 µm are inner lens). Rows are organized by region according to WGA stain (Equatorial, Anterior, and Posterior). Images with and without WGA overlay shown. Scale bars are 10 µm.

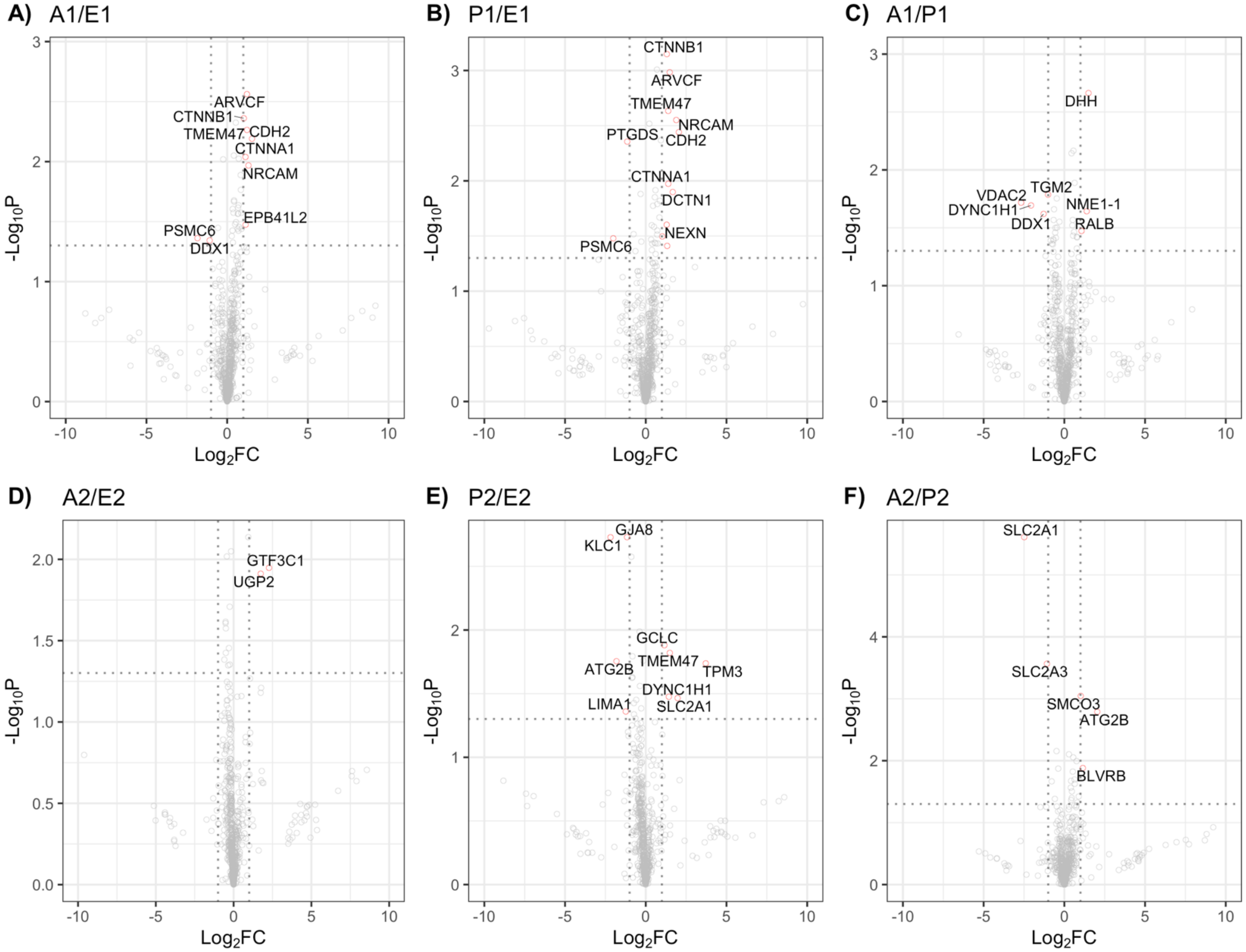

Figure 5-10 Volcano plots to compare protein expression as a function of suture proximity. 700 proteins were used to compare all samples with significance cutoffs (dotted lines) at 1 Log2FC and p < 0.05. Several insignificant changes are filtered to enhance visualization on the x-axis. Complete list of significant differences are available in Supplementary Data.

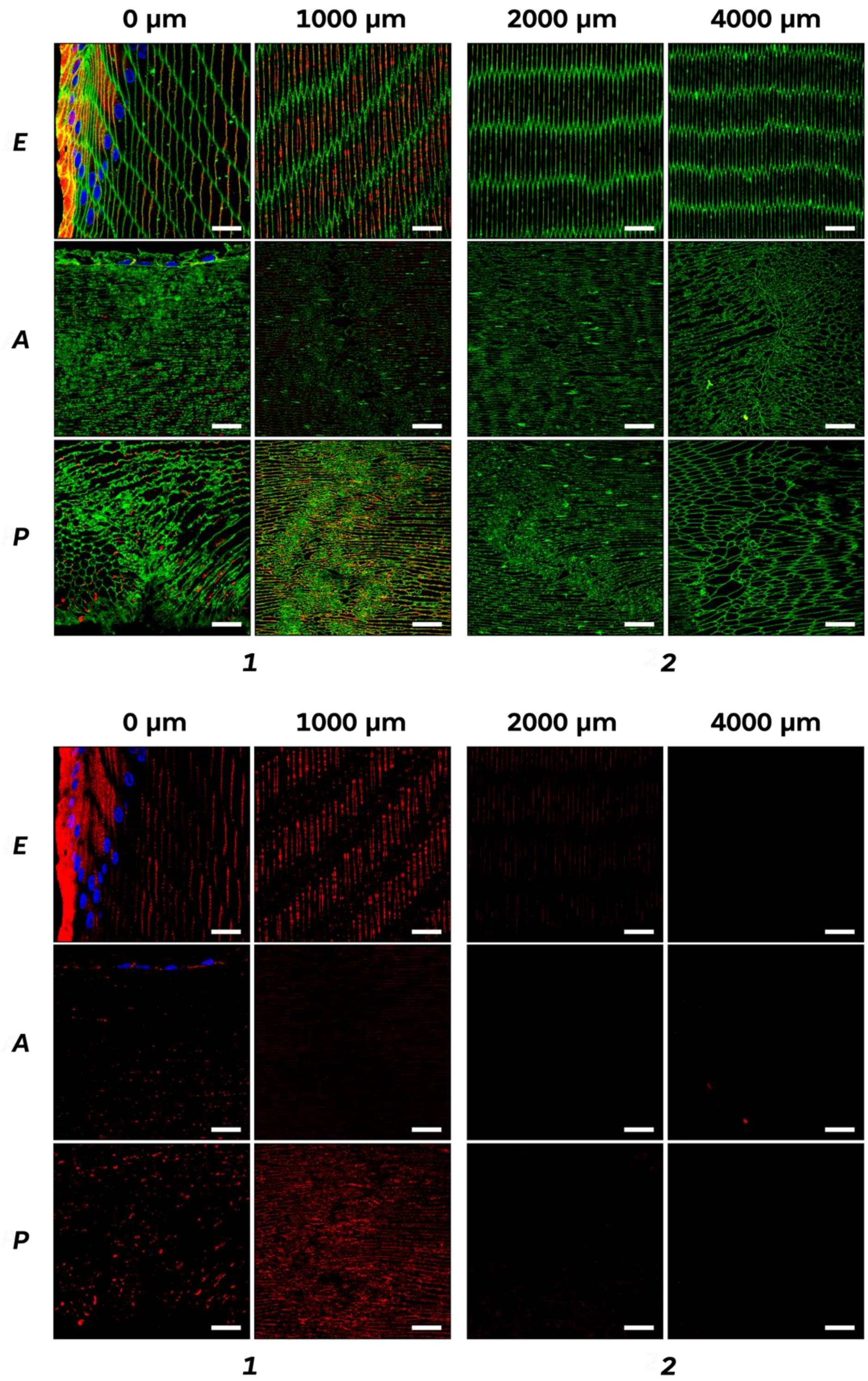

Figure 5-11 - Immunohistochemical imaging of Connexin 50 (GJA8, red) throughout the lens. Columns are organized by depth (0 and 1000 µm are outer lens, 2000 and 4000 µm are inner lens). Rows are organized by region according to WGA labeling (green) (Equatorial, Anterior, and Posterior). Images with (top) and without (bottom) WGA overlay shown. Scale bars are 10 µm.

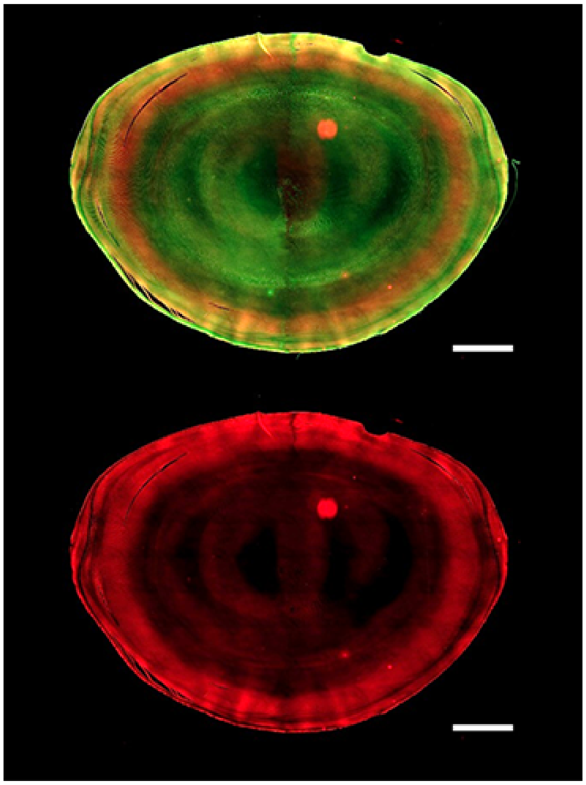

Figure 5-12 - AxioScan images of fixed lens with (top) overlay of connexin 50 (GJA8, red), and WGA stain and (bottom) exclusively GJA8 stain. Scale bars are 2000 µm.

Table 5-1 - Significant Panther Slim GO from Volcano Plot significant proteins, filtered for specificity and redundancy. Unlisted comparisons had no enrichment. A full list of significant terms is available in Supplementary Data.

Gene Ontology Statistical Overrepresentation Analysis

Panther Term	**Fold Enrichment**	**p-value**	**FDR**
A1/E1			
homophilic cell adhesion via plasma membrane adhesion molecules (GO:0007156)	50.34	6.41E-05	2.24E-02
cell-cell junction assembly (GO:0007043)	41.95	9.55E-05	2.67E-02
intrinsic component of postsynaptic specialization membrane (GO:0098948)	55.93	1.23E-03	2.87E-02
postsynaptic specialization membrane (GO:0099634)	41.95	1.83E-03	2.93E-02
intercalated disc (GO:0014704)	41.95	1.83E-03	2.65E-02
adherens junction (GO:0005912)	33.56	2.10E-08	2.12E-06
neuron to neuron synapse (GO:0098984)	27.97	3.37E-03	4.66E-02
lamellipodium (GO:0030027)	27.97	3.37E-03	3.66E-02
cadherin binding (GO:0045296)	25.82	2.16E-05	3.56E-03
E1/A1			
transcription initiation from RNA polymerase II promoter (GO:0006367)	> 100	5.08E-05	3.54E-02
ubiquitin-dependent ERAD pathway (GO:0030433)	93.22	2.36E-04	4.71E-02
positive regulation of macromolecule biosynthetic process (GO:0010557)	69.92	3.79E-04	3.53E-02
response to organonitrogen compound (GO:0010243)	39.95	1.01E-03	5.20E-02
P1/E1			
homophilic cell adhesion via plasma membrane adhesion molecules (GO:0007156)	51.63	3.96E-06	1.38E-03
cell-cell junction assembly (GO:0007043)	32.27	2.22E-04	1.72E-02
axon development (GO:0061564)	17.21	1.12E-04	2.60E-02
locomotion (GO:0040011)	9.93	7.19E-04	3.72E-02
intrinsic component of postsynaptic specialization membrane (GO:0098948)	43.03	2.10E-03	4.55E-02
adherens junction (GO:0005912)	25.82	1.60E-07	1.62E-05
cadherin binding (GO:0045296)	19.86	6.98E-05	1.15E-02
E1/P1			
RNA polymerase II preinitiation complex assembly (GO:0051123)	> 100	5.08E-05	7.09E-02
ubiquitin-dependent ERAD pathway (GO:0030433)	93.22	2.36E-04	4.71E-02
positive regulation of cellular component biogenesis (GO:0044089)	93.22	2.36E-04	2.75E-02
positive regulation of RNA metabolic process (GO:0051254)	69.92	3.79E-04	3.11E-02
response to organonitrogen compound (GO:0010243)	39.95	1.01E-03	5.20E-02
P2/A2			
carbohydrate transmembrane transport (GO:0034219)	> 100	2.02E-07	2.82E-04
transmembrane transport (GO:0055085)	69.92	4.59E-06	2.14E-03
structural molecule activity (GO:0005198)	3.75	1.14E-04	3.75E-02

5.4.3. Differences between anterior and posterior suture tips

In addition to comparisons between suture tips and the equator, several differences between the anterior and posterior suture tips were measured. In the outer suture, we identified desert hedgehog (DHH), nucleoside diphosphate kinase (NME1-1), and Ras-related protein B (RALB) as anterior enriched relative to posterior. STRING analysis of these proteins suggests no protein-protein interaction. Activation of RALB in nutrient deprived environments results in autophagosome formation (Bodemann et al., 2011) with DHH having inhibitory effect towards autophagosome formation (Jimenez-Sanchez et al., 2012). In addition to cellular organelle degradation, autophagosome formation has a putative role in trafficking of aquaporin-5, a critical water channel in MCS (Gletten et al., 2022a). Enriched in the outer posterior suture relative to anterior suture, we identified DYNC1H1, an ATP-dependent RNA helicase (DDX1), and transglutaminase 2 (TGM2). Among various functions of TGM2, it may catalyze cross-link formation between α-crystallin, β-crystallin, and vimentin (Shridas et al., 2001; Shin et al., 2004). Disruption of tertiary structure may then lead to protein dimer aggregation and subsequently cataract formation in the lens posterior.

Finally, we evaluated differences between the inner suture tips (Figure 5-10F). Relative to the posterior, the anterior suture is enriched for autophagosome-related protein ATG2B, functionally uncharacterized single-pass membrane protein SMCO3, and flavin reductase (BLVRB). Autophagosome activity in these inner fiber cell sutures may have a role in protein transport or degradation. Reductase activity may play an integral role in oxidative stress homeostasis at the anterior suture (Y. Huang et al., 2022). Most interestingly, we measured GLUT1 and GLUT3 as enriched in the posterior suture relative to anterior. We visually confirmed this relationship with immunohistochemical stain (Figure 5-13, 5-14). GLUT1 fluorescence emphasizes the abundance of GLUT family proteins in the inner lens. While measured in the outermost equatorial region, the qualitative abundance of GLUT1 is lower in progressively interior fiber cells until weak GLUT1 fluorescence emerges in equatorial fiber cells 4.4 mm interior to the periphery. By contrast, GLUT3 is measured throughout the posterior suture and in the inner anterior suture. Spatial enrichment of GLUT1 and GLUT3 was found concurrent to carbohydrate transmembrane transport (GO:0034219) protein network enrichment between these samples.

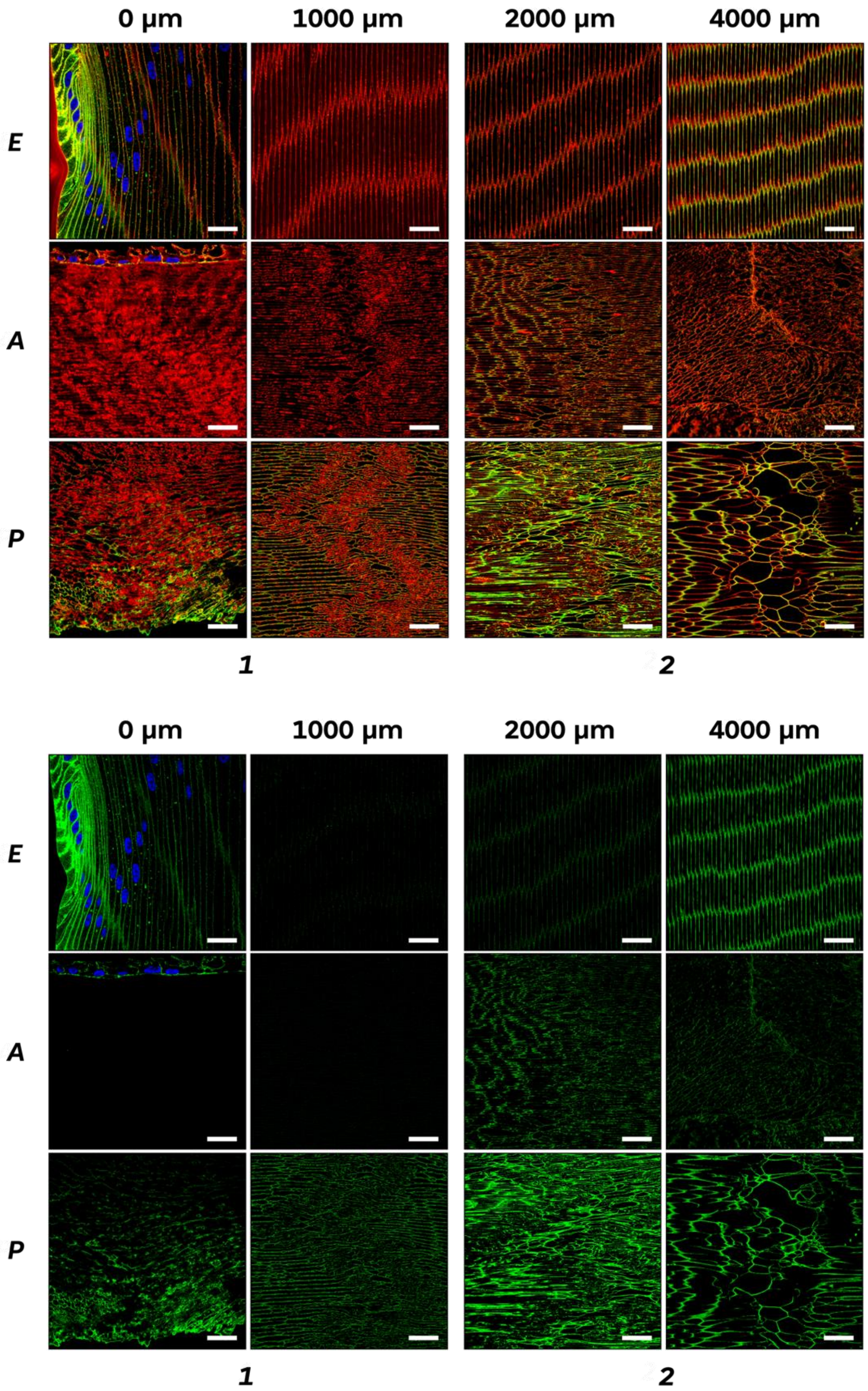

Figure 5-13 - Immunohistochemical imaging of facilitated glucose transporter 1 (GLUT1, green) throughout the lens. Columns are organized by depth (0 and 1000 µm are outer lens, 2000 and 4000 µm are inner lens). Rows are organized by region according to WGA labeling (red) (Equatorial, Anterior, and Posterior). Images with (top) and without (bottom) WGA overlay shown. Scale bars are 10 µm.

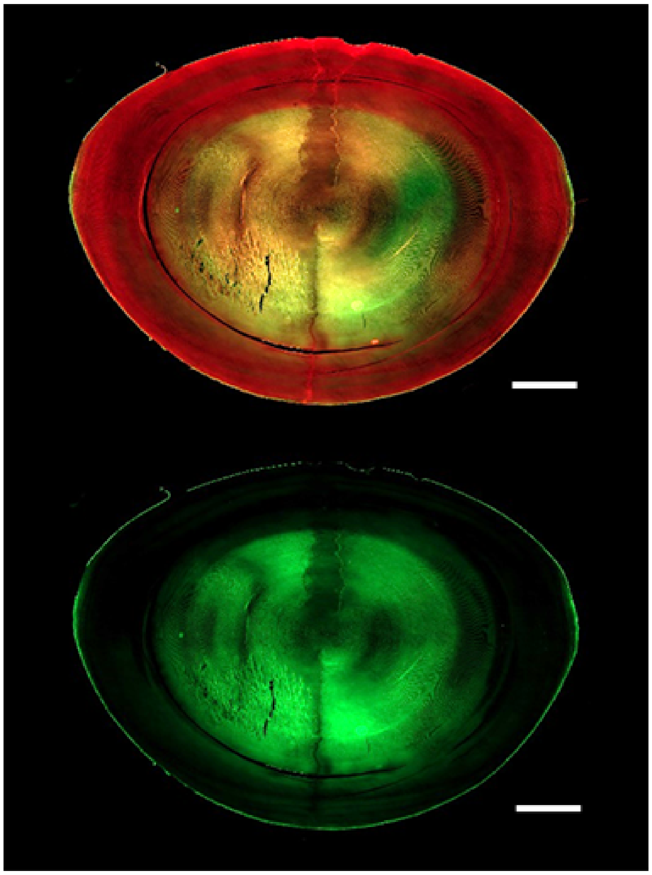

Figure 5-14 - AxioScan images of fixed lens with (top) overlay of glucose transporter 1 (GLUT1, green) and WGA stain and (bottom) exclusively GLUT1 stain. Scale bars are 2000 µm.

5.5. Discussion

In this work, we used spatially resolved proteomics to define proteins in the influx pathways of the lens microcirculation system. In addition to collecting tissue of varying proximity to the sutures, we made measurements at multiple depths to evaluate how protein networks along the suture change with proximity to the lens nucleus. With a high sensitivity MS-based proteomic measurement, we quantified 700 distinct proteins. Using a dimensional reduction approach, we demonstrate that the most significant change in protein network abundance occurs as a function of fiber cell growth layer and not as a result of suture proximity. Subsequent evaluation of differential expression between lens regions demonstrated that adherens junctions and CLIC5 are enriched in the outer suture tips relative to outer equator, that connexin proteins are not abundant on outer suture tips, and that GLUT1/3 proteins are enriched in inner sutures.

5.5.1. Canonical microcirculation influx

In this work, the inner growth layer of the lens was designated as the region where the extracellular space between sutures was decreased relative to the outer growth layers. We found that gap junction connexins GJA8 and GJA3 show trends toward equatorial enrichment in the inner growth layer of the lens. Though critical in establishment of MCS efflux current, depletion at the sutures suggests that connexins are unlikely to be involved in hemichannel uptake of non-specific substrates along the sutures in the inner lens fiber cells. Substrate-specific, ATP-independent channels and carrier proteins in the MCS, including aquaporins and solute carrier proteins, may be essential in lens transparency (Swarup et al., 2018); however, other substrate-specific transporters, such as GSH transporters MRP4 and MRP5 (Umapathy et al., 2013), rely on ATP or alternative energy sources for active transport across the plasma membrane. This ATP dependence highlights the importance of glucose delivery to the lens nucleus, where anaerobic glycolysis generates the required energy supply.

A second finding is that CLIC5, a chloride channel, is enriched in outer suture tips relative to equatorial counterparts. Though located throughout the fiber cell, it has been suggested that chloride uptake is primarily accomplished by suture-derived CLIC5 with supplemental uptake performed through the extracellular space between less mature fiber cells (Kuszak, Zoltoski, & Sivertson, 2004; Paterson, 1970). Aside from counterion balancing of cation circulation, the primary role of chloride in the lens is volume regulation (Mathias et al., 2007). Inhibition of putative CLIC5 channel results in damage to fiber cell morphology by water accumulation (Webb et al., 2004; Young et al., 2000). Therefore, it is anticipated that the suture plays a role in cellular volume regulation in addition to transparent structure generation and nutrient delivery to inner fiber cells (Kuszak, Zoltoski, & Tiedemann, 2004).

5.5.2. Spatial disruption of adherens junction complexes

Though adherens junction components ARVCF and CDH2 were enriched in the outer lens suture tips relative to the outer equator region, a congruent trend was not observed inner sutures of the lens. The importance of adherens junctions towards lens pathology has been supported by prior ARVCF knockout, where the mutant lens experiences cortical cataract after organ development (Martin et al., 2022). The loss of adherens junction enrichment in the suture likely reflects both cell-age-related protein loss and suture remodeling (Beebe et al., 2001; Cantrell & Schey, 2021b). In the chick lens, CDH2 is present only in immature fiber cells that have not yet formed sutures (Beebe et al., 2001). Conversely, actin-binding proteins vinculin and paxillin are most abundant in the mature, suture connected fiber cells. We did not measure either actin interacting protein here, however this may be a result of our fixed-tissue proteomics approach (Griesser et al., 2020). Further work should then be done to establish the functional impact of vinculin and paxillin on suture formation and fiber cell polarization as part of the focal adhesions complex (Turner et al., 1990).

5.5.3. Glucose transporter organization

A striking feature of differential expression between the inner suture tips and the outer suture tips was enrichment of GLUT1 and GLUT3 in the inner suture region. Additionally, posterior suture enrichment of each GLUT protein was observed relative to anterior suture tips. While typically studied as a glucose transporter, GLUT1 and GLUT3 have secondary specificity for dehydroascorbic acid (DHA), the oxidized product of antioxidant vitamin C (J. C. Lim, Caballero Arredondo, et al., 2020). The role of GLUT differential expression in the inner sutures may then have a role in either anaerobic glycolysis or redox homeostasis.

Delivery of glucose through the vitreous humor to the lens core is essential for preservation of anaerobic glycolysis, as previously reviewed (Kinoshita, 1965). The posterior-adjacent vitreous humor has a higher content of glucose than the anterior-adjacent aqueous humor (Chylack & Kinoshita, 1972), which may result in preferential positioning of GLUT transporters near the posterior suture relative to anterior suture. Interestingly, Zahraei et al. observed that lenticular glucose uptake first occurs at the equator of the lens, not at the anterior and posterior poles (Zahraei et al., 2022). However, this is anticipated in the short, 30-minute time-course measured by Zahraei as GLUT transporters are lower in abundance at the young suture. It is also possible that imaging mass spectrometry experiments used by Zahraei are limited by spatial resolution of available instrumentation. It is anticipated that in longer experiments, on the order of 4-hours as measured by Vaghefi et al. (Vaghefi & Donaldson, 2018), and with higher spatial resolution, glucose uptake could be mapped to the inner sutures.

Delivery of DHA to the lens nucleus in its native oxidized form is damaging to lens transparency, where oxidation eventually cause aggregated, light-scattering products (J. C. Lim, Caballero Arredondo, et al., 2020; Truscott, 2005). On its own, media supplementation of DHA to cultured rabbit lenses results in >50% decrease of GSH and 20-fold increase in oxidized GSH relative to control (Sasaki et al., 1995). However, lenses incubated in glucose and DHA-supplemented media results in only a 10% decrease in GSH content and 3-fold enrichment of oxidized GSH relative to control suggesting that DHA transport to the nucleus is not altogether cataractogenic. Oxidation of GSH is a result of DHA reduction to vitamin C, potentially upregulating activity of the pentose phosphate shunt in anaerobic glycolysis (Eggleston & Krebs, 1974; Fan et al., 2017). Therefore, the GLUT-mediated transport of both DHA and glucose has a putative role in generating antioxidant vitamin C, enhancing rate of anaerobic glycolysis, and regenerating GSH thereafter.

5.5.4. Antioxidant delivery

Oxidation is believed to be a key initiator of age-related cataract, perturbing protein folded state and solubility (Truscott, 2005). Glutathione and vitamin C are the predominant antioxidants in the lens, however the precise delivery mechanism of each to the lens nucleus is unclear (Umapathy et al., 2013). GLUT transporters are apparent transporters of DHA, which may be reduced to vitamin C *in situ* as previously discussed. However, the delivery mechanism for GSH remains unclear. Uptake of lenticular GSH is thought to be mediated by organic anion transporter 3 or sodium-dependent dicarboxylate transporter 3, not measured in the current study, but recently identified in a higher sensitivity measurement of the human lens (Cantrell et al., 2023).

Though unable to assign influx transporters for GSH, we did identify GCLC in all 24 samples within the study. While GCLC was more abundant in the outer fiber cells, we did measure GCLC as enriched in the inner posterior suture relative to the equator. Especially in nucleated fiber cells, synthesis of GSH is highly active. However, GSH is unlikely to travel retrograde to microcirculation current. Therefore, populations of antioxidants in the lens core must be synthesized *in situ* or delivered to the innermost lens fiber cells. Enrichment of GCLC in the inner posterior suture suggests that GSH synthesis may be more active in the posterior, where anaerobic glycolysis may also be enriched. It is then anticipated that *de novo* synthesis and subsequent antioxidative capacity is greater in the posterior suture entryway than in the anterior.

5.5.5. Generation of solute influx current

Prior work by Vaghefi et al. establish that small molecules substrates travel through extracellular suture space faster than passive diffusion alone (Vaghefi & Donaldson, 2018), suggesting molecular facilitation of influx. The key finding of GLUT enrichment in the inner suture space relative to outer suture and age-matched equator regions (A2/P2 relative to A1/P1 and E2, respectively) suggests a putative route of solute current generation. The extracellular space of lens tissue, the aqueous and vitreous humor, are rich in glucose relative to the inner nucleus. The osmotic differential across the lenticular fiber cell membrane may then generate an “osmotic funnel” of glucose from extracellular space to intercellular space. However, once glucose is delivered through the sutures to inner suture spaces, a transporter protein is required for cellular uptake of glucose. Once taken up, the MCS currents may deliver glucose or its metabolic byproducts throughout the entirety of the fiber cell or to progressively younger fiber cells (Zahraei et al., 2022). The osmotic gradient established between the humor and fiber cell cytosol is then preserved, allowing continued delivery and facilitated uptake.

5.6. Conclusions

To the best of our knowledge, this is the first study to analyze the proteome of suture tips and equatorial fiber cells of equivalent cell age. To evaluate spatial differences in protein expression, we measured fiber cell populations in two sample groups consistent with the cell-age-related narrowing of extracellular suture space. Principally, we find that the most significant change throughout the study occurred as fiber cells age. Novel, suture-specific changes were found for GJA8, CLIC5, GLUT1, GLUT3, and several other protein groups. We hypothesize that each of these proteins has a role in MCS influx through maintenance of an osmotic gradient for solutes such as glucose. Our results support previous findings that suggest CLIC5 is responsible for chloride influx at the outer anterior suture. Finally, measurement of GLUT1 and GLUT3 as enriched in the inner suture space suggests a role in DHA and glucose delivery to the inner-most fiber cells. As a result of aqueous and vitreous humor glucose concentration relative to fiber cell concentrations, it is hypothesized that osmotic pressure results in funneling of glucose and potentially other nutrients to the lens inner nucleus to establish influx currents in the lens.

6. CHAPTER 6

SUMMARY AND FUTURE DIRECTIONS

6.1. Summary of key findings

In this thesis, MS proteomics methods have been used to measure the lens proteome, especially as it relates to fiber cell aging, human aging, and organization of MCS. Prior to this work, DIA methods had not been applied to the lens, and studies towards the spatial organization of the aging lens were not capable of measuring low abundance proteins measured by DIA exclusively. Several studies had established the importance of crystallin removal from the lens to identify low abundance proteins, and others had used multidimensional chromatography to enhance accessibility to low abundance proteins not typically measured with co-eluted with crystallins. Further, many of the studies that had evaluated the lens proteome on high-resolution instrumentation did so on non-human tissues. Thus, a key goal of this dissertation work was to implement state-of-the-art analytical methods to enhance coverage of the human lens and use the rich resulting dataset to better characterize biological changes in the lens, especially related to cataract formation and establishment of the MCS.

In this work, we used low-resolution linear ion trap instrumentation to optimize sample preparation methods before proceeding to high-resolution instrumentation for quantitative comparisons. Using membrane solubility fractionation, on-filter digestion of precipitated proteins, and BRP fractionation, more bovine lens proteins were identified than possible with prior methods. Further, the in-house developed BRP method exceeded commercial options for BRP fractionation by using readily accessible materials. Next, a more modern search algorithm, MSFragger, was adapted from a high-resolution specific identification algorithm to one capable of identifying low-resolution data from the utilized Velos Pro linear ion trap instrument. Though attempted, the MS1-based quantitation algorithm implemented by FragPipe was not able to be adapted for this low-resolution dataset. Altogether, this work demonstrated the utility of low-resolution instruments in sample preparation optimization in pilot experiments before proceeding to high-resolution instrumentation.

After optimizing sample preparations and instrumentation methods, an 18-year-old lens was used to evaluate optimized methods for quantitation of lens lysates without BRP fractionation. DDA and DIA methods were used on the state-of-the-art Exploris 480 orbitrap instrument. In that study, it was clear that DIA performance exceeds the identification abilities of DDA, and that library-free DIA analysis is a robust method for identification of lens proteins without modifications and with deamidation modifications. After acquisition of that dataset, a new pipeline for the analysis of DIA data was developed implementing tools for statistical comparisons and using ontology tool sets whose underlying assumptions matched those of a proteomics experiment. Finally, changes associated with fiber cell aging were delineated, extracting known lens biology, and assigning greater molecular detail to the changes with cell age.

A second approach to DIA proteomics built on the findings of the prior study, expanding the sample cohort from a single human subject lens to sixteen healthy lenses, ranging from 15-74 years of age. In response to changes in instrument firmware, a new method was developed for this analysis that enabled identification of marginally fewer proteins than previously demonstrated. Nonetheless, sufficient proteins were measured to annotate proteome changes at a depth never achieved with DDA methods. Contrary to research towards lens fiber cell aging, investigation was done towards specific fiber cell population changes with age. It was then discovered that a proteome remodeling event occurs at approximately 50 years of age. Associated with this event, GJA8, AQP5, and SLC24A2 showed distinct decreases in abundance with implications of each in MCS inhibition. Though not discussed in the manuscript, MAP4K4 demonstrated a significant ($p < 0.01$, Log2FC >2, Wilcoxon t-test) increase in the old cortex relative to young cortex while HSPB3, RTL8C, and MAIP1 showed significant age-related increases in the inner nucleus. No protein increased in abundance with age in the outer nucleus. Manual evaluation of HSPB3 abundances demonstrates that it is a high abundance heat shock proteins with trends towards significant changes as a function of the 50-year threshold set in this study. However, greater dispersion of abundance was observed for younger lenses, suggesting that its abundance increase is not necessarily correlated with the remodeling event measured, and may belong to an alternative aging process. Further studies, including imaging mass spectrometry, could be done to spatially evaluate the abundance of HSPB3 as a function of position within the lens and human age. The presentation of these findings also highlighted the presence of several transporters of GSH and GSH-utilizing proteins which may be bound to the plasma membrane as part of oxidative stress response. Statistical enrichment at the ontology level and at the single-protein level demonstrate that there is need to functionally evaluate the role of calcium signaling in lens aging and the effects of metabolite concentration changes in the lens with age.

The final approach used in this work was focused on measurement of proteomes differentially present at the suture tips relative to the equator. Prior work had been done to identify CDH2 and ARVCF among protein enriched at the suture relative to non-suture fiber cells, but depth of approach was enhanced by implementation of a fixed-tissue DIA method and by measuring proteins at multiple depths along the suture. In brief, a limiting quantity of proteins was identified due to tissue fixation, which was essential to maintain cell morphology. The quantitative profile of the measured proteins clearly demonstrated that the most significant changes in the lens proteome are related to aging and not to position along the length of the fiber cell. However, consistent with prior studies, adherens junction networks were found enriched in the outer suture relative to the age-matched equatorial fiber cell. In the inner suture, adherens junctions are not enriched, however a surprising enrichment of SLC2A1 and SLC2A3 (GLUT1/3) was measured relative to the equator. This suggested that adherens junctions are less essential to maintenance of fiber cell suture structure in cells where the extracellular space is reduced. Additionally, that glucose uptake may be preferred in the lens nucleus along the suture to direct anaerobic glycolysis towards the most metabolically inactive fiber cells. There may also be a role of GLUT1/3 in taking up dehydroascorbic acid before it is putatively reduced by GSH, but reduction mechanism of the oxidized antioxidant cannot be clearly assigned. GLUT-mediated influx may be partially responsible for lens osmotic regulation and oxidative stress response. Additional changes included depletion of connexin 50 along the suture relative to the equator, especially in outer growth layers, and enrichment of CLIC5, TMEM47, and GCLC in outer sutures relative to the equator.

Successful completion of each aim resulted in a more intricate description of the lens MCS organization and how efflux mechanisms along the lens equator are regulated as a function of human and fiber cell age. A hallmark of high-sensitivity proteomics, several proteins including SLC24A2, AQP5, GLUT1, GLUT3, and CLIC5 were identified as transporters that may play a role in MCS function. However, discovery of spatial organization of these proteins leads to further questions about functionality in the metabolically inactive lens. Studies to this end must be done before assigning biological certainty to results. Additional mass spectrometry proteomics approaches are also desirable, both to enhance the current methods and to determine primary structure of proteoforms not accessible in a discovery proteomics assay. Successful completion of these studies would provide a more complete representation of functional regulation of MCS in context of age-related perturbation. Though no work was directed towards cataract lens proteomics in the current work, it is suggested that ongoing modification of the lens proteome manifests as ARNC, and so the pathways regulated here undergo continued damage before aggregate-caused light scattering occurs.

6.2. Proposed future directions

In response to findings of aim 1 and aim 2, three multipart studies should be completed to 1) further enhance methodological advances of DIA-MS in an expanded cohort of aging human lenses, 2) assess functionality of protein networks that were measured as differentially expressed in the lens, especially those outside of the canonical MCS model, and 3) implement alternative mass spectrometry approaches to characterize aquaporin-5 truncation, transcriptional response under oxidative stress, and further improved measurement of transporters along the lens suture.

6.2.1. Methodological and cohort advancement for measurement of lens aging and cataract development

In aim 1, multiple methodological improvements were made from sample preparation to analytical approach to evaluate the aging human lens proteome. Instrumental acquisition improvements were made, allowing >250% increase in proteins and peptides measured in all samples respective to equivalent DDA methods and >500% improvements over previous approaches, with earlier high-resolution instruments and different preparative approaches (Cantrell & Schey, 2021b; Z. Wang et al., 2013). By extending the highly sensitive DIA approach to 16 human lenses, age-related inferences were made towards changes in the aging lens and in response to human aging. Nonetheless, several limitations were observed in this approach or progress made in the field that enhances capabilities in future studies. Overcoming shortfalls of the presented study should be done by assessing appropriate instrumentation for DIA reproducibility, using a novel search approach for PTM inclusion in DIA search, and incorporating best technical methods in an enhanced cohort to allow regression modeling of aging in healthy human lenses and classification with feature selection methodology in comparison of age-matched healthy and cataractous lenses.

If each of these strategies are effective, proteins in the lens will be more rigorously quantified in shorter acquisitions, searched with incorporation of PTMs, and modeled with multiple machine learning approaches for more sensitive identification of proteins and protein networks that are changed with age and cataract formation. Additionally, evaluation of modifications that occur on the proteins changed with age or cataract may lead to future functional studies that putatively contribute to cataract formation.

Assessment of instrumental approaches for reproducible DIA

A challenge of all orbitrap mass analyzer experiments is the transient time needed to resolve fragment peaks at sufficient resolution. While DIA rapidly scans all theoretical fragments by narrowing the mass range to maximum likelihood peptides, it must do so at sufficient resolving power to separate multiple peptide spectra in subsequent search (Venable et al., 2004). Full scan cycles may then take 2-4 seconds depending on method setup (Searle et al., 2020). Coupled to nLC systems, single peptide elution profiles spanned 9 – 45 seconds in presented experiments, with most peptides eluting in less than 15 seconds. This results in 4-6 scans per peptide as implemented here, sufficient for reproducible spectra as demonstrated by Searle et al (Searle et al., 2020). This also comes at the cost of 95-minute LC gradients, limiting throughput to approximately 9 samples per day with appropriate column wash. As presented in chapter 1, TOF instrumentation is an attractive approach to decrease scan cycles to <200 ms, decreasing the necessary time for sampling 4-6 peaks to approximately 1 second (Aballo et al., 2021). Current approaches with diaPASEF or qTOF instruments in DIA may run 15–30-minute gradients which compress peptide elution profiles 2.5-6-fold. Nonetheless, LC gradient compression on 200 ms scan cycles may result in up to 200% increase in scans per peptide, putatively leading to more reproducible measurement with better determination of peak shape for area under curve integration. Up to 18 samples may be measured per day with this approach. Dual-bore or dual-trap chromatography may improve this throughput to >36 samples per day but comes at the cost of chromatographic variability with analytical column trapping and is beyond the scope of comparison (Kreimer et al., 2022).

To assess TOF implementation, lens lysates as prepared in aim 1 should be measured as suggested by Meier on a timsTOF (Meier et al., 2020) or Messner on a qTOF (Messner et al., 2021). It is anticipated that more identifications can be made within TOF approaches, but more important to assess the reproducibility of measurement. For undigested protein from protein preparations, technical replicates of digests should be performed for several samples to determine peptide intensity CVs on both Exploris and TOF systems. Pino et al. suggest that increase of MS2 scans from four to eight results in 15-fold reduction of integration error in 95% confidence interval (Pino et al., 2020). Incorporation of this instrumental setup is then suggested for further experiments. For further suggested experiments, it is noted that DIA-NN and MSFragger are the only suitable academic-use search approaches for diaPASEF data at time of writing and that EncyclopeDIA does not support the PASEF data to improve identification and q-value estimation.

Incorporation of post-translational modifications in DIA

A key development in aim 2 was the incorporation of spectral and chromatogram libraries to DIA search. Spectral libraries are conventionally compiled from empirically derived spectra, DDA or DIA, and used as a reduced search space database for complex DIA spectra. While library-free approaches have emerged (Demichev et al., 2020; Gessulat et al., 2019), no method is optimized for incorporation of all user-defined PTMs to the spectral library. To address this, MSFragger DIA search uses a true spectrum centric search where an empirical spectral library is not generated, and mass offsets are instead studied (Kong et al., 2017). This approach may be successful in the future but requires significantly more demanding computational resources than other tools and while specific, PSM q-value estimation is empirically indeterminate at the time of writing. Therefore, it is suggested that the enhanced instrumentation approach described above be used to establish an appropriate spectral library.

In aim 2, a spectral library was compiled from a filtered DIA-NN empirical library, DDA of representative samples and GPF-DIA data. While modifications were not discussed, this was effective in the identification of deamidation, N-terminal acetylation, and non-methionine oxidations among other non-preparatory PTMs. In the human lens, it is expected that the proteoform-ome is densely populated and homogeneity cannot be assumed between young fiber cells and old fiber cells. Thus, spectral library generation for PTM analysis should group lenses lysates into multiple age-grouped fiber cell populations. Re-implementation of the spectral library generation method in aim 2 is not appropriate for this approach as spectral library generation time and instrumental cost will rapidly reach that of the sample cohort in whole (*Samples for Spectral library = number of groups * (6 + number of samples per group)*). Additionally, DDA data does not resemble that of DIA data since

DIA assumes a +3 charge state while charge detectors can assign a more appropriate normalized collision energy to isolated peptides (Pino et al., 2020). Instead, it is suggested that GPF-DIA be used for each group and that the data be searched in DIA-NN in library-free search and again in DIA-Umpire for pseudo DDA spectra generation and PTM identification. Result files from each algorithm should be compiled to one spectral library, searched in a separate program such as EncyclopeDIA for final match of empirical PSMs and quantitation. If successful, incorporation of PTM analysis into DIA may improve biological relevance, especially in highly modified protein lysates such as the lens. In context of lens biology, it is anticipated that previously unmeasured non-methionine oxidations are increased in older lenses, as demonstrated by Schey and Finley (Schey & Finley, 2000).

Expanded cohort approach for age regression and cataract classification

A limitation of the current study, tissue procurement was slowed by conditions of the COVID-19 pandemic. While sufficient samples were measured to identify the proteome remodeling event, further sampling is required to define statistical change at fifty years of age with greater statistical power than achieved here. Additionally, incorporation of more samples may allow more rigorous statistical evaluation of age-related changes in the lens by using a regression approach. In the current cohort, incorporation of model flexibility will result in undue regression bias. A more flexible model will allow greater definition of age-related changes. For example, calcium cation concentration follows a clear parabolic curve in the lens with a minima at fifty years of age (Tang et al., 2003). However, the proteome as described here undergoes a switch-like or piecewise linear peak shape. Time course plotting of calcium abundance in the lens does not support this claim and instead suggests a quadratic model may be more appropriate (Tang et al., 2003).

After expanding the healthy lens cohort, inclusion of cataractous samples is suggested to enhance evaluation of the lens proteome. While brunescent browned lenses were incorporated in Aim 1, opacified lenses were not. It is suggested that a change occurs in the lens proteome between aged healthy and age-matched cataractous lenses that results in opacification. Thus, an equivalent methodological approach is suggested to identify proteoforms and subsequent modifications that are unique to the opacified lens and develop a model for classification of healthy and cataract lens. Development of the regression model to further characterize aging and classification of cataractogenesis features then serves as a robust machine-learning approach to quantify changes at the global proteome scale.

6.2.2. Directed assessment of differentially expressed protein networks in aging and spatially differentiated fiber cells

As demonstrated in each aim and in potential impact of cohort expansion, protein networks have been measured as changed with age or position along the fiber cell with respect the sutures, yet functional studies were not done to validate assignments. Anucleate fiber cells are metabolically less active and functional validation must be done to characterize assigned changes. Results from measurements of aging human lenses and in positioning along the length of the fiber cell suggest that calcium-associated proteins, whether transporters or calcium-dependent for function, undergo abundance decline with age. Additionally, glucose transporters GLUT1 and GLUT3 were identified as suture enriched in the inner bovine lens suture. To characterize these proteins, previously used methods in the lens should be applied to define spatial positioning of SLC24A2, evaluate directionality of calcium convection in MCS through SLC24A2, characterize fiber cell organization and geometry under elevated and depleted calcium incubation, assess affinity for substrate-specific uptake of glucose and dehydroascorbic acid through the suture, and evaluate reliance of MCS on GLUT1/3 function. If all experiments are successful, significant advances will be made to identify the role of SLC24A2, GLUT1, and GLUT3 in lens homeostasis.

Definition of SLC24A2 localization in the lenticular fiber cell membrane

Perhaps the most interesting novel molecular differentiation occurring in aim 1, SLC24A2 was identified as a differentially expressed, calcium transporter in the lens. It is not anticipated that this transporter contributes to calcium-induced organelle degradation but that it is instead decreased with age to result in inhibited calcium export through the lens MCS. Therefore, confirmation of SLC24A2 distribution throughout the lens with age is desired in addition to evaluation of hexagonal fiber cell plasma membrane localization.

To accomplish spatial validation of SLC24A2, it is suggested that immunofluorescence methods be performed on young, middle aged, and old human lenses with and without cataract. Extension of methods for AxioScan imaging as presented in aim 2 shows utility of whole lens section imaging. Qualitative assessment can then be done to confirm the finding that nuclear SLC24A2 is decreased in the old lens. In further support of the role of SLC24A2 in calcium export from the lens, confocal imaging as presented in Aim 2 should be used to define if SLC24A2 is more associated with the broad or narrow side of the membrane, visualized in sections captured along the equatorial axis. If found to associate closely with the broad side of the membrane as does connexin proteins, it is inferred that SLC24A2 contributes to calcium ion removal from the lens and suggested by directionality of MCS current. If localized along the narrow side, no clear role emerges for the transporter. Solute carrier proteins are not intracellular transporters, but some extracellular space exists between fiber cells that may accumulate calcium before being transported across the plasma membrane of adjacent fiber cells. Since SLC24A2 was measured in the equatorial section of the lens in aim 1, it is anticipated that intercellular transport is mediated by SLC24A2. Functionality of SLC24A2 under this intercellular model must be evaluated, but age-related reduction of fiber cell extracellular space may play a role in functional and total protein decrease in nuclear fiber cells with age.

Identify directionality and extent of calcium convection via SLC24A2 in MCS

Consistent with the directionality of MCS current, it has been assumed to this point that calcium experiences influx through the sutures and export through the cross section of fiber cells, from the broad side of the plasma membrane (Schey et al., 2017; Vaghefi & Donaldson, 2018). Functionally, SLC24A2 transports 1 Ca^{2+} and 1 K^+ in exchange for 4 Na^+ (Prinsen et al., 2000). This results in a net charge accumulation on one side of the plasma membrane, and if directionality of Na^+ current is preserved, it is anticipated that calcium then travels in the opposite direction of MCS. A transporter for chloride counterion uptake may be paired to this mechanism but was beyond the scope of the current study. In identification of SLC24A2 decline, SLC30A1 was also identified as significantly decreased in abundance in the lens nucleus. Interestingly, zinc transporter SLC30A1 has a secondary role in prevention of zinc influx (Segal et al., 2004). It is then imperative to not only classify the localization of SLC24A2, but also its functional direction.

To determine directionality of SLC24A2 calcium transport, the intact lens should be measured for efflux and influx of calcium. To date, no small molecule inhibitor of SCL24A2 has been made commercially available and biologic antagonists are not small enough to cross the capsule in a tissue culture experiment. If a small molecule inhibitor were to become available, incubation in artificial aqueous humor with and without inhibitor could be done, with readout by imaging laser ablation inductively coupled plasma MS. Cell culture in isotopically labeled calcium would allow direct measurement of intake in culture and subsequent assignment of ion movement if experiments are done in time course. Alternative methods for calcium isotope imaging includes autoradiography (Purdy et al., 1996), though at lower resolution than an IMS approach. Efflux may alternatively be measured through Ussing-type chamber experiments after incubation in drug or vehicle treated culture. Net calcium efflux can then be measured with a colorimetric calcium assay. Effectiveness of this approach assumes that calcium uptake mechanism is independent of efflux and that uptake mechanism is not inhibited by an SLC24A2 inhibitor.

Aside from direct measurement of cultured lenses, genetic mutation of SLC24A2 may be done to determine the physiological effect of SLC24A2. To inhibit functionality, point mutations in the binding pocket are suggested, as previously demonstrated by Parry et al. on Glu188 and Asp548 (Parry et al., 2013). Prior site-directed mutagenesis of γ-crystallins has been successfully performed in the zebrafish lens, supporting its use in SLC24A2 studies (S.-Y. Wu et al., 2016). Physiological assessment may then be done by a fundoscopy approach. If based on directionality of MCS sodium ion current and the role of SLC24A2 and SLC30A1 in other cell systems, it is hypothesized that SLC24A2 plays a protective and calcium export role until its degradation whereby accumulation of calcium is then allowed to occur in the lens. This would represent an example contradicting the standard hypotheses of MCS that molecules may be exported from the lens sutures instead of imported. If successful, this approach will identify the directionality of calcium transport in the lens as modulated by SLC24A2 and define the physiological significance of its inactivity in homeostasis.

Fiber cell organization and geometry under calcium treatment

A key finding of aim 2 was that adherens junction assembly was enriched at the outer suture tips relative to the age-matched equator. As discussed in chapter 5, a recent study by Martin and colleagues demonstrated that ARVCF, a member of the catenin family, is essential for lenticular fiber ball-and-socket structure and adherens junction stability (Martin et al., 2022). Under ARVCF knockout conditions, cortical cataract forms within 6 months, hexagonal fiber cell lattice organization is disrupted, cadherin nanocluster size is decreased, while N-cadherin, αN- and β-catenin are delocalized from the plasma membrane. This finding provides clear evidence that adherens junctions are essential to the establishment of fiber cell organization at and away from the suture tips. To further evaluate the role of calcium transport in the lens, culture in calcium rich and depleted environments is suggested for evaluation of adherens junction. It is hypothesized that there is a necessary balance of calcium in the lens, where calcium mediates the assembly and integrity of adherens junctions. Simultaneously, excess calcium may result in the activation of CaM inhibition of square junctions and activation of UPS and calpain proteases. It is expected that calcium treatment then leads to inhibition of fiber cell permeability as suggested in aim 1.

To assess fiber cell organizational integrity, electron microscopy experiments as used by Martin et al. is suggested in addition to confocal imaging to evaluate plasma membrane organization and spaces between fiber cells (Martin et al., 2022). The observation of fiber cell organization at the suture tip will characterize the role that adherens junction have on the tight packing of sutures, and any structure deformations at the suture. To evaluate results of increased calcium treatment, similar imaging should be done alongside proteomic measurement of truncation products and quantitative evaluation of α-crystallin chaperone concentration. Decreased abundance of α-crystallin may result in degradation of the proteostatic state and induction of cataract after the binding capacity of remaining α-crystallin is reached. If successful, this experiment will further support the significance of lenticular adherens junction in fiber cell organization and quantify the effect that calcium treatment has on proteasome-mediated degradation or protease activity on other proteins.

Uptake of glucose and dehydroascorbic acid through suture localized GLUT1/3

A key finding of enrichment measurement in aim 2 was that GLUT1/3 are enriched in the inner sutures, especially in the posterior of the fiber cell. This suggests a mechanism for the influx of either glucose or dehydroascorbic acid through the suture space to the nucleus, delivering glucose for anaerobic glycolysis *in situ* or an oxidized form of vitamin C which is readily reduced in presence of GSH. The functionality of GLUT1 may be assessed with the inhibitor fasentin (Wood et al., 2008) and GLUT3 functionality assessed with inhibitor G3iA (Iancu et al., 2022, p. 3). To establish, cultured incubation in presence or absence of inhibitors should be done. Imaging of GLUT related substrates is aided by method development related to GLUT1/3 enrichment in cancerous cells (Iancu et al., 2022; Wood et al., 2008).

Imaging of glucose uptake is readily achieved with co-incubation in isotopically labelled fluorodeoxyglucose followed by positive emission tomography (PET) imaging (Croteau et al., 2016). The rate of accumulation can qualitatively be assessed from time-course experiments accompanying an initial imaging experiment. Concurrently, C11 vitamin C and C11 dehydroascorbic acid can be generated for PET (Carroll et al., 2016). As with glucose transporters, the rate of transport of vitamin C and dehydroascorbic acid can then be determined. Further studies into GSH generation concurrent to reduction of dehydroascorbic acid are beyond the scope of study here but may be essential to describing another route of antioxidant generation in the lens.

As a live imaging technique, PET may subsequently be used to characterize rate of glucose transport through the suture. It is anticipated that some glucose taken up by the equator as shown by Zahraei et al. (Zahraei et al., 2021), thus consideration of glucose current in the lens and its delivery to each various growth layers should be done independent of the peripheral cortex. To add relevancy to evaluations of glucose uptake, incubation should be attempted in an artificial vitreous media or at least a hyperglycemic media to better represent glycemic pressure experienced by the posterior of the lens (Chylack & Kinoshita, 1972; Davies et al., 1984; Zilg et al., 2009). Incubation of the anterior pole in a hyperglycemic media may result in a diabetic cataract model (Davies et al., 1984), suggesting that longer incubations may not be possible in such a media if it is not possible to sequester the anterior from the posterior pole. As a possible solution, incubation of the lens in an Ussing-type chamber or some chamber where lens regions are separated by an O-ring may allow simultaneous incubation of the anterior in artificial aqueous humor and posterior in artificial vitreous humor. Throughout the proposed experiments, it is anticipated that the uptake of glucose and dehydroascorbic acid is most rapid through the inner suture to allow delivery of nutrients to the nucleus.

6.2.3. Further mass spectrometry methods for annotation of lens homeostasis

While discovery-scale proteomics methods such as those employed in aim 1 and 2 lead to many future studies, three distinct questions arose from presented data that could be answered by alternative mass spectrometry approaches. First, how is aquaporin-5 truncated, and is there a functional consequence for its water permeability thereafter? Second, how does oxidative stress induction alter control of transcription and protein synthesis in germinative epithelial cells, and third, what additional transporters are accessible to measurement in the lens suture?

Aquaporin-5 truncation and functional consequence

Protein truncation has previously been established to occur on critical components of the MCS including AQP0, GJA3, and GJA8 (Korlimbinis et al., 2009; Slavi et al., 2016; Srivastava & Srivastava, 2003; L. J. Takemoto, 1995; Wenke et al., 2015). In evaluation of protein degradation as part of human aging, AQP5 abundance undergoes an age-related decline that is inconsistent with the accumulation of deamidation. This suggests that degradation or an unmeasured modification such as truncation occurs on AQP5. To date, several AQP5 sites have been reported (Schey et al., 2022). Consistent with western blot results, AQP5 undergoes minor C-terminal truncation in the lens core (A. C. Grey et al., 2013; Petrova et al., 2015). Using highly sensitive mass spectrometry techniques, some truncation of AQP5 at residues F199, T264, D248, D246 and E244 in the human lens core can be detected (Schey, unpublished data). The functional consequences of AQP5 truncation have not been studied, but loss of the major AQP5 phosphorylation site (T259) is expected to have functional consequences in regard to protein interactions. In support, the C-terminal peptides GTYEPDEDWEEQR and GTYEPDEDWEEQREER show low abundance in the old inner nucleus if measured, while an 8-fold or greater abundance is measured in the cortex. It is anticipated that truncation occurs on AQP5 as a function of age concurrent to AQP0 truncation. To investigate, lysate from the oldest inner nucleus samples should be measured by DDA after tryptic and non-tryptic digest. Complimentary digestion approaches may provide support that this peptide is indeed not measured (relative to positive control young cortex lysate) (Choudhary et al., 2003). Site or sites of modification may be further defined with a semi-specific search. Consistent with AQP0 and presented data, it is expected that AQP5 undergoes C-terminal truncation.

The functional consequence of AQP0 truncation was originally thought to be a decrease of water permeability by correlation with barrier formation (Korlimbinis et al., 2009), however C-terminal truncation products to 1-243, 1-246, 1-249, and 1-259 demonstrate sustained functionality (S. Kumari & Varadaraj, 2014). The aforementioned peptide begins with G241, so functional consequences should not be inferred based on the functionality of AQP0. Instead, the functionality of identified truncation sites should be assessed by following methods of Kumari and Varadaraj (S. Kumari & Varadaraj, 2014). Briefly, site-directed mutagenesis protein constructs should be transfected in a model system such as xenopus oocytes. After expression, osmotic swelling assays should be performed to evaluate water permeability. An alternative methodological approach may be similar to that of Yang and colleagues (B. Yang & Verkman, 1997, p. 5). It is anticipated that AQP5 truncation, if functionally deleterious, is inhibitory to MCS current as a result of cataract induction in the AQP5 knockout model (Sindhu Kumari & Varadaraj, 2013). Therefore, successful completion of this study may result in a future technique to evaluate age-related truncation of AQP5 while simultaneously assessing the functional consequence of truncation of MCS current generation.

Transcriptional and proteomic profiling of oxidatively stressed germinative epithelial cells

The work in aim 1 was directed towards measurement of the proteome state in anucleate fiber cells as a consequence of age. These fiber cells undergo substantial modification and there are progressive physiological consequences. What was not evaluated was how transcriptional control is regulated by induction of oxidative stress to lens epithelial cells. Several studies have been done towards the transcriptional and proteomic control of oxidative stress induction in a human lens epithelial culture model, however, tissue-derived measurements have not been made (Nagineni & Bhat, 1992; Paron et al., 2004; Kubo et al., 2010; S. Wang et al., 2022). To accomplish this, a lens culture system should be optimized for human or other model organisms with incubation in artificial aqueous humor. It is most desirable to leave ciliary fibers intact in culture to avoid TRPV1/4-controlled hydrostatic stress response upon severing (Delamere & Shahidullah, 2022; Nakazawa et al., 2021). Cultured lens models could then be compared upon treatment with vehicle and an oxidative stress inducing drug such as tert-butyl hydroperoxide. To cease drug treatment prior to non-physiological damage, the lens should then be washed and frozen. Using a similar method to aim 1, an equatorial disk should be collected where only the cross section of fiber cells and the germinative epithelium surrounding them remains. If thawed in a walk-in refrigerator, the capsule and adjacent monolayer germinative epithelium can then be separated from the fiber cell population. Transcriptional and proteomic profiling should then be done to evaluate the change induced by oxidative drug treatment in this system. To evaluate the validity of cell culture models, an equivalent experiment should be done to assess biological consistency. The penetrance of drug to fiber cells under such a model has not yet been evaluated but should be measured by shaving the outermost fiber cells from the unencapsulated fiber cell disk. Consistent with lens biology and results in aim 1, it is anticipated that a transcriptional response is active *in vivo* and that the predominant transcripts differentially expressed are α-crystallin and antioxidant response elements of Nrf2 transcriptional activation including glutathione synthase, GCLC, glutathione-s-transferase, glutathione peroxidase, heme oxidase 1, and superoxide dismutase (Ferreira et al., 2018, p. 2; Y. Huang et al., 2022, p. 2; Q. Ma, 2013, p. 2). It is also anticipated that metabolism and subsequent activity of Na/K ATPases and MCS current are upregulated. MCS current enhancement should be evaluated using Ussing-type chamber experiments. Successful completion of these experiments will allow evaluation of the cell culture system validity, particularly under oxidative stress induction, provide a druggable model for lens culture for transcriptional control in the outermost cortex, and provide further insights towards the relationship of transcriptional control in oxidative stress and MCS activation.

Enhanced measurement of transporters in the lens suture

Building on results from aim 1 and aim 2, the limitation of few proteins measured in the fixed lens suture should be addressed. In aim 2, only 700 proteins were measured and while this was a substantial improvement over the approximate 300 measured in comparable DDA methods, this fell short of the multiple thousand proteins measured in human lenses in aim 1. Further measurement of the lens suture proteome is desirable because nutrient influx proteins remain unidentified in the sutures. Specifically, the influx of GSH, sodium, and calcium remain of great interest. Proteins of ongoing interest include SLC24A2, OAT3, NaDC3, MRP4, MRP5, XCT, 4F2, and SVCT2. The functions of these proteins are listed in table 4-1. It is not anticipated that substrate specific transporters of these nutrients will be measured with alternative mass spectrometry methods with equivalent preparations. However, it is possible that incorporation of membrane enrichment by urea solubilization will increase the likelihood of transporter measurement. The rationale for not including the proposed enrichment in the current study was that fractionation removes approximately 95% of lens protein (Z. Wang et al., 2021). Collection of tissue by LCM remains the limiting aspect of this approach, where the majority of lens sections do not dry in flat sections or fail to exit the LCM PEN membrane slide if water is trapped beneath the section when tissue is wet mounted. As an alternative to discovery proteomics, a targeted assay may be appropriate to identify several measurable peptides from a bulk fixed tissue sample preparation. Alternatively, the measurement of low abundance proteins may be boosted by a carrier channel as demonstrated in single-cell proteomic approaches (Budnik et al., 2018). By introducing a urea-insoluble fraction of the membrane proteome as a carrier channel, the ion selection and quantitative measurement of low abundance peptides may be possible along the suture without sample fractionation. Naturally, it is hypothesized that each of the proteins of interest are enriched in the suture, but measurement to this end may find that several of these proteins are suture depleted, as was GJA8. This may be an indication of influx to the lens nucleus by an alternative route to the suture-directed influx. It may also be found that GSH, vitamin C, cysteine, glycine, and glutamate are delivered to the lens nucleus by a substrate-unspecific method. If successful, this approach would allow quantitation of select proteins potentially implicated in MCS influx.

In conclusion, this work has identified protein networks that are regulated by fiber cell age, subject age, or positioning along the length of the fiber cell with respect to the sutures. This work resulted in the most-in-depth analysis of any lens proteome, including proteins involved in MCS current establishment and age-related regulation. Significant further studies should be performed to characterize function of the measured protein networks, allowing more clear definition of the link between protein presence and function. The result of studies that come from the presented work may lead to enhanced understanding of ARNC formation and possible targets for development of an antagonist to cataract formation.

APPENDIX

A. Table of ontological enrichment between the cortex and inner nucleus, measured with DIA analysis

Complete list of ontologies (n=206) enriched in either the cortex or inner nucleus over the other region. Ontology calculations performed by PSEA-quant with CV tolerance 0.5, 10,000 iterations used for p-value calculation. DIA data was used to perform these calculations.

GO Term	Annotation	PES	p-value	Proteins in Set
	Enriched in Cortex over Inner Nucleus			
GO:0006886	Intracellular protein transport	132.798	<1.0E-4	207
GO:0005518	Collagen binding	8.166	<1.0E-4	10
GO:0019058	Viral life cycle	47.577	<1.0E-4	61
GO:0045047	Protein targeting to ER	48.341	<1.0E-4	62
GO:0071840	Cellular component organization or biogenesis	436.404	<1.0E-4	731
GO:0015075	Ion transmembrane transporter activity	48.948	<1.0E-4	70
GO:0016032	Viral process	137.269	<1.0E-4	219
GO:0006605	Protein targeting	73.126	<1.0E-4	103
GO:0005788	Endoplasmic reticulum lumen	21.232	<1.0E-4	28
GO:0006810	Transport	383.795	<1.0E-4	630
GO:0043230	Extracellular organelle	34.137	<1.0E-4	49
GO:0000956	Nuclear transcribed mRNA catabolic process	55.991	<1.0E-4	79
GO:0034655	Nucleobase-containing compound catabolic process	125.115	<1.0E-4	191
GO:0043062	Extracellular structure organization	49.858	<1.0E-4	68
GO:0006612	Protein targeting to membrane	57.925	<1.0E-4	76
GO:0015078	Proton transmembrane transporter activity	16.387	0.0001	22
GO:0015077	Monovalent inorganic cation transmembrane transporter activity	24.829	0.0001	35
GO:0045259	Proton-transporting ATP synthase complex	7.105	0.0001	8
GO:0031410	Cytoplasmic vesicle	105.704	0.0001	168
GO:0009056	Catabolic process	288.440	0.0001	481
GO:0044248	Cellular catabolic process	238.114	0.0001	394
GO:0005759	Mitochondrial matrix	31.201	0.0001	46
GO:0015985	Energy coupled proton transport, down electrochemical gradient	5.270	0.0002	6
GO:0015986	ATP synthesis coupled proton transport	5.270	0.0002	6
GO:0009146	Purine nucleoside triphosphate catabolic process	50.143	0.0002	78
GO:0032774	RNA biosynthetic process	114.369	0.0002	183
GO:0042625	ATPase-coupled ion transmembrane transporter activity	13.749	0.0003	19
GO:0001501	Skeletal system development	11.825	0.0003	16
GO:0042776	Mitochondrial ATP synthesis coupled proton transport	5.270	0.0003	6
GO:0046130	Purine ribonucleoside catabolic process	51.183	0.0003	80
GO:0097485	Neuron projection guidance	61.001	0.0003	96
GO:0006152	Purine nucleoside catabolic process	51.183	0.0003	80
GO:0005544	Calcium-dependent phospholipid binding	7.894	0.0004	10
GO:0043256	Laminin complex	4.400	0.0004	5
GO:0009207	Purine ribonucleoside triphosphate catabolic process	49.573	0.0004	77
GO:0032993	Protein-DNA complex	10.451	0.0004	14
GO:0009166	Nucleotide catabolic process	57.048	0.0004	90
GO:0043492	ATPase activity, coupled to movement of substances	15.979	0.0005	23
GO:0006812	Cation transport	47.043	0.0005	73
GO:0009143	Nucleoside triphosphate catabolic process	50.143	0.0005	78
GO:0017111	Nucleoside-triphosphatase activity	129.377	0.0005	211
GO:0031589	Cell-substrate adhesion	19.896	0.0005	29
GO:0071407	Cellular response to organic cyclic compound	19.290	0.0005	28
GO:0009203	Ribonucleoside triphosphate catabolic process	49.573	0.0006	77
GO:0005811	Lipid droplet	13.605	0.0006	19
GO:0008509	Anion transmembrane transporter activity	19.273	0.0007	28
GO:0009158	Ribonucleoside monophosphate catabolic process	18.299	0.0007	27
GO:0009205	Purine ribonucleoside triphosphate metabolic process	56.594	0.0007	89
GO:0005886	Plasma membrane	285.227	0.0007	477
GO:0019897	Extrinsic component of plasma membrane	17.956	0.0007	26

GO Term	Annotation	PES	p-value	Proteins in Set
GO:0009057	Macromolecule catabolic process	138.725	0.0007	227
GO:0000149	SNARE binding	8.881	0.0008	12
GO:0022904	Respiratory electron transport chain	23.596	0.0008	35
GO:0022804	Active transmembrane transporter activity	27.957	0.0008	42
GO:0007411	Axon guidance	61.001	0.0008	96
GO:0042454	Ribonucleoside catabolic process	52.150	0.0008	82
GO:0009261	Ribonucleotide catabolic process	51.715	0.0008	81
GO:0005509	Calcium ion binding	49.814	0.0009	78
GO:0048598	Embryonic morphogenesis	20.368	0.0009	30
GO:0030667	Secretory granule membrane	8.888	0.0010	12
GO:0034728	Nucleosome organization	8.151	0.0010	11
GO:0009154	Purine ribonucleotide catabolic process	51.297	0.0010	80
GO:0042626	ATPase-coupled transmembrane transporter activity	15.979	0.0010	23
KEGG	ECM receptor interaction	17.433	<1.0E-4	21
KEGG	Ribosome	44.271	<1.0E-4	56
KEGG	Huntington’s disease	34.656	<1.0E-4	50
KEGG	Parkinson’s disease	27.879	<1.0E-4	39
KEGG	Small cell lung cancer	15.338	0.0005	21
Reactome	Signaling by ROBO receptors	78.339	<1.0E-4	120
Reactome	Collagen biosynthesis and modifying enzymes	11.348	<1.0E-4	14
Reactome	Collagen chain trimerization	8.755	<1.0E-4	10
Reactome	Regulation of expression of SLITS and ROBOS	70.531	<1.0E-4	105
Reactome	SRP dependent cotranslational protein targeting to membrane	48.490	<1.0E-4	62
Reactome	Influenza infection	55.688	<1.0E-4	76
Reactome	Infectious disease	148.255	<1.0E-4	237
Reactome	rRNA processing	49.889	<1.0E-4	67
Reactome	Eukaryotic translation initiation	60.094	<1.0E-4	85
Reactome	Assembly of collagen fibrils and other multimeric structures	11.157	<1.0E-4	14
Reactome	Non integrin membrane and ECM interaction	21.158	<1.0E-4	26
Reactome	Laminin interactions	17.723	<1.0E-4	19
Reactome	Metabolism of amino acids and derivatives	97.229	<1.0E-4	152
Reactome	Elastic fiber formation	8.034	<1.0E-4	9
Reactome	Collagen formation	13.750	<1.0E-4	18
Reactome	Developmental biology	169.153	<1.0E-4	265
Reactome	Selenoamino acid metabolism	52.953	<1.0E-4	72
Reactome	Nervous system development	147.024	<1.0E-4	229
Reactome	Nonsense mediated decay NMD	50.557	<1.0E-4	68
Reactome	Proteoglycans	19.007	<1.0E-4	23
Reactome	Eukaryotic translation elongation	46.678	<1.0E-4	60
Reactome	Extracellular matrix organization	49.277	<1.0E-4	66
Reactome	Translation	87.055	<1.0E-4	134
Reactome	Collagen degradation	10.640	<1.0E-4	13
Reactome	Molecules associated with elastic fibers	8.034	<1.0E-4	9
Reactome	Integrin cell surface interactions	19.396	<1.0E-4	23
Reactome	Degradation of extracellular matrix	24.656	<1.0E-4	31
Reactome	Response of EIF2AK4 GCN2 to amino acid deficiency	47.225	<1.0E-4	61
Reactome	NCAM signaling for neurite outgrowth	15.634	0.0001	21
Reactome	Smooth muscle contraction	11.529	0.0001	15
Reactome	NCAM1 interactions	8.337	0.0001	10
Reactome	Cristae formation	7.329	0.0002	9
Reactome	Synthesis of very long chain fatty acyl CoAs	4.442	0.0002	5
Reactome	The citric acid TCA cycle and respiratory electron transport	41.046	0.0002	62
Reactome	Regulation of insulin like growth factor IGF transport and uptake by insulin like growth factor binding protein IGFBPS	16.363	0.0003	23
Reactome	Muscle contraction	24.005	0.0004	35
Reactome	Fatty acyl CoA biosynthesis	7.790	0.0005	10
Reactome	Formation of ATP by chemiosmotic coupling	5.270	0.0005	6
Reactome	Binding and uptake of ligands by scavenger receptors	12.459	0.0006	17
Reactome	Scavenging by class A receptors	5.782	0.0006	6

GO Term	Annotation	PES	p-value	Proteins in Set
Reactome	Met activates PTK2 signaling	7.956	0.0007	10
Reactome	Disease	215.795	0.0008	352
	Enriched in Inner Nucleus over Cortex			
GO:0050953	Sensory perception of light stimulus	21.407	<1.0E-4	34
GO:0016052	Carbohydrate catabolic process	25.547	<1.0E-4	44
GO:0007601	Visual perception	21.407	<1.0E-4	34
GO:0019752	Carboxylic acid metabolic process	111.111	<1.0E-4	207
GO:0006082	Organic acid metabolic process	120.847	<1.0E-4	226
GO:0043169	Cation binding	245.757	<1.0E-4	467
GO:0046872	Metal ion binding	242.297	<1.0E-4	460
GO:0043436	Oxoacid metabolic process	118.767	<1.0E-4	222
GO:0006576	Cellular biogenic amine metabolic process	12.119	<1.0E-4	20
GO:0008270	Zinc ion binding	58.543	<1.0E-4	106
GO:0044106	Cellular amine metabolic process	12.119	<1.0E-4	20
GO:0046365	Monosaccharide catabolic process	20.689	<1.0E-4	35
GO:0071704	Organic substance metabolic process	671.295	<1.0E-4	1297
GO:0007600	Sensory perception	32.996	<1.0E-4	57
GO:0022400	Regulation of rhodopsin mediated signaling pathway	5.315	<1.0E-4	8
GO:0003824	Catalytic activity	563.920	<1.0E-4	1078
GO:0050877	Nervous system process	45.577	<1.0E-4	82
GO:0005996	Monosaccharide metabolic process	41.643	<1.0E-4	74
GO:0019320	Hexose catabolic process	18.952	<1.0E-4	32
GO:0044281	Small molecule metabolic process	307.207	<1.0E-4	586
GO:0002088	Lens development in camera-type eye	8.695	<1.0E-4	12
GO:0044283	Small molecule biosynthetic process	50.366	<1.0E-4	91
GO:0046914	Transition metal ion binding	80.952	<1.0E-4	150
GO:1901566	Organonitrogen compound biosynthetic process	72.319	<1.0E-4	133
GO:0006520	Cellular amino acid metabolic process	67.794	<1.0E-4	125
GO:0019318	Hexose metabolic process	38.241	<1.0E-4	68
GO:0016765	Transferase activity, transferring alkyl or aryl (other than methyl) groups	11.301	<1.0E-4	18
GO:0008233	Peptidase activity	59.087	<1.0E-4	108
GO:0005212	Structural constituent of eye lens	13.334	<1.0E-4	17
GO:0006007	Glucose catabolic process	15.772	0.0001	27
GO:0008238	Exopeptidase activity	16.044	0.0001	27
GO:0005737	Cytoplasm	478.335	0.0001	921
GO:0046394	Carboxylic acid biosynthetic process	37.483	0.0001	68
GO:0044238	Primary metabolic process	642.853	0.0001	1242
GO:0016740	Transferase activity	154.590	0.0001	293
GO:0070011	Peptidase activity, acting on L-amino acid peptides	56.882	0.0001	104
GO:0071482	Cellular response to light stimulus	7.492	0.0002	12
GO:0006006	Glucose metabolic process	32.270	0.0002	58
GO:0005829	Cytosol	424.116	0.0002	816
GO:0042803	Protein homodimerization activity	72.404	0.0002	134
GO:0042802	Identical protein binding	111.921	0.0002	210
GO:1901607	Alpha-amino acid biosynthetic process	14.162	0.0003	24
GO:0045762	Positive regulation of adenylate cyclase activity	4.081	0.0003	6
GO:0004177	Aminopeptidase activity	7.617	0.0003	13
GO:0097354	Prenylation	3.458	0.0003	5
GO:0006508	Proteolysis	95.201	0.0003	178
GO:0006790	Sulfur compound metabolic process	32.594	0.0004	59
GO:0044272	Sulfur compound biosynthetic process	15.609	0.0004	27
GO:0009308	Amine metabolic process	13.074	0.0004	22
GO:0016056	Rhodopsin mediated signaling pathway	5.315	0.0004	8
GO:0008152	Metabolic process	713.007	0.0004	1380
GO:0005975	Carbohydrate metabolic process	87.500	0.0004	164
GO:0006555	Methionine metabolic process	8.011	0.0005	13
GO:0018342	Protein prenylation	3.458	0.0005	5

GO Term	Annotation	PES	p-value	Proteins in Set
GO:0072422	Signal transduction involved in DNA damage checkpoint	18.699	0.0005	35
GO:1900740	Positive regulation of protein insertion into mitochondrial membrane involved in apoptotic signaling pathway	5.363	0.0005	9
GO:1900544	Positive regulation of purine nucleotide metabolic process	5.786	0.0006	9
GO:0031281	Positive regulation of cyclase activity	4.081	0.0006	6
GO:0071158	Positive regulation of cell cycle arrest	19.706	0.0006	37
GO:1900739	Regulation of protein insertion into mitochondrial membrane involved in apoptotic signaling pathway	5.363	0.0006	9
GO:0016570	Histone modification	13.365	0.0007	23
GO:0045981	Positive regulation of nucleotide metabolic process	5.786	0.0007	9
GO:0000097	Sulfur amino acid biosynthetic process	6.892	0.0007	11
GO:0072401	Signal transduction involved in DNA integrity checkpoint	18.699	0.0007	35
GO:0005615	Extracellular space	54.448	0.0007	101
GO:0072395	Signal transduction involved in cell cycle checkpoint	18.699	0.0007	35
GO:0004659	Prenyltransferase activity	4.656	0.0007	7
GO:0051186	Cofactor metabolic process	46.746	0.0008	86
GO:0000096	Sulfur amino acid metabolic process	13.399	0.0008	23
GO:0031397	Negative regulation of protein ubiquitination	23.881	0.0008	45
GO:0019321	Pentose metabolic process	4.602	0.0008	8
GO:0008318	Protein prenyltransferase activity	3.458	0.0008	5
GO:0006977	DNA damage response, signal transduction by p53 class mediator resulting in cell cycle arrest	18.699	0.0008	35
GO:1900373	Positive regulation of purine nucleotide biosynthetic process	5.090	0.0010	8
GO:0072431	Signal transduction involved in mitotic G1 DNA damage checkpoint	18.699	0.0010	35
GO:0004518	Nuclease activity	12.021	0.0010	22
KEGG	Cysteine and methionine metabolism	10.190	<1.0E-4	16
KEGG	Glutathione metabolism	13.176	<1.0E-4	23
KEGG	Purine metabolism	19.964	0.0001	37
KEGG	Proteasome	17.099	0.0004	32
Reactome	TP53 regulates transcription of genes involved in cytochrome c release	3.129	<1.0E-4	4
Reactome	Metabolism of carbohydrates	45.777	<1.0E-4	82
Reactome	Regulation of lipid metabolism by pparalpha	4.516	<1.0E-4	6
Reactome	TP53 regulates transcription of cell death genes	6.711	<1.0E-4	10
Reactome	Fructose metabolism	2.850	0.0001	4
Reactome	The phototransduction cascade	5.315	0.0003	8
Reactome	UCH proteinases	24.025	0.0004	45
Reactome	Transcriptional regulation by TP53	40.350	0.0006	74
Reactome	Transcriptional regulation of white adipocyte differentiation	4.049	0.0006	6
Reactome	Rna polymerase ii transcription	89.153	0.0006	168
Reactome	Negative regulation of notch 4 signaling	19.756	0.0006	37
Reactome	APC C CDH1 mediated degradation of CD20 and other APC C CDHA1 targeted proteins in late mitosis early G1	19.253	0.0007	36
Reactome	Glycolysis	16.920	0.0008	30
Reactome	Asymmetric localization of PCP proteins	18.699	0.0009	35
Reactome	Degradation of axin	18.699	0.0010	35

B. Table of ontological enrichment between the cortex and inner nucleus, measured with DDA analysis

Complete list of ontologies (n=59) enriched in either the cortex or inner nucleus over the other region. Outputs calculated based on DDA dataset. Ontology calculations performed by PSEA-quant with CV tolerance 0.5, 10,000 iterations used for p-value calculation.

GO Term	Annotation	PES	p-value	Proteins in Set
	Enriched in Cortex over Inner Nucleus			
GO:0065010	Extracellular membrane-bounded organelle	26.528	$<1.0x10^{-4}$	31
GO:0005604	Basement membrane	5.360	$<1.0x10^{-4}$	6
GO:0022617	Extracellular matrix disassembly	6.196	$<1.0x10^{-4}$	7
GO:0005201	Extracellular matrix structural constituent	7.032	$<1.0x10^{-4}$	8
GO:0043230	Extracellular organelle	26.528	$<1.0x10^{-4}$	31
GO:0043062	Extracellular structure organization	16.364	$<1.0x10^{-4}$	19
GO:0005576	Extracellular region	33.821	$<1.0x10^{-4}$	40
GO:0019901	Protein kinase binding	25.414	$<1.0x10^{-4}$	30
GO:0031982	Vesicle	69.578	$<1.0x10^{-4}$	83
GO:0030198	Extracellular matrix organization	16.364	$<1.0x10^{-4}$	19
GO:0070062	Extracellular exosome	26.528	$<1.0x10^{-4}$	31
GO:0019898	Extrinsic component of membrane	13.839	$<1.0x10^{-4}$	16
GO:0071840	Cellular component organization or biogenesis	167.76	$<1.0x10^{-4}$	203
GO:0032963	Collagen metabolic process	5.300	0.0001	6
GO:0043236	Laminin binding	2.707	0.0001	3
GO:0010927	Cellular component assembly involved in morphogenesis	7.821	0.0001	9
GO:0045185	Maintenance of protein location	6.139	0.0001	7
GO:0016043	Cellular component organization	167.760	0.0002	203
GO:0050808	Synapse organization	9.475	0.0002	11
GO:0034330	Cell junction organization	20.432	0.0002	24
GO:0034329	Cell junction assembly	17.910	0.0002	21
GO:0030574	Collagen catabolic process	5.300	0.0002	6
GO:0042267	Natural killer cell mediated cytotoxicity	2.689	0.0002	3
GO:0005886	Plasma membrane	115.320	0.0002	139
GO:0051235	Maintenance of location	6.139	0.0002	7
GO:0019897	Extrinsic component of plasma membrane	7.796	0.0002	9
GO:0005856	Cytoskeleton	58.546	0.0002	70
GO:0019900	Kinase binding	29.517	0.0003	35
GO:0002449	Lymphocyte mediated immunity	3.535	0.0004	4
GO:0030935	Sheet-forming collagen trimer	3.564	0.0004	4
GO:0050840	Extracellular matrix binding	2.707	0.0004	3
GO:0005587	Collagen type IV trimer	3.564	0.0005	4
GO:0031012	Extracellular matrix	20.335	0.0007	24
GO:0001909	Leukocyte mediated cytotoxicity	3.535	0.0007	4
GO:0044782	Cilium organization	3.546	0.0007	4
GO:0016323	Basolateral plasma membrane	14.482	0.0008	17
GO:0002228	Natural killer cell mediated immunity	2.689	0.0008	3
GO:0045121	Membrane raft	14.471	0.0009	17
KEGG	Small cell lung cancer	4.467	$<1.0x10^{-4}$	5
KEGG	ECM receptor interaction	5.367	0.0001	6
Reactome	Non integrin membrane ECM interactions	7.117	$<1.0x10^{-4}$	8
Reactome	Laminin interactions	8.067	$<1.0x10^{-4}$	9
Reactome	Extracellular matrix organization	17.242	$<1.0x10^{-4}$	20
Reactome	Degradation of the extracellular matrix	12.339	$<1.0x10^{-4}$	14
Reactome	ECM proteoglycans	7.857	0.0001	9
Reactome	Collagen biosynthesis and modifying enzymes	4.442	0.0001	5
Reactome	Collagen degradation	5.300	0.0003	6
Reactome	Collagen chain trimerization	4.442	0.0003	5
Reactome	Assembly of collagen fibrils and other multimeric structures	5.250	0.0004	6
Reactome	Crosslinking of collagen fibrils	3.564	0.0006	4
Reactome	Anchoring fibril formation	3.564	0.0006	4

GO Term	Annotation	PES	p-value	Proteins in Set
Reactome	Collagen formation	5.250	0.0009	6
	Enriched in Inner Nucleus over Cortex			
GO:0005212	Structural constituent of eye lens	16.220	$<1.0\text{x}10^{-4}$	18
GO:0048037	Cofactor binding	20.604	$<1.0\text{x}10^{-4}$	23
GO:0050662	Coenzyme binding	16.186	$<1.0\text{x}10^{-4}$	18
GO:0007423	Sensory organ development	2.790	0.0002	3
GO:0043010	Camera-type eye development	2.790	0.0003	3
GO:0050661	NADP binding	9.981	0.0005	11
GO:0043086	Negative regulation of catalytic activity	46.510	0.0007	53
GO:0001654	Eye development	2.790	0.0008	3

C. Table of differential protein abundance between lens regions, measured with DIA

Complete protein group and gene group ID of each protein identified as differentially enriched in Figure 3-7 A-C (n=53). Differential expression data is compiled from DIA library-free search with one variable deamidation enabled. Only proteins with limma moderated p-values below 1E-6 and Log2 FC in excess of 4 are shown. For protein groups with multiple assigned proteins in the group, all proteins are shown with semi-colons and line delimiters between groups. Gene name identifiers are supplied for only the leading protein group as presented in Figure 3-6.

Identifier		**Cortex – Inner Nucleus**		**Cortex – Outer Nucleus**		**Outer Nucleus – Inner Nucleus**	
Protein Group	*Gene Name*	*Log2FC*	*p-value*	*Log2FC*	*p-value*	*Log2FC*	*p-value*
P07315	CRYGC	-6.32	1.33E-09	-6.32	1.82E-09	-0.01	0.93
P05141;P12235; P12236	SLC25A5	5.59	4.22E-09	5.57	7.57E-09	0.02	0.90
P36957	DLST	6.43	5.66E-09	6.20	2.01E-08	0.23	0.34
P62805	H4C1	7.55	1.30E-08	7.28	7.56E-09	0.27	0.28
P07315;P07316; P11844	CRYGC	-4.04	1.41E-08	-3.96	2.65E-08	-0.08	0.46
Q6PCB7	SLC27A1	-5.34	1.49E-08	-5.48	1.57E-07	0.14	0.56
P12235;P12236	SLC25A4	4.06	2.03E-08	3.84	1.58E-07	0.22	0.26
P30101	PDIA3	5.70	2.31E-08	5.83	5.40E-08	-0.13	0.60
P05141;P12236	SLC25A5	4.96	3.04E-08	4.96	5.89E-09	0.00	0.99
P25705	ATP5F1A	6.90	3.32E-08	6.30	1.17E-09	0.60	0.04
P05556	ITGB1	4.37	3.55E-08	4.51	2.23E-08	-0.14	0.45
P68371	TUBB4B	5.65	4.38E-08	5.41	9.40E-07	0.24	0.47
Q9UHG3	PCYOX1	5.06	4.48E-08	5.22	4.10E-07	-0.15	0.59
P23284	PPIB	4.22	6.48E-08	4.13	1.19E-07	0.09	0.62
P13073	COX4I1	6.39	6.76E-08	6.48	2.72E-08	-0.08	0.78
P0DMV8;P0DMV9	HSPA1A	4.30	8.10E-08	4.03	1.02E-07	0.27	0.22
Q13424;Q13425; Q13884	SNTA1	4.31	8.41E-08	4.15	2.13E-06	0.16	0.58
Q12797	ASPH	5.22	1.10E-07	2.82	0.16	2.40	0.24
Q13425	SNTB2	4.72	1.31E-07	4.23	3.90E-05	0.49	0.29
P84243	NA	8.23	1.41E-07	NA	NA	NA	NA
P14625	HSP90B1	4.50	1.46E-07	4.83	3.03E-08	-0.33	0.17
P08133	ANXA6	4.91	1.69E-07	4.74	2.47E-07	0.17	0.54
O95837;P19086; P29992;P50148; Q03113;Q14344	GNA14	4.20	1.89E-07	4.38	4.37E-06	-0.18	0.59
Q9NR31;Q9Y6B6	SAR1A	4.74	2.14E-07	4.54	1.12E-08	0.20	0.38
P67812	SEC11A	4.83	2.26E-07	4.52	2.33E-06	0.31	0.37
P09038	FGF2	4.06	2.57E-07	3.83	7.65E-08	0.23	0.30
P49755	TMED10	4.61	3.98E-07	4.16	2.16E-07	0.45	0.12
P12235	SLC25A4	4.87	4.00E-07	5.00	3.75E-07	-0.13	0.68
O15211	RGL2	-5.34	4.09E-07	-5.51	1.87E-06	0.18	0.59
P53007	SLC25A1	4.10	4.75E-07	4.13	1.26E-06	-0.03	0.92
Q00325	SLC25A3	5.31	5.05E-07	5.51	2.97E-07	-0.20	0.55
P39656	OST48	6.12	7.25E-07	NA	NA	NA	NA
Q6UW68	TMEM205	5.55	7.67E-07	5.16	6.79E-09	0.39	0.23
P62917	RPL8	5.55	7.71E-07	5.34	5.12E-07	0.21	0.58
O60762	DPM1	4.79	7.72E-07	5.20	3.66E-06	-0.41	0.34
P61604	HSPE1	4.47	7.72E-07	4.60	6.18E-07	-0.13	0.68
P07437;P68371; Q13885;Q9BVA1	TUBB	4.73	7.93E-07	4.48	1.15E-06	0.24	0.47
P02794	FTH1	6.36	8.51E-07	6.02	7.67E-06	0.34	0.55
P08572	COL4A2	4.05	8.55E-07	4.06	1.60E-07	-0.01	0.94
O96000	NDUFB10	3.89	9.81E-07	4.08	2.45E-06	-0.18	0.57
Q9H7D0	DOCK5	-4.08	9.88E-07	-3.45	3.81E-05	-0.63	0.13

Identifier		**Cortex – Inner Nucleus**		**Cortex – Outer Nucleus**		**Outer Nucleus – Inner Nucleus**	
Protein Group	*Gene Name*	*Log2FC*	*p-value*	*Log2FC*	*p-value*	*Log2FC*	*p-value*
P26885	FKBP2	3.89	1.27E-06	4.00	8.48E-08	-0.11	0.67
P22352	GPX3	4.65	2.39E-06	4.83	5.27E-07	-0.18	0.62
P11117	ACP2	4.55	2.69E-06	4.03	8.39E-08	0.52	0.14
P62701	RPS4X	6.12	2.82E-06	6.50	1.09E-07	-0.38	0.42
P36542	ATP5F1C	6.79	3.32E-06	6.27	1.40E-08	0.53	0.29
P12236	SLC25A6	7.33	3.38E-06	6.65	5.24E-07	0.67	0.26
L0R6Q1	SLC35A4	3.84	4.40E-06	4.00	6.92E-07	-0.16	0.59
P35268	RPL22	4.91	7.83E-06	4.96	3.32E-08	-0.05	0.91
Q9H8H3	METTL7A	4.82	2.83E-04	4.24	9.46E-08	0.58	0.42
Q14956	GPNMB	NA	NA	9.76	1.28E-08	NA	NA
Q04837	SSBP1	NA	NA	5.22	7.15E-08	NA	NA
P10412;P16403	H14	NA	NA	8.61	7.88E-07	NA	NA

D. Table of differential protein expression between age groups in each lens region

Protein groups filtered as differentially expressed in at least one lens region between young lenses and old lenses. Young lenses were defined as from human subject donors younger than 50 years, and older lenses from human subject donors older than 50 years. Protein groups determined as significant volcano plot analysis are highlighted with their corresponding sample group (e.g., cortex significant proteins are highlighted red, outer nucleus significant proteins are colored green, and inner nucleus significant proteins are colored blue).

Protein Group	Gene Group	Protein Description	Cortex p-value	Cortex Log2FC	Outer Nucleus p-value	Outer Nucleus Log2FC	Inner Nucleus p-value	Inner Nucleus Log2FC
P04350; P07437; P68371; Q13885; Q9BVA1	TUBB; TUBB2A; TUBB2B; TUBB4A; TUBB4B	Tubulin beta-4A chain	1.12E-03	-4.30	5.43E-01	0.24	NA	NA
P07099	EPHX1	Epoxide hydrolase 1	2.19E-03	-3.83	NA	NA	NA	NA
Q16778; Q8N257	H2BC21; H2BU1	Histone H2B type 2-E	1.62E-03	-3.72	NA	NA	NA	NA
Q6UW68	TMEM205	Transmembrane protein 205	1.34E-03	-3.7	NA	NA	NA	NA
Q9UEW8	STK39	STE20/SPS1-related proline-alanine-rich protein kinase	1.16E-04	-3.66	NA	NA	NA	NA
P36578	RPL4	60S ribosomal protein L4	2.94E-04	-3.60	NA	NA	NA	NA
P04350; P68371	TUBB4A; TUBB4B	Tubulin beta-4A chain	5.68E-04	-3.59	7.69E-01	-0.26	NA	NA
Q9Y3D6	FIS1	Mitochondrial fission 1 protein	2.72E-04	-3.58	NA	NA	NA	NA
P45880	VDAC2	Voltage-dependent anion-selective channel protein 2	9.11E-04	-3.54	4.02E-02	-1.87	1.19E-02	-1.92
P07437; P68371; Q13885; Q9BVA1	TUBB; TUBB2A; TUBB2B; TUBB4B	Tubulin beta chain	1.01E-04	-3.54	NA	NA	NA	NA
P35613	BSG	Basigin	1.07E-03	-3.52	NA	NA	NA	NA
P20339	RAB5A	Ras-related protein Rab-5A	2.28E-04	-3.50	NA	NA	NA	NA
P00403	MT-CO2	Cytochrome c oxidase subunit 2	8.22E-04	-3.49	2.19E-02	-1.59	NA	NA
P14625	HSP90B1	Endoplasmin	8.00E-04	-3.46	NA	NA	NA	NA
P06576	ATP5F1B	ATP synthase subunit beta, mitochondrial	1.12E-03	-3.43	NA	NA	NA	NA
Q9Y3B3	TMED7	Transmembrane emp24 domain-containing protein 7	8.64E-04	-3.43	NA	NA	NA	NA
P27824	CANX	Calnexin	1.15E-05	-3.42	NA	NA	NA	NA
P40429	RPL13A	60S ribosomal protein L13a	9.18E-05	-3.41	NA	NA	6.65E-02	-1.27
P35579; P35749; Q7Z406	MYH11; MYH14; MYH9	Myosin-9	3.48E-04	-3.39	NA	NA	NA	NA
P31930	UQCRC1	Cytochrome b-c1 complex subunit 1, mitochondrial	1.81E-03	-3.36	NA	NA	NA	NA

Protein Group	Gene Group	Protein Description	Cortex p-value	Cortex Log2FC	Outer Nucleus p-value	Outer Nucleus Log2FC	Inner Nucleus p-value	Inner Nucleus Log2FC
P55072	VCP	Transitional endoplasmic reticulum ATPase	5.96E-06	-3.35	2.26E-01	-0.67	3.38E-01	-0.47
P21796	VDAC1	Voltage-dependent anion-selective channel protein 1	3.96E-03	-3.33	NA	NA	NA	NA
O00148; Q13838	DDX39A; DDX39B	ATP-dependent RNA helicase DDX39A	1.93E-05	-3.32	NA	NA	NA	NA
Q99733	NAP1L4	Nucleosome assembly protein 1-like 4	3.04E-05	-3.32	NA	NA	NA	NA
Q00325	SLC25A3	Phosphate carrier protein, mitochondrial	5.48E-03	-3.26	5.96E-01	-0.26	1.12E-01	-0.79
P0DMV8;P0DMV9	HSPA1A; HSPA1B	Heat shock 70 kDa protein 1A	1.88E-06	-3.26	NA	NA	NA	NA
Q15365	PCBP1	Poly(rC)-binding protein 1	5.07E-04	-3.24	NA	NA	NA	NA
Q6PGP7	TTC37	Tetratricopeptide repeat protein 37	2.79E-04	-3.21	NA	NA	NA	NA
Q9NZ01	TECR	Very-long-chain enoyl-CoA reductase	2.57E-03	-3.19	NA	NA	NA	NA
P53618	COPB1	Coatomer subunit beta	3.53E-04	-3.19	NA	NA	NA	NA
P13073	COX4I1	Cytochrome c oxidase subunit 4 isoform 1, mitochondrial	5.15E-03	-3.18	NA	NA	NA	NA
P11021; P11142; P54652	HSPA2; HSPA5; HSPA8	Endoplasmic reticulum chaperone BiP	3.48E-06	-3.17	NA	NA	NA	NA
P46781	RPS9	40S ribosomal protein S9	1.14E-03	-3.13	1.03E-01	-0.93	1.11E-01	-1.08
P39023	RPL3	60S ribosomal protein L3	2.69E-04	-3.13	1.36E-01	-0.72	1.29E-01	-1.01
P53007	SLC25A1	Tricarboxylate transport protein, mitochondrial	6.92E-04	-3.08	NA	NA	5.21E-01	-0.36
P07900; P08238; Q58FF8	HSP90AA1; HSP90AB1; HSP90AB2P	Heat shock protein HSP 90-alpha	2.48E-04	-3.06	1.32E-03	-2.23	3.52E-05	-3.30
P12235	SLC25A4	ADP/ATP translocase 1	6.16E-04	-3.06	NA	NA	NA	NA
Q9Y512	SAMM50	Sorting and assembly machinery component 50 homolog	2.77E-03	-3.04	NA	NA	NA	NA
P07437	TUBB	Tubulin beta chain	7.09E-04	-3.04	7.74E-03	-2.05	NA	NA
P84243	H3-3A	Histone H3.3	3.18E-03	-3.02	3.37E-03	-2.45	NA	NA
P16104; Q8IUE6	H2AC21; H2AX	Histone H2AX	8.03E-03	-3.02	NA	NA	NA	NA
P24539	ATP5PB	ATP synthase F(0) complex subunit B1, mitochondrial	1.64E-03	-3.00	8.54E-02	-0.75	1.44E-04	-2.24
P43007	SLC1A4	Neutral amino acid transporter A	2.53E-04	-3.00	NA	NA	NA	NA
O15020	SPTBN2	Spectrin beta chain, non-erythrocytic 2	3.88E-04	-2.95	2.77E-02	-1.14	4.11E-03	-1.43
P04350; P07437; P68371;	TUBB; TUBB2A; TUBB2B;	Tubulin beta-4A chain	1.91E-04	-2.95	NA	NA	NA	NA

Protein Group	Gene Group	Protein Description	Cortex p-value	Cortex Log2FC	Outer Nucleus p-value	Outer Nucleus Log2FC	Inner Nucleus p-value	Inner Nucleus Log2FC
Q13509; Q13885; Q9BUF5;Q9BVA1	TUBB3; TUBB4A; TUBB4B; TUBB6							
P62906	RPL10A	60S ribosomal protein L10a	3.50E-03	-2.94	NA	NA	NA	NA
P07900; P08238	HSP90AA1;HSP90AB1	Heat shock protein HSP 90-alpha	5.15E-04	-2.94	2.92E-01	-0.27	2.53E-01	-0.31
P14923	JUP	Junction plakoglobin	7.97E-04	-2.94	NA	NA	NA	NA
P84243; Q5TEC6	H3-2; H3-3A	Histone H3.3	3.72E-03	-2.94	NA	NA	NA	NA
P57053; Q16778	H2BC21; H2BS1	Histone H2B type F-S	7.70E-03	-2.93	NA	NA	NA	NA
O76024	WFS1	Wolframin	2.41E-04	-2.91	2.58E-02	-1.33	3.43E-03	-1.39
O00571; O15523	DDX3X; DDX3Y	ATP-dependent RNA helicase DDX3X	7.80E-04	-2.90	NA	NA	NA	NA
Q14697	GANAB	Neutral alpha-glucosidase AB	9.75E-04	-2.90	5.83E-01	0.17	8.37E-01	0.08
Q15366	PCBP2	Poly(rC)-binding protein 2	8.47E-04	-2.86	NA	NA	NA	NA
Q15363	TMED2	Transmembrane emp24 domain-containing protein 2	6.72E-04	-2.86	NA	NA	NA	NA
Q15365; Q15366	PCBP1; PCBP2	Poly(rC)-binding protein 1	2.56E-06	-2.83	1.85E-02	-1.00	7.26E-01	-0.12
P17931	LGALS3	Galectin-3	5.02E-03	-2.83	NA	NA	NA	NA
P31946	YWHAB	14-3-3 protein beta/alpha	9.55E-04	-2.83	NA	NA	NA	NA
P04350	TUBB4A	Tubulin beta-4A chain	2.42E-04	-2.83	1.57E-02	-2.28	NA	NA
P04899	GNAI2	Guanine nucleotide-binding protein G(i) subunit alpha-2	3.06E-04	-2.82	NA	NA	NA	NA
P05141; P12235; P12236	SLC25A4; SLC25A5; SLC25A6	ADP/ATP translocase 2	6.67E-03	-2.80	3.57E-01	-0.45	3.52E-02	-1.35
P31948	STIP1	Stress-induced-phosphoprotein 1	5.74E-03	-2.76	NA	NA	NA	NA
P19022	CDH2	Cadherin-2	1.11E-03	-2.73	4.77E-03	-2.55	1.90E-03	-3.06
Q9BXM0	PRX	Periaxin	4.26E-04	-2.71	2.27E-03	-2.79	8.08E-04	-2.5
P62805	H4C1	Histone H4	4.89E-03	-2.71	5.73E-02	-1.35	1.29E-02	-1.84
P35579; P35749	MYH11; MYH9	Myosin-9	2.65E-03	-2.71	NA	NA	NA	NA
P55209	NAP1L1	Nucleosome assembly protein 1-like 1	8.54E-04	-2.71	4.68E-02	-1.30	NA	NA
O75367; Q9P0M6	MACROH2A1; MACROH2A2	Core histone macro-H2A.1	4.62E-03	-2.70	NA	NA	NA	NA
P11142; P54652	HSPA2; HSPA8	Heat shock cognate 71 kDa protein	3.30E-04	-2.68	6.96E-03	-1.55	1.89E-01	-0.57
P13489	RNH1	Ribonuclease inhibitor	5.71E-03	-2.67	1.30E-01	-0.92	9.55E-03	-1.47
P27348	YWHAQ	14-3-3 protein theta	3.68E-04	-2.67	6.29E-02	-0.89	4.05E-01	-0.57
Q7L099	RUFY3	Protein RUFY3	5.31E-04	-2.66	NA	NA	NA	NA

Protein Group	Gene Group	Protein Description	Cortex p-value	Cortex Log2FC	Outer Nucleus p-value	Outer Nucleus Log2FC	Inner Nucleus p-value	Inner Nucleus Log2FC
P07900; P08238; Q58FF6;Q58FF7;Q58FF8	HSP90AA1;HSP90AB1;HSP90AB2P;HSP90AB3P; HSP90AB4P	Heat shock protein HSP 90-alpha	3.05E-04	-2.66	NA	NA	NA	NA
P26232	CTNNA2	Catenin alpha-2	2.17E-03	-2.65	1.17E-03	-2.56	2.60E-04	-1.71
O00203	AP3B1	AP-3 complex subunit beta-1	8.48E-04	-2.65	NA	NA	NA	NA
O94874	UFL1	E3 UFM1-protein ligase 1	1.15E-04	-2.65	NA	NA	NA	NA
Q96HC4	PDLIM5	PDZ and LIM domain protein 5	6.04E-04	-2.64	NA	NA	NA	NA
P00450	CP	Ceruloplasmin	7.36E-07	-2.63	NA	NA	NA	NA
P04920	SLC4A2	Anion exchange protein 2	2.58E-04	-2.62	NA	NA	NA	NA
Q92597	NDRG1	Protein NDRG1	5.25E-03	-2.62	7.94E-02	-1.04	1.02E-01	-1.22
P51991	HNRNPA3	Heterogeneous nuclear ribonucleoprotein A3	2.54E-04	-2.62	NA	NA	NA	NA
P12236	SLC25A6	ADP/ATP translocase 3	6.01E-03	-2.59	NA	NA	NA	NA
Q07960	ARHGAP1	Rho GTPase-activating protein 1	2.06E-03	-2.59	5.43E-01	0.24	2.38E-01	-0.59
Q8IXS6	PALM2	Paralemmin-2	1.31E-04	-2.57	3.35E-04	-3.94	NA	NA
Q02318	CYP27A1	Sterol 26-hydroxylase, mitochondrial	6.02E-03	-2.56	NA	NA	NA	NA
Q04637	EIF4G1	Eukaryotic translation initiation factor 4 gamma 1	7.20E-05	-2.56	1.07E-02	-0.83	2.67E-01	-0.49
Q14974	KPNB1	Importin subunit beta-1	8.29E-04	-2.56	1.55E-02	-0.95	7.42E-03	-1.39
O00410	IPO5	Importin-5	2.06E-03	-2.55	6.13E-02	-0.81	4.88E-03	-1.18
P63027; Q15836	VAMP2; VAMP3	Vesicle-associated membrane protein 2	4.06E-04	-2.54	NA	NA	NA	NA
P49755	TMED10	Transmembrane emp24 domain-containing protein 10	6.38E-03	-2.53	NA	NA	NA	NA
Q12955	ANK3	Ankyrin-3	9.37E-05	-2.53	4.91E-05	-1.49	5.52E-03	-1.63
P55290	CDH13	Cadherin-13	8.39E-03	-2.52	NA	NA	NA	NA
P19086; P29992; P50148; Q14344	GNA11; GNA13; GNAQ; GNAZ	Guanine nucleotide-binding protein G(z) subunit alpha	3.28E-04	-2.51	NA	NA	NA	NA
O95747	OXSR1	Serine/threonine-protein kinase OSR1	4.79E-04	-2.50	NA	NA	NA	NA
P0DMV8;P0DMV9;P48741	HSPA1A; HSPA1B; HSPA7	Heat shock 70 kDa protein 1A	1.09E-03	-2.50	8.76E-01	-0.10	1.39E-01	-0.90
Q9H853	TUBA4B	Putative tubulin-like protein alpha-4B	1.68E-04	-2.49	1.19E-02	-1.53	6.21E-04	-1.26
Q9H0A8	COMMD4	COMM domain-containing protein 4	8.15E-05	-2.48	NA	NA	NA	NA
O14880	MGST3	Microsomal glutathione S-transferase 3	8.90E-04	-2.48	NA	NA	2.69E-01	-0.74
P04632	CAPNS1	Calpain small subunit 1	5.78E-04	-2.48	NA	NA	NA	NA
O43390	HNRNPR	Heterogeneous nuclear ribonucleoprotein R	4.28E-03	-2.47	NA	NA	NA	NA

Protein Group	Gene Group	Protein Description	Cortex p-value	Cortex Log2FC	Outer Nucleus p-value	Outer Nucleus Log2FC	Inner Nucleus p-value	Inner Nucleus Log2FC
O00519	FAAH	Fatty-acid amide hydrolase 1	1.25E-03	-2.47	NA	NA	NA	NA
Q9H3Z4	DNAJC5	DnaJ homolog subfamily C member 5	1.45E-03	-2.47	NA	NA	NA	NA
P06396	GSN	Gelsolin	3.42E-04	-2.47	3.41E-02	-0.91	7.79E-01	-0.12
P21964	COMT	Catechol O-methyltransferase	1.40E-03	-2.46	1.08E-02	-1.56	NA	NA
P57088	TMEM33	Transmembrane protein 33	4.89E-03	-2.44	NA	NA	NA	NA
P68366; Q9BQE3;Q9H853	TUBA1C; TUBA4A; TUBA4B	Tubulin alpha-4A chain	4.48E-05	-2.44	2.48E-02	-1.17	1.08E-03	-2.19
Q13492	PICALM	Phosphatidylinositol-binding clathrin assembly protein	1.30E-03	-2.43	NA	NA	NA	NA
P08238; P14625	HSP90AB1;HSP90B1	Heat shock protein HSP 90-beta	5.34E-03	-2.42	2.23E-02	-1.27	NA	NA
P04083	ANXA1	Annexin A1	6.26E-03	-2.42	6.51E-01	-0.25	1.20E-02	-1.58
Q5T4S7	UBR4	E3 ubiquitin-protein ligase UBR4	5.44E-05	-2.42	1.94E-01	-0.40	3.50E-01	0.25
P35221	CTNNA1	Catenin alpha-1	7.61E-04	-2.41	NA	NA	NA	NA
P53992	SEC24C	Protein transport protein Sec24C	2.63E-03	-2.41	NA	NA	NA	NA
P55209; Q99733	NAP1L1; NAP1L4	Nucleosome assembly protein 1-like 1	8.09E-04	-2.40	8.34E-01	-0.10	2.34E-01	-0.60
Q5T5P2	KIAA1217	Sickle tail protein homolog	1.07E-03	-2.40	4.43E-01	-0.40	NA	NA
P08195	SLC3A2	4F2 cell-surface antigen heavy chain	2.01E-03	-2.40	NA	NA	NA	NA
Q8NHG7	SVIP	Small VCP/p97-interacting protein	3.11E-04	-2.40	NA	NA	NA	NA
Q9C0E8	LNPK	Endoplasmic reticulum junction formation protein lunapark	1.01E-03	-2.39	NA	NA	NA	NA
O14949	UQCRQ	Cytochrome b-c1 complex subunit 8	5.85E-03	-2.38	NA	NA	8.99E-02	-0.94
P25686	DNAJB2	DnaJ homolog subfamily B member 2	3.60E-03	-2.37	6.45E-02	-1.35	NA	NA
O96000	NDUFB10	NADH dehydrogenase [ubiquinone] 1 beta subcomplex subunit 10	9.31E-03	-2.36	NA	NA	NA	NA
O60282; P33176; Q12840	KIF5A; KIF5B; KIF5C	Kinesin heavy chain isoform 5C	1.96E-03	-2.36	NA	NA	NA	NA
P07900	HSP90AA1	Heat shock protein HSP 90-alpha	2.75E-04	-2.36	3.05E-03	-1.13	4.93E-04	-1.70
P61019	RAB2A	Ras-related protein Rab-2A	5.16E-04	-2.36	NA	NA	NA	NA
Q16643	DBN1	Drebrin	3.33E-03	-2.35	NA	NA	NA	NA
Q8N126	CADM3	Cell adhesion molecule 3	1.41E-04	-2.35	1.97E-03	-2.95	1.14E-02	-1.23
Q7Z406	MYH14	Myosin-14	1.11E-04	-2.34	1.03E-03	-1.2	8.28E-04	-1.55
O15031	PLXNB2	Plexin-B2	6.00E-03	-2.34	NA	NA	NA	NA
P30153	PPP2R1A	Serine/threonine-protein phosphatase 2A	3.73E-03	-2.32	2.28E-04	-1.19	5.74E-03	-1.57

Protein Group	Gene Group	Protein Description	Cortex p-value	Cortex Log2FC	Outer Nucleus p-value	Outer Nucleus Log2FC	Inner Nucleus p-value	Inner Nucleus Log2FC
		65 kDa regulatory subunit A alpha isoform						
O43390; O60506	HNRNPR; SYNCRIP	Heterogeneous nuclear ribonucleoprotein R	4.90E-03	-2.31	NA	NA	6.62E-02	-1.05
Q02978	SLC25A11	Mitochondrial 2-oxoglutarate/malate carrier protein	4.64E-03	-2.31	9.57E-01	-0.02	3.61E-01	-0.43
O75964	ATP5MG	ATP synthase subunit g, mitochondrial	5.20E-03	-2.29	3.18E-01	0.47	2.57E-01	-0.54
Q9NQT8	KIF13B	Kinesin-like protein KIF13B	2.53E-05	-2.29	NA	NA	NA	NA
P46821	MAP1B	Microtubule-associated protein 1B	1.58E-04	-2.29	NA	NA	NA	NA
P53794	SLC5A3	Sodium/myo-inositol cotransporter	5.11E-03	-2.28	NA	NA	NA	NA
P78310	CXADR	Coxsackievirus and adenovirus receptor	1.17E-03	-2.27	NA	NA	NA	NA
Q9NZJ7	MTCH1	Mitochondrial carrier homolog 1	7.70E-03	-2.27	5.00E-01	0.36	5.29E-01	-0.43
O60664	PLIN3	Perilipin-3	6.96E-04	-2.26	8.25E-03	-1.66	7.97E-03	-1.45
P53675; Q00610	CLTC; CLTCL1	Clathrin heavy chain 2	4.26E-03	-2.25	1.20E-02	-1.06	7.92E-05	-2.12
P35580	MYH10	Myosin-10	5.89E-04	-2.25	NA	NA	NA	NA
P13861	PRKAR2A	cAMP-dependent protein kinase type II-alpha regulatory subunit	1.23E-04	-2.24	NA	NA	NA	NA
P32856	STX2	Syntaxin-2	1.78E-04	-2.23	NA	NA	NA	NA
P11117	ACP2	Lysosomal acid phosphatase	9.84E-03	-2.23	NA	NA	NA	NA
P62820	RAB1A	Ras-related protein Rab-1A	3.08E-04	-2.21	1.53E-03	-2.34	3.74E-04	-3.02
P63218	GNG5	Guanine nucleotide-binding protein G(I)/G(S)/G(O) subunit gamma-5	1.50E-04	-2.21	7.39E-04	-4.38	NA	NA
Q00610	CLTC	Clathrin heavy chain 1	2.24E-03	-2.21	2.52E-03	-0.82	3.79E-01	-0.27
P07384	CAPN1	Calpain-1 catalytic subunit	6.97E-03	-2.21	NA	NA	NA	NA
Q6XZF7	DNMBP	Dynamin-binding protein	3.82E-04	-2.21	2.51E-01	-0.63	NA	NA
Q92734	TFG	Protein TFG	5.69E-06	-2.21	NA	NA	6.07E-02	-1.41
O14787; Q92973	TNPO1; TNPO2	Transportin-2	2.65E-04	-2.20	8.45E-03	-0.72	1.02E-01	0.83
P06213	INSR	Insulin receptor	2.65E-03	-2.19	NA	NA	NA	NA
O75369; P21333; Q14315	FLNA; FLNB; FLNC	Filamin-B	2.52E-04	-2.19	1.01E-03	-2.13	NA	NA
P08574	CYC1	Cytochrome c1, heme protein, mitochondrial	1.51E-03	-2.19	1.14E-01	-0.69	3.05E-03	-2.43
Q92973	TNPO1	Transportin-1	1.19E-03	-2.19	8.81E-02	-0.64	3.23E-02	-1.07
P35579	MYH9	Myosin-9	2.35E-03	-2.19	3.59E-01	-0.24	7.64E-02	-0.68
P54709	ATP1B3	Sodium/potassium-transporting ATPase subunit beta-3	7.98E-03	-2.17	4.12E-02	-1.9	NA	NA
O75695	RP2	Protein XRP2	1.80E-04	-2.17	3.20E-04	-2.75	1.26E-02	-2.00

Protein Group	Gene Group	Protein Description	Cortex p-value	Cortex Log2FC	Outer Nucleus p-value	Outer Nucleus Log2FC	Inner Nucleus p-value	Inner Nucleus Log2FC
P12956	XRCC6	X-ray repair cross-complementing protein 6	2.72E-04	-2.17	5.69E-01	-0.16	3.70E-03	-1.43
P61764	STXBP1	Syntaxin-binding protein 1	3.13E-04	-2.16	6.06E-01	0.24	5.04E-02	-1.36
Q96FZ7	CHMP6	Charged multivesicular body protein 6	4.40E-03	-2.16	NA	NA	NA	NA
Q96QR8	PURB	Transcriptional activator protein Pur-beta	2.77E-04	-2.15	8.07E-01	-0.10	1.69E-04	-1.84
Q14008	CKAP5	Cytoskeleton-associated protein 5	1.49E-03	-2.15	NA	NA	NA	NA
P01111; P01112	HRAS; NRAS	GTPase NRas	5.01E-03	-2.15	NA	NA	NA	NA
P63010	AP2B1	AP-2 complex subunit beta	1.19E-03	-2.14	6.33E-01	-0.18	1.52E-02	-1.31
O43707	ACTN4	Alpha-actinin-4	1.82E-03	-2.13	9.88E-01	-0.01	2.19E-03	-1.73
P29992; P50148	GNA11; GNAQ	Guanine nucleotide-binding protein subunit alpha-11	3.45E-04	-2.12	NA	NA	NA	NA
Q12846	STX4	Syntaxin-4	2.44E-03	-2.12	NA	NA	NA	NA
P61020	RAB5B	Ras-related protein Rab-5B	2.92E-03	-2.12	1.18E-03	-2.43	NA	NA
P21333; Q14315	FLNA; FLNC	Filamin-A	1.11E-04	-2.12	1.68E-02	-1.66	7.64E-04	-1.94
Q12905	ILF2	Interleukin enhancer-binding factor 2	3.78E-03	-2.11	2.06E-01	-0.59	1.24E-01	-1.17
Q9NZW5	PALS2	Protein PALS2	2.16E-03	-2.11	NA	NA	NA	NA
P35222	CTNNB1	Catenin beta-1	1.66E-03	-2.11	2.74E-02	-1.34	4.18E-03	-1.45
Q86VP6	CAND1	Cullin-associated NEDD8-dissociated protein 1	1.04E-03	-2.10	7.50E-05	-1.29	6.91E-04	-1.79
P09543	CNP	2',3'-cyclic-nucleotide 3'-phosphodiesterase	3.77E-04	-2.10	NA	NA	NA	NA
Q14203	DCTN1	Dynactin subunit 1	4.74E-04	-2.10	4.44E-02	-0.79	7.45E-03	-1.83
Q14194; Q14195; Q16555	CRMP1; DPYSL2; DPYSL3	Dihydropyrimidinase-related protein 1	5.72E-04	-2.09	NA	NA	NA	NA
Q9NZU5	LMCD1	LIM and cysteine-rich domains protein 1	6.44E-03	-2.08	5.90E-02	-1.03	1.48E-01	-0.86
P11277	SPTB	Spectrin beta chain, erythrocytic	2.03E-04	-2.06	2.45E-03	-1.51	1.54E-04	-2.32
P61106	RAB14	Ras-related protein Rab-14	1.29E-04	-2.06	2.63E-03	-1.74	5.21E-03	-1.65
P00533	EGFR	Epidermal growth factor receptor	5.05E-03	-2.05	NA	NA	NA	NA
P26447	S100A4	Protein S100-A4	4.78E-03	-2.05	5.58E-01	0.33	5.85E-01	-0.24
O00505; O00629	KPNA3; KPNA4	Importin subunit alpha-4	2.93E-03	-2.05	7.76E-01	0.07	4.56E-04	-1.7
P11277; Q01082	SPTB; SPTBN1	Spectrin beta chain, erythrocytic	1.34E-03	-2.04	4.48E-02	-1.13	NA	NA
P55060	CSE1L	Exportin-2	1.69E-03	-2.04	1.01E-01	-0.57	3.96E-03	-1.49
Q13449	LSAMP	Limbic system-associated membrane protein	7.73E-04	-2.03	9.83E-04	-2.81	2.50E-04	-2.36
P21333	FLNA	Filamin-A	6.55E-04	-2.02	4.40E-02	-0.98	4.00E-01	-0.28

Protein Group	Gene Group	Protein Description	Cortex p-value	Cortex Log2FC	Outer Nucleus p-value	Outer Nucleus Log2FC	Inner Nucleus p-value	Inner Nucleus Log2FC
Q93050	ATP6V0A1	V-type proton ATPase 116 kDa subunit a1	8.32E-04	-2.02	NA	NA	NA	NA
Q13557	CAMK2D	Calcium/calmodulin-dependent protein kinase type II subunit delta	3.59E-03	-2.02	NA	NA	NA	NA
P05023	ATP1A1	Sodium/potassium-transporting ATPase subunit alpha-1	7.79E-04	-2.01	9.83E-04	-3.04	NA	NA
P50570; Q9UQ16	DNM2; DNM3	Dynamin-2	3.62E-04	-2.01	NA	NA	NA	NA
P46783	RPS10	40S ribosomal protein S10	9.27E-03	-2.01	NA	NA	NA	NA
Q9HBH5	RDH14	Retinol dehydrogenase 14	8.86E-03	-2.01	NA	NA	NA	NA
P11142	HSPA8	Heat shock cognate 71 kDa protein	5.20E-04	-2.00	1.68E-04	-1.95	8.38E-04	-1.88
Q13162	PRDX4	Peroxiredoxin-4	1.79E-03	-1.99	2.76E-01	-0.75	7.09E-01	0.20
Q6ZUX7	LHFPL2	LHFPL tetraspan subfamily member 2 protein	1.50E-03	-1.98	NA	NA	NA	NA
O76003	GLRX3	Glutaredoxin-3	4.43E-03	-1.98	NA	NA	NA	NA
O60437	PPL	Periplakin	2.53E-04	-1.97	8.38E-02	-1.05	4.57E-02	-1.56
Q00577	PURA	Transcriptional activator protein Pur-alpha	1.20E-03	-1.97	8.66E-02	-0.69	4.12E-02	-1.13
Q01484; Q12955	ANK2; ANK3	Ankyrin-2	1.72E-03	-1.97	5.97E-02	-0.71	1.32E-02	-1.02
P17980	PSMC3	26S proteasome regulatory subunit 6A	1.33E-03	-1.97	NA	NA	NA	NA
Q9UNF1	MAGED2	Melanoma-associated antigen D2	9.54E-04	-1.96	6.26E-03	-1.85	8.66E-02	-1.15
Q13443	ADAM9	Disintegrin and metalloproteinase domain-containing protein 9	7.12E-05	-1.96	NA	NA	NA	NA
Q93008	USP9X	Probable ubiquitin carboxyl-terminal hydrolase FAF-X	4.27E-03	-1.96	7.95E-01	0.09	4.61E-01	-0.38
P26232; P35221	CTNNA1; CTNNA2	Catenin alpha-2	7.11E-03	-1.95	7.04E-03	-1.64	1.21E-01	-0.67
Q9BTU6	PI4K2A	Phosphatidylinositol 4-kinase type 2-alpha	7.15E-03	-1.95	NA	NA	NA	NA
P10301	RRAS	Ras-related protein R-Ras	3.44E-04	-1.94	NA	NA	NA	NA
P53985	SLC16A1	Monocarboxylate transporter 1	7.46E-03	-1.94	NA	NA	NA	NA
P62330	ARF6	ADP-ribosylation factor 6	2.65E-03	-1.94	NA	NA	NA	NA
P62826	RAN	GTP-binding nuclear protein Ran	6.24E-06	-1.94	1.16E-01	-0.74	5.01E-01	-0.21
Q5VYK3	ECPAS	Proteasome adapter and scaffold protein ECM29	3.74E-03	-1.94	NA	NA	NA	NA
Q96LR9	APOLD1	Apolipoprotein L domain-containing protein 1	2.83E-04	-1.94	NA	NA	NA	NA

Protein Group	Gene Group	Protein Description	Cortex p-value	Cortex Log2FC	Outer Nucleus p-value	Outer Nucleus Log2FC	Inner Nucleus p-value	Inner Nucleus Log2FC
P20042	EIF2S2	Eukaryotic translation initiation factor 2 subunit 2	5.43E-03	-1.93	NA	NA	NA	NA
Q01484	ANK2	Ankyrin-2	2.56E-03	-1.92	1.52E-02	-1.15	1.46E-04	-1.91
Q14964	RAB39A	Ras-related protein Rab-39A	2.90E-04	-1.92	NA	NA	NA	NA
Q6IAA8	LAMTOR1	Ragulator complex protein LAMTOR1	3.77E-05	-1.92	2.29E-04	-1.59	1.23E-02	-1.35
P54289	CACNA2D1	Voltage-dependent calcium channel subunit alpha-2/delta-1	1.84E-03	-1.91	NA	NA	NA	NA
O15020; Q01082	SPTBN1; SPTBN2	Spectrin beta chain, non-erythrocytic 2	3.51E-03	-1.90	2.89E-01	-0.44	1.76E-03	-1.23
Q9NZH0	GPRC5B	G-protein coupled receptor family C group 5 member B	2.72E-03	-1.90	NA	NA	NA	NA
Q99436	PSMB7	Proteasome subunit beta type-7	1.68E-03	-1.90	NA	NA	NA	NA
Q96CS3	FAF2	FAS-associated factor 2	6.38E-04	-1.90	8.69E-01	-0.08	NA	NA
Q14204	DYNC1H1	Cytoplasmic dynein 1 heavy chain 1	6.35E-04	-1.89	8.63E-02	-0.53	1.88E-02	-1.06
P18084	ITGB5	Integrin beta-5	5.62E-03	-1.88	NA	NA	NA	NA
Q9H0E2	TOLLIP	Toll-interacting protein	8.71E-04	-1.88	4.82E-04	-1.99	NA	NA
P84085	ARF5	ADP-ribosylation factor 5	3.08E-04	-1.88	1.81E-02	-0.99	1.48E-03	-1.78
P62495	ETF1	Eukaryotic peptide chain release factor subunit 1	1.36E-04	-1.88	8.23E-01	-0.09	5.25E-01	-0.26
P20339; P51148; P61020	RAB5A; RAB5B; RAB5C	Ras-related protein Rab-5A	1.33E-03	-1.88	8.83E-02	-0.92	3.13E-02	-1.05
P01111; P01112; P01116	HRAS; KRAS; NRAS	GTPase NRas	1.45E-03	-1.87	6.06E-02	-0.99	NA	NA
P07355	ANXA2	Annexin A2	2.58E-03	-1.86	2.58E-02	-1.11	4.79E-03	-1.73
Q15149	PLEC	Plectin	9.10E-04	-1.86	4.30E-03	-1.16	1.04E-02	-1.33
Q9NZJ9	NUDT4	Diphosphoinositol polyphosphate phosphohydrolase 2	1.50E-05	-1.86	6.08E-01	-0.22	1.50E-03	-2.17
P11717	IGF2R	Cation-independent mannose-6-phosphate receptor	6.63E-03	-1.85	NA	NA	NA	NA
P23396	RPS3	40S ribosomal protein S3	1.13E-03	-1.85	3.01E-01	0.38	3.82E-01	0.44
P01116	KRAS	GTPase KRas	1.12E-03	-1.85	1.92E-03	-2.13	7.45E-04	-1.70
P55011	SLC12A2	Solute carrier family 12 member 2	7.05E-03	-1.83	6.65E-03	-2.52	NA	NA
P61019; Q8WUD1	RAB2A;RAB2B	Ras-related protein Rab-2A	1.14E-04	-1.83	6.46E-03	-1.42	1.71E-02	-1.36
Q58EX2	SDK2	Protein sidekick-2	1.07E-03	-1.83	NA	NA	NA	NA
Q9NP72	RAB18	Ras-related protein Rab-18	2.41E-03	-1.81	1.86E-02	-1.21	9.18E-02	-0.74
Q8TD20	SLC2A12	Solute carrier family 2, facilitated glucose transporter member 12	1.66E-03	-1.81	2.57E-02	-1.83	NA	NA

Protein Group	Gene Group	Protein Description	Cortex p-value	Cortex Log2FC	Outer Nucleus p-value	Outer Nucleus Log2FC	Inner Nucleus p-value	Inner Nucleus Log2FC
P33527	ABCC1	Multidrug resistance-associated protein 1	3.82E-03	-1.81	NA	NA	NA	NA
P53621	COPA	Coatomer subunit alpha	3.54E-03	-1.80	9.72E-01	-0.01	NA	NA
P35579; P35580; P35749; Q7Z406	MYH10; MYH11; MYH14; MYH9	Myosin-9	4.12E-03	-1.79	NA	NA	2.77E-02	-1.48
P02786	TFRC	Transferrin receptor protein 1	3.17E-03	-1.78	NA	NA	NA	NA
O75781	PALM	Paralemmin-1	3.72E-03	-1.78	1.22E-02	-1.61	4.29E-04	-1.52
P05023; P13637	ATP1A1; ATP1A3	Sodium/potassium-transporting ATPase subunit alpha-1	1.43E-04	-1.77	9.53E-03	-2.49	NA	NA
Q9H0U4	RAB1B	Ras-related protein Rab-1B	7.51E-03	-1.77	1.08E-03	-2.75	NA	NA
Q9UL25	RAB21	Ras-related protein Rab-21	6.56E-03	-1.77	3.78E-03	-1.72	1.33E-02	-1.24
Q9Y6G9	DYNC1LI1	Cytoplasmic dynein 1 light intermediate chain 1	4.20E-03	-1.76	9.71E-01	-0.02	NA	NA
P05023; P13637; P50993	ATP1A1; ATP1A2; ATP1A3	Sodium/potassium-transporting ATPase subunit alpha-1	1.83E-03	-1.76	4.67E-03	-2.45	NA	NA
Q13619; Q13620	CUL4A; CUL4B	Cullin-4A	9.36E-04	-1.76	4.34E-01	-0.22	2.03E-01	-0.63
P04899; P08754; P11488; P63096	GNAI1; GNAI2; GNAI3; GNAT1	Guanine nucleotide-binding protein G(i) subunit alpha-2	4.93E-04	-1.76	NA	NA	NA	NA
P08238; Q58FF7	HSP90AB1;HSP90AB3P	Heat shock protein HSP 90-beta	2.85E-03	-1.75	NA	NA	NA	NA
Q7L9L4; Q9H8S9	MOB1A; MOB1B	MOB kinase activator 1B	5.22E-04	-1.73	1.29E-01	-0.64	1.10E-02	-1.91
O43491	EPB41L2	Band 4.1-like protein 2	1.15E-07	-1.73	2.80E-03	-1.75	1.33E-03	-2.24
Q8TAT6	NPLOC4	Nuclear protein localization protein 4 homolog	1.63E-04	-1.71	NA	NA	3.66E-02	-0.98
P08237	PFKM	ATP-dependent 6-phosphofructokinase, muscle type	1.84E-03	-1.71	5.75E-02	-0.82	4.91E-01	-0.44
P12814	ACTN1	Alpha-actinin-1	3.95E-03	-1.71	1.67E-01	-0.58	6.81E-02	-0.92
P26641	EEF1G	Elongation factor 1-gamma	5.50E-03	-1.71	1.25E-01	-0.55	3.69E-01	-0.39
O43681	GET3	ATPase GET3	3.45E-03	-1.70	NA	NA	4.42E-02	-0.96
O00192	ARVCF	Armadillo repeat protein deleted in velo-cardio-facial syndrome	8.97E-04	-1.70	8.42E-03	-1.75	1.52E-05	-2.06
Q68EM7	ARHGAP17	Rho GTPase-activating protein 17	5.42E-04	-1.70	2.55E-01	-0.55	NA	NA
O43795	MYO1B	Unconventional myosin-Ib	1.81E-03	-1.69	3.34E-02	-0.89	7.87E-03	-1.34
P20339; P61020	RAB5A; RAB5B	Ras-related protein Rab-5A	1.82E-03	-1.69	NA	NA	NA	NA
Q7L576	CYFIP1	Cytoplasmic FMR1-interacting protein 1	3.08E-03	-1.69	NA	NA	NA	NA

Protein Group	Gene Group	Protein Description	Cortex p-value	Cortex Log2FC	Outer Nucleus p-value	Outer Nucleus Log2FC	Inner Nucleus p-value	Inner Nucleus Log2FC
O60763	USO1	General vesicular transport factor p115	6.92E-03	-1.68	2.80E-01	-0.43	2.69E-02	-1.09
P14923; P35222	CTNNB1; JUP	Junction plakoglobin	9.72E-03	-1.68	1.04E-01	-0.83	4.61E-02	-0.71
P43353	ALDH3B1	Aldehyde dehydrogenase family 3 member B1	4.06E-03	-1.68	NA	NA	NA	NA
P13591	NCAM1	Neural cell adhesion molecule 1	4.83E-03	-1.67	1.95E-04	-2.13	1.08E-02	-1.89
O60749; Q13596	SNX1; SNX2	Sorting nexin-2	4.30E-03	-1.67	NA	NA	NA	NA
Q8WVC6	DCAKD	Dephospho-CoA kinase domain-containing protein	4.68E-03	-1.67	4.96E-03	0.92	6.28E-01	-0.18
P13473	LAMP2	Lysosome-associated membrane glycoprotein 2	1.41E-03	-1.67	NA	NA	NA	NA
P61026	RAB10	Ras-related protein Rab-10	1.99E-04	-1.67	1.18E-03	-1.84	2.54E-03	-1.66
Q13617	CUL2	Cullin-2	7.46E-05	-1.66	1.19E-01	-0.49	1.72E-01	-0.53
O43707; P12814	ACTN1; ACTN4	Alpha-actinin-4	3.76E-03	-1.65	3.56E-01	0.39	9.79E-02	-0.85
Q9Y2Z0	SUGT1	Protein SGT1 homolog	1.24E-03	-1.64	NA	NA	NA	NA
P51149	RAB7A	Ras-related protein Rab-7a	1.84E-03	-1.63	1.77E-03	-2.30	4.57E-04	-2.42
P42224	STAT1	Signal transducer and activator of transcription 1-alpha/beta	3.57E-03	-1.63	2.31E-01	0.55	3.05E-01	-0.62
Q96CW1	AP2M1	AP-2 complex subunit mu	1.91E-03	-1.62	3.85E-02	-0.75	3.37E-02	-0.73
P05023; P13637; P50993; Q13733	ATP1A1; ATP1A2; ATP1A3; ATP1A4	Sodium/potassium-transporting ATPase subunit alpha-1	2.65E-03	-1.62	5.72E-03	-2.67	NA	NA
P07900; P08238; Q58FF7	HSP90AA1;HSP90AB1;HSP90AB3P	Heat shock protein HSP 90-alpha	1.34E-03	-1.61	NA	NA	NA	NA
P61204; P84077	ARF1; ARF3	ADP-ribosylation factor 3	9.00E-04	-1.61	6.98E-02	-0.60	2.10E-02	-1.07
Q92729	PTPRU	Receptor-type tyrosine-protein phosphatase U	3.82E-03	-1.61	1.05E-01	-0.83	NA	NA
P21926	CD9	CD9 antigen	6.99E-03	-1.61	NA	NA	NA	NA
P11234	RALB	Ras-related protein Ral-B	2.85E-04	-1.60	4.91E-03	-1.68	3.47E-02	-0.95
O60331	PIP5K1C	Phosphatidylinositol 4-phosphate 5-kinase type-1 gamma	4.78E-03	-1.59	1.32E-02	-1.44	NA	NA
P01112	HRAS	GTPase HRas	9.95E-03	-1.59	NA	NA	NA	NA
Q8N3E9	PLCD3	1-phosphatidylinositol 4,5-bisphosphate phosphodiesterase delta-3	1.86E-04	-1.59	4.35E-03	-1.34	NA	NA
P48165	GJA8	Gap junction alpha-8 protein	1.33E-04	-1.57	6.19E-04	-1.53	8.35E-04	-2.48
Q13555	CAMK2G	Calcium/calmodulin-dependent protein	8.23E-03	-1.57	1.55E-02	-1.06	NA	NA

Protein Group	Gene Group	Protein Description	Cortex p-value	Cortex Log2FC	Outer Nucleus p-value	Outer Nucleus Log2FC	Inner Nucleus p-value	Inner Nucleus Log2FC
		kinase type II subunit gamma						
P43490	NAMPT	Nicotinamide phosphoribosyltransferase	1.10E-04	-1.57	1.90E-01	-0.58	NA	NA
O43865; Q96HN2	AHCYL1; AHCYL2	S-adenosylhomocysteine hydrolase-like protein 1	8.75E-03	-1.56	NA	NA	NA	NA
P61225	RAP2B	Ras-related protein Rap-2b	3.41E-03	-1.56	1.96E-02	-1.96	NA	NA
P61224; P62834	RAP1A; RAP1B	Ras-related protein Rap-1b	7.36E-04	-1.56	5.82E-02	-0.88	2.05E-02	-1.16
Q8NCW6	GALNT11	Polypeptide N-acetylgalactosaminyltransferase 11	1.23E-03	-1.56	4.08E-02	-1.07	5.05E-03	-2.13
O00159	MYO1C	Unconventional myosin-Ic	1.42E-03	-1.56	8.41E-02	-0.69	5.74E-03	-1.51
P63096	GNAI1	Guanine nucleotide-binding protein G(i) subunit alpha-1	1.16E-03	-1.56	NA	NA	NA	NA
Q14152	EIF3A	Eukaryotic translation initiation factor 3 subunit A	6.79E-03	-1.55	3.70E-02	-0.83	1.11E-02	-1.16
Q9Y3S1	WNK2	Serine/threonine-protein kinase WNK2	2.37E-04	-1.54	8.73E-01	-0.11	3.01E-02	-0.98
P26196	DDX6	Probable ATP-dependent RNA helicase DDX6	6.24E-03	-1.54	NA	NA	NA	NA
O00231	PSMD11	26S proteasome non-ATPase regulatory subunit 11	5.90E-03	-1.54	3.17E-02	-0.76	2.46E-04	-1.84
Q6IQ22	RAB12	Ras-related protein Rab-12	1.89E-03	-1.54	1.56E-03	-2.04	3.49E-02	-1.66
P63010; Q10567	AP1B1; AP2B1	AP-2 complex subunit beta	9.65E-03	-1.54	4.65E-01	-0.19	2.65E-04	-1.98
Q13555; Q13557; Q9UQM7	CAMK2A; CAMK2D; CAMK2G	Calcium/calmodulin-dependent protein kinase type II subunit gamma	9.76E-04	-1.54	9.09E-07	-2.51	7.79E-04	-3.63
Q14964; Q96DA2	RAB39A; RAB39B	Ras-related protein Rab-39A	5.25E-05	-1.53	NA	NA	NA	NA
O94973	AP2A2	AP-2 complex subunit alpha-2	1.06E-03	-1.52	9.18E-02	-0.56	7.69E-02	-0.76
Q9HA65	TBC1D17	TBC1 domain family member 17	3.74E-03	-1.52	2.17E-01	-0.40	1.28E-01	-0.55
P15260	IFNGR1	Interferon gamma receptor 1	6.63E-04	-1.51	4.61E-03	-1.19	NA	NA
Q13045	FLII	Protein flightless-1 homolog	7.25E-03	-1.51	8.61E-01	0.06	NA	NA
P35579; P35580	MYH10; MYH9	Myosin-9	6.79E-03	-1.51	2.12E-02	-0.95	2.00E-04	-1.71
P54136	RARS1	Arginine--tRNA ligase, cytoplasmic	1.61E-03	-1.51	3.48E-01	-0.33	1.98E-02	-0.94
Q01968	OCRL	Inositol polyphosphate 5-phosphatase OCRL	9.34E-03	-1.50	NA	NA	NA	NA
Q9Y2J2	EPB41L3	Band 4.1-like protein 3	5.48E-06	-1.49	1.62E-02	-1.50	1.57E-03	-1.99

Protein Group	Gene Group	Protein Description	Cortex p-value	Cortex Log2FC	Outer Nucleus p-value	Outer Nucleus Log2FC	Inner Nucleus p-value	Inner Nucleus Log2FC
P63092; Q5JWF2	GNAS	Guanine nucleotide-binding protein G(s) subunit alpha isoforms short	1.02E-03	-1.49	3.62E-03	-2.03	2.08E-03	-1.67
Q8N0X7	SPART	Spartin	3.03E-03	-1.48	1.51E-03	-1.67	NA	NA
O14576	DYNC1I1	Cytoplasmic dynein 1 intermediate chain 1	8.57E-04	-1.48	8.02E-01	-0.11	7.65E-03	-1.50
Q8TCT0	CERK	Ceramide kinase	6.09E-03	-1.45	7.63E-05	-2.07	5.67E-04	-2.35
Q9NV96	TMEM30A	Cell cycle control protein 50A	6.51E-03	-1.45	2.39E-03	-1.50	9.04E-03	-1.91
O15498	YKT6	Synaptobrevin homolog YKT6	2.45E-03	-1.44	6.57E-02	-1.16	2.05E-03	-1.97
P62820; Q9H0U4	RAB1A;RAB1B	Ras-related protein Rab-1A	5.82E-03	-1.43	1.98E-03	-1.92	2.09E-03	-1.15
O14818	PSMA7	Proteasome subunit alpha type-7	3.83E-05	-1.43	3.40E-02	-0.72	4.74E-03	-1.91
Q99426	TBCB	Tubulin-folding cofactor B	2.53E-03	-1.43	1.02E-04	-1.59	1.15E-03	-1.92
P11171; Q9Y2J2	EPB41; EPB41L3	Protein 4.1	3.60E-03	-1.42	9.76E-03	-1.98	6.30E-02	-1.00
Q9NX46	ADPRS	ADP-ribose glycohydrolase ARH3	1.68E-03	-1.42	6.25E-04	-1.27	1.26E-03	-1.54
Q8NFZ8	CADM4	Cell adhesion molecule 4	3.19E-04	-1.42	7.88E-03	-1.85	NA	NA
P13987	CD59	CD59 glycoprotein	9.78E-03	-1.38	2.02E-02	-2.07	9.94E-05	-3.71
Q5T9C9	PIP5KL1	Phosphatidylinositol 4-phosphate 5-kinase-like protein 1	8.74E-05	-1.37	4.47E-03	-1.62	1.58E-04	-2.62
P47756	CAPZB	F-actin-capping protein subunit beta	1.48E-04	-1.36	1.71E-01	-0.55	9.11E-04	-2.09
Q9NXG0	CNTLN	Centlein	5.49E-04	-1.35	5.44E-03	-2.05	NA	NA
P09382	LGALS1	Galectin-1	5.53E-03	-1.35	6.48E-03	-2.34	7.18E-04	-2.87
P04899; P08754; P63096	GNAI1; GNAI2; GNAI3	Guanine nucleotide-binding protein G(i) subunit alpha-2	6.61E-03	-1.33	3.34E-02	-1.24	9.40E-05	-2.75
P40227; Q92526	CCT6A; CCT6B	T-complex protein 1 subunit zeta	3.89E-03	-1.32	1.07E-01	-0.70	6.72E-04	-1.87
Q01082	SPTBN1	Spectrin beta chain, non-erythrocytic 1	2.38E-03	-1.30	4.80E-02	-0.88	5.23E-04	-1.57
Q08722	CD47	Leukocyte surface antigen CD47	4.50E-03	-1.29	7.32E-03	-2.26	1.56E-03	-3.20
P22748	CA4	Carbonic anhydrase 4	9.30E-04	-1.27	3.77E-04	-1.84	6.66E-03	-2.19
Q01484; Q9Y4W6	AFG3L2; ANK2	Ankyrin-2	5.58E-03	-1.25	2.27E-03	-1.15	1.11E-03	-1.70
Q15126	PMVK	Phosphomevalonate kinase	9.07E-03	-1.24	8.70E-01	0.07	5.13E-03	-1.61
Q9Y5L0	TNPO3	Transportin-3	3.51E-03	-1.23	2.87E-01	-0.47	4.77E-03	-2.20
Q93034	CUL5	Cullin-5	1.49E-04	-1.18	1.47E-01	-0.58	5.27E-05	-1.79
P11171; Q9H4G0	EPB41; EPB41L1	Protein 4.1	3.65E-03	-1.17	3.39E-03	-1.74	2.99E-03	-2.39
Q96DA2	RAB39B	Ras-related protein Rab-39B	7.16E-03	-1.13	2.06E-04	-1.66	5.25E-03	-1.80

Protein Group	Gene Group	Protein Description	Cortex p-value	Cortex Log2FC	Outer Nucleus p-value	Outer Nucleus Log2FC	Inner Nucleus p-value	Inner Nucleus Log2FC
P05026	ATP1B1	Sodium/potassium-transporting ATPase subunit beta-1	7.63E-03	-1.09	1.50E-03	-2.37	1.34E-03	-4.41
P53816	PLAAT3	Phospholipase A and acyltransferase 3	5.76E-03	-1.05	2.56E-03	-1.06	3.10E-03	-1.66
P20340; Q9NRW1	RAB6A; RAB6B	Ras-related protein Rab-6A	8.46E-03	-1.04	1.57E-04	-1.56	1.40E-04	-2.44
P08134; P61586; P62745	RHOA; RHOB; RHOC	Rho-related GTP-binding protein RhoC	7.27E-03	-1.00	1.93E-03	-1.75	6.82E-01	-0.20
Q99829	CPNE1	Copine-1	4.34E-03	-0.93	5.69E-03	-1.66	NA	NA
P13693	TPT1	Translationally-controlled tumor protein	5.80E-03	-0.89	7.50E-02	-0.97	4.66E-03	-2.06
Q9H977	WDR54	WD repeat-containing protein 54	4.75E-03	1.70	3.17E-02	0.66	7.60E-02	-0.92
P07315	CRYGC	Gamma-crystallin C	1.78E-03	1.79	8.80E-02	0.57	9.50E-02	-0.67
Q9BXT8	RNF17	RING finger protein 17	8.55E-04	1.90	2.30E-01	0.50	3.91E-01	-0.36
P07205	PGK2	Phosphoglycerate kinase 2	5.99E-03	1.91	3.29E-01	0.41	3.28E-01	-0.57
Q64LD2	WDR25	WD repeat-containing protein 25	9.02E-04	2.00	8.35E-03	1.28	3.82E-01	0.45
P32754	HPD	4-hydroxyphenylpyruvate dioxygenase	6.61E-04	2.10	4.16E-02	1.16	1.52E-01	0.91
P07900; P08238; Q58FF6;Q58FF8	HSP90AA1;HSP90AB1;HSP90AB2P; HSP90AB4P	Heat shock protein HSP 90-alpha	NA	NA	2.05E-04	-2.86	NA	NA
P80723	BASP1	Brain acid soluble protein 1	5.77E-01	-0.39	4.76E-03	-3.21	2.82E-04	-4.77
Q16270	IGFBP7	Insulin-like growth factor-binding protein 7	1.04E-01	-0.72	3.96E-03	-3.11	NA	NA
O94856	NFASC	Neurofascin	2.34E-02	-1.13	4.48E-04	-2.84	2.31E-04	-3.05
O43491; Q9Y2J2	EPB41L2; EPB41L3	Band 4.1-like protein 2	6.82E-02	-0.65	2.06E-03	-2.67	NA	NA
Q8N3J6	CADM2	Cell adhesion molecule 2	4.24E-02	-1.16	4.80E-03	-2.63	2.91E-04	-2.86
Q6N022;Q9P273	TENM3; TENM4	Teneurin-4	6.08E-01	-0.23	3.67E-03	-2.53	NA	NA
Q8IXI1	RHOT2	Mitochondrial Rho GTPase 2	6.91E-02	-0.80	5.03E-03	-2.48	NA	NA
O14960	LECT2	Leukocyte cell-derived chemotaxin-2	9.27E-01	0.08	2.01E-03	-2.47	NA	NA
Q9BY67	CADM1	Cell adhesion molecule 1	1.12E-02	-1.73	2.71E-03	-2.47	NA	NA
P11233	RALA	Ras-related protein Ral-A	1.28E-01	-0.61	2.33E-04	-2.39	1.92E-05	-3.41
P06899; P23527; P33778; Q16778; Q8N257;Q99880	H2BC11; H2BC13; H2BC17; H2BC21; H2BC3; H2BU1	Histone H2B type 1-J	NA	NA	7.18E-03	-2.39	NA	NA

Protein Group	Gene Group	Protein Description	Cortex p-value	Cortex Log2FC	Outer Nucleus p-value	Outer Nucleus Log2FC	Inner Nucleus p-value	Inner Nucleus Log2FC
P39060	COL18A1	Collagen alpha-1(XVIII) chain	2.67E-02	-2.13	3.41E-03	-2.38	NA	NA
P63165	SUMO1	Small ubiquitin-related modifier 1	1.97E-02	-1.30	8.96E-03	-2.36	NA	NA
O60884	DNAJA2	DnaJ homolog subfamily A member 2	4.49E-02	-0.97	4.70E-04	-2.35	NA	NA
P35241	RDX	Radixin	3.66E-02	-1.24	3.84E-03	-2.34	5.16E-03	-2.52
Q9ULX7	CA14	Carbonic anhydrase 14	1.34E-01	-0.73	4.44E-04	-2.33	8.97E-04	-3.28
Q9BX67	JAM3	Junctional adhesion molecule C	2.47E-02	-1.24	2.43E-03	-2.23	1.13E-03	-2.63
Q9NTI2	ATP8A2	Phospholipid-transporting ATPase IB	9.54E-02	-0.86	1.46E-03	-2.20	2.83E-03	-1.84
Q9UGT4	SUSD2	Sushi domain-containing protein 2	1.04E-02	-1.94	2.58E-03	-2.20	NA	NA
P08754	GNAI3	Guanine nucleotide-binding protein G(i) subunit alpha-3	1.31E-02	-1.45	3.88E-03	-2.18	NA	NA
O95715	CXCL14	C-X-C motif chemokine 14	3.78E-02	-1.87	5.97E-03	-2.17	NA	NA
Q9UHN6	CEMIP2	Cell surface hyaluronidase	1.55E-02	-1.45	4.14E-03	-2.12	1.14E-03	-2.81
Q6N022	TENM4	Teneurin-4	1.51E-01	-0.63	7.95E-03	-2.11	NA	NA
P20340	RAB6A	Ras-related protein Rab-6A	4.33E-02	-0.57	2.77E-04	-2.11	1.47E-03	-2.11
Q8IVW8	SPNS2	Protein spinster homolog 2	8.65E-02	-0.86	1.35E-03	-2.10	NA	NA
Q9UI40	SLC24A2	Sodium/potassium/calcium exchanger 2	3.55E-02	-0.82	1.09E-03	-2.07	2.02E-04	-2.96
P08134; P61586	RHOA; RHOC	Rho-related GTP-binding protein RhoC	8.45E-01	-0.14	1.37E-03	-2.06	3.95E-04	-2.23
P34096	RNASE4	Ribonuclease 4	5.00E-01	-0.36	8.18E-03	-2.06	NA	NA
P04156	PRNP	Major prion protein	3.81E-02	-0.79	5.19E-03	-2.01	1.43E-03	-2.49
Q9NQ79	CRTAC1	Cartilage acidic protein 1	6.29E-02	-0.85	4.60E-03	-1.97	6.09E-05	-3.24
Q6UWM7	LCTL	Lactase-like protein	2.07E-02	-1.28	5.96E-04	-1.95	1.66E-03	-1.88
P48509	CD151	CD151 antigen	7.48E-02	-1.06	6.43E-03	-1.95	4.19E-03	-2.45
O94812	BAIAP3	BAI1-associated protein 3	NA	NA	2.74E-03	-1.94	NA	NA
P26038	MSN	Moesin	4.98E-02	-0.99	4.77E-04	-1.93	7.93E-04	-1.61
Q92823	NRCAM	Neuronal cell adhesion molecule	1.39E-02	-1.31	5.65E-03	-1.93	8.66E-05	-3.02
O75955	FLOT1	Flotillin-1	3.90E-02	-0.79	3.84E-04	-1.92	2.16E-04	-2.58
P29317	EPHA2	Ephrin type-A receptor 2	1.80E-02	-1.08	1.65E-03	-1.89	NA	NA
P0DOY2;P0DOY3	IGLC2; IGLC3	Immunoglobulin lambda constant 2	8.44E-01	0.09	4.00E-03	-1.88	1.42E-03	-2.35
P01034	CST3	Cystatin-C	8.97E-01	-0.10	6.13E-03	-1.87	4.56E-03	-2.73
P36955	SERPINF1	Pigment epithelium-derived factor	6.88E-01	0.24	5.31E-03	-1.84	NA	NA
O95490	ADGRL2	Adhesion G protein-coupled receptor L2	1.10E-01	-0.87	6.96E-03	-1.83	6.09E-04	-2.51
P15153; P17081; P60953;	CDC42; RAC1; RAC2; RHOG;	Ras-related C3 botulinum toxin substrate 2	3.02E-01	0.69	4.40E-03	-1.82	NA	NA

Protein Group	Gene Group	Protein Description	Cortex p-value	Cortex Log2FC	Outer Nucleus p-value	Outer Nucleus Log2FC	Inner Nucleus p-value	Inner Nucleus Log2FC
P63000; P84095	RHOQ							
Q9Y624	F11R	Junctional adhesion molecule A	1.74E-02	-0.98	7.06E-03	-1.75	NA	NA
Q96ST8	CEP89	Centrosomal protein of 89 kDa	1.79E-01	-0.76	6.85E-03	-1.75	9.31E-04	-3.54
P61586	RHOA	Transforming protein RhoA	7.12E-01	-0.15	3.61E-04	-1.71	1.05E-02	-2.17
P04216	THY1	Thy-1 membrane glycoprotein	4.05E-01	-0.46	3.65E-03	-1.70	1.32E-03	-3.51
P11233; P11234	RALA; RALB	Ras-related protein Ral-A	2.16E-01	-0.52	2.87E-04	-1.70	6.82E-03	-1.40
Q15223	NECTIN1	Nectin-1	4.61E-01	-0.36	8.62E-03	-1.68	NA	NA
P31946; P61981	YWHAB; YWHAG	14-3-3 protein beta/alpha	1.33E-02	-1.98	8.14E-04	-1.68	NA	NA
P31946; P61981.1	YWHAB; YWHAG	14-3-3 protein beta/alpha	NA	NA	8.14E-04	-1.68	NA	NA
P10909	CLU	Clusterin	8.82E-02	-1.05	6.87E-03	-1.65	3.13E-03	-1.76
Q13515	BFSP2	Phakinin	1.05E-01	-0.62	6.58E-04	-1.64	1.13E-03	-1.99
Q96KP4	CNDP2	Cytosolic non-specific dipeptidase	8.94E-02	-0.57	9.59E-04	-1.64	3.65E-04	-2.20
P11171	EPB41	Protein 4.1	2.68E-02	-1.36	6.52E-03	-1.61	4.98E-05	-2.18
P12268; P20839	IMPDH1; IMPDH2	Inosine-5'-monophosphate dehydrogenase 2	9.31E-02	-0.73	2.48E-03	-1.60	NA	NA
P01857; P01860	IGHG1; IGHG3	Immunoglobulin heavy constant gamma 1	9.31E-01	-0.06	4.91E-03	-1.57	2.48E-03	-2.00
P62714; P67775	PPP2CA; PPP2CB	Serine/threonine-protein phosphatase 2A catalytic subunit beta isoform	NA	NA	8.53E-03	-1.53	NA	NA
Q1MSJ5	CSPP1	Centrosome and spindle pole-associated protein 1	3.86E-01	0.44	1.10E-03	-1.53	1.20E-03	-2.33
O75436; Q4G0F5	VPS26A; VPS26B	Vacuolar protein sorting-associated protein 26A	1.23E-01	0.83	2.18E-03	1.98	9.44E-02	0.91
Q13555; Q13557; Q9UQM7.1	CAMK2A; CAMK2D; CAMK2G	Calcium/calmodulin-dependent protein kinase type II subunit gamma	NA	NA	NA	NA	7.79E-04	-3.63
O43491; Q9H4G0;Q9Y2J2	EPB41L1; EPB41L2; EPB41L3	Band 4.1-like protein 2	1.81E-02	-1.46	1.80E-02	-1.43	8.12E-05	-3.32
Q14254	FLOT2	Flotillin-2	1.51E-02	-1.06	1.06E-02	-2.10	1.39E-04	-3.03
P04899; P08754; P63096.1	GNAI1; GNAI2; GNAI3	Guanine nucleotide-binding protein G(i) subunit alpha-2	NA	NA	NA	NA	9.40E-05	-2.75
P60953	CDC42	Cell division control protein 42 homolog	2.60E-01	-0.44	2.43E-02	-1.14	2.70E-05	-2.70
P06733; P09104; P13929	ENO1; ENO2; ENO3	Alpha-enolase	8.27E-02	-0.93	1.14E-01	-1.10	9.51E-03	-2.68

Protein Group	Gene Group	Protein Description	Cortex p-value	Cortex Log2FC	Outer Nucleus p-value	Outer Nucleus Log2FC	Inner Nucleus p-value	Inner Nucleus Log2FC
Q9H0C3	TMEM117	Transmembrane protein 117	4.14E-01	-0.33	4.05E-02	-0.91	3.28E-04	-2.61
Q9BQJ4	TMEM47	Transmembrane protein 47	7.41E-01	-0.19	9.29E-02	-0.95	1.77E-03	-2.60
O94760	DDAH1	N(G),N(G)-dimethylarginine dimethylaminohydrolase 1	3.43E-01	-0.47	3.46E-02	-1.48	4.43E-04	-2.59
P0C7U9	FAM87A	Protein FAM87A	NA	NA	NA	NA	3.57E-05	-2.58
Q03135	CAV1	Caveolin-1	7.86E-01	-0.16	4.52E-02	-1.22	1.28E-03	-2.57
P36969	GPX4	Phospholipid hydroperoxide glutathione peroxidase	3.11E-01	0.40	2.08E-02	-1.29	5.88E-04	-2.56
Q14244	MAP7	Ensconsin	7.36E-01	-0.19	2.46E-02	-1.30	1.09E-04	-2.53
Q92743	HTRA1	Serine protease HTRA1	9.23E-01	-0.06	4.44E-02	-1.25	7.65E-03	-2.46
Q92542	NCSTN	Nicastrin	1.90E-01	-0.42	4.25E-02	-1.25	1.94E-04	-2.43
P09972	ALDOC	Fructose-bisphosphate aldolase C	1.11E-01	-0.53	6.33E-03	-1.18	1.27E-04	-2.42
P08237; P17858	PFKL; PFKM	ATP-dependent 6-phosphofructokinase, muscle type	7.58E-01	0.12	2.67E-01	-0.38	9.36E-05	-2.39
P27361; P28482	MAPK1; MAPK3	Mitogen-activated protein kinase 3	3.31E-02	-0.60	2.13E-02	-1.04	3.39E-04	-2.37
P04792	HSPB1	Heat shock protein beta-1	4.04E-02	-1.20	1.16E-02	-1.43	7.74E-04	-2.36
Q9BWS9	CHID1	Chitinase domain-containing protein 1	3.28E-01	-0.40	6.98E-02	-1.30	3.52E-04	-2.33
P63000	RAC1	Ras-related C3 botulinum toxin substrate 1	8.31E-01	0.10	1.50E-02	-1.66	8.96E-05	-2.32
P15151	PVR	Poliovirus receptor	1.61E-02	-1.43	1.55E-02	-1.34	4.02E-04	-2.29
P61626	LYZ	Lysozyme C	8.51E-01	-0.11	1.22E-02	-1.87	7.01E-03	-2.23
Q08357	SLC20A2	Sodium-dependent phosphate transporter 2	5.37E-02	-1.23	1.68E-01	-0.81	2.84E-04	-2.21
P21860	ERBB3	Receptor tyrosine-protein kinase erbB-3	6.28E-01	-0.27	3.86E-02	-1.54	9.71E-03	-2.19
P09960	LTA4H	Leukotriene A-4 hydrolase	9.58E-01	-0.02	2.72E-02	-0.95	1.71E-04	-2.17
Q15286	RAB35	Ras-related protein Rab-35	1.04E-02	-1.30	2.18E-02	-1.63	2.84E-03	-2.15
P10301; P62070	RRAS; RRAS2	Ras-related protein R-Ras	2.78E-02	-1.61	8.21E-02	-0.77	1.11E-03	-2.11
P10301; P62070.1	RRAS; RRAS2	Ras-related protein R-Ras	NA	NA	8.21E-02	-0.77	1.11E-03	-2.11
P22059	OSBP	Oxysterol-binding protein 1	3.51E-02	-0.66	1.85E-01	-0.56	5.61E-03	-2.01
P06733	ENO1	Alpha-enolase	5.00E-01	-0.31	5.48E-02	-0.99	6.04E-04	-1.99
P09488; P28161	GSTM1; GSTM2	Glutathione S-transferase Mu 1	NA	NA	NA	NA	4.77E-03	-1.99
Q9Y6D5	ARFGEF2	Brefeldin A-inhibited guanine nucleotide-exchange protein 2	4.67E-01	0.20	8.70E-03	-1.38	2.40E-05	-1.95
P09211	GSTP1	Glutathione S-transferase P	4.46E-02	-1.14	6.72E-03	-1.05	2.34E-03	-1.95
Q99832	CCT7	T-complex protein 1 subunit eta	4.03E-02	-0.92	8.16E-03	-0.94	5.74E-05	-1.94

Protein Group	Gene Group	Protein Description	Cortex p-value	Cortex Log2FC	Outer Nucleus p-value	Outer Nucleus Log2FC	Inner Nucleus p-value	Inner Nucleus Log2FC
P17081; P60953; P63000; P84095	CDC42; RAC1; RHOG; RHOQ	Rho-related GTP-binding protein RhoQ	NA	NA	NA	NA	8.96E-04	-1.93
P55344	LIM2	Lens fiber membrane intrinsic protein	7.91E-01	0.19	1.85E-01	-0.69	2.95E-03	-1.93
P52888	THOP1	Thimet oligopeptidase	NA	NA	NA	NA	7.18E-04	-1.92
P55064	AQP5	Aquaporin-5	3.64E-01	-0.53	2.44E-01	-0.77	9.48E-03	-1.91
Q96F07	CYFIP2	Cytoplasmic FMR1-interacting protein 2	2.97E-02	-1.21	9.41E-03	-1.13	8.82E-04	-1.91
O75663	TIPRL	TIP41-like protein	2.17E-01	-0.45	2.86E-03	-1.10	3.99E-04	-1.91
P23528	CFL1	Cofilin-1	8.90E-02	-0.61	2.32E-02	-1.04	7.07E-03	-1.91
P60900	PSMA6	Proteasome subunit alpha type-6	3.49E-01	-0.38	2.12E-01	-0.24	1.89E-04	-1.89
P13639	EEF2	Elongation factor 2	6.89E-02	-0.57	9.34E-03	-0.82	8.53E-04	-1.87
P38919	EIF4A3	Eukaryotic initiation factor 4A-III	5.64E-02	-0.77	4.85E-01	-0.31	1.43E-03	-1.85
P56192	MARS1	Methionine--tRNA ligase, cytoplasmic	2.10E-02	-1.57	8.18E-01	-0.11	8.03E-03	-1.85
P26639	TARS1	Threonine--tRNA ligase 1, cytoplasmic	2.56E-01	-0.48	6.43E-02	-0.74	6.39E-04	-1.85
O75083	WDR1	WD repeat-containing protein 1	8.79E-01	-0.05	5.74E-01	-0.24	3.77E-03	-1.83
Q9Y281	CFL2	Cofilin-2	3.80E-02	-0.93	4.40E-01	-0.28	1.37E-03	-1.83
Q9UJW0	DCTN4	Dynactin subunit 4	3.23E-02	-1.21	3.64E-01	-0.24	2.77E-04	-1.83
P04406	GAPDH	Glyceraldehyde-3-phosphate dehydrogenase	1.38E-01	0.52	1.77E-01	-0.72	2.67E-04	-1.78
Q9BTW9	TBCD	Tubulin-specific chaperone D	1.48E-02	-1.10	1.13E-01	-0.71	3.44E-03	-1.78
P28482	MAPK1	Mitogen-activated protein kinase 1	4.04E-02	-0.96	8.26E-02	-0.79	1.23E-03	-1.77
Q12934	BFSP1	Filensin	1.09E-01	-0.54	4.91E-02	-0.70	1.20E-03	-1.77
O75935	DCTN3	Dynactin subunit 3	9.61E-01	-0.03	1.98E-01	0.59	1.53E-03	-1.76
Q13619	CUL4A	Cullin-4A	2.29E-02	-0.85	1.19E-01	-0.62	1.52E-03	-1.76
P62258	YWHAE	14-3-3 protein epsilon	9.98E-02	-0.94	2.54E-01	-0.37	3.29E-03	-1.76
Q9NY33	DPP3	Dipeptidyl peptidase 3	1.70E-01	0.63	2.15E-01	-0.54	8.91E-04	-1.75
Q9UJ70	NAGK	N-acetyl-D-glucosamine kinase	1.43E-01	0.41	1.76E-01	-0.42	4.24E-04	-1.74
P50747	HLCS	Biotin--protein ligase	1.22E-01	0.65	6.06E-01	-0.19	6.66E-04	-1.74
P61201	COPS2	COP9 signalosome complex subunit 2	2.61E-02	-0.78	4.28E-01	-0.35	9.44E-04	-1.74
P48449	LSS	Lanosterol synthase	3.38E-01	-0.41	5.10E-02	-0.83	3.07E-04	-1.72
P0C870	JMJD7	Bifunctional peptidase and (3S)-lysyl hydroxylase JMJD7	6.31E-02	0.79	2.48E-01	-0.45	2.72E-03	-1.72
P48739	PITPNB	Phosphatidylinositol transfer protein beta isoform	1.12E-01	-0.81	3.99E-01	-0.35	9.19E-03	-1.72
B3SHH9	TMEM114	Transmembrane protein 114	1.38E-01	-0.88	2.61E-02	-1.40	1.14E-04	-1.71
A2RU48	SMCO3	Single-pass membrane and coiled-coil domain-containing protein 3	9.35E-01	0.03	6.98E-04	-1.30	3.22E-04	-1.70
Q7L5N1	COPS6	COP9 signalosome complex subunit 6	3.59E-01	-0.37	5.06E-01	-0.22	1.29E-03	-1.68

Protein Group	Gene Group	Protein Description	Cortex p-value	Cortex Log2FC	Outer Nucleus p-value	Outer Nucleus Log2FC	Inner Nucleus p-value	Inner Nucleus Log2FC
P61163	ACTR1A	Alpha-centractin	6.75E-01	0.13	1.11E-02	-1.12	9.66E-03	-1.67
O95352	ATG7	Ubiquitin-like modifier-activating enzyme ATG7	1.85E-01	-0.43	4.73E-01	-0.31	6.01E-03	-1.66
P17252	PRKCA	Protein kinase C alpha type	NA	NA	NA	NA	4.16E-03	-1.66
E9PAV3;Q13765	NACA	Nascent polypeptide-associated complex subunit alpha, muscle-specific form	1.20E-02	-0.84	3.20E-03	-1.45	6.82E-03	-1.65
O95834	EML2	Echinoderm microtubule-associated protein-like 2	2.88E-01	0.40	2.21E-01	-0.41	2.17E-03	-1.65
P08238	HSP90AB1	Heat shock protein HSP 90-beta	3.94E-02	-1.24	1.68E-03	-1.05	3.88E-03	-1.65
P28070	PSMB4	Proteasome subunit beta type-4	6.96E-01	0.14	1.39E-01	-0.46	1.61E-04	-1.64
O95861	BPNT1	3'(2'),5'-bisphosphate nucleotidase 1	8.37E-01	-0.08	6.62E-01	-0.16	6.45E-04	-1.63
P60510	PPP4C	Serine/threonine-protein phosphatase 4 catalytic subunit	NA	NA	7.21E-01	0.17	3.61E-03	-1.63
Q9P2R3	ANKFY1	Rabankyrin-5	NA	NA	6.66E-02	-0.73	1.57E-03	-1.61
P49327	FASN	Fatty acid synthase	4.20E-02	-0.70	5.75E-02	-0.71	4.40E-04	-1.61
Q9UBQ5	EIF3K	Eukaryotic translation initiation factor 3 subunit K	NA	NA	NA	NA	3.47E-03	-1.61
P53602	MVD	Diphosphomevalonate decarboxylase	5.90E-01	0.24	1.57E-01	-0.63	8.25E-03	-1.61
Q70IA6	MOB2	MOB kinase activator 2	8.18E-02	-0.61	1.68E-02	-0.68	2.82E-03	-1.61
P29218	IMPA1	Inositol monophosphatase 1	8.21E-01	0.07	2.41E-01	-0.48	1.47E-03	-1.60
O43813	LANCL1	Glutathione S-transferase LANCL1	1.93E-01	0.52	4.25E-02	-0.61	7.03E-04	-1.60
P13010	XRCC5	X-ray repair cross-complementing protein 5	7.71E-02	-0.93	1.28E-01	-0.56	1.06E-03	-1.60
Q16401	PSMD5	26S proteasome non-ATPase regulatory subunit 5	2.12E-01	-0.68	3.46E-01	-0.46	1.49E-03	-1.60
Q8IW45	NAXD	ATP-dependent (S)-NAD(P)H-hydrate dehydratase	5.67E-01	0.22	9.62E-02	-0.55	4.07E-03	-1.58
O95163	ELP1	Elongator complex protein 1	6.53E-02	-0.76	3.90E-01	-0.36	2.02E-04	-1.58
P30566	ADSL	Adenylosuccinate lyase	2.56E-01	0.36	3.25E-01	-0.35	9.58E-03	-1.57
Q9Y3F4	STRAP	Serine-threonine kinase receptor-associated protein	1.44E-01	-0.57	3.40E-02	-0.92	5.34E-03	-1.57
Q7L523	RRAGA	Ras-related GTP-binding protein A	3.25E-01	-0.36	7.44E-01	-0.13	2.26E-03	-1.57
P23528; Q9Y281	CFL1; CFL2	Cofilin-1	7.76E-01	0.11	3.16E-01	-0.34	1.78E-03	-1.57
P54920	NAPA	Alpha-soluble NSF attachment protein	2.03E-01	-0.81	7.09E-02	-0.76	3.38E-04	-1.56
P08758	ANXA5	Annexin A5	2.30E-02	-1.28	1.49E-01	-0.55	1.22E-03	-1.56

Protein Group	Gene Group	Protein Description	Cortex p-value	Cortex Log2FC	Outer Nucleus p-value	Outer Nucleus Log2FC	Inner Nucleus p-value	Inner Nucleus Log2FC
P14324	FDPS	Farnesyl pyrophosphate synthase	5.93E-01	-0.17	7.68E-04	-1.14	2.67E-04	-1.55
Q9H0R4	HDHD2	Haloacid dehalogenase-like hydrolase domain-containing protein 2	4.50E-01	-0.24	8.05E-03	-0.67	1.60E-03	-1.55
P21980	TGM2	Protein-glutamine gamma-glutamyltransferase 2	3.41E-02	-1.19	1.78E-01	-0.51	3.29E-03	-1.55
Q06830	PRDX1	Peroxiredoxin-1	1.25E-01	-0.66	5.75E-01	-0.18	2.84E-03	-1.54
P07737	PFN1	Profilin-1	4.63E-02	-1.26	3.07E-02	-1.56	1.25E-03	-1.52
P27361	MAPK3	Mitogen-activated protein kinase 3	5.73E-02	-0.81	1.74E-01	-0.59	2.55E-03	-1.51
Q9UQN3	CHMP2B	Charged multivesicular body protein 2b	6.96E-01	-0.17	6.54E-03	-1.07	5.47E-03	-1.50
0P17987	TCP1	T-complex protein 1 subunit alpha	5.71E-01	-0.22	1.01E-01	-0.48	3.78E-03	-1.50

E. Table of Gene Ontologies enriched in the young (<50 y.o.) lens cortex relative to old (>50 y.o.) lens cortex

Gene Ontologies calculated as enriched by PSEA-Quant in the cortex of the Young Lens relative to the Old Lens. Significance was determined at a p-value < 0.01 and FDR < 0.1. PSEA-Quant was operated in labeled mode with 1,000,000 iterations used to empirically evaluate p-values. P-values below 1/1,000,000 ($1x10^{-6}$) are marked as such and correspond to distributions of protein enrichment not similar to prior distributions evaluated in 1,000,000 iterations. Number of proteins refers to proteins detected in dataset (no missing values from 16 samples) with the corresponding annotation.

Gene Ontology Enrichment in Young Lens Cortex relative to Old Lens Cortex	**P-Value**	**FDR**	**Number of Proteins with Annotation in Dataset**
GO:0090150 Establishment of protein localization to membrane	<1E-06	1.75E-02	30
GO:0006334 Nucleosome assembly	<1E-06	1.75E-02	11
GO:0044391 Ribosomal subunit	<1E-06	1.75E-02	14
GO:0031224 Intrinsic component of membrane	<1E-06	1.75E-02	206
GO:0005886 Plasma membrane	<1E-06	1.75E-02	295
GO:0006605 Protein targeting	<1E-06	1.75E-02	40
GO:0006612 Protein targeting to membrane	<1E-06	1.75E-02	22
GO:0006810 Transport	<1E-06	1.75E-02	347
GO:0006886 Intracellular protein transport	<1E-06	1.75E-02	104
GO:0015031 Protein transport	<1E-06	1.75E-02	178
GO:0016020 Membrane	<1E-06	1.75E-02	502
GO:0016818 Hydrolase activity, acting on acid anhydrides, in phosphorus-containing anhydrides	<1E-06	1.75E-02	140
GO:0017111 Nucleoside-triphosphatase activity	<1E-06	1.75E-02	133
GO:0031090 Organelle membrane	<1E-06	1.75E-02	254
GO:0032991 Protein-containing complex	<1E-06	1.75E-02	472
GO:0042470 Melanosome	<1E-06	1.75E-02	50
GO:0045184 Establishment of protein localization	<1E-06	1.75E-02	182
GO:0046907 Intracellular transport	<1E-06	1.75E-02	165
GO:0048770 Pigment granule	<1E-06	1.75E-02	50
GO:0051234 Establishment of localization	<1E-06	1.75E-02	350
GO:0051649 Establishment of localization in cell	<1E-06	1.75E-02	201
GO:0065004 Protein-DNA complex assembly	<1E-06	1.75E-02	11
GO:0065008 Regulation of biological quality	<1E-06	1.75E-02	283
GO:0071702 Organic substance transport	<1E-06	1.75E-02	230
GO:0034655 Nucleobase-containing compound catabolic process	1.00E-06	1.75E-02	93
GO:0019058 Viral life cycle	2.00E-06	1.75E-02	16
GO:0016462 Pyrophosphatase activity	2.00E-06	1.75E-02	139
GO:0006415 Translational termination	2.00E-06	1.75E-02	12
GO:0071824 Protein-DNA complex subunit organization	2.00E-06	1.75E-02	12
GO:0016482 Cytosolic transport	2.00E-06	1.75E-02	74
GO:0034728 Nucleosome organization	2.00E-06	1.75E-02	12
GO:0016817 Hydrolase activity, acting on acid anhydrides	2.00E-06	1.75E-02	141
GO:0005789 Endoplasmic reticulum membrane	3.00E-06	1.75E-02	45
GO:0072599 Establishment of protein localization to endoplasmic reticulum	3.00E-06	1.75E-02	12
GO:0015075 Ion transmembrane transporter activity	4.00E-06	1.75E-02	50
GO:0000184 Nuclear-transcribed mRNA catabolic process, nonsense-mediated decay	4.00E-06	1.75E-02	18
GO:0006613 Cotranslational protein targeting to membrane	5.00E-06	1.75E-02	12
GO:0006614 SRP-dependent cotranslational protein targeting to membrane	7.00E-06	1.75E-02	12
GO:0005575 Cellular component	8.00E-06	1.75E-02	1201
GO:0019083 Viral transcription	9.00E-06	1.75E-02	11
GO:0045047 Protein targeting to ER	9.00E-06	1.75E-02	12

Gene Ontology Enrichment in Young Lens Cortex relative to Old Lens Cortex	P-Value	FDR	Number of Proteins with Annotation in Dataset
GO:0031410 Cytoplasmic vesicle	1.10E-05	1.75E-02	124
GO:0016021 Integral component of membrane	1.50E-05	1.75E-02	198
GO:0031982 Vesicle	2.30E-05	1.75E-02	154
GO:0032993 Protein-DNA complex	2.40E-05	1.75E-02	13
GO:0030433 Ubiquitin-dependent ERAD pathway	3.30E-05	1.75E-02	7
GO:0044270 Cellular nitrogen compound catabolic process	5.50E-05	1.75E-02	99
GO:0043624 Cellular protein complex disassembly	6.00E-05	2.36E-02	16
GO:0072594 Establishment of protein localization to organelle	6.00E-05	2.36E-02	43
GO:0006414 Translational elongation	6.80E-05	2.36E-02	17
GO:0005515 Protein binding	6.90E-05	2.36E-02	810
GO:0000956 Nuclear-transcribed mRNA catabolic process	7.00E-05	2.36E-02	25
GO:0005743 Mitochondrial inner membrane	7.20E-05	2.36E-02	45
GO:0022890 Inorganic cation transmembrane transporter activity	7.30E-05	2.36E-02	27
GO:0019866 Organelle inner membrane	8.00E-05	2.36E-02	46
GO:0006402 mRNA catabolic process	8.60E-05	2.36E-02	28
GO:0046700 Heterocycle catabolic process	9.60E-05	2.36E-02	100
GO:0022857 Transmembrane transporter activity	1.01E-04	2.36E-02	65
GO:0015934 Large ribosomal subunit	1.10E-04	2.36E-02	5
GO:0022625 Cytosolic large ribosomal subunit	1.12E-04	2.36E-02	5
GO:0006996 Organelle organization	1.29E-04	2.36E-02	182
GO:0019439 Aromatic compound catabolic process	1.40E-04	2.36E-02	104
GO:0003735 Structural constituent of ribosome	1.49E-04	2.36E-02	12
GO:0005793 Endoplasmic reticulum-golgi intermediate compartment	1.58E-04	2.36E-02	10
GO:0006401 RNA catabolic process	1.60E-04	2.36E-02	29
GO:0071840 Cellular component organization or biogenesis	2.24E-04	2.36E-02	376
GO:0016043 Cellular component organization	2.39E-04	2.36E-02	376
GO:0030176 Integral component of endoplasmic reticulum membrane	2.48E-04	2.36E-02	6
GO:0032984 Protein-containing complex disassembly	2.54E-04	2.36E-02	17
GO:0031966 Mitochondrial membrane	2.65E-04	2.36E-02	58
GO:0016192 Vesicle-mediated transport	2.84E-04	2.36E-02	119
GO:0031227 Intrinsic component of endoplasmic reticulum membrane	2.93E-04	2.36E-02	6
GO:0009125 Nucleoside monophosphate catabolic process	3.57E-04	2.36E-02	20
GO:0016887 ATP hydrolysis activity	3.65E-04	2.36E-02	52
GO:0009169 Purine ribonucleoside monophosphate catabolic process	3.74E-04	2.36E-02	20
GO:0009158 Ribonucleoside monophosphate catabolic process	3.93E-04	2.36E-02	20
GO:0009128 Purine nucleoside monophosphate catabolic process	4.02E-04	2.36E-02	20
GO:0008509 Anion transmembrane transporter activity	4.33E-04	2.36E-02	22
GO:0009203 Ribonucleoside triphosphate catabolic process	4.39E-04	2.36E-02	54
GO:0009207 Purine ribonucleoside triphosphate catabolic process	4.52E-04	2.36E-02	54
GO:0016071 mRNA metabolic process	4.56E-04	2.36E-02	80
GO:0008324 Cation transmembrane transporter activity	5.11E-04	2.36E-02	33
GO:0005215 Transporter activity	5.78E-04	2.36E-02	106
GO:0005783 Endoplasmic reticulum	6.02E-04	2.36E-02	60
GO:0009146 Purine nucleoside triphosphate catabolic process	6.29E-04	2.36E-02	55
GO:0009261 Ribonucleotide catabolic process	6.42E-04	2.36E-02	55
GO:0009154 Purine ribonucleotide catabolic process	6.63E-04	2.36E-02	55
GO:0009143 Nucleoside triphosphate catabolic process	6.64E-04	2.36E-02	55
GO:0046130 Purine ribonucleoside catabolic process	8.06E-04	2.36E-02	55
GO:0006152 Purine nucleoside catabolic process	8.52E-04	2.36E-02	55
GO:0044815 DNA packaging complex	8.61E-04	2.36E-02	7
GO:1990104 DNA bending complex	8.72E-04	2.36E-02	7
GO:0000398 mRNA splicing, via spliceosome	9.02E-04	2.36E-02	9
GO:0008380 RNA splicing	9.18E-04	2.36E-02	16
GO:0000375 RNA splicing, via transesterification reactions	9.26E-04	2.36E-02	9

Gene Ontology Enrichment in Young Lens Cortex relative to Old Lens Cortex	P-Value	FDR	Number of Proteins with Annotation in Dataset
GO:0000786 Nucleosome	9.32E-04	2.36E-02	7
GO:0000377 RNA splicing, via transesterification reactions with bulged adenosine as nucleophile	9.63E-04	2.36E-02	9
GO:0003774 Cytoskeletal motor activity	9.78E-04	2.36E-02	15
GO:0009166 Nucleotide catabolic process	1.10E-03	2.36E-02	58
GO:0030662 Coated vesicle membrane	1.15E-03	2.36E-02	15
GO:0044265 Cellular macromolecule catabolic process	1.16E-03	2.36E-02	103
GO:0006195 Purine nucleotide catabolic process	1.25E-03	2.36E-02	56
GO:0022411 Cellular component disassembly	1.27E-03	2.36E-02	39
GO:0072523 Purine-containing compound catabolic process	1.29E-03	2.36E-02	56
GO:0050839 Cell adhesion molecule binding	1.31E-03	2.36E-02	15
GO:0014704 Intercalated disc	1.33E-03	2.36E-02	11
GO:1901361 Organic cyclic compound catabolic process	1.39E-03	2.36E-02	111
GO:0043933 Protein-containing complex subunit organization	1.50E-03	3.08E-02	161
GO:0003924 GTPase activity	1.59E-03	3.08E-02	71
GO:0097480 Establishment of synaptic vesicle localization	1.63E-03	3.55E-02	7
GO:0044291 Cell-cell contact zone	1.72E-03	3.55E-02	12
GO:0048489 Synaptic vesicle transport	1.73E-03	3.55E-02	7
GO:0006986 Response to unfolded protein	1.76E-03	3.55E-02	20
GO:0009295 Nucleoid	1.85E-03	3.55E-02	4
GO:0042645 Mitochondrial nucleoid	1.92E-03	3.55E-02	4
GO:1901292 Nucleoside phosphate catabolic process	1.94E-03	3.55E-02	59
GO:0009164 Nucleoside catabolic process	1.97E-03	3.55E-02	56
GO:1901658 Glycosyl compound catabolic process	2.01E-03	3.55E-02	56
GO:0006397 mRNA processing	2.02E-03	3.55E-02	20
GO:0030117 Membrane coat	2.07E-03	3.95E-02	11
GO:0042454 Ribonucleoside catabolic process	2.08E-03	3.95E-02	56
GO:0006836 Neurotransmitter transport	2.23E-03	3.95E-02	7
GO:0015078 Proton transmembrane transporter activity	2.25E-03	3.95E-02	15
GO:0032469 Endoplasmic reticulum calcium ion homeostasis	2.59E-03	3.95E-02	3
GO:0045296 Cadherin binding	2.65E-03	3.95E-02	8
GO:0033116 Endoplasmic reticulum-golgi intermediate compartment membrane	2.67E-03	3.95E-02	4
GO:0006839 Mitochondrial transport	2.67E-03	3.95E-02	19
GO:0009205 Purine ribonucleoside triphosphate metabolic process	2.73E-03	3.95E-02	61
GO:0006901 Vesicle coating	2.74E-03	3.95E-02	12
GO:0006413 Translational initiation	2.85E-03	4.58E-02	31
GO:0022627 Cytosolic small ribosomal subunit	3.10E-03	5.00E-02	7
GO:0009199 Ribonucleoside triphosphate metabolic process	3.10E-03	5.00E-02	62
GO:0016323 Basolateral plasma membrane	3.34E-03	5.00E-02	34
GO:0046943 Carboxylic acid transmembrane transporter activity	3.35E-03	5.00E-02	9
GO:0005342 Organic acid transmembrane transporter activity	3.42E-03	5.00E-02	9
GO:0042383 Sarcolemma	3.46E-03	5.00E-02	11
GO:0051235 Maintenance of location	3.58E-03	5.00E-02	16
GO:0045185 Maintenance of protein location	3.71E-03	6.10E-02	12
GO:0050817 Coagulation	4.04E-03	6.10E-02	69
GO:0046034 ATP metabolic process	4.11E-03	6.10E-02	24
GO:0007596 Blood coagulation	4.14E-03	6.10E-02	69
GO:0046434 Organophosphate catabolic process	4.60E-03	8.38E-02	64
GO:0050878 Regulation of body fluid levels	4.68E-03	8.38E-02	78
GO:0005840 Ribosome	4.72E-03	8.38E-02	8
GO:0032507 Maintenance of protein location in cell	4.81E-03	8.88E-02	10
GO:0065007 Biological regulation	4.82E-03	8.88E-02	709
GO:0048205 Cop I coating of golgi vesicle	4.97E-03	8.94E-02	6
GO:0048200 Golgi transport vesicle coating	5.01E-03	8.94E-02	6

Gene Ontology Enrichment in Young Lens Cortex relative to Old Lens Cortex	P-Value	FDR	Number of Proteins with Annotation in Dataset
GO:0032940 Secretion by cell	5.14E-03	8.94E-02	43
GO:0043229 Intracellular organelle	5.16E-03	8.94E-02	720
GO:0023061 Signal release	5.18E-03	8.94E-02	10
GO:0001505 Regulation of neurotransmitter levels	5.31E-03	8.94E-02	8
GO:0007599 Hemostasis	5.32E-03	8.94E-02	71
GO:0051650 Establishment of vesicle localization	5.40E-03	8.94E-02	9
GO:0034622 Cellular protein-containing complex assembly	5.45E-03	8.94E-02	64
GO:0019001 Guanyl nucleotide binding	5.67E-03	9.50E-02	96
GO:0005525 GTP binding	5.68E-03	9.50E-02	96
GO:0034976 Response to endoplasmic reticulum stress	5.72E-03	9.50E-02	15
GO:0032561 Guanyl ribonucleotide binding	5.76E-03	9.50E-02	96
GO:0005253 Anion channel activity	5.79E-03	9.50E-02	5
GO:0008022 Protein c-terminus binding	5.92E-03	9.50E-02	18
GO:0046873 Metal ion transmembrane transporter activity	6.19E-03	9.50E-02	12
GO:0030120 Vesicle coat	6.21E-03	9.50E-02	10
GO:0005200 Structural constituent of cytoskeleton	6.21E-03	9.50E-02	27
GO:0030968 Endoplasmic reticulum unfolded protein response	6.22E-03	9.50E-02	11
GO:0034620 Cellular response to unfolded protein	6.30E-03	9.50E-02	11
GO:0019903 Protein phosphatase binding	6.35E-03	9.50E-02	16
GO:0016050 Vesicle organization	6.37E-03	9.50E-02	25
GO:0009144 Purine nucleoside triphosphate metabolic process	6.38E-03	9.50E-02	64
GO:0044087 Regulation of cellular component biogenesis	6.94E-03	9.50E-02	62
GO:0031226 Intrinsic component of plasma membrane	6.97E-03	9.50E-02	58
GO:0048193 Golgi vesicle transport	6.98E-03	9.50E-02	39
GO:0005911 Cell-cell junction	7.07E-03	9.50E-02	46

F. Table of Gene Ontologies enriched in the old (>50 y.o.) lens cortex relative to young (<50 y.o.) lens cortex

Gene Ontologies calculated as enriched by PSEA-Quant in the cortex region of the Old Lens relative to the Young Lens. Significance was determined at a p-value < 0.01 and FDR < 0.1. PSEA-Quant was operated in labeled mode with 1,000,000 iterations used to empirically evaluate p-values. P-values below 1/1,000,000 ($1x10^{-6}$) are marked as such and correspond to distributions of protein enrichment not similar to prior distributions evaluated in 1,000,000 iterations. Number of proteins refers to proteins detected in dataset (no missing values from 16 samples) with the corresponding annotation.

Gene Ontology Enrichment in Old Lens Cortex relative to Young Lens Cortex	P-Value	FDR	Number of Proteins with Annotation in Dataset
GO:0003824 Catalytic activity	<1E-06	1.25E-02	614
GO:0005737 Cytoplasm	<1E-06	1.25E-02	508
GO:0005829 Cytosol	<1E-06	1.25E-02	504
GO:0005975 Carbohydrate metabolic process	<1E-06	1.25E-02	106
GO:0005996 Monosaccharide metabolic process	<1E-06	1.25E-02	61
GO:0006006 Glucose metabolic process	<1E-06	1.25E-02	50
GO:0006082 Organic acid metabolic process	<1E-06	1.25E-02	128
GO:0006520 Cellular amino acid metabolic process	<1E-06	1.25E-02	75
GO:0006558 L-phenylalanine metabolic process	<1E-06	1.25E-02	6
GO:0006559 L-phenylalanine catabolic process	<1E-06	1.25E-02	6
GO:0006807 Nitrogen compound metabolic process	<1E-06	1.25E-02	362
GO:0008152 Metabolic process	<1E-06	1.25E-02	736
GO:0009058 Biosynthetic process	<1E-06	1.25E-02	261
GO:0009063 Cellular amino acid catabolic process	<1E-06	1.25E-02	16
GO:0009072 Aromatic amino acid family metabolic process	<1E-06	1.25E-02	6
GO:0009074 Aromatic amino acid family catabolic process	<1E-06	1.25E-02	6
GO:0016052 Carbohydrate catabolic process	<1E-06	1.25E-02	38
GO:0016054 Organic acid catabolic process	<1E-06	1.25E-02	24
GO:0016740 Transferase activity	<1E-06	1.25E-02	142
GO:0019318 Hexose metabolic process	<1E-06	1.25E-02	56
GO:0019320 Hexose catabolic process	<1E-06	1.25E-02	28
GO:0019752 Carboxylic acid metabolic process	<1E-06	1.25E-02	122
GO:0043167 Ion binding	<1E-06	1.25E-02	530
GO:0043436 Oxoacid metabolic process	<1E-06	1.25E-02	126
GO:0044237 Cellular metabolic process	<1E-06	1.25E-02	678
GO:0044238 Primary metabolic process	<1E-06	1.25E-02	655
GO:0044249 Cellular biosynthetic process	<1E-06	1.25E-02	226
GO:0044281 Small molecule metabolic process	<1E-06	1.25E-02	368
GO:0044282 Small molecule catabolic process	<1E-06	1.25E-02	38
GO:0046365 Monosaccharide catabolic process	<1E-06	1.25E-02	31
GO:0046395 Carboxylic acid catabolic process	<1E-06	1.25E-02	24
GO:0046872 Metal ion binding	<1E-06	1.25E-02	247
GO:0071704 Organic substance metabolic process	<1E-06	1.25E-02	682
GO:1901564 Organonitrogen compound metabolic process	<1E-06	1.25E-02	202
GO:1901566 Organonitrogen compound biosynthetic process	<1E-06	1.25E-02	66
GO:1901576 Organic substance biosynthetic process	<1E-06	1.25E-02	258
GO:1901605 Alpha-amino acid metabolic process	<1E-06	1.25E-02	33
GO:1901606 Alpha-amino acid catabolic process	<1E-06	1.25E-02	14
GO:1902221 Erythrose 4-phosphate/phosphoenolpyruvate family amino acid metabolic process	<1E-06	1.25E-02	6
GO:1902222 Erythrose 4-phosphate/phosphoenolpyruvate family amino acid catabolic process	<1E-06	1.25E-02	6
GO:0005212 Structural constituent of eye lens	1.00E-06	1.25E-02	17
GO:0016614 Oxidoreductase activity, acting on CH-OH group of donors	1.00E-06	1.25E-02	29

Gene Ontology Enrichment in Old Lens Cortex relative to Young Lens Cortex	P-Value	FDR	Number of Proteins with Annotation in Dataset
GO:0034641 Cellular nitrogen compound metabolic process	1.00E-06	1.25E-02	335
GO:0043169 Cation binding	2.00E-06	1.25E-02	253
GO:0016616 Oxidoreductase activity, acting on the CH-OH group of donors, NAD or NADP as acceptor	2.00E-06	1.25E-02	29
GO:0006007 Glucose catabolic process	2.00E-06	1.25E-02	25
GO:0042803 Protein homodimerization activity	4.00E-06	1.25E-02	90
GO:0042180 Cellular ketone metabolic process	6.00E-06	1.25E-02	8
GO:0044283 Small molecule biosynthetic process	6.00E-06	1.25E-02	57
GO:0042802 Identical protein binding	1.20E-05	1.25E-02	134
GO:0050661 NADP binding	1.60E-05	1.25E-02	14
GO:0046394 Carboxylic acid biosynthetic process	3.90E-05	1.25E-02	39
GO:0016053 Organic acid biosynthetic process	5.20E-05	1.25E-02	39
GO:0006570 Tyrosine metabolic process	6.20E-05	1.25E-02	3
GO:0006572 Tyrosine catabolic process	7.10E-05	1.25E-02	3
GO:0016810 Hydrolase activity, acting on carbon-nitrogen (but not peptide) bonds	7.20E-05	1.25E-02	16
GO:0006739 NADP metabolic process	7.70E-05	1.25E-02	11
GO:0002088 Lens development in camera-type eye	9.20E-05	1.25E-02	9
GO:0043094 Cellular metabolic compound salvage	9.40E-05	1.25E-02	9
GO:0016829 Lyase activity	9.60E-05	1.25E-02	30
GO:0016853 Isomerase activity	9.60E-05	1.25E-02	34
GO:0000287 Magnesium ion binding	9.90E-05	1.25E-02	34
GO:0006096 Glycolytic process	1.02E-04	1.25E-02	20
GO:0008652 Cellular amino acid biosynthetic process	1.04E-04	1.25E-02	23
GO:0006790 Sulfur compound metabolic process	1.20E-04	1.25E-02	33
GO:1901575 Organic substance catabolic process	1.32E-04	1.25E-02	253
GO:0019321 Pentose metabolic process	1.47E-04	1.25E-02	8
GO:0006144 Purine nucleobase metabolic process	1.64E-04	1.25E-02	11
GO:0009056 Catabolic process	1.66E-04	1.25E-02	278
GO:0006081 Cellular aldehyde metabolic process	1.72E-04	1.25E-02	17
GO:0016772 Transferase activity, transferring phosphorus-containing groups	1.95E-04	2.20E-02	80
GO:0044271 Cellular nitrogen compound biosynthetic process	2.17E-04	2.20E-02	121
GO:0016701 Oxidoreductase activity, acting on single donors with incorporation of molecular oxygen	2.33E-04	2.20E-02	2
GO:1901137 Carbohydrate derivative biosynthetic process	2.33E-04	2.20E-02	44
GO:0009112 Nucleobase metabolic process	2.37E-04	2.20E-02	17
GO:0016702 Oxidoreductase activity, acting on single donors with incorporation of molecular oxygen, incorporation of two atoms of oxygen	2.39E-04	2.20E-02	2
GO:1901661 Quinone metabolic process	2.42E-04	2.20E-02	7
GO:0016903 Oxidoreductase activity, acting on the aldehyde or oxo group of donors	2.50E-04	2.20E-02	11
GO:0006044 N-acetylglucosamine metabolic process	2.53E-04	2.20E-02	6
GO:0006575 Cellular modified amino acid metabolic process	2.69E-04	2.20E-02	33
GO:0044262 Cellular carbohydrate metabolic process	2.78E-04	2.20E-02	31
GO:0090407 Organophosphate biosynthetic process	3.83E-04	2.61E-02	64
GO:0036094 Small molecule binding	3.99E-04	2.61E-02	348
GO:0008237 Metallopeptidase activity	4.00E-04	2.61E-02	19
GO:0042558 Pteridine-containing compound metabolic process	4.04E-04	2.61E-02	6
GO:0016861 Intramolecular oxidoreductase activity, interconverting aldoses and ketoses	4.06E-04	2.61E-02	8
GO:1901360 Organic cyclic compound metabolic process	4.87E-04	2.61E-02	327
GO:0005977 Glycogen metabolic process	4.94E-04	2.61E-02	13
GO:0044264 Cellular polysaccharide metabolic process	4.94E-04	2.61E-02	13

Gene Ontology Enrichment in Old Lens Cortex relative to Young Lens Cortex	P-Value	FDR	Number of Proteins with Annotation in Dataset
GO:0044042 Glucan metabolic process	5.06E-04	2.61E-02	13
GO:0005976 Polysaccharide metabolic process	5.08E-04	2.61E-02	13
GO:0006073 Cellular glucan metabolic process	5.12E-04	2.61E-02	13
GO:1901071 Glucosamine-containing compound metabolic process	5.16E-04	2.61E-02	8
GO:0019362 Pyridine nucleotide metabolic process	5.25E-04	2.61E-02	18
GO:0046496 Nicotinamide nucleotide metabolic process	5.36E-04	2.61E-02	18
GO:0072524 Pyridine-containing compound metabolic process	5.59E-04	2.61E-02	18
GO:0006725 Cellular aromatic compound metabolic process	6.08E-04	2.61E-02	305
GO:1901293 Nucleoside phosphate biosynthetic process	6.21E-04	2.61E-02	38
GO:0009165 Nucleotide biosynthetic process	6.31E-04	2.61E-02	38
GO:0072522 Purine-containing compound biosynthetic process	6.35E-04	2.61E-02	26
GO:0016620 Oxidoreductase activity, acting on the aldehyde or oxo group of donors, NAD or NADP as acceptor	7.24E-04	2.61E-02	10
GO:0005524 ATP binding	7.32E-04	2.61E-02	187
GO:0016051 Carbohydrate biosynthetic process	7.34E-04	2.61E-02	37
GO:0016774 Phosphotransferase activity, carboxyl group as acceptor	7.73E-04	2.61E-02	2
GO:0016491 Oxidoreductase activity	7.78E-04	3.28E-02	95
GO:0043603 Cellular amide metabolic process	8.14E-04	3.28E-02	29
GO:0004618 Phosphoglycerate kinase activity	8.43E-04	3.28E-02	2
GO:0008235 Metalloexopeptidase activity	8.71E-04	3.28E-02	5
GO:0034660 ncRNA metabolic process	9.00E-04	3.28E-02	31
GO:0016301 Kinase activity	9.16E-04	3.28E-02	72
GO:0006740 NADPH regeneration	9.58E-04	3.28E-02	7
GO:0015949 Nucleobase-containing small molecule interconversion	9.79E-04	3.82E-02	7
GO:0008233 Peptidase activity	9.85E-04	3.82E-02	66
GO:0042559 Pteridine-containing compound biosynthetic process	1.01E-03	3.82E-02	4
GO:0044272 Sulfur compound biosynthetic process	1.05E-03	3.82E-02	14
GO:0033559 Unsaturated fatty acid metabolic process	1.08E-03	3.82E-02	11
GO:0032559 Adenyl ribonucleotide binding	1.08E-03	3.82E-02	192
GO:1901568 Fatty acid derivative metabolic process	1.08E-03	3.82E-02	11
GO:0006690 Icosanoid metabolic process	1.10E-03	3.82E-02	11
GO:0030554 Adenyl nucleotide binding	1.10E-03	3.82E-02	195
GO:0019322 Pentose biosynthetic process	1.17E-03	4.55E-02	4
GO:0043412 Macromolecule modification	1.34E-03	5.07E-02	199
GO:0016788 Hydrolase activity, acting on ester bonds	1.37E-03	5.07E-02	68
GO:0008238 Exopeptidase activity	1.42E-03	5.07E-02	19
GO:0036211 Protein modification process	1.52E-03	5.07E-02	197
GO:0006464 Cellular protein modification process	1.53E-03	5.07E-02	197
GO:0061134 Peptidase regulator activity	1.54E-03	5.07E-02	17
GO:0019262 N-acetylneuraminate catabolic process	1.73E-03	5.76E-02	3
GO:0005997 Xylulose metabolic process	1.81E-03	6.43E-02	3
GO:0006040 Amino sugar metabolic process	1.88E-03	6.85E-02	9
GO:0004177 Aminopeptidase activity	1.94E-03	6.85E-02	9
GO:0051260 Protein homooligomerization	2.01E-03	6.85E-02	25
GO:0016570 Histone modification	2.18E-03	6.85E-02	11
GO:0009055 Electron transfer activity	2.21E-03	7.48E-02	14
GO:0019438 Aromatic compound biosynthetic process	2.32E-03	7.60E-02	113
GO:0004033 Aldo-keto reductase (NADP) activity	2.34E-03	7.60E-02	5
GO:0016765 Transferase activity, transferring alkyl or aryl (other than methyl) groups	2.47E-03	7.60E-02	14
GO:0018130 Heterocycle biosynthetic process	2.47E-03	7.60E-02	112

Gene Ontology Enrichment in Old Lens Cortex relative to Young Lens Cortex	P-Value	FDR	Number of Proteins with Annotation in Dataset
GO:0016846 Carbon-sulfur lyase activity	2.58E-03	7.60E-02	2
GO:0033293 Monocarboxylic acid binding	2.66E-03	7.60E-02	8
GO:0006720 Isoprenoid metabolic process	2.76E-03	7.60E-02	10
GO:0043101 Purine-containing compound salvage	2.78E-03	7.60E-02	3
GO:0005634 Nucleus	2.82E-03	7.60E-02	322
GO:0046348 Amino sugar catabolic process	2.83E-03	7.60E-02	6
GO:0042440 Pigment metabolic process	2.87E-03	7.60E-02	9
GO:0000096 Sulfur amino acid metabolic process	2.93E-03	7.60E-02	14
GO:1901362 Organic cyclic compound biosynthetic process	2.98E-03	7.60E-02	129
GO:0019205 Nucleobase-containing compound kinase activity	3.08E-03	7.60E-02	5
GO:0007286 Spermatid development	3.17E-03	7.60E-02	3
GO:0016857 Racemase and epimerase activity, acting on carbohydrates and derivatives	3.23E-03	7.60E-02	3
GO:0046483 Heterocycle metabolic process	3.28E-03	7.60E-02	297
GO:0016854 Racemase and epimerase activity	3.28E-03	7.60E-02	3
GO:0044106 Cellular amine metabolic process	3.33E-03	7.60E-02	12
GO:0006576 Cellular biogenic amine metabolic process	3.34E-03	7.60E-02	12
GO:0004180 Carboxypeptidase activity	3.39E-03	7.60E-02	4
GO:0042182 Ketone catabolic process	3.43E-03	7.60E-02	2
GO:0009308 Amine metabolic process	3.46E-03	7.60E-02	12
GO:0008270 Zinc ion binding	3.58E-03	7.60E-02	51
GO:0016769 Transferase activity, transferring nitrogenous groups	3.59E-03	7.91E-02	5
GO:0016866 Intramolecular transferase activity	3.68E-03	7.91E-02	10
GO:1901135 Carbohydrate derivative metabolic process	3.75E-03	7.91E-02	123
GO:0051287 NAD binding	3.79E-03	7.91E-02	15
GO:0006098 Pentose-phosphate shunt	3.86E-03	7.91E-02	6
GO:0006012 Galactose metabolic process	3.97E-03	8.15E-02	5
GO:0004812 Aminoacyl-tRNA ligase activity	4.00E-03	8.15E-02	20
GO:0009584 Detection of visible light	4.00E-03	8.15E-02	8
GO:0007602 Phototransduction	4.00E-03	8.15E-02	8
GO:0009583 Detection of light stimulus	4.01E-03	8.15E-02	8
GO:0043039 tRNA aminoacylation	4.04E-03	8.15E-02	20
GO:0046148 Pigment biosynthetic process	4.07E-03	8.51E-02	8
GO:0006796 Phosphate-containing compound metabolic process	4.08E-03	8.51E-02	216
GO:0006418 tRNA aminoacylation for protein translation	4.08E-03	8.51E-02	20
GO:0016875 Ligase activity, forming carbon-oxygen bonds	4.10E-03	8.51E-02	20
GO:0007603 Phototransduction, visible light	4.15E-03	8.90E-02	8
GO:0043038 Amino acid activation	4.17E-03	8.90E-02	20
GO:0004181 Metallocarboxypeptidase activity	4.19E-03	8.90E-02	2

G. Table of Gene Ontologies enriched in the young (<50 y.o.) lens outer nucleus relative to old (>50 y.o.) lens outer nucleus

Gene Ontologies calculated as enriched by PSEA-Quant in the outer nucleus of the Young Lens relative to the Old Lens. Significance was determined at a p-value < 0.01 and FDR < 0.1. PSEA-Quant was operated in labeled mode with 1,000,000 iterations used to empirically evaluate p-values. P-values below 1/1,000,000 ($1x10^{-6}$) are marked as such and correspond to distributions of protein enrichment not similar to prior distributions evaluated in 1,000,000 iterations. Number of proteins refers to proteins detected in dataset (no missing values from 16 samples) with the corresponding annotation.

Gene Ontology Enrichment in Young Lens Outer Nucleus relative to Old Lens Outer Nucleus	**P-Value**	**FDR**	**Number of Proteins with Annotation in Dataset**
GO:0019001 Guanyl nucleotide binding	<1E-06	1.35E-02	75
GO:0034329 Cell junction assembly	<1E-06	1.35E-02	23
GO:0034330 Cell junction organization	<1E-06	1.35E-02	26
GO:0005525 GTP binding	<1E-06	1.35E-02	75
GO:0005886 Plasma membrane	<1E-06	1.35E-02	204
GO:0007155 Cell adhesion	<1E-06	1.35E-02	43
GO:0007264 Small GTPase mediated signal transduction	<1E-06	1.35E-02	58
GO:0016020 Membrane	<1E-06	1.35E-02	344
GO:0016021 Integral component of membrane	<1E-06	1.35E-02	113
GO:0019898 Extrinsic component of membrane	<1E-06	1.35E-02	19
GO:0022610 Biological adhesion	<1E-06	1.35E-02	43
GO:0031224 Intrinsic component of membrane	<1E-06	1.35E-02	119
GO:0032561 Guanyl ribonucleotide binding	<1E-06	1.35E-02	75
GO:0045216 Cell-cell junction organization	2.00E-06	1.35E-02	23
GO:0031410 Cytoplasmic vesicle	3.00E-06	1.35E-02	71
GO:0031012 Extracellular matrix	6.00E-06	1.35E-02	14
GO:0031982 Vesicle	9.00E-06	1.35E-02	99
GO:0003924 GTPase activity	1.00E-05	1.35E-02	55
GO:0017111 Nucleoside-triphosphatase activity	1.70E-05	1.35E-02	102
GO:0050817 Coagulation	4.70E-05	1.35E-02	44
GO:0016462 Pyrophosphatase activity	4.80E-05	1.35E-02	108
GO:0007596 Blood coagulation	5.00E-05	1.35E-02	44
GO:0016818 Hydrolase activity, acting on acid anhydrides, in phosphorus-containing anhydrides	5.10E-05	1.35E-02	109
GO:0007599 Hemostasis	5.90E-05	1.35E-02	46
GO:0016817 Hydrolase activity, acting on acid anhydrides	6.80E-05	1.35E-02	109
GO:0006928 Movement of cell or subcellular component	6.80E-05	1.35E-02	103
GO:0032502 Developmental process	7.00E-05	1.35E-02	232
GO:0007156 Homophilic cell adhesion via plasma membrane adhesion molecules	1.45E-04	1.35E-02	5
GO:0007411 Axon guidance	1.48E-04	1.35E-02	42
GO:0097485 Neuron projection guidance	1.48E-04	1.35E-02	42
GO:0005834 Heterotrimeric G-protein complex	1.69E-04	1.35E-02	5
GO:0050794 Regulation of cellular process	1.69E-04	1.35E-02	512
GO:0009986 Cell surface	1.73E-04	1.35E-02	21
GO:0031344 Regulation of cell projection organization	2.05E-04	1.35E-02	23
GO:0019897 Extrinsic component of plasma membrane	2.28E-04	1.35E-02	12
GO:0008366 Axon ensheathment	2.52E-04	1.35E-02	4
GO:0007272 Ensheathment of neurons	2.79E-04	1.35E-02	4
GO:0031225 Anchored component of membrane	3.05E-04	1.35E-02	6
GO:0006813 Potassium ion transport	3.27E-04	1.35E-02	4
GO:0007157 Heterophilic cell-cell adhesion via plasma membrane cell adhesion molecules	3.34E-04	1.35E-02	4
GO:0007267 Cell-cell signaling	3.35E-04	1.35E-02	34

Gene Ontology Enrichment in Young Lens Outer Nucleus relative to Old Lens Outer Nucleus	**P-Value**	**FDR**	**Number of Proteins with Annotation in Dataset**
GO:0045121 Membrane raft	3.36E-04	1.35E-02	19
GO:0008324 Cation transmembrane transporter activity	3.83E-04	1.35E-02	17
GO:0046039 GTP metabolic process	3.86E-04	1.35E-02	29
GO:0032989 Cellular component morphogenesis	3.92E-04	1.35E-02	32
GO:0065007 Biological regulation	4.25E-04	1.35E-02	564
GO:0048770 Pigment granule	5.05E-04	1.35E-02	31
GO:1901068 Guanosine-containing compound metabolic process	5.23E-04	1.35E-02	31
GO:0042470 Melanosome	5.25E-04	1.35E-02	31
GO:0050767 Regulation of neurogenesis	5.28E-04	1.35E-02	26
GO:0046873 Metal ion transmembrane transporter activity	5.31E-04	1.35E-02	7
GO:0051960 Regulation of nervous system development	5.40E-04	1.35E-02	26
GO:0048731 System development	5.42E-04	1.35E-02	31
GO:0050900 Leukocyte migration	5.46E-04	1.35E-02	17
GO:0034332 Adherens junction organization	5.79E-04	1.35E-02	16
GO:0050896 Response to stimulus	6.31E-04	1.35E-02	444
GO:0007165 Signal transduction	6.39E-04	1.35E-02	286
GO:0050789 Regulation of biological process	6.55E-04	1.35E-02	534
GO:0016323 Basolateral plasma membrane	6.90E-04	1.35E-02	22
GO:0019829 ATPase-coupled cation transmembrane transporter activity	7.31E-04	1.35E-02	9
GO:0031234 Extrinsic component of cytoplasmic side of plasma membrane	7.31E-04	1.35E-02	6
GO:0042625 ATPase-coupled ion transmembrane transporter activity	7.44E-04	1.35E-02	9
GO:0030054 Cell junction	7.53E-04	1.35E-02	67
GO:0050808 Synapse organization	7.93E-04	1.35E-02	10
GO:0019003 GDP binding	8.21E-04	1.35E-02	18
GO:1901069 Guanosine-containing compound catabolic process	8.58E-04	2.17E-02	26
GO:0060089 Molecular transducer activity	9.12E-04	2.17E-02	38
GO:0030198 Extracellular matrix organization	9.16E-04	2.17E-02	13
GO:0009205 Purine ribonucleoside triphosphate metabolic process	9.55E-04	2.17E-02	44
GO:0009653 Anatomical structure morphogenesis	9.59E-04	2.17E-02	65
GO:0043062 Extracellular structure organization	9.65E-04	2.17E-02	13
GO:0003382 Epithelial cell morphogenesis	9.86E-04	2.17E-02	4
GO:0009199 Ribonucleoside triphosphate metabolic process	1.01E-03	2.17E-02	44
GO:0048856 Anatomical structure development	1.06E-03	2.17E-02	151
GO:1900542 Regulation of purine nucleotide metabolic process	1.09E-03	2.17E-02	19
GO:0043194 Axon initial segment	1.10E-03	2.17E-02	3
GO:0000902 Cell morphogenesis	1.15E-03	2.17E-02	14
GO:0040011 Locomotion	1.20E-03	2.17E-02	49
GO:0023052 Signaling	1.27E-03	2.17E-02	38
GO:0009144 Purine nucleoside triphosphate metabolic process	1.31E-03	2.17E-02	47
GO:0051056 Regulation of small GTPase mediated signal transduction	1.41E-03	3.19E-02	24
GO:0048869 Cellular developmental process	1.44E-03	3.19E-02	98
GO:0008104 Protein localization	1.51E-03	4.21E-02	40
GO:0033010 Paranodal junction	1.56E-03	5.05E-02	2
GO:0031226 Intrinsic component of plasma membrane	1.57E-03	5.05E-02	36
GO:0030139 Endocytic vesicle	1.58E-03	5.05E-02	11
GO:0065008 Regulation of biological quality	1.58E-03	5.05E-02	220
GO:0033270 Paranode region of axon	1.59E-03	5.83E-02	3
GO:0009141 Nucleoside triphosphate metabolic process	1.62E-03	5.83E-02	48
GO:0050878 Regulation of body fluid levels	1.66E-03	5.83E-02	55
GO:0042626 ATPase-coupled transmembrane transporter activity	1.80E-03	7.62E-02	10
GO:0051179 Localization	1.90E-03	7.89E-02	48
GO:0045664 Regulation of neuron differentiation	1.90E-03	7.89E-02	20
GO:0030154 Cell differentiation	1.95E-03	7.89E-02	57

Gene Ontology Enrichment in Young Lens Outer Nucleus relative to Old Lens Outer Nucleus	P-Value	FDR	Number of Proteins with Annotation in Dataset
GO:0033268 Node of ranvier	2.01E-03	7.89E-02	2
GO:0010927 Cellular component assembly involved in morphogenesis	2.02E-03	7.89E-02	7
GO:0015081 Sodium ion transmembrane transporter activity	2.10E-03	7.89E-02	5
GO:0033036 Macromolecule localization	2.25E-03	7.89E-02	41
GO:0060560 Developmental growth involved in morphogenesis	2.27E-03	7.89E-02	3
GO:0045761 Regulation of adenylate cyclase activity	2.30E-03	8.20E-02	7
GO:0031279 Regulation of cyclase activity	2.31E-03	8.20E-02	7
GO:0005391 P-type sodium:potassium-exchanging transporter activity	2.36E-03	8.20E-02	3
GO:0015662 P-type ion transporter activity	2.39E-03	8.20E-02	3
GO:0098533 ATPase dependent transmembrane transport complex	2.40E-03	8.20E-02	3
GO:0005890 Sodium:potassium-exchanging ATPase complex	2.40E-03	8.20E-02	3
GO:0008556 P-type potassium transmembrane transporter activity	2.41E-03	8.20E-02	3
GO:0090533 Cation-transporting ATPase complex	2.44E-03	8.20E-02	3
GO:0015079 Potassium ion transmembrane transporter activity	2.51E-03	8.59E-02	3
GO:0002685 Regulation of leukocyte migration	2.59E-03	8.59E-02	5
GO:0001525 Angiogenesis	2.67E-03	8.59E-02	16
GO:0051339 Regulation of lyase activity	2.68E-03	8.59E-02	8
GO:0045202 Synapse	2.76E-03	8.59E-02	17
GO:0016324 Apical plasma membrane	2.88E-03	8.59E-02	16
GO:0005768 Endosome	2.91E-03	9.02E-02	34
GO:0050870 Positive regulation of t cell activation	2.94E-03	9.02E-02	13
GO:0060491 Regulation of cell projection assembly	2.97E-03	9.02E-02	8
GO:0042552 Myelination	3.08E-03	9.02E-02	3
GO:0086080 Protein binding involved in heterotypic cell-cell adhesion	3.22E-03	9.49E-02	2
GO:0045162 Clustering of voltage-gated sodium channels	3.26E-03	9.49E-02	2
GO:0050839 Cell adhesion molecule binding	3.28E-03	9.49E-02	10
GO:0010975 Regulation of neuron projection development	3.30E-03	9.49E-02	17

H. Table of Gene Ontologies enriched in the old (>50 y.o.) lens outer nucleus relative to young (<50 y.o.) lens outer nucleus

Gene Ontologies calculated as enriched by PSEA-Quant in the outer nucleus region of the Old Lens relative to the Young Lens. Significance was determined at a p-value < 0.01 and FDR < 0.1. PSEA-Quant was operated in labeled mode with 1,000,000 iterations used to empirically evaluate p-values. P-values below 1/1,000,000 ($1x10^{-6}$) are marked as such and correspond to distributions of protein enrichment not similar to prior distributions evaluated in 1,000,000 iterations. Number of proteins refers to proteins detected in dataset (no missing values from 16 samples) with the corresponding annotation.

Gene Ontology Enrichment in Old Lens Outer Nucleus relative to Young Lens Outer Nucleus	P-Value	FDR	Number of Proteins with Annotation in Dataset
GO:0003824 Catalytic activity	<1E-06	2.94E-02	517
GO:0008152 Metabolic process	<1E-06	2.94E-02	604
GO:0016491 Oxidoreductase activity	<1E-06	2.94E-02	81
GO:0043170 Macromolecule metabolic process	<1E-06	2.94E-02	357
GO:0044237 Cellular metabolic process	<1E-06	2.94E-02	559
GO:0044238 Primary metabolic process	<1E-06	2.94E-02	543
GO:0044281 Small molecule metabolic process	<1E-06	2.94E-02	312
GO:0071704 Organic substance metabolic process	<1E-06	2.94E-02	565
GO:0019538 Protein metabolic process	2.00E-06	2.94E-02	263
GO:0005829 Cytosol	2.00E-06	2.94E-02	436
GO:0044260 Cellular macromolecule metabolic process	3.00E-06	2.94E-02	330
GO:1902494 Catalytic complex	6.00E-06	2.94E-02	72
GO:0005739 Mitochondrion	1.20E-05	2.94E-02	142
GO:0006464 Cellular protein modification process	1.50E-05	2.94E-02	165
GO:0036211 Protein modification process	1.60E-05	2.94E-02	165
GO:0043412 Macromolecule modification	2.50E-05	2.94E-02	167
GO:0044267 Cellular protein metabolic process	3.40E-05	2.94E-02	234
GO:1990204 Oxidoreductase complex	4.10E-05	2.94E-02	11
GO:0009058 Biosynthetic process	4.10E-05	2.94E-02	228
GO:1901576 Organic substance biosynthetic process	4.80E-05	2.94E-02	226
GO:0044249 Cellular biosynthetic process	7.70E-05	2.94E-02	198
GO:0005654 Nucleoplasm	1.48E-04	2.94E-02	82
GO:0006807 Nitrogen compound metabolic process	1.73E-04	2.94E-02	312
GO:0034641 Cellular nitrogen compound metabolic process	1.91E-04	2.94E-02	289
GO:0006082 Organic acid metabolic process	1.95E-04	2.94E-02	114
GO:0019752 Carboxylic acid metabolic process	2.32E-04	2.94E-02	110
GO:0043436 Oxoacid metabolic process	2.50E-04	2.94E-02	112
GO:0019318 Hexose metabolic process	3.03E-04	2.94E-02	53
GO:0031966 Mitochondrial membrane	3.25E-04	2.94E-02	39
GO:0005743 Mitochondrial inner membrane	4.40E-04	4.76E-02	28
GO:0019866 Organelle inner membrane	4.42E-04	4.76E-02	28
GO:0005747 Mitochondrial respiratory chain complex I	4.56E-04	4.76E-02	7
GO:0045271 Respiratory chain complex I	4.63E-04	4.76E-02	7
GO:0030964 NADH dehydrogenase complex	4.82E-04	4.76E-02	7
GO:0016655 Oxidoreductase activity, acting on NAD(P)H, quinone or similar compound as acceptor	5.80E-04	4.76E-02	11
GO:1901575 Organic substance catabolic process	6.19E-04	4.76E-02	217
GO:0006091 Generation of precursor metabolites and energy	6.25E-04	4.76E-02	63
GO:0016651 Oxidoreductase activity, acting on NAD(P)H	8.12E-04	7.69E-02	18
GO:0005996 Monosaccharide metabolic process	8.54E-04	7.69E-02	58
GO:0048145 Regulation of fibroblast proliferation	8.97E-04	7.69E-02	9
GO:0071482 Cellular response to light stimulus	9.23E-04	7.69E-02	6
GO:0005737 Cytoplasm	9.84E-04	7.69E-02	432
GO:0006006 Glucose metabolic process	1.00E-03	7.69E-02	48

Gene Ontology Enrichment in Old Lens Outer Nucleus relative to Young Lens Outer Nucleus	**P-Value**	**FDR**	**Number of Proteins with Annotation in Dataset**
GO:0004497 Monooxygenase activity	1.18E-03	7.69E-02	5
GO:0022900 Electron transport chain	1.19E-03	7.69E-02	12
GO:0016702 Oxidoreductase activity, acting on single donors with incorporation of molecular oxygen, incorporation of two atoms of oxygen	1.19E-03	7.69E-02	4
GO:0005506 Iron ion binding	1.21E-03	7.69E-02	9
GO:0022904 Respiratory electron transport chain	1.21E-03	7.69E-02	12
GO:0051213 Dioxygenase activity	1.24E-03	7.69E-02	4
GO:0048146 Positive regulation of fibroblast proliferation	1.24E-03	7.69E-02	5
GO:0005975 Carbohydrate metabolic process	1.26E-03	7.69E-02	88
GO:0016701 Oxidoreductase activity, acting on single donors with incorporation of molecular oxygen	1.30E-03	7.69E-02	4
GO:0046906 Tetrapyrrole binding	1.32E-03	7.69E-02	5
GO:0020037 Heme binding	1.32E-03	7.69E-02	5
GO:0051726 Regulation of cell cycle	1.48E-03	7.69E-02	82
GO:0032787 Monocarboxylic acid metabolic process	1.49E-03	7.69E-02	36
GO:0032446 Protein modification by small protein conjugation	1.51E-03	7.69E-02	60
GO:0015718 Monocarboxylic acid transport	1.54E-03	9.09E-02	6
GO:0071478 Cellular response to radiation	1.55E-03	1.00E-01	7
GO:1901360 Organic cyclic compound metabolic process	1.56E-03	1.00E-01	282
GO:0046483 Heterocycle metabolic process	1.57E-03	1.00E-01	255
GO:0006839 Mitochondrial transport	1.58E-03	1.00E-01	13
GO:0070647 Protein modification by small protein conjugation or removal	1.58E-03	1.00E-01	76
GO:0022402 Cell cycle process	1.70E-03	1.00E-01	106
GO:0050136 NADH dehydrogenase (quinone) activity	1.71E-03	1.00E-01	6
GO:0008137 NADH dehydrogenase (ubiquinone) activity	1.76E-03	1.00E-01	6
GO:0003954 NADH dehydrogenase activity	1.77E-03	1.00E-01	6
GO:0009056 Catabolic process	1.78E-03	1.00E-01	234
GO:0006725 Cellular aromatic compound metabolic process	1.79E-03	1.00E-01	261
GO:0090304 Nucleic acid metabolic process	1.82E-03	1.00E-01	150
GO:0016567 Protein ubiquitination	1.83E-03	1.00E-01	57
GO:0010803 Regulation of tumor necrosis factor-mediated signaling pathway	1.91E-03	1.00E-01	3
GO:1901566 Organonitrogen compound biosynthetic process	1.91E-03	1.00E-01	63
GO:0016070 RNA metabolic process	1.95E-03	1.00E-01	131
GO:0019371 Cyclooxygenase pathway	2.36E-03	1.00E-01	4
GO:0042168 Heme metabolic process	2.86E-03	1.00E-01	4
GO:0010467 Gene expression	2.95E-03	1.00E-01	93
GO:0000082 G1/S transition of mitotic cell cycle	3.02E-03	1.00E-01	43
GO:0033554 Cellular response to stress	3.14E-03	1.00E-01	101
GO:0071013 Catalytic step 2 spliceosome	3.19E-03	1.00E-01	2

I. Table of Gene Ontologies enriched in the young (<50 y.o.) lens inner nucleus relative to old (>50 y.o.) lens inner nucleus

Gene Ontologies calculated as enriched by PSEA-Quant in the inner nucleus of the Young Lens relative to the Old Lens. Significance was determined at a p-value < 0.01 and FDR < 0.1. PSEA-Quant was operated in labeled mode with 1,000,000 iterations used to empirically evaluate p-values. P-values below 1/1,000,000 (1x10^{-6}) are marked as such and correspond to distributions of protein enrichment not similar to prior distributions evaluated in 1,000,000 iterations. Number of proteins refers to proteins detected in dataset (no missing values from 16 samples) with the corresponding annotation.

Gene Ontology Enrichment in Young Lens Inner Nucleus relative to Old Lens Inner Nucleus	**P-Value**	**FDR**	**Number of Proteins with Annotation in Dataset**
GO:0005886 Plasma membrane	<1E-06	2.63E-02	174
GO:0007155 Cell adhesion	<1E-06	2.63E-02	35
GO:0016020 Membrane	<1E-06	2.63E-02	302
GO:0022610 Biological adhesion	<1E-06	2.63E-02	35
GO:0031224 Intrinsic component of membrane	<1E-06	2.63E-02	97
GO:0034330 Cell junction organization	<1E-06	2.63E-02	23
GO:0045121 Membrane raft	<1E-06	2.63E-02	16
GO:0045216 Cell-cell junction organization	<1E-06	2.63E-02	20
GO:0050870 Positive regulation of T-cell activation	<1E-06	2.63E-02	10
GO:0002696 Positive regulation of leukocyte activation	2.00E-06	2.63E-02	11
GO:0050867 Positive regulation of cell activation	2.00E-06	2.63E-02	11
GO:0051251 Positive regulation of lymphocyte activation	3.00E-06	2.63E-02	11
GO:0031226 Intrinsic component of plasma membrane	3.00E-06	2.63E-02	26
GO:0034329 Cell junction assembly	5.00E-06	2.63E-02	20
GO:0050863 Regulation of T-cell activation	9.00E-06	2.63E-02	15
GO:0009986 Cell surface	4.60E-05	2.63E-02	18
GO:0001525 Angiogenesis	5.70E-05	2.63E-02	13
GO:0007411 Axon guidance	8.20E-05	2.63E-02	40
GO:0051249 Regulation of lymphocyte activation	8.20E-05	2.63E-02	16
GO:0031225 Anchored component of membrane	9.10E-05	2.63E-02	6
GO:0097485 Neuron projection guidance	9.50E-05	2.63E-02	40
GO:0002694 Regulation of leukocyte activation	1.00E-04	2.63E-02	16
GO:0016021 Integral component of membrane	1.08E-04	2.63E-02	91
GO:0019898 Extrinsic component of membrane	1.09E-04	2.63E-02	16
GO:0005887 Integral component of plasma membrane	1.20E-04	2.63E-02	23
GO:0032502 Developmental process	1.21E-04	2.63E-02	193
GO:0005901 Caveola	1.23E-04	2.63E-02	8
GO:0048646 Anatomical structure formation involved in morphogenesis	1.42E-04	2.63E-02	27
GO:0030054 Cell junction	1.60E-04	2.63E-02	57
GO:0050865 Regulation of cell activation	1.74E-04	2.63E-02	18
GO:0050817 Coagulation	3.83E-04	2.63E-02	42
GO:0007596 Blood coagulation	4.29E-04	2.63E-02	42
GO:0045785 Positive regulation of cell adhesion	5.15E-04	2.63E-02	8
GO:0002684 Positive regulation of immune system process	5.16E-04	2.63E-02	36
GO:0034332 Adherens junction organization	5.30E-04	7.69E-02	13

J. Table of Gene Ontologies enriched in the old (<50 y.o.) lens inner nucleus relative to young (>50 y.o.) lens inner nucleus

Gene Ontologies calculated as enriched by PSEA-Quant in the inner nucleus region of the Old Lens relative to the Young Lens. Significance was determined at a p-value < 0.01 and FDR < 0.1. PSEA-Quant was operated in labeled mode with 1,000,000 iterations used to empirically evaluate p-values. P-values below 1/1,000,000 ($1x10^{-6}$) are marked as such and correspond to distributions of protein enrichment not similar to prior distributions evaluated in 1,000,000 iterations. Number of proteins refers to proteins detected in dataset (no missing values from 16 samples) with the corresponding annotation.

Gene Ontology Enrichment in Old Lens Inner Nucleus relative to Young Lens Inner Nucleus	**P-Value**	**FDR**	**Number of Proteins with Annotation in Dataset**
GO:0016491 Oxidoreductase activity	9.60E-05	1.00E-01	78
GO:0004867 Serine-type endopeptidase inhibitor activity	1.34E-04	1.00E-01	4
GO:0051346 Negative regulation of hydrolase activity	1.44E-04	1.00E-01	14
GO:0010951 Negative regulation of endopeptidase activity	2.56E-04	1.00E-01	11
GO:0010466 Negative regulation of peptidase activity	2.78E-04	1.00E-01	11
GO:0010948 Negative regulation of cell cycle process	4.53E-04	1.00E-01	34
GO:0046906 Tetrapyrrole binding	5.20E-04	1.00E-01	4
GO:0016705 Oxidoreductase activity, acting on paired donors, with incorporation or reduction of molecular oxygen	5.34E-04	1.00E-01	10
GO:0020037 Heme binding	5.39E-04	1.00E-01	4

REFERENCES

2010 Cataract Tables. (2010). National Eye Institute. https://www.nei.nih.gov/learn-about-eye-health/resources-for-health-educators/eye-health-data-and-statistics/cataract-data-and-statistics/cataract-tables

Aballo, T. J., Roberts, D. S., Melby, J. A., Buck, K. M., Brown, K. A., & Ge, Y. (2021). Ultrafast and Reproducible Proteomics from Small Amounts of Heart Tissue Enabled by Azo and timsTOF Pro. *Journal of Proteome Research*, *20*(8), 4203–4211. https://doi.org/10.1021/acs.jproteome.1c00446

Adusumilli, R., & Mallick, P. (2017). Data Conversion with ProteoWizard msConvert. *Methods in Molecular Biology (Clifton, N.J.)*, *1550*, 339–368. https://doi.org/10.1007/978-1-4939-6747-6_23

Albert, D. M., & Edwards, D. D. (Eds.). (1996). *The history of ophthalmology*. Blackwell Science.

Alnemri, E. S., Livingston, D. J., Nicholson, D. W., Salvesen, G., Thornberry, N. A., Wong, W. W., & Yuan, J. (1996). Human ICE/CED-3 protease nomenclature. *Cell*, *87*(2), 171. https://doi.org/10.1016/s0092-8674(00)81334-3

Amodei, D., Egertson, J., MacLean, B. X., Johnson, R., Merrihew, G. E., Keller, A., Marsh, D., Vitek, O., Mallick, P., & MacCoss, M. J. (2019). Improving Precursor Selectivity in Data-Independent Acquisition Using Overlapping Windows. *Journal of the American Society for Mass Spectrometry*, *30*(4), 669–684. https://doi.org/10.1007/s13361-018-2122-8

Anderson, D. M., Nye-Wood, M. G., Rose, K. L., Donaldson, P. J., Grey, A. C., & Schey, K. L. (2020). MALDI imaging mass spectrometry of β- and γ-crystallins in the ocular lens. *Journal of Mass Spectrometry: JMS*, *55*(4), e4473. https://doi.org/10.1002/jms.4473

Angelidis, I., Simon, L. M., Fernandez, I. E., Strunz, M., Mayr, C. H., Greiffo, F. R., Tsitsiridis, G., Ansari, M., Graf, E., Strom, T.-M., Nagendran, M., Desai, T., Eickelberg, O., Mann, M., Theis, F. J., & Schiller, H. B. (2019). An atlas of the aging lung mapped by single cell transcriptomics and deep tissue proteomics. *Nature Communications*, *10*(1), 963. https://doi.org/10.1038/s41467-019-08831-9

Aquilina, J. A., Benesch, J. L. P., Ding, L. L., Yaron, O., Horwitz, J., & Robinson, C. V. (2004). Phosphorylation of αB-Crystallin Alters Chaperone Function through Loss of Dimeric Substructure. *Journal of Biological Chemistry*, *279*(27), 28675–28680. https://doi.org/10.1074/jbc.M403348200

Aragonès, G., Rowan, S., G Francisco, S., Yang, W., Weinberg, J., Taylor, A., & Bejarano, E. (2020). Glyoxalase System as a Therapeutic Target against Diabetic Retinopathy. *Antioxidants (Basel, Switzerland)*, *9*(11), E1062. https://doi.org/10.3390/antiox9111062

Arrojo e Drigo, R., Lev-Ram, V., Tyagi, S., Ramachandra, R., Deerinck, T., Bushong, E., Phan, S., Orphan, V., Lechene, C., Ellisman, M. H., & Hetzer, M. W. (2019). Age Mosaicism across Multiple Scales in Adult Tissues. *Cell Metabolism*, *30*(2), 343-351.e3. https://doi.org/10.1016/j.cmet.2019.05.010

Ashburner, M., Ball, C. A., Blake, J. A., Botstein, D., Butler, H., Cherry, J. M., Davis, A. P., Dolinski, K., Dwight, S. S., Eppig, J. T., Harris, M. A., Hill, D. P., Issel-Tarver, L., Kasarskis, A., Lewis, S., Matese, J. C., Richardson, J. E., Ringwald, M., Rubin, G. M., & Sherlock, G. (2000). Gene ontology: Tool for the unification of biology. The Gene Ontology Consortium. *Nature Genetics*, *25*(1), 25–29. https://doi.org/10.1038/75556

Atreya, P. L., Barnes, J., Katar, M., Alcala, J., & Maisel, H. (1989). N-cadherin of the human lens. *Current Eye Research*, *8*(9), 947–956.

Augusteyn, R. C. (2007). Growth of the human eye lens. *Molecular Vision*, *13*, 252–257.

Aziz, A., Santhoshkumar, P., Sharma, K. K., & Abraham, E. C. (2007). Cleavage of the C-Terminal Serine of Human αA-Crystallin Produces αA $_{1\text{-}172}$ with Increased Chaperone Activity and Oligomeric Size †. *Biochemistry*, *46*(9), 2510–2519. https://doi.org/10.1021/bi0618722

Bada, J. L., & Protsch, R. (1973). Racemization Reaction of Aspartic Acid and Its Use in Dating Fossil Bones. *Proceedings of the National Academy of Sciences*, *70*(5), 1331–1334. https://doi.org/10.1073/pnas.70.5.1331

Baillie, J. K., Bates, M. G. D., Thompson, A. A. R., Waring, W. S., Partridge, R. W., Schnopp, M. F., Simpson, A., Gulliver-Sloan, F., Maxwell, S. R. J., & Webb, D. J. (2007). Endogenous urate production augments plasma antioxidant capacity in healthy lowland subjects exposed to high altitude. *Chest*, *131*(5), 1473–1478. https://doi.org/10.1378/chest.06-2235

Baldo, G. J., & Mathias, R. T. (1992). Spatial variations in membrane properties in the intact rat lens. *Biophysical Journal*, *63*(2), 518–529. https://doi.org/10.1016/S0006-3495(92)81624-7

Ball, L. E., Little, M., Nowak, M. W., Garland, D. L., Crouch, R. K., & Schey, K. L. (2003). Water Permeability of C-Terminally Truncated Aquaporin 0 (AQP0 1-243) Observed in the Aging Human Lens. *Investigative Opthalmology & Visual Science*, *44*(11), 4820. https://doi.org/10.1167/iovs.02-1317

Ballatori, N., Krance, S. M., Marchan, R., & Hammond, C. L. (2009). Plasma membrane glutathione transporters and their roles in cell physiology and pathophysiology. *Molecular Aspects of Medicine*, *30*(1–2), 13–28. https://doi.org/10.1016/j.mam.2008.08.004

Banh, A., Bantseev, V., Choh, V., Moran, K. L., & Sivak, J. G. (2006). The lens of the eye as a focusing device and its response to stress. *Progress in Retinal and Eye Research*, *25*(2), 189–206. https://doi.org/10.1016/j.preteyeres.2005.10.001

Barraquer, R. I., Michael, R., Abreu, R., Lamarca, J., & Tresserra, F. (2006). Human Lens Capsule Thickness as a Function of Age and Location along the Sagittal Lens Perimeter. *Investigative Opthalmology & Visual Science*, *47*(5), 2053. https://doi.org/10.1167/iovs.05-1002

Bassnett, S. (1992). Mitochondrial dynamics in differentiating fiber cells of the mammalian lens. *Current Eye Research*, *11*(12), 1227–1232. https://doi.org/10.3109/02713689208999548

Bassnett, S. (1995). The fate of the Golgi apparatus and the endoplasmic reticulum during lens fiber cell differentiation. *Investigative Ophthalmology & Visual Science*, *36*(9), 1793–1803.

Bassnett, S. (2002). Lens organelle degradation. *Experimental Eye Research*, *74*(1), 1–6. https://doi.org/10.1006/exer.2001.1111

Bassnett, S., & Beebe, D. C. (1992). Coincident loss of mitochondria and nuclei during lens fiber cell differentiation. *Developmental Dynamics: An Official Publication of the American Association of Anatomists*, *194*(2), 85–93. https://doi.org/10.1002/aja.1001940202

Bassnett, S., & Costello, M. J. (2017). The cause and consequence of fiber cell compaction in the vertebrate lens. *Experimental Eye Research*, *156*, 50–57. https://doi.org/10.1016/j.exer.2016.03.009

Bassnett, S., & Mataic, D. (1997). Chromatin Degradation in Differentiating Fiber Cells of the Eye Lens. *Journal of Cell Biology*, *137*(1), 37–49. https://doi.org/10.1083/jcb.137.1.37

Bassnett, S., Wilmarth, P. A., & David, L. L. (2009). The membrane proteome of the mouse lens fiber cell. *Molecular Vision*, *15*, 2448–2463.

Beebe, D. C., & Cerrelli, S. (1989). Cytochalasin prevents cell elongation and increases potassium efflux from embryonic lens epithelial cells: Implications for the mechanism of lens fiber cell elongation. *Lens and Eye Toxicity Research*, *6*(4), 589–601.

Beebe, D. C., Compart, P. J., Johnson, M. C., Feagans, D. E., & Feinberg, R. N. (1982). The mechanism of cell elongation during lens fiber cell differentiation. *Developmental Biology*, *92*(1), 54–59. https://doi.org/10.1016/0012-1606(82)90149-X

Beebe, D. C., & Truscott, R. J. W. (2010). Counterpoint: The Lens Fluid Circulation Model—A Critical Appraisal. *Investigative Opthalmology & Visual Science*, *51*(5), 2306. https://doi.org/10.1167/iovs.10-5350a

Beebe, D. C., Vasiliev, O., Guo, J., & Bassnett, S. (2001). Changes in Adhesion Complexes Define Stages in the Differentiation of Lens Fiber Cells. *Investigative Ophthalmology & Visual Science*, *42*, 727–734.

Bekker-Jensen, D. B., Bernhardt, O. M., Hogrebe, A., Martinez-Val, A., Verbeke, L., Gandhi, T., Kelstrup, C. D., Reiter, L., & Olsen, J. V. (2020). Rapid and site-specific deep phosphoproteome profiling by data-independent acquisition without the need for spectral libraries. *Nature Communications*, *11*(1). https://doi.org/10.1038/s41467-020-14609-1

Bekker-Jensen, D. B., Martínez-Val, A., Steigerwald, S., Rüther, P., Fort, K. L., Arrey, T. N., Harder, A., Makarov, A., & Olsen, J. V. (2020). A Compact Quadrupole-Orbitrap Mass Spectrometer with FAIMS Interface Improves Proteome Coverage in Short LC Gradients. *Molecular & Cellular Proteomics: MCP*, *19*(4), 716–729. https://doi.org/10.1074/mcp.TIR119.001906

Berthoud, V. M., & Beyer, E. C. (2009). Oxidative stress, lens gap junctions, and cataracts. *Antioxidants & Redox Signaling*, *11*(2), 339–353. https://doi.org/10.1089/ars.2008.2119

Berthoud, V. M., Minogue, P. J., Osmolak, P., Snabb, J. I., & Beyer, E. C. (2014). Roles and regulation of lens epithelial cell connexins. *FEBS Letters*, *588*(8), 1297–1303. https://doi.org/10.1016/j.febslet.2013.12.024

Betts, M. J., Wichmann, O., Utz, M., Andre, T., Petsalaki, E., Minguez, P., Parca, L., Roth, F. P., Gavin, A.-C., Bork, P., & Russell, R. B. (2017). Systematic identification of phosphorylation-mediated protein interaction switches. *PLOS Computational Biology*, *13*(3), e1005462. https://doi.org/10.1371/journal.pcbi.1005462

Biswas, S. K., Lee, J. E., Brako, L., Jiang, J. X., & Lo, W.-K. (2010). Gap junctions are selectively associated with interlocking ball-and-sockets but not protrusions in the lens. *Molecular Vision*, *16*, 2328–2341.

Bloemendal, H., de Jong, W., Jaenicke, R., Lubsen, N. H., Slingsby, C., & Tardieu, A. (2004). Ageing and vision: Structure, stability and function of lens crystallins. *Progress in Biophysics and Molecular Biology*, *86*(3), 407–485. https://doi.org/10.1016/j.pbiomolbio.2003.11.012

Bodemann, B. O., Orvedahl, A., Cheng, T., Ram, R. R., Ou, Y.-H., Formstecher, E., Maiti, M., Hazelett, C. C., Wauson, E. M., Balakireva, M., Camonis, J. H., Yeaman, C., Levine, B., & White, M. A. (2011). RalB and the Exocyst Mediate the Cellular Starvation Response by Direct Activation of Autophagosome Assembly. *Cell*, *144*(2), 253–267. https://doi.org/10.1016/j.cell.2010.12.018

Breljak, D., Ljubojević, M., Hagos, Y., Micek, V., Balen Eror, D., Vrhovac Madunić, I., Brzica, H., Karaica, D., Radović, N., Kraus, O., Anzai, N., Koepsell, H., Burckhardt, G., Burckhardt, B. C., & Sabolić, I. (2016). Distribution of organic anion transporters NaDC3 and OAT1-3 along the human nephron. *American Journal of Physiology-Renal Physiology*, *311*(1), F227–F238. https://doi.org/10.1152/ajprenal.00113.2016

Brian, G., & Taylor, H. (2001). Cataract blindness—Challenges for the 21st century. *Bulletin of the World Health Organization*, *79*(3), 249–256.

Bridges, R. J., Natale, N. R., & Patel, S. A. (2012). System xc$^-$ cystine/glutamate antiporter: An update on molecular pharmacology and roles within the CNS. *British Journal of Pharmacology*, *165*(1), 20–34. https://doi.org/10.1111/j.1476-5381.2011.01480.x

Buckingham, R. H. (1972). The behaviour of reduced proteins from normal and cataractous lenses in highly dissociating media: Cross-linked protein in cataractous lenses. *Experimental Eye Research*, *14*(2), 123–129. https://doi.org/10.1016/0014-4835(72)90057-7

Budnik, B., Levy, E., Harmange, G., & Slavov, N. (2018). SCoPE-MS: Mass spectrometry of single mammalian cells quantifies proteome heterogeneity during cell differentiation. *Genome Biology*, *19*(1). https://doi.org/10.1186/s13059-018-1547-5

Bush, K. T., Wu, W., Lun, C., & Nigam, S. K. (2017). The drug transporter OAT3 (SLC22A8) and endogenous metabolite communication via the gut-liver-kidney axis. *The Journal of Biological Chemistry*, *292*(38), 15789–15803. https://doi.org/10.1074/jbc.M117.796516

Cai, X., Ge, W., Yi, X., Sun, R., Zhu, J., Lu, C., Sun, P., Zhu, T., Ruan, G., Yuan, C., Liang, S., Lyu, M., Huang, S., Zhu, Y., & Guo, T. (2021). PulseDIA: Data-Independent Acquisition Mass Spectrometry Using Multi-Injection Pulsed Gas-Phase Fractionation. *Journal of Proteome Research*, *20*(1), 279–288. https://doi.org/10.1021/acs.jproteome.0c00381

Candia, O. A., Mathias, R., & Gerometta, R. (2012). Fluid Circulation Determined in the Isolated Bovine Lens. *Investigative Opthalmology & Visual Science*, *53*(11), 7087. https://doi.org/10.1167/iovs.12-10295

Candia, O. A., & Zamudio, A. C. (2002). Regional distribution of the Na $^+$ and K $^+$ currents around the crystalline lens of rabbit. *American Journal of Physiology-Cell Physiology*, *282*(2), C252–C262. https://doi.org/10.1152/ajpcell.00360.2001

Cantrell, L. S., Gletten, R. B., & Schey, K. L. (2023). Proteome Remodeling of the Eye Lens at 50 Years Identified With Data-Independent Acquisition. *Molecular & Cellular Proteomics*, *22*(1), 100453. https://doi.org/10.1016/j.mcpro.2022.100453

Cantrell, L. S., & Schey, K. L. (2021a). Proteomic characterization of the human lens and Cataractogenesis. *Expert Review of Proteomics*, 1–17. https://doi.org/10.1080/14789450.2021.1913062

Cantrell, L. S., & Schey, K. L. (2021b). Data-Independent Acquisition Mass Spectrometry of the Human Lens Enhances Spatiotemporal Measurement of Fiber Cell Aging. *Journal of the American Society for Mass Spectrometry*, jasms.1c00193. https://doi.org/10.1021/jasms.1c00193

Carroll, V. N., Truillet, C., Shen, B., Flavell, R. R., Shao, X., Evans, M. J., VanBrocklin, H. F., Scott, P. J. H., Chin, F. T., & Wilson, D. M. (2016). [^{11} C]Ascorbic and [^{11} C]dehydroascorbic acid, an endogenous redox pair for sensing reactive oxygen species using positron emission tomography. *Chemical Communications*, *52*(27), 4888–4890. https://doi.org/10.1039/C6CC00895J

Chaurand, P., Latham, J. C., Lane, K. B., Mobley, J. A., Polosukhin, V. V., Wirth, P. S., Nanney, L. B., & Caprioli, R. M. (2008). Imaging mass spectrometry of intact proteins from alcohol-preserved tissue specimens: Bypassing formalin fixation. *Journal of Proteome Research*, *7*(8), 3543–3555. https://doi.org/10.1021/pr800286z

Chen, Y., Petrova, R. S., Qiu, C., & Donaldson, P. J. (2022). Intracellular hydrostatic pressure regulation in the bovine lens: A role in the regulation of lens optics? *American Journal of Physiology. Regulatory,* *Integrative and Comparative Physiology*, *322*(3), R263–R279. https://doi.org/10.1152/ajpregu.00309.2021

Chen, Z.-L., Meng, J.-M., Cao, Y., Yin, J.-L., Fang, R.-Q., Fan, S.-B., Liu, C., Zeng, W.-F., Ding, Y.-H., Tan, D., Wu, L., Zhou, W.-J., Chi, H., Sun, R.-X., Dong, M.-Q., & He, S.-M. (2019). A high-speed search engine pLink 2 with systematic evaluation for proteome-scale identification of cross-linked peptides. *Nature Communications*, *10*(1), 3404. https://doi.org/10.1038/s41467-019-11337-z

Cheng, C., Nowak, R. B., & Fowler, V. M. (2017). The lens actin filament cytoskeleton: Diverse structures for complex functions. *Experimental Eye Research*, *156*, 58–71. https://doi.org/10.1016/j.exer.2016.03.005

Cheng, H.-M., Yen, L. I., Barnett, P., Miglior, S., Eagon, J. C., González, G., & Brady, T. J. (1987). Proton magnetic resonance imaging of the ocular lens. *Experimental Eye Research*, *45*(6), 875–882. https://doi.org/10.1016/S0014-4835(87)80103-3

Chepelinsky, A. B. (2009). Structural function of MIP/aquaporin 0 in the eye lens; genetic defects lead to congenital inherited cataracts. *Handbook of Experimental Pharmacology*, *190*, 265–297. https://doi.org/10.1007/978-3-540-79885-9_14

Chiou, S.-H., Huang, C.-H., Lee, I.-L., Wang, Y.-T., Liu, N.-Y., Tsay, Y.-G., & Chen, Y.-J. (2010). Identification of in vivo phosphorylation sites of lens proteins from porcine eye lenses by a gel-free phosphoproteomics approach. *Molecular Vision*, *16*, 294–302.

Choudhary, G., Wu, S.-L., Shieh, P., & Hancock, W. S. (2003). Multiple Enzymatic Digestion for Enhanced Sequence Coverage of Proteins in Complex Proteomic Mixtures Using Capillary LC with Ion Trap MS/MS. *Journal of Proteome Research*, *2*(1), 59–67. https://doi.org/10.1021/pr025557n

Chylack, L. T., & Kinoshita, J. H. (1972). The interaction of the lens and the vitreous. *Experimental Eye Research*, *14*(1), 58–64. https://doi.org/10.1016/0014-4835(72)90143-1

Cioffi, D. L., Barry, C. J., & Stevens, T. (2011). Role of Calcium as a Second Messenger in Signaling: A Focus on Endothelium. In J. X.-J. Yuan, J. G. N. Garcia, J. B. West, C. A. Hales, S. Rich, & S. L. Archer (Eds.), *Textbook of Pulmonary Vascular Disease* (pp. 261–272). Springer US. https://doi.org/10.1007/978-0-387-87429-6_15

Clark, J. I., Clark, J. M., David, L. L., & Matsushima, H. (1999). Lens cytoskeleton and transparency: A model. *Eye*, *13*(3), 417–424. https://doi.org/10.1038/eye.1999.116

Cournoyer, J. J., Lin, C., & O'Connor, P. B. (2006). Detecting Deamidation Products in Proteins by Electron Capture Dissociation. *Analytical Chemistry*, *78*(4), 1264–1271. https://doi.org/10.1021/ac051691q

Cox, J., & Mann, M. (2008). MaxQuant enables high peptide identification rates, individualized p.p.b.-range mass accuracies and proteome-wide protein quantification. *Nature Biotechnology*, *26*(12), 1367–1372. https://doi.org/10.1038/nbt.1511

Cox, J., Neuhauser, N., Michalski, A., Scheltema, R. A., Olsen, J. V., & Mann, M. (2011). Andromeda: A Peptide Search Engine Integrated into the MaxQuant Environment. *Journal of Proteome Research*, *10*(4), 1794–1805. https://doi.org/10.1021/pr101065j

Croteau, E., Renaud, J. M., Richard, M. A., Ruddy, T. D., Bénard, F., & deKemp, R. A. (2016). PET Metabolic Biomarkers for Cancer. *Biomarkers in Cancer*, *8*(Suppl 2), 61–69. https://doi.org/10.4137/BIC.S27483

Cryar, A., Groves, K., & Quaglia, M. (2017). Online Hydrogen-Deuterium Exchange Traveling Wave Ion Mobility Mass Spectrometry (HDX-IM-MS): A Systematic Evaluation. *Journal of the American Society for Mass Spectrometry*, *28*(6), 1192–1202. https://doi.org/10.1007/s13361-017-1633-z

Dahm, R., Gribbon, C., Quinlan, R. A., & Prescott, A. R. (1998). Changes in the nucleolar and coiled body compartments precede lamina and chromatin reorganization during fibre cell denucleation in the bovine lens. *European Journal of Cell Biology*, *75*(3), 237–246. https://doi.org/10.1016/S0171-9335(98)80118-0

Dargelos, E., Poussard, S., Brulé, C., Daury, L., & Cottin, P. (2008). Calcium-dependent proteolytic system and muscle dysfunctions: A possible role of calpains in sarcopenia. *Biochimie*, *90*(2), 359–368. https://doi.org/10.1016/j.biochi.2007.07.018

Dasari, S., Chambers, M. C., Slebos, R. J., Zimmerman, L. J., Ham, A.-J. L., & Tabb, D. L. (2010). TagRecon: High-Throughput Mutation Identification through Sequence Tagging. *Journal of Proteome Research*, *9*(4), 1716–1726. https://doi.org/10.1021/pr900850m

Davies, P. D., Duncan, G., Pynsent, P. B., Arber, D. L., & Lucas, V. A. (1984). Aqueous humour glucose concentration in cataract patients and its effect on the lens. *Experimental Eye Research*, *39*(5), 605–609. https://doi.org/10.1016/0014-4835(84)90060-5

Dean, W. L., Delamere, N. A., Borchman, D., Moseley, A. E., & Ahuja, R. P. (1996). Studies on lipids and the activity of Na,K-ATPase in lens fibre cells. *The Biochemical Journal*, *314 (Pt 3)*, 961–967. https://doi.org/10.1042/bj3140961

Delamere, N. A., & Dean, W. L. (1993). Distribution of lens sodium-potassium-adenosine triphosphatase. *Investigative Ophthalmology & Visual Science*, *34*(7), 2159–2163.

Delamere, N. A., Dean, W. L., Stidam, J. M., & Moseley, A. E. (1996). Differential expression of sodium pump catalytic subunits in the lens epithelium and fibers. *Ophthalmic Research*, *28 Suppl 1*, 73–76. https://doi.org/10.1159/000267975

Delamere, N. A., & Shahidullah, M. (2022). Ion Transport Regulation by TRPV4 and TRPV1 in Lens and Ciliary Epithelium. *Frontiers in Physiology*, *12*, 834916. https://doi.org/10.3389/fphys.2021.834916

Delamere, N. A., & Tamiya, S. (2004). Expression, regulation and function of Na,K-ATPase in the lens. *Progress in Retinal and Eye Research*, *23*(6), 593–615. https://doi.org/10.1016/j.preteyeres.2004.06.003

Demichev, V., Messner, C. B., Vernardis, S. I., Lilley, K. S., & Ralser, M. (2020). DIA-NN: Neural networks and interference correction enable deep proteome coverage in high throughput. *Nature Methods*, *17*(1), 41–44. https://doi.org/10.1038/s41592-019-0638-x

Deniaud, A., Sharaf el dein, O., Maillier, E., Poncet, D., Kroemer, G., Lemaire, C., & Brenner, C. (2008). Endoplasmic reticulum stress induces calcium-dependent permeability transition, mitochondrial outer membrane permeabilization and apoptosis. *Oncogene*, *27*(3), 285–299. https://doi.org/10.1038/sj.onc.1210638

Dilley, K. J., & Pirie, A. (1974). Changes to the proteins of the human lens nucleus in cataract. *Experimental Eye Research*, *19*(1), 59–72. https://doi.org/10.1016/0014-4835(74)90073-6

Doerr, A. (2015). DIA mass spectrometry. *Nature Methods*, *12*(1), 35–35. https://doi.org/10.1038/nmeth.3234

Donaldson, P. J., Musil, L. S., & Mathias, R. T. (2010). Point: A Critical Appraisal of the Lens Circulation Model—An Experimental Paradigm for Understanding the Maintenance of Lens Transparency? *Investigative Opthalmology & Visual Science*, *51*(5), 2303. https://doi.org/10.1167/iovs.10-5350

Dou, M., Clair, G., Tsai, C.-F., Xu, K., Chrisler, W. B., Sontag, R. L., Zhao, R., Moore, R. J., Liu, T., Pasa-Tolic, L., Smith, R. D., Shi, T., Adkins, J. N., Qian, W.-J., Kelly, R. T., Ansong, C., & Zhu, Y. (2019). High-Throughput Single Cell Proteomics Enabled by Multiplex Isobaric Labeling in a Nanodroplet Sample Preparation Platform. *Analytical Chemistry*, *91*(20), 13119–13127. https://doi.org/10.1021/acs.analchem.9b03349

Duncan, G., & Jacob, T. J. C. (2008). Calcium and the Physiology of Cataract. In J. Nugent & J. Whelan (Eds.), *Novartis Foundation Symposia* (pp. 132–162). John Wiley & Sons, Ltd. https://doi.org/10.1002/9780470720875.ch8

Ebihara, L., Korzyukov, Y., Kothari, S., & Tong, J.-J. (2014). Cx46 hemichannels contribute to the sodium leak conductance in lens fiber cells. *American Journal of Physiology. Cell Physiology*, *306*(5), C506-513. https://doi.org/10.1152/ajpcell.00353.2013

Eden, E., Geva-Zatorsky, N., Issaeva, I., Cohen, A., Dekel, E., Danon, T., Cohen, L., Mayo, A., & Alon, U. (2011). Proteome half-life dynamics in living human cells. *Science (New York, N.Y.)*, *331*(6018), 764–768. https://doi.org/10.1126/science.1199784

Egertson, J. D., Kuehn, A., Merrihew, G. E., Bateman, N. W., MacLean, B. X., Ting, Y. S., Canterbury, J. D., Marsh, D. M., Kellmann, M., Zabrouskov, V., Wu, C. C., & MacCoss, M. J. (2013). Multiplexed MS/MS for improved data-independent acquisition. *Nature Methods*, *10*(8), 744–746. https://doi.org/10.1038/nmeth.2528

Eggleston, L. V., & Krebs, H. A. (1974). Regulation of the pentose phosphate cycle. *The Biochemical Journal*, *138*(3), 425–435. https://doi.org/10.1042/bj1380425

Eng, J. K., McCormack, A. L., & Yates, J. R. (1994). An approach to correlate tandem mass spectral data of peptides with amino acid sequences in a protein database. *Journal of the American Society for Mass Spectrometry*, *5*(11), 976–989. https://doi.org/10.1016/1044-0305(94)80016-2

Fan, X., Monnier, V. M., & Whitson, J. (2017). Lens glutathione homeostasis: Discrepancies and gaps in knowledge standing in the way of novel therapeutic approaches. *Experimental Eye Research*, *156*, 103–111. https://doi.org/10.1016/j.exer.2016.06.018

Ferreira, F. S., Biasibetti-Brendler, H., Pierozan, P., Schmitz, F., Bertó, C. G., Prezzi, C. A., Manfredini, V., & Wyse, A. T. S. (2018). Kynurenic Acid Restores Nrf2 Levels and Prevents Quinolinic Acid-Induced

Toxicity in Rat Striatal Slices. *Molecular Neurobiology*, *55*(11), 8538–8549. https://doi.org/10.1007/s12035-018-1003-2

Fields, J. B., Németh-Cahalan, K. L., Freites, J. A., Vorontsova, I., Hall, J. E., & Tobias, D. J. (2017). Calmodulin Gates Aquaporin 0 Permeability through a Positively Charged Cytoplasmic Loop. *The Journal of Biological Chemistry*, *292*(1), 185–195. https://doi.org/10.1074/jbc.M116.743724

Finn, R. N., & Cerdà, J. (2015). Evolution and functional diversity of aquaporins. *The Biological Bulletin*, *229*(1), 6–23. https://doi.org/10.1086/BBLv229n1p6

Fischbarg, J., Diecke, F. P., Kuang, K., Yu, B., Kang, F., Iserovich, P., Li, Y., Rosskothen, H., & Koniarek, J. P. (1999). Transport of fluid by lens epithelium. *The American Journal of Physiology*, *276*(3), C548-557. https://doi.org/10.1152/ajpcell.1999.276.3.C548

Fisher, R. F., & Pettet, B. E. (1973). Presbyopia and the water content of the human crystalline lens. *The Journal of Physiology*, *234*(2), 443–447. https://doi.org/10.1113/jphysiol.1973.sp010353

Forsythe, H. M., Vetter, C. J., Jara, K. A., Reardon, P. N., David, L. L., Barbar, E. J., & Lampi, K. J. (2019). Altered Protein Dynamics and Increased Aggregation of Human γS-Crystallin Due to Cataract-Associated Deamidations. *Biochemistry*, *58*(40), 4112–4124. https://doi.org/10.1021/acs.biochem.9b00593

Francis, P., Berry, V., Bhattacharya, S., & Moore, A. (2000). Congenital progressive polymorphic cataract caused by a mutation in the major intrinsic protein of the lens, MIP (AQP0). *The British Journal of Ophthalmology*, *84*(12), 1376–1379. https://doi.org/10.1136/bjo.84.12.1376

Freel, C. D., al-Ghoul, K. J., Kuszak, J. R., & Costello, M. J. (2003). Analysis of nuclear fiber cell compaction in transparent and cataractous diabetic human lenses by scanning electron microscopy. *BMC Ophthalmology*, *3*, 1. https://doi.org/10.1186/1471-2415-3-1

Friedrich, M. G., Wang, Z., Schey, K. L., & Truscott, R. J. W. (2018). Spontaneous cross-linking of proteins at aspartate and asparagine residues is mediated via a succinimide intermediate. *Biochemical Journal*, *475*(20), 3189–3200. https://doi.org/10.1042/BCJ20180529

Fritzsche, R., Ihling, C. H., Götze, M., & Sinz, A. (2012). Optimizing the enrichment of cross-linked products for mass spectrometric protein analysis: Enrichment of cross-linked products for MS protein analysis. *Rapid Communications in Mass Spectrometry*, *26*(6), 653–658. https://doi.org/10.1002/rcm.6150

Fuchser, J., Cornett, S., & Becker, M. (2014). *High Resolution Molecular Imaging of Pharmaceuticals at Therapeutic Levels*.

Fujii, N., Takata, T., Kim, I., & Matsubara, T. (2020). Simultaneous and Rapid Detection of Multiple Epimers and Isomers of Aspartyl Residues in Lens Proteins Using an LC-MS-MRM Method. *ACS Omega*, *5*(42), 27626–27632. https://doi.org/10.1021/acsomega.0c04197

Fujii, N., Takemoto, L. J., Momose, Y., Matsumoto, S., Hiroki, K., & Akaboshi, M. (1999). Formation of four isomers at the asp-151 residue of aged human alphaA-crystallin by natural aging. *Biochemical and Biophysical Research Communications*, *265*(3), 746–751. https://doi.org/10.1006/bbrc.1999.1748

Gao, J., Sun, X., Martinez-Wittinghan, F. J., Gong, X., White, T. W., & Mathias, R. T. (2004). Connections Between Connexins, Calcium, and Cataracts in the Lens. *Journal of General Physiology*, *124*(4), 289–300. https://doi.org/10.1085/jgp.200409121

Gao, J., Sun, X., White, T. W., Delamere, N. A., & Mathias, R. T. (2015). Feedback Regulation of Intracellular Hydrostatic Pressure in Surface Cells of the Lens. *Biophysical Journal*, *109*(9), 1830–1839. https://doi.org/10.1016/j.bpj.2015.09.018

Gao, J., Sun, X., Yatsula, V., Wymore, R. S., & Mathias, R. T. (2000). Isoform-specific function and distribution of Na/K pumps in the frog lens epithelium. *The Journal of Membrane Biology*, *178*(2), 89–101. https://doi.org/10.1007/s002320010017

Garland, D. L., Duglas-Tabor, Y., Jimenez-Asensio, J., Datiles, M. B., & Magno, B. (1996). The Nucleus of the Human Lens: Demonstration of a Highly Characteristic Protein Pattern by Two-Dimensional Electrophoresis and Introduction of a New Method of Lens Dissection. *Experimental Eye Research*, *62*(3), 285–292. https://doi.org/10.1006/exer.1996.0034

Gessulat, S., Schmidt, T., Zolg, D. P., Samaras, P., Schnatbaum, K., Zerweck, J., Knaute, T., Rechenberger, J., Delanghe, B., Huhmer, A., Reimer, U., Ehrlich, H.-C., Aiche, S., Kuster, B., & Wilhelm, M. (2019). Prosit: Proteome-wide prediction of peptide tandem mass spectra by deep learning. *Nature Methods*, *16*(6), 509–518. https://doi.org/10.1038/s41592-019-0426-7

Giblin, F. J., Padgaonkar, V. A., Leverenz, V. R., Lin, L.-R., Lou, M. F., Unakar, N. J., Dang, L., Dickerson, J. E., & Reddy, V. N. (1995). Nuclear light scattering, disulfide formation and membrane damage in lenses of older guinea pigs treated with hyperbaric oxygen. *Experimental Eye Research*, *60*(3), 219–235. https://doi.org/10.1016/S0014-4835(05)80105-8

Gillet, L. C., Navarro, P., Tate, S., Röst, H., Selevsek, N., Reiter, L., Bonner, R., & Aebersold, R. (2012). Targeted Data Extraction of the MS/MS Spectra Generated by Data-independent Acquisition: A New Concept for Consistent and Accurate Proteome Analysis. *Molecular & Cellular Proteomics*, *11*(6), O111.016717. https://doi.org/10.1074/mcp.O111.016717

Glazier, A. N. (2022). Proposed Role for Internal Lens Pressure as an Initiator of Age-Related Lens Protein Aggregation Diseases. *Clinical Ophthalmology*, *Volume 16*, 2329–2340. https://doi.org/10.2147/OPTH.S369676

Gletten, R. B., Cantrell, L. S., Bhattacharya, S., & Schey, K. L. (2022a). *Lens aquaporin-5 inserts into bovine fiber cell plasma membranes through mitochondria-associated lysosome secretion* [Preprint]. Cell Biology. https://doi.org/10.1101/2022.02.16.480789

Gletten, R. B., Cantrell, L. S., Bhattacharya, S., & Schey, K. L. (2022b). Lens Aquaporin-5 Inserts Into Bovine Fiber Cell Plasma Membranes Via Unconventional Protein Secretion. *Investigative Opthalmology & Visual Science*, *63*(8), 5. https://doi.org/10.1167/iovs.63.8.5

Goltsev, Y., Samusik, N., Kennedy-Darling, J., Bhate, S., Hale, M., Vazquez, G., Black, S., & Nolan, G. P. (2018). Deep Profiling of Mouse Splenic Architecture with CODEX Multiplexed Imaging. *Cell*, *174*(4), 968-981.e15. https://doi.org/10.1016/j.cell.2018.07.010

Götze, M., Pettelkau, J., Schaks, S., Bosse, K., Ihling, C. H., Krauth, F., Fritzsche, R., Kühn, U., & Sinz, A. (2012). StavroX—A Software for Analyzing Crosslinked Products in Protein Interaction Studies. *Journal of The American Society for Mass Spectrometry*, *23*(1), 76–87. https://doi.org/10.1007/s13361-011-0261-2

Grey, A. C., Demarais, N. J., West, B. J., & Donaldson, P. J. (2019). A quantitative map of glutathione in the aging human lens. *International Journal of Mass Spectrometry*, *437*, 58–68. https://doi.org/10.1016/j.ijms.2017.10.008

Grey, A. C., Jacobs, M. D., Gonen, T., Kistler, J., & Donaldson, P. J. (2003). Insertion of MP20 into lens fibre cell plasma membranes correlates with the formation of an extracellular diffusion barrier. *Experimental Eye Research*, *77*(5), 567–574. https://doi.org/10.1016/s0014-4835(03)00192-1

Grey, A. C., & Schey, K. L. (2008). Distribution of bovine and rabbit lens alpha-crystallin products by MALDI imaging mass spectrometry. *Molecular Vision*, *14*, 171–179.

Grey, A. C., Walker, K. L., Petrova, R. S., Han, J., Wilmarth, P. A., David, L. L., Donaldson, P. J., & Schey, K. L. (2013). Verification and spatial localization of aquaporin-5 in the ocular lens. *Experimental Eye Research*, *108*, 94–102. https://doi.org/10.1016/j.exer.2012.12.004

Grey, A., & Schey, K. (2009). Age-related changes in the spatial distribution of human lens alpha-crystallin products by MALDI imaging mass spectrometry. *Investigative Ophthalmology & Visual Science*, *50*(9), 4319–4329. https://doi.org/10.1167/iovs.09-3522

Griesser, E., Wyatt, H., Ten Have, S., Stierstorfer, B., Lenter, M., & Lamond, A. I. (2020). Quantitative Profiling of the Human Substantia Nigra Proteome from Laser-capture Microdissected FFPE Tissue. *Molecular & Cellular Proteomics*, *19*(5), 839–851. https://doi.org/10.1074/mcp.RA119.001889

Griffin, R. C., Chamberlain, A. T., Hotz, G., Penkman, K. E. H., & Collins, M. J. (2009). Age estimation of archaeological remains using amino acid racemization in dental enamel: A comparison of morphological, biochemical, and known ages-at-death. *American Journal of Physical Anthropology*, *140*(2), 244–252. https://doi.org/10.1002/ajpa.21058

Gutierrez, D. B., Garland, D. L., Schwacke, J. H., Hachey, D. L., & Schey, K. L. (2016). Spatial distributions of phosphorylated membrane proteins aquaporin 0 and MP20 across young and aged human lenses. *Experimental Eye Research*, *149*, 59–65. https://doi.org/10.1016/j.exer.2016.06.015

Gutierrez, D. B., Garland, D., & Schey, K. L. (2011). Spatial analysis of human lens aquaporin-0 post-translational modifications by MALDI mass spectrometry tissue profiling. *Experimental Eye Research*, *93*(6), 912–920. https://doi.org/10.1016/j.exer.2011.10.007

Hägglund, P., Mariotti, M., & Davies, M. J. (2018). Identification and characterization of protein cross-links induced by oxidative reactions. *Expert Review of Proteomics*, *15*(8), 665–681. https://doi.org/10.1080/14789450.2018.1509710

Hagos, Y., Burckhardt, G., & Burckhardt, B. C. (2013). Human organic anion transporter OAT1 is not responsible for glutathione transport but mediates transport of glutamate derivatives. *American Journal of Physiology. Renal Physiology*, *304*(4), F403-409. https://doi.org/10.1152/ajprenal.00412.2012

Haik, G. M., Lo, T. W. C., & Thornalley, P. J. (1994). Methylglyoxal Concentration and Glyoxalase Activities in the Human Lens. *Experimental Eye Research*, *59*(4), 497–500. https://doi.org/10.1006/exer.1994.1135

Haimann, M. H., & Abrams, G. W. (1984). Prevention of lens opacification during diabetic vitrectomy. *Ophthalmology*, *91*(2), 116–121. https://doi.org/10.1016/s0161-6420(84)34324-x

Hains, P. G., & Truscott, R. J. W. (2008). Proteomic analysis of the oxidation of cysteine residues in human age-related nuclear cataract lenses. *Biochimica et Biophysica Acta (BBA) - Proteins and Proteomics*, *1784*(12), 1959–1964. https://doi.org/10.1016/j.bbapap.2008.07.016

Hains, P. G., & Truscott, R. J. W. (2010a). Age-dependent deamidation of lifelong proteins in the human lens. *Investigative Ophthalmology & Visual Science*, *51*(6), 3107–3114. https://doi.org/10.1167/iovs.09-4308

Hains, P. G., & Truscott, R. J. W. (2010b). Age-dependent deamidation of lifelong proteins in the human lens. *Investigative Ophthalmology & Visual Science*, *51*(6), 3107–3114. https://doi.org/10.1167/iovs.09-4308

Herrmann, H., Bär, H., Kreplak, L., Strelkov, S. V., & Aebi, U. (2007). Intermediate filaments: From cell architecture to nanomechanics. *Nature Reviews Molecular Cell Biology*, *8*(7), 562–573. https://doi.org/10.1038/nrm2197

Hoffer, K. J. (1993). Axial dimension of the human cataractous lens. *Archives of Ophthalmology (Chicago, Ill.: 1960)*, *111*(7), 914–918. https://doi.org/10.1001/archopht.1993.01090070032014

Hooi, M. Y. S., Raftery, M. J., & Truscott, R. J. W. (2012). Racemization of Two Proteins over Our Lifespan: Deamidation of Asparagine 76 in γS Crystallin Is Greater in Cataract than in Normal Lenses across the Age Range. *Investigative Opthalmology & Visual Science*, *53*(7), 3554. https://doi.org/10.1167/iovs.11-9085

Hooi, M. Y. S., & Truscott, R. J. W. (2011). Racemisation and human cataract. D-Ser, d-Asp/Asn and d-Thr are higher in the lifelong proteins of cataract lenses than in age-matched normal lenses. *AGE*, *33*(2), 131–141. https://doi.org/10.1007/s11357-010-9171-7

Hoopmann, M. R., Zelter, A., Johnson, R. S., Riffle, M., MacCoss, M. J., Davis, T. N., & Moritz, R. L. (2015). Kojak: Efficient Analysis of Chemically Cross-Linked Protein Complexes. *Journal of Proteome Research*, *14*(5), 2190–2198. https://doi.org/10.1021/pr501321h

Horwitz, J. (1992). Alpha-crystallin can function as a molecular chaperone. *Proceedings of the National Academy of Sciences*, *89*(21), 10449–10453. https://doi.org/10.1073/pnas.89.21.10449

Hu, Q., Noll, R. J., Li, H., Makarov, A., Hardman, M., & Graham Cooks, R. (2005). The Orbitrap: A new mass spectrometer. *Journal of Mass Spectrometry: JMS*, *40*(4), 430–443. https://doi.org/10.1002/jms.856

Huang, C.-H., Wang, Y.-T., Tsai, C.-F., Chen, Y.-J., Lee, J.-S., & Chiou, S.-H. (2011). Phosphoproteomics characterization of novel phosphorylated sites of lens proteins from normal and cataractous human eye lenses. *Molecular Vision*, *17*, 186–198.

Huang, W. H., Wang, Y., & Askari, A. (1992). (Na+ + K+)-ATPase: Inactivation and degradation induced by oxygen radicals. *The International Journal of Biochemistry*, *24*(4), 621–626. https://doi.org/10.1016/0020-711x(92)90337-z

Huang, Y., Li, J., Li, W., Ai, N., & Jin, H. (2022). Biliverdin/Bilirubin Redox Pair Protects Lens Epithelial Cells against Oxidative Stress in Age-Related Cataract by Regulating NF-κB/iNOS and Nrf2/HO-1 Pathways. *Oxidative Medicine and Cellular Longevity*, *2022*, 7299182. https://doi.org/10.1155/2022/7299182

Iancu, C. V., Bocci, G., Ishtikhar, M., Khamrai, M., Oreb, M., Oprea, T. I., & Choe, J. (2022). GLUT3 inhibitor discovery through in silico ligand screening and in vivo validation in eukaryotic expression systems. *Scientific Reports*, *12*(1), 1429. https://doi.org/10.1038/s41598-022-05383-9

Ismail, V. S., Mosely, J. A., Tapodi, A., Quinlan, R. A., & Sanderson, J. M. (2016). The lipidation profile of aquaporin-0 correlates with the acyl composition of phosphoethanolamine lipids in lens membranes. *Biochimica et Biophysica Acta (BBA) - Biomembranes*, *1858*(11), 2763–2768. https://doi.org/10.1016/j.bbamem.2016.06.026

Jensen, L. J., Kuhn, M., Stark, M., Chaffron, S., Creevey, C., Muller, J., Doerks, T., Julien, P., Roth, A., Simonovic, M., Bork, P., & von Mering, C. (2009). STRING 8—A global view on proteins and their functional interactions in 630 organisms. *Nucleic Acids Research*, *37*(Database), D412–D416. https://doi.org/10.1093/nar/gkn760

Jimenez-Sanchez, M., Menzies, F. M., Chang, Y.-Y., Simecek, N., Neufeld, T. P., & Rubinsztein, D. C. (2012). The Hedgehog signalling pathway regulates autophagy. *Nature Communications*, *3*, 1200. https://doi.org/10.1038/ncomms2212

Johnson, D., Boyes, B., Fields, T., Kopkin, R., & Orlando, R. (2013). Optimization of data-dependent acquisition parameters for coupling high-speed separations with LC-MS/MS for protein identifications. *Journal of Biomolecular Techniques: JBT*, *24*(2), 62–72. https://doi.org/10.7171/jbt.13-2402-003

Käll, L., Canterbury, J. D., Weston, J., Noble, W. S., & MacCoss, M. J. (2007). Semi-supervised learning for peptide identification from shotgun proteomics datasets. *Nature Methods*, *4*(11), 923–925. https://doi.org/10.1038/nmeth1113

Kamei, A., Takamura, S., Nagai, M., & Takeuchi, N. (2004). Phosphoproteome Analysis of Hereditary Cataractous Rat Lens α-Crystallin. *Biological & Pharmaceutical Bulletin*, *27*(12), 1923–1931. https://doi.org/10.1248/bpb.27.1923

Kamradt, M. C., Chen, F., & Cryns, V. L. (2001). The small heat shock protein alpha B-crystallin negatively regulates cytochrome c- and caspase-8-dependent activation of caspase-3 by inhibiting its autoproteolytic maturation. *The Journal of Biological Chemistry*, *276*(19), 16059–16063. https://doi.org/10.1074/jbc.C100107200

Kanehisa, M., & Goto, S. (2000). KEGG: Kyoto encyclopedia of genes and genomes. *Nucleic Acids Research*, *28*(1), 27–30. https://doi.org/10.1093/nar/28.1.27

Kantorow, M., & Piatigorsky, J. (1998). Phosphorylations of αA- and αB-crystallin. *International Journal of Biological Macromolecules*, *22*(3–4), 307–314. https://doi.org/10.1016/S0141-8130(98)00028-2

Kastner, C., Löbler, M., Sternberg, K., Reske, T., Stachs, O., Guthoff, R., & Schmitz, K.-P. (2013). Permeability of the Anterior Lens Capsule for Large Molecules and Small Drugs. *Current Eye Research*, *38*(10), 1057–1063. https://doi.org/10.3109/02713683.2013.803288

Katori, T., Bannai, C., Hayashi, Y., & Yamashita, K. (1999). Decreased Na,K-ATPase Activity by Glycation at the Catalytic Center. *Hormone and Metabolic Research*, *31*(01), 5–7. https://doi.org/10.1055/s-2007-978687

Kinoshita, J. H. (1965). PATHWAYS OF GLUCOSE METABOLISM IN THE LENS. *Investigative Ophthalmology*, *4*, 619–628.

Kiontke, A., Oliveira-Birkmeier, A., Opitz, A., & Birkemeyer, C. (2016). Electrospray Ionization Efficiency Is Dependent on Different Molecular Descriptors with Respect to Solvent pH and Instrumental Configuration. *PloS One*, *11*(12), e0167502. https://doi.org/10.1371/journal.pone.0167502

Kong, A. T., Leprevost, F. V., Avtonomov, D. M., Mellacheruvu, D., & Nesvizhskii, A. I. (2017). MSFragger: Ultrafast and comprehensive peptide identification in mass spectrometry-based proteomics. *Nature Methods*, *14*(5), 513–520. https://doi.org/10.1038/nmeth.4256

Kopylova, L. V., Cherepanov, I. V., Snytnikova, O. A., Rumyantseva, Y. V., Kolosova, N. G., Tsentalovich, Y. P., & Sagdeev, R. Z. (2011). Age-related changes in the water-soluble lens protein composition of Wistar and accelerated-senescence OXYS rats. *Molecular Vision*, *17*, 1457–1467.

Korlimbinis, A., Berry, Y., Thibault, D., Schey, K. L., & Truscott, R. J. W. (2009). Protein aging: Truncation of aquaporin 0 in human lens regions is a continuous age-dependent process. *Experimental Eye Research*, *88*(5), 966–973. https://doi.org/10.1016/j.exer.2008.12.008

Kreimer, S., Haghani, A., Binek, A., Hauspurg, A., Seyedmohammad, S., Rivas, A., Momenzadeh, A., Meyer, J. G., Raedschelders, K., & Van Eyk, J. E. (2022). Parallelization with Dual-Trap Single-Column Configuration Maximizes Throughput of Proteomic Analysis. *Analytical Chemistry*, *94*(36), 12452–12460. https://doi.org/10.1021/acs.analchem.2c02609

Krey, J. F., Wilmarth, P. A., Shin, J.-B., Klimek, J., Sherman, N. E., Jeffery, E. D., Choi, D., David, L. L., & Barr-Gillespie, P. G. (2014). Accurate label-free protein quantitation with high- and low-resolution mass spectrometers. *Journal of Proteome Research*, *13*(2), 1034–1044. https://doi.org/10.1021/pr401017h

Kubo, E., Hasanova, N., Tanaka, Y., Fatma, N., Takamura, Y., Singh, D. P., & Akagi, Y. (2010). Protein expression profiling of lens epithelial cells from Prdx6-depleted mice and their vulnerability to UV radiation exposure. *American Journal of Physiology-Cell Physiology*, *298*(2), C342–C354. https://doi.org/10.1152/ajpcell.00336.2009

Kuck, J. F., Kuwabara, T., & Kuck, K. D. (1981). The Emory mouse cataract: An animal model for human senile cataract. *Current Eye Research*, *1*(11), 643–649. https://doi.org/10.3109/02713688109001868

Kumari, S. S., & Varadaraj, K. (2009). Intact AQP0 performs cell-to-cell adhesion. *Biochemical and Biophysical Research Communications*, *390*(3), 1034–1039. https://doi.org/10.1016/j.bbrc.2009.10.103

Kumari, S., & Varadaraj, K. (2014). Intact and N- or C-terminal end truncated AQP0 function as open water channels and cell-to-cell adhesion proteins: End truncation could be a prelude for adjusting the refractive index of the lens to prevent spherical aberration. *Biochimica et Biophysica Acta (BBA) - General Subjects*, *1840*(9), 2862–2877. https://doi.org/10.1016/j.bbagen.2014.05.002

Kuszak, J. R., Bertram, B. A., Macsai, M. S., & Rae, J. L. (1984). Sutures of the crystalline lens: A review. *Scanning Electron Microscopy*, *Pt 3*, 1369–1378.

Kuszak, J. R., Zoltoski, R. K., & Sivertson, C. (2004). Fibre cell organization in crystalline lenses. *Experimental Eye Research*, *78*(3), 673–687. https://doi.org/10.1016/j.exer.2003.09.016

Kuszak, J. R., Zoltoski, R. K., & Tiedemann, C. E. (2004). Development of lens sutures. *The International Journal of Developmental Biology*, *48*(8–9), 889–902. https://doi.org/10.1387/ijdb.041880jk

Kuwabara, T., & Imaizumi, M. (1974). Denucleation Process of the Lens. *Investigative Ophthalmology & Visual Science*, *13*, 973–981.

Lampi, K. J., Ma, Z., Hanson, S. R. A., Azuma, M., Shih, M., Shearer, T. R., Smith, D. L., Smith, J. B., & David, L. L. (1998). Age-related Changes in Human Lens Crystallins Identified by Two-dimensional Electrophoresis and Mass Spectrometry. *Experimental Eye Research*, *67*(1), 31–43. https://doi.org/10.1006/exer.1998.0481

Land, M. F., & Fernald, R. D. (1992). The Evolution of Eyes. *Annual Review of Neuroscience*, *15*(1), 1–29. https://doi.org/10.1146/annurev.ne.15.030192.000245

Lash, L. H., Putt, D. A., Xu, F., & Matherly, L. H. (2007). Role of rat organic anion transporter 3 (Oat3) in the renal basolateral transport of glutathione. *Chemico-Biological Interactions*, *170*(2), 124–134. https://doi.org/10.1016/j.cbi.2007.07.004

Lavallée-Adam, M., Rauniyar, N., McClatchy, D. B., & Yates, J. R. (2014). PSEA-Quant: A protein set enrichment analysis on label-free and label-based protein quantification data. *Journal of Proteome Research*, *13*(12), 5496–5509. https://doi.org/10.1021/pr500473n

Lee, H.-J., Kim, H.-J., & Liebler, D. C. (2016). Efficient Microscale Basic Reverse Phase Peptide Fractionation for Global and Targeted Proteomics. *Journal of Proteome Research*, *15*(7), 2346–2354. https://doi.org/10.1021/acs.jproteome.6b00102

Lehmann, W. D., Schlosser, A., Erben, G., Pipkorn, R., Bossemeyer, D., & Kinzel, V. (2000). Analysis of isoaspartate in peptides by electrospray tandem mass spectrometry. *Protein Science: A Publication of the Protein Society*, *9*(11), 2260–2268. https://doi.org/10.1110/ps.9.11.2260

Lei, J., Amhare, A. F., Wang, L., Lv, Y., Deng, H., Gao, H., Guo, X., Han, J., & Lammi, M. J. (2020). Proteomic analysis of knee cartilage reveals potential signaling pathways in pathological mechanism of Kashin-Beck disease compared with osteoarthritis. *Scientific Reports*, *10*(1). https://doi.org/10.1038/s41598-020-63932-6

Leong, L., Menko, A. S., & Grunwald, G. B. (2000). Differential expression of N- and B-cadherin during lens development. *Investigative Ophthalmology & Visual Science*, *41*(11), 3503–3510.

Lewandowska, A. E., Fel, A., Thiel, M., Czaplewska, P., Łukaszuk, K., Wiśniewski, J. R., & Ołdziej, S. (2021). Compatibility of Distinct Label-Free Proteomic Workflows in Absolute Quantification of Proteins Linked to the Oocyte Quality in Human Follicular Fluid. *International Journal of Molecular Sciences*, *22*(14), 7415. https://doi.org/10.3390/ijms22147415

Li, Y., & Ding, Y. (2017). Embryonic Development of the Human Lens. In Y. Liu (Ed.), *Pediatric Lens Diseases* (pp. 1–9). Springer Singapore. https://doi.org/10.1007/978-981-10-2627-0_1

Lim, J. C., Caballero Arredondo, M., Braakhuis, A. J., & Donaldson, P. J. (2020). Vitamin C and the Lens: New Insights into Delaying the Onset of Cataract. *Nutrients*, *12*(10), 3142. https://doi.org/10.3390/nu12103142

Lim, J. C., Grey, A. C., Zahraei, A., & Donaldson, P. J. (2020). Age-dependent changes in glutathione metabolism pathways in the lens: New insights into therapeutic strategies to prevent cataract formation—A review. *Clinical & Experimental Ophthalmology*, *48*(8), 1031–1042. https://doi.org/10.1111/ceo.13801

Lim, J. C., Lam, L., Li, B., & Donaldson, P. J. (2013). Molecular identification and cellular localization of a potential transport system involved in cystine/cysteine uptake in human lenses. *Experimental Eye Research*, *116*, 219–226. https://doi.org/10.1016/j.exer.2013.09.002

Lim, J. C., Perwick, R. D., Li, B., & Donaldson, P. J. (2017). Comparison of the expression and spatial localization of glucose transporters in the rat, bovine and human lens. *Experimental Eye Research*, *161*, 193–204. https://doi.org/10.1016/j.exer.2017.06.012

Lim, J. C., Umapathy, A., & Donaldson, P. J. (2016). Tools to fight the cataract epidemic: A review of experimental animal models that mimic age related nuclear cataract. *Experimental Eye Research*, *145*, 432–443. https://doi.org/10.1016/j.exer.2015.09.007

Lim, J., Li, L., Jacobs, M. D., Kistler, J., & Donaldson, P. J. (2007). Mapping of Glutathione and Its Precursor Amino Acids Reveals a Role for GLYT2 in Glycine Uptake in the Lens Core. *Investigative Opthalmology & Visual Science*, *48*(11), 5142. https://doi.org/10.1167/iovs.07-0649

Lim, J., Lorentzen, K. A., Kistler, J., & Donaldson, P. J. (2006). Molecular identification and characterisation of the glycine transporter (GLYT1) and the glutamine/glutamate transporter (ASCT2) in the rat lens. *Experimental Eye Research*, *83*(2), 447–455. https://doi.org/10.1016/j.exer.2006.01.028

Lindsey, K. M., Crouch, R. K., & Schey, K. L. (2004). Protein–Protein Interactions of Lens Aquaporin 0 with Cytoskeletal Proteins. *Investigative Ophthalmology & Visual Science*, *45*(13), 3994–3994.

Lindsey Rose, K. M., Wang, Z., Magrath, G. N., Hazard, E. S., Hildebrandt, J. D., & Schey, K. L. (2008). Aquaporin 0−Calmodulin Interaction and the Effect of Aquaporin 0 Phosphorylation. *Biochemistry*, *47*(1), 339–347. https://doi.org/10.1021/bi701980t

Linetsky, M., Hill, J. M. W., LeGrand, R. D., & Hu, F. (2004). Dehydroalanine crosslinks in human lens. *Experimental Eye Research*, *79*(4), 499–512. https://doi.org/10.1016/j.exer.2004.06.026

Linetsky, M., Shipova, E., Cheng, R., & Ortwerth, B. J. (2008). Glycation by ascorbic acid oxidation products leads to the aggregation of lens proteins. *Biochimica et Biophysica Acta (BBA) - Molecular Basis of Disease*, *1782*(1), 22–34. https://doi.org/10.1016/j.bbadis.2007.10.003

Liu, J., Ek Vitorin, J. F., Weintraub, S. T., Gu, S., Shi, Q., Burt, J. M., & Jiang, J. X. (2011). Phosphorylation of Connexin 50 by Protein Kinase A Enhances Gap Junction and Hemichannel Function. *Journal of Biological Chemistry*, *286*(19), 16914–16928. https://doi.org/10.1074/jbc.M111.218735

Liu, J., Riquelme, M. A., Li, Z., Li, Y., Tong, Y., Quan, Y., Pei, C., Gu, S., & Jiang, J. X. (2020). Mechanosensitive collaboration between integrins and connexins allows nutrient and antioxidant transport into the lens. *Journal of Cell Biology*, *219*(12), e202002154. https://doi.org/10.1083/jcb.202002154

Liu, K., Lyu, L., Chin, D., Gao, J., Sun, X., Shang, F., Caceres, A., Chang, M.-L., Rowan, S., Peng, J., Mathias, R., Kasahara, H., Jiang, S., & Taylor, A. (2015). Altered ubiquitin causes perturbed calcium homeostasis, hyperactivation of calpain, dysregulated differentiation, and cataract. *Proceedings of the National Academy of Sciences of the United States of America*, *112*(4), 1071–1076. https://doi.org/10.1073/pnas.1404059112

Liu, M., Zhang, Z., Zang, T., Spahr, C., Cheetham, J., Ren, D., & Zhou, Z. S. (2013). Discovery of undefined protein cross-linking chemistry: A comprehensive methodology utilizing 18O-labeling and mass spectrometry. *Analytical Chemistry*, *85*(12), 5900–5908. https://doi.org/10.1021/ac400666p

Logan, C. M., Bowen, C. J., & Menko, A. S. (2018). Functional role for stable microtubules in lens fiber cell elongation. *Experimental Cell Research*, *362*(2), 477–488. https://doi.org/10.1016/j.yexcr.2017.12.012

Lou, M. F. (2003). Redox regulation in the lens. *Progress in Retinal and Eye Research*, *22*(5), 657–682. https://doi.org/10.1016/s1350-9462(03)00050-8

Lou, M. F., & Dickerson, J. E. (1992). Protein-thiol mixed disulfides in human lens. *Experimental Eye Research*, *55*(6), 889–896. https://doi.org/10.1016/0014-4835(92)90015-K

Lou, M. F., Dickerson, J. E., & Garadi, R. (1990). The role of protein-thiol mixed disulfides in cataractogenesis. *Experimental Eye Research*, *50*(6), 819–826. https://doi.org/10.1016/0014-4835(90)90133-F

Lu, J. Y., Mohammed, T. A., Donohue, S. T., & Al-Ghoul, K. J. (2008). Distribution of basal membrane complex components in elongating lens fibers. *Molecular Vision*, *14*, 1187–1203.

Luthra, M., Ranganathan, D., Ranganathan, S., & Balasubramanian, D. (1994). Racemization of tyrosine in the insoluble protein fraction of brunescent aging human lenses. *The Journal of Biological Chemistry*, *269*(36), 22678–22682.

Ma, Q. (2013). Role of nrf2 in oxidative stress and toxicity. *Annual Review of Pharmacology and Toxicology*, *53*, 401–426. https://doi.org/10.1146/annurev-pharmtox-011112-140320

Ma, Z.-Q., Dasari, S., Chambers, M. C., Litton, M. D., Sobecki, S. M., Zimmerman, L. J., Halvey, P. J., Schilling, B., Drake, P. M., Gibson, B. W., & Tabb, D. L. (2009). IDPicker 2.0: Improved protein assembly with high discrimination peptide identification filtering. *Journal of Proteome Research*, *8*(8), 3872–3881. https://doi.org/10.1021/pr900360j

MacCoss, M. J., McDonald, W. H., Saraf, A., Sadygov, R., Clark, J. M., Tasto, J. J., Gould, K. L., Wolters, D., Washburn, M., Weiss, A., Clark, J. I., & Yates, J. R. (2002). Shotgun identification of protein modifications from protein complexes and lens tissue. *Proceedings of the National Academy of Sciences of the United States of America*, *99*(12), 7900–7905. https://doi.org/10.1073/pnas.122231399

MacLean, B., Tomazela, D. M., Shulman, N., Chambers, M., Finney, G. L., Frewen, B., Kern, R., Tabb, D. L., Liebler, D. C., & MacCoss, M. J. (2010). Skyline: An open source document editor for creating and analyzing targeted proteomics experiments. *Bioinformatics*, *26*(7), 966–968. https://doi.org/10.1093/bioinformatics/btq054

Magami, K., Kim, I., & Fujii, N. (2020). A single Asp isomer substitution in an αA-crystallin-derived peptide induces a large change in peptide properties. *Experimental Eye Research*, *192*, 107930. https://doi.org/10.1016/j.exer.2020.107930

Mandal, A., Shahidullah, M., & Delamere, N. A. (2018). TRPV1-dependent ERK1/2 activation in porcine lens epithelium. *Experimental Eye Research*, *172*, 128–136. https://doi.org/10.1016/j.exer.2018.04.006

Marian, M. J., Li, H., Borchman, D., & Paterson, C. A. (2005). Plasma membrane Ca2+-ATPase expression in the human lens. *Experimental Eye Research*, *81*(1), 57–64. https://doi.org/10.1016/j.exer.2005.01.011

Marian, M. J., Mukhopadhyay, P., Borchman, D., & Paterson, C. A. (2008). Plasma Membrane Ca^{2+}-ATPase Isoform Expression in Human Cataractous Lenses Compared to Age-Matched Clear Lenses. *Ophthalmic Research*, *40*(2), 86–93. https://doi.org/10.1159/000113886

Martin, J. B., Herman, K., Houssin, N. S., Rich, W., Reilly, M. A., & Plageman, T. F. (2022). Arvcf Dependent Adherens Junction Stability is Required to Prevent Age-Related Cortical Cataracts. *Frontiers in Cell and Developmental Biology*, *10*, 840129. https://doi.org/10.3389/fcell.2022.840129

Martínez-García, M. C., Martínez, T., Pañeda, C., Gallego, P., Jimenez, A. I., & Merayo, J. (2013). Differential expression and localization of transient receptor potential vanilloid 1 in rabbit and human eyes. *Histology and Histopathology*, *28*(11), 1507–1516. https://doi.org/10.14670/HH-28.1507

Mathias, R. T., Kistler, J., & Donaldson, P. (2007). The Lens Circulation. *Journal of Membrane Biology*, *216*(1), 1–16. https://doi.org/10.1007/s00232-007-9019-y

Mathias, R. T., & Rae, J. L. (1985). Transport properties of the lens. *American Journal of Physiology-Cell Physiology*, *249*(3), C181–C190. https://doi.org/10.1152/ajpcell.1985.249.3.C181

Mathias, R. T., & Rae, J. L. (2004). The lens: Local transport and global transparency. *Experimental Eye Research*, *78*(3), 689–698. https://doi.org/10.1016/j.exer.2003.07.001

Mathias, R. T., Rae, J. L., & Baldo, G. J. (1997). Physiological properties of the normal lens. *Physiological Reviews*, *77*(1), 21–50. https://doi.org/10.1152/physrev.1997.77.1.21

Mathias, R. T., Rae, J. L., & Eisenberg, R. S. (1981). The lens as a nonuniform spherical syncytium. *Biophysical Journal*, *34*(1), 61–83. https://doi.org/10.1016/S0006-3495(81)84837-0

Mathias, R. T., White, T. W., & Gong, X. (2010). Lens Gap Junctions in Growth, Differentiation, and Homeostasis. *Physiological Reviews*, *90*(1), 179–206. https://doi.org/10.1152/physrev.00034.2009

McAvoy, J. W. (1978). Cell division, cell elongation and distribution of alpha-, beta- and gamma-crystallins in the rat lens. *Journal of Embryology and Experimental Morphology*, *44*, 149–165.

McCarty, C. A., Mukesh, B. N., Fu, C. L., & Taylor, H. R. (1999). The epidemiology of cataract in Australia. *American Journal of Ophthalmology*, *128*(4), 446–465. https://doi.org/10.1016/s0002-9394(99)00218-4

McFall-Ngai, M. J., Ding, L. L., Takemoto, L. J., & Horwitz, J. (1985). Spatial and temporal mapping of the age-related changes in human lens crystallins. *Experimental Eye Research*, *41*(6), 745–758. https://doi.org/10.1016/0014-4835(85)90183-6

Meier, F., Brunner, A.-D., Frank, M., Ha, A., Bludau, I., Voytik, E., Kaspar-Schoenefeld, S., Lubeck, M., Raether, O., Bache, N., Aebersold, R., Collins, B. C., Röst, H. L., & Mann, M. (2020). diaPASEF: Parallel accumulation-serial fragmentation combined with data-independent acquisition. *Nature Methods*, *17*(12), 1229–1236. https://doi.org/10.1038/s41592-020-00998-0

Meier, F., Geyer, P. E., Virreira Winter, S., Cox, J., & Mann, M. (2018). BoxCar acquisition method enables single-shot proteomics at a depth of 10,000 proteins in 100 minutes. *Nature Methods*, *15*(6), 440–448. https://doi.org/10.1038/s41592-018-0003-5

Melkonian, E. A., & Schury, M. P. (2022). Biochemistry, Anaerobic Glycolysis. In *StatPearls*. StatPearls Publishing. http://www.ncbi.nlm.nih.gov/books/NBK546695/

Merriman-Smith, B. R., Krushinsky, A., Kistler, J., & Donaldson, P. J. (2003). Expression Patterns for Glucose Transporters GLUT1 and GLUT3 in the Normal Rat Lens and in Models of Diabetic Cataract. *Investigative Opthalmology & Visual Science*, *44*(8), 3458. https://doi.org/10.1167/iovs.02-1235

Messner, C. B., Demichev, V., Bloomfield, N., Yu, J. S. L., White, M., Kreidl, M., Egger, A.-S., Freiwald, A., Ivosev, G., Wasim, F., Zelezniak, A., Jürgens, L., Suttorp, N., Sander, L. E., Kurth, F., Lilley, K. S., Mülleder, M., Tate, S., & Ralser, M. (2021). Ultra-fast proteomics with Scanning SWATH. *Nature Biotechnology*, *39*(7), 846–854. https://doi.org/10.1038/s41587-021-00860-4

Michalski, A., Cox, J., & Mann, M. (2011). More than 100,000 Detectable Peptide Species Elute in Single Shotgun Proteomics Runs but the Majority is Inaccessible to Data-Dependent LC−MS/MS. *Journal of Proteome Research*, *10*(4), 1785–1793. https://doi.org/10.1021/pr101060v

Modak, S. P., & Bollum, F. J. (1970). Terminal lens cell differentiation. 3. Initiator activity of DNA during nuclear degeneration. *Experimental Cell Research*, *62*(2), 421–432. https://doi.org/10.1016/0014-4827(70)90573-2

Moffat, B. A., Landman, K. A., Truscott, R. J. W., Sweeney, M. H. J., & Pope, J. M. (1999). Age-related Changes in the Kinetics of Water Transport in Normal Human Lenses. *Experimental Eye Research*, *69*(6), 663–669. https://doi.org/10.1006/exer.1999.0747

Moroni, M., & Garland, D. (2001). In vitro dephosphorylation of α-crystallin is dependent on the state of oligomerization. *Biochimica et Biophysica Acta (BBA) - Protein Structure and Molecular Enzymology*, *1546*(2), 282–290. https://doi.org/10.1016/S0167-4838(01)00154-6

Moseley, A. E., Dean, W. L., & Delamere, N. A. (1996). Isoforms of Na,K-ATPase in rat lens epithelium and fiber cells. *Investigative Ophthalmology & Visual Science*, *37*(8), 1502–1508.

Moseley, M. A., Hughes, C. J., Juvvadi, P. R., Soderblom, E. J., Lennon, S., Perkins, S. R., Thompson, J. W., Steinbach, W. J., Geromanos, S. J., Wildgoose, J., Langridge, J. I., Richardson, K., & Vissers, J. P. C. (2018). Scanning Quadrupole Data-Independent Acquisition, Part A: Qualitative and Quantitative Characterization. *Journal of Proteome Research*, *17*(2), 770–779. https://doi.org/10.1021/acs.jproteome.7b00464

Mukherjee, R., Das, A., Chakrabarti, S., & Chakrabarti, O. (2017). Calcium dependent regulation of protein ubiquitination – Interplay between E3 ligases and calcium binding proteins. *Biochimica et Biophysica Acta (BBA) - Molecular Cell Research*, *1864*(7), 1227–1235. https://doi.org/10.1016/j.bbamcr.2017.03.001

Mukherjee, S., Fang, M., Kok, W. M., Kapp, E. A., Thombare, V. J., Huguet, R., Hutton, C. A., Reid, G. E., & Roberts, B. R. (2019). Establishing Signature Fragments for Identification and Sequencing of Dityrosine Cross-Linked Peptides Using Ultraviolet Photodissociation Mass Spectrometry. *Analytical Chemistry*, *91*(19), 12129–12133. https://doi.org/10.1021/acs.analchem.9b02986

Murphy, E., & Steenbergen, C. (2008). Mechanisms underlying acute protection from cardiac ischemia-reperfusion injury. *Physiological Reviews*, *88*(2), 581–609. https://doi.org/10.1152/physrev.00024.2007

Muszbek, L., Haramura, G., Cluette-Brown, J. E., Van Cott, E. M., & Laposata, M. (1999). The pool of fatty acids covalently bound to platelet proteins by thioester linkages can be altered by exogenously supplied fatty acids. *Lipids*, *34*(S1), S331–S337. https://doi.org/10.1007/BF02562334

Nagamoto, T., Eguchi, G., & Beebe, D. C. (2000). Alpha-smooth muscle actin expression in cultured lens epithelial cells. *Investigative Ophthalmology & Visual Science*, *41*(5), 1122–1129.

Nagaraj, R. H., Nahomi, R. B., Shanthakumar, S., Linetsky, M., Padmanabha, S., Pasupuleti, N., Wang, B., Santhoshkumar, P., Panda, A. K., & Biswas, A. (2012). Acetylation of αA-crystallin in the human lens: Effects on structure and chaperone function. *Biochimica Et Biophysica Acta*, *1822*(2), 120–129. https://doi.org/10.1016/j.bbadis.2011.11.011

Nagaraj, R. H., Sell, D. R., Prabhakaram, M., Ortwerth, B. J., & Monnier, V. M. (1991). High correlation between pentosidine protein crosslinks and pigmentation implicates ascorbate oxidation in human lens senescence and cataractogenesis. *Proceedings of the National Academy of Sciences*, *88*(22), 10257–10261. https://doi.org/10.1073/pnas.88.22.10257

Nagineni, C. N., & Bhat, S. P. (1992). Lens fiber cell differentiation and expression of crystallins in Co-cultures of human fetal lens epithelial cells and fibroblasts. *Experimental Eye Research*, *54*(2), 193–200. https://doi.org/10.1016/S0014-4835(05)80208-8

Nahomi, R. B., Oya-Ito, T., & Nagaraj, R. H. (2013). The combined effect of acetylation and glycation on the chaperone and anti-apoptotic functions of human α-crystallin. *Biochimica et Biophysica Acta (BBA) - Molecular Basis of Disease*, *1832*(1), 195–203. https://doi.org/10.1016/j.bbadis.2012.08.015

Nakazawa, Y., Petrova, R. S., Sugiyama, Y., Nagai, N., Tamura, H., & Donaldson, P. J. (2021). Regulation of the Membrane Trafficking of the Mechanosensitive Ion Channels TRPV1 and TRPV4 by Zonular Tension, Osmotic Stress and Activators in the Mouse Lens. *International Journal of Molecular Sciences*, *22*(23), 12658. https://doi.org/10.3390/ijms222312658

Nesvizhskii, A. I., Keller, A., Kolker, E., & Aebersold, R. (2003). A statistical model for identifying proteins by tandem mass spectrometry. *Analytical Chemistry*, *75*(17), 4646–4658. https://doi.org/10.1021/ac0341261

Nishi, O., Nishi, K., Akaishi, T., & Shirasawa, E. (1997). Detection of cell adhesion molecules in lens epithelial cells of human cataracts. *Investigative Ophthalmology & Visual Science*, *38*(3), 579–585.

Nye-Wood, M. G., Spraggins, J. M., Caprioli, R. M., Schey, K. L., Donaldson, P. J., & Grey, A. C. (2017). Spatial distributions of glutathione and its endogenous conjugates in normal bovine lens and a model of lens aging. *Experimental Eye Research*, *154*, 70–78. https://doi.org/10.1016/j.exer.2016.11.008

Ohtani, S., & Yamamoto, T. (2010). Age estimation by amino acid racemization in human teeth. *Journal of Forensic Sciences*, *55*(6), 1630–1633. https://doi.org/10.1111/j.1556-4029.2010.01472.x

Ong, M. D., Payne, D. M., & Garner, M. H. (2003). Differential protein expression in lens epithelial whole-mounts and lens epithelial cell cultures. *Experimental Eye Research*, *77*(1), 35–49. https://doi.org/10.1016/s0014-4835(03)00090-3

Orsburn, B. C. (2021). Proteome Discoverer-A Community Enhanced Data Processing Suite for Protein Informatics. *Proteomes*, *9*(1), 15. https://doi.org/10.3390/proteomes9010015

Padgaonkar, V. A., Leverenz, V. R., Fowler, K. E., Reddy, V. N., & Giblin, F. J. (2000). The effects of hyperbaric oxygen on the crystallins of cultured rabbit lenses: A possible catalytic role for copper. *Experimental Eye Research*, *71*(4), 371–383. https://doi.org/10.1006/exer.2000.0887

Park, J. Y., Jang, S. Y., Shin, Y. K., Suh, D. J., & Park, H. T. (2013). Calcium-dependent proteasome activation is required for axonal neurofilament degradation. *Neural Regeneration Research*, *8*(36), 3401–3409. https://doi.org/10.3969/j.issn.1673-5374.2013.36.005

Paron, I., D'Elia, A., D'Ambrosio, C., Scaloni, A., D'Aurizio, F., Prescott, A., Damante, G., & Tell, G. (2004). A proteomic approach to identify early molecular targets of oxidative stress in human epithelial lens cells. *The Biochemical Journal*, *378*(Pt 3), 929–937. https://doi.org/10.1042/BJ20031190

Parry, D. A., Poulter, J. A., Logan, C. V., Brookes, S. J., Jafri, H., Ferguson, C. H., Anwari, B. M., Rashid, Y., Zhao, H., Johnson, C. A., Inglehearn, C. F., & Mighell, A. J. (2013). Identification of Mutations in SLC24A4, Encoding a Potassium-Dependent Sodium/Calcium Exchanger, as a Cause of Amelogenesis Imperfecta. *The American Journal of Human Genetics*, *92*(2), 307–312. https://doi.org/10.1016/j.ajhg.2013.01.003

Paterson, C. A. (1969). Distribution of sodium and potassium in ox lenses. *Experimental Eye Research*, *8*(4), 442–446. https://doi.org/10.1016/s0014-4835(69)80011-4

Paterson, C. A. (1970). Extracellular space of the crystalline lens. *The American Journal of Physiology*, *218*(3), 797–802. https://doi.org/10.1152/ajplegacy.1970.218.3.797

Patil, R. V., Saito, I., Yang, X., & Wax, M. B. (1997). Expression of aquaporins in the rat ocular tissue. *Experimental Eye Research*, *64*(2), 203–209. https://doi.org/10.1006/exer.1996.0196

Pavelka, N., Fournier, M. L., Swanson, S. K., Pelizzola, M., Ricciardi-Castagnoli, P., Florens, L., & Washburn, M. P. (2008). Statistical Similarities between Transcriptomics and Quantitative Shotgun Proteomics Data. *Molecular & Cellular Proteomics*, *7*(4), 631–644. https://doi.org/10.1074/mcp.M700240-MCP200

Pereira, P., Shang, F., Hobbs, M., Girão, H., & Taylor, A. (2003). Lens fibers have a fully functional ubiquitin-proteasome pathway. *Experimental Eye Research*, *76*(5), 623–631. https://doi.org/10.1016/s0014-4835(03)00020-4

Petrova, R. S., Bavana, N., Zhao, R., Schey, K. L., & Donaldson, P. J. (2020). Changes to Zonular Tension Alters the Subcellular Distribution of AQP5 in Regions of Influx and Efflux of Water in the Rat Lens. *Investigative Opthalmology & Visual Science*, *61*(11), 36. https://doi.org/10.1167/iovs.61.11.36

Petrova, R. S., Schey, K. L., Donaldson, P. J., & Grey, A. C. (2015). Spatial distributions of AQP5 and AQP0 in embryonic and postnatal mouse lens development. *Experimental Eye Research*, *132*, 124–135. https://doi.org/10.1016/j.exer.2015.01.011

Petrova, R. S., Webb, K. F., Vaghefi, E., Walker, K., Schey, K. L., & Donaldson, P. J. (2018). Dynamic functional contribution of the water channel AQP5 to the water permeability of peripheral lens fiber cells. *American Journal of Physiology-Cell Physiology*, *314*(2), C191–C201. https://doi.org/10.1152/ajpcell.00214.2017

Piatigorsky, J., Rothschild, S. S., & Wollberg, M. (1973). Stimulation by Insulin of Cell Elongation and Microtubule Assembly in Embryonic Chick-Lens Epithelia. *Proceedings of the National Academy of Sciences*, *70*(4), 1195–1198. https://doi.org/10.1073/pnas.70.4.1195

Piehowski, P. D., Zhu, Y., Bramer, L. M., Stratton, K. G., Zhao, R., Orton, D. J., Moore, R. J., Yuan, J., Mitchell, H. D., Gao, Y., Webb-Robertson, B.-J. M., Dey, S. K., Kelly, R. T., & Burnum-Johnson, K. E. (2020). Automated mass spectrometry imaging of over 2000 proteins from tissue sections at 100-μm spatial resolution. *Nature Communications*, *11*(1). https://doi.org/10.1038/s41467-019-13858-z

Pino, L. K., Just, S. C., MacCoss, M. J., & Searle, B. C. (2020). Acquiring and Analyzing Data Independent Acquisition Proteomics Experiments without Spectrum Libraries. *Molecular & Cellular Proteomics: MCP*, *19*(7), 1088–1103. https://doi.org/10.1074/mcp.P119.001913

Pinto, B. I., Pupo, A., García, I. E., Mena-Ulecia, K., Martínez, A. D., Latorre, R., & Gonzalez, C. (2017). Calcium binding and voltage gating in Cx46 hemichannels. *Scientific Reports*, *7*(1), 15851. https://doi.org/10.1038/s41598-017-15975-5

Plumb, R. S., Johnson, K. A., Rainville, P., Smith, B. W., Wilson, I. D., Castro-Perez, J. M., & Nicholson, J. K. (2006). UPLC/MS(E); a new approach for generating molecular fragment information for biomarker structure elucidation. *Rapid Communications in Mass Spectrometry: RCM*, *20*(13), 1989–1994. https://doi.org/10.1002/rcm.2550

Pontoriero, G. F., Smith, A. N., Miller, L.-A. D., Radice, G. L., West-Mays, J. A., & Lang, R. A. (2009). Co-operative roles for E-cadherin and N-cadherin during lens vesicle separation and lens epithelial cell survival. *Developmental Biology*, *326*(2), 403–417. https://doi.org/10.1016/j.ydbio.2008.10.011

Preston, G. M., Smith, B. L., Zeidel, M. L., Moulds, J. J., & Agre, P. (1994). Mutations in aquaporin-1 in phenotypically normal humans without functional CHIP water channels. *Science (New York, N.Y.)*, *265*(5178), 1585–1587. https://doi.org/10.1126/science.7521540

Prinsen, C. F. M., Szerencsei, R. T., & Schnetkamp, P. P. M. (2000). Molecular Cloning and Functional Expression of the Potassium-Dependent Sodium–Calcium Exchanger from Human and Chicken Retinal Cone Photoreceptors. *The Journal of Neuroscience*, *20*(4), 1424–1434. https://doi.org/10.1523/JNEUROSCI.20-04-01424.2000

Purdy, P. D., Horowitz, M. B., Mathews, D., Walker, B. S., Carstens, G. J., Devous, M. D., White, C. L., Kulkarni, P., Constantinescu, A., & Batjer, H. H. (1996). Calcium 45 autoradiography and dual-isotope single-photon emission CT in a canine model of cerebral ischemia and middle cerebral artery occlusion. *AJNR. American Journal of Neuroradiology*, *17*(6), 1161–1170.

Qin, Y. J., Chan, S. O., Lin, H. L., Zhang, Y. Q., Chen, Y. L., Niu, Y. Y., Xie, W. J., Chu, W. K., Pang, C. P., & Zhang, H. Y. (2020). Elevated level of uric acid in aqueous humour is associated with posterior subcapsular cataract in human lens. *Clinical & Experimental Ophthalmology*, *48*(9), 1183–1191. https://doi.org/10.1111/ceo.13835

Quinlan, R. A., Carte, J. M., Sandilands, A., & Prescott, A. R. (1996). The beaded filament of the eye lens: An unexpected key to intermediate filament structure and function. *Trends in Cell Biology*, *6*(4), 123–126. https://doi.org/10.1016/0962-8924(96)20001-7

Rabl, C. (1899). *Über den Bau und die Entwicklung der Linse. III. Die Linse der Säugethiere: Rückblick und Schluss* (Vol. 1–III). Engelmann.

Rafferty, N. S., & Rafferty, K. A. (1981). Cell population kinetics of the mouse lens epithelium. *Journal of Cellular Physiology*, *107*(3), 309–315. https://doi.org/10.1002/jcp.1041070302

Rajasekaran, A. K., & Rajasekaran, S. A. (2003). Role of Na-K-ATPase in the assembly of tight junctions. *American Journal of Physiology-Renal Physiology*, *285*(3), F388–F396. https://doi.org/10.1152/ajprenal.00439.2002

Raju, M., Santhoshkumar, P., & Sharma, K. K. (2017). Lens Endogenous Peptide αA66-80 Generates Hydrogen Peroxide and Induces Cell Apoptosis. *Aging and Disease*, *8*(1), 57. https://doi.org/10.14336/AD.2016.0805

Rao, P. V., Huang, Q. L., Horwitz, J., & Zigler, J. S. (1995). Evidence that alpha-crystallin prevents non-specific protein aggregation in the intact eye lens. *Biochimica Et Biophysica Acta*, *1245*(3), 439–447. https://doi.org/10.1016/0304-4165(95)00125-5

Rao, P. V., & Maddala, R. (2006). The role of the lens actin cytoskeleton in fiber cell elongation and differentiation. *Seminars in Cell & Developmental Biology*, *17*(6), 698–711. https://doi.org/10.1016/j.semcdb.2006.10.011

Rappsilber, J., Ishihama, Y., & Mann, M. (2003). Stop and Go Extraction Tips for Matrix-Assisted Laser Desorption/Ionization, Nanoelectrospray, and LC/MS Sample Pretreatment in Proteomics. *Analytical Chemistry*, *75*(3), 663–670. https://doi.org/10.1021/ac026117i

Reddy, V. N. (1990). Glutathione and its function in the lens—An overview. *Experimental Eye Research*, *50*(6), 771–778. https://doi.org/10.1016/0014-4835(90)90127-G

Reddy, Venkatn., & Giblin, F. J. (2008). Metabolism and Function of Glutathione in the Lens. In J. Nugent & J. Whelan (Eds.), *Novartis Foundation Symposia* (pp. 65–87). John Wiley & Sons, Ltd. https://doi.org/10.1002/9780470720875.ch5

Reubsaet, L., Sweredoski, M. J., & Moradian, A. (2019). Data-Independent Acquisition for the Orbitrap Q Exactive HF: A Tutorial. *Journal of Proteome Research*, *18*(3), 803–813. https://doi.org/10.1021/acs.jproteome.8b00845

Rhodes, J. D., & Sanderson, J. (2009). The mechanisms of calcium homeostasis and signalling in the lens. *Experimental Eye Research*, *88*(2), 226–234. https://doi.org/10.1016/j.exer.2008.10.025

Riley, M. L., & Harding, J. J. (1995). The reaction of methylglyoxal with human and bovine lens proteins. *Biochimica et Biophysica Acta (BBA) - Molecular Basis of Disease*, *1270*(1), 36–43. https://doi.org/10.1016/0925-4439(94)00069-3

Rinner, O., Seebacher, J., Walzthoeni, T., Mueller, L. N., Beck, M., Schmidt, A., Mueller, M., & Aebersold, R. (2008). Identification of cross-linked peptides from large sequence databases. *Nature Methods*, *5*(4), 315–318. https://doi.org/10.1038/nmeth.1192

Ritchie, M. E., Phipson, B., Wu, D., Hu, Y., Law, C. W., Shi, W., & Smyth, G. K. (2015). Limma powers differential expression analyses for RNA-sequencing and microarray studies. *Nucleic Acids Research*, *43*(7), e47–e47. https://doi.org/10.1093/nar/gkv007

Robinson, M. D., & Oshlack, A. (2010). A scaling normalization method for differential expression analysis of RNA-seq data. *Genome Biology*, *11*(3), R25. https://doi.org/10.1186/gb-2010-11-3-r25

Robinson, N. E., Lampi, K. J., McIver, R. T., Williams, R. H., Muster, W. C., Kruppa, G., & Robinson, A. B. (2005). Quantitative measurement of deamidation in lens betaB2-crystallin and peptides by direct electrospray injection and fragmentation in a Fourier transform mass spectrometer. *Molecular Vision*, *11*, 1211–1219.

Rosenberger, G., Koh, C. C., Guo, T., Röst, H. L., Kouvonen, P., Collins, B. C., Heusel, M., Liu, Y., Caron, E., Vichalkovski, A., Faini, M., Schubert, O. T., Faridi, P., Ebhardt, H. A., Matondo, M., Lam, H., Bader, S. L., Campbell, D. S., Deutsch, E. W., … Aebersold, R. (2014). A repository of assays to quantify 10,000 human proteins by SWATH-MS. *Scientific Data*, *1*(1). https://doi.org/10.1038/sdata.2014.31

Rowan, S., Chang, M.-L., Reznikov, N., & Taylor, A. (2017). Disassembly of the lens fiber cell nucleus to create a clear lens: The p27 descent. *Experimental Eye Research*, *156*, 72–78. https://doi.org/10.1016/j.exer.2016.02.011

Ruiz, F. M., Gilles, U., Ludwig, A.-K., Sehad, C., Shiao, T. C., García Caballero, G., Kaltner, H., Lindner, I., Roy, R., Reusch, D., Romero, A., & Gabius, H.-J. (2018). Chicken GRIFIN: Structural characterization in crystals and in solution. *Biochimie*, *146*, 127–138. https://doi.org/10.1016/j.biochi.2017.12.003

Ryan, D. J., Patterson, N. H., Putnam, N. E., Wilde, A. D., Weiss, A., Perry, W. J., Cassat, J. E., Skaar, E. P., Caprioli, R. M., & Spraggins, J. M. (2019). MicroLESA: Integrating Autofluorescence Microscopy, In Situ Micro-Digestions, and Liquid Extraction Surface Analysis for High Spatial Resolution Targeted Proteomic Studies. *Analytical Chemistry*, *91*(12), 7578–7585. https://doi.org/10.1021/acs.analchem.8b05889

Sanders, E. J., & Parker, E. (2002). The role of mitochondria, cytochrome c and caspase-9 in embryonic lens fibre cell denucleation. *Journal of Anatomy*, *201*(2), 121–135. https://doi.org/10.1046/j.1469-7580.2002.00081.x

Sandilands, A., Prescott, A. R., Carter, J. M., Hutcheson, A. M., Quinlan, R. A., Richards, J., & FitzGerald, P. G. (1995). Vimentin and CP49/filensin form distinct networks in the lens which are independently modulated during lens fibre cell differentiation. *Journal of Cell Science*, *108*(4), 1397–1406. https://doi.org/10.1242/jcs.108.4.1397

Sandilands, A., Prescott, A. R., Hutcheson, A. M., Quinlan, R. A., Casselman, J. T., & FitzGerald, P. G. (1995). Filensin is proteolytically processed during lens fiber cell differentiation by multiple independent pathways. *European Journal of Cell Biology*, *67*(3), 238–253.

Sargaeva, N. P., Lin, C., & O'Connor, P. B. (2009). Identification of aspartic and isoaspartic acid residues in amyloid beta peptides, including Abeta1-42, using electron-ion reactions. *Analytical Chemistry*, *81*(23), 9778–9786. https://doi.org/10.1021/ac901677t

Sasaki, H., Giblin, F. J., Winkler, B. S., Chakrapani, B., Leverenz, V., & Shu, C. C. (1995). A protective role for glutathione-dependent reduction of dehydroascorbic acid in lens epithelium. *Investigative Ophthalmology & Visual Science*, *36*(9), 1804–1817.

Satoh, K., Takemura, Y., Satoh, M., Ozaki, K., & Kubota, S. (2021). Loss of FYCO1 leads to cataract formation. *Scientific Reports*, *11*(1), 13771. https://doi.org/10.1038/s41598-021-93110-1

Sautin, Y. Y., & Johnson, R. J. (2008). Uric acid: The oxidant-antioxidant paradox. *Nucleosides, Nucleotides & Nucleic Acids*, *27*(6), 608–619. https://doi.org/10.1080/15257770802138558

Scarborough, G. A. (2002). Molecular mechanism of the P-type ATPases. *Journal of Bioenergetics and Biomembranes*, *34*(4), 235–250. https://doi.org/10.1023/a:1020211016696

Scavelli, K., Chatterjee, A., & Rhee, D. J. (2015). Secreted Protein Acidic and Rich in Cysteine in Ocular Tissue. *Journal of Ocular Pharmacology and Therapeutics: The Official Journal of the Association for Ocular Pharmacology and Therapeutics*, *31*(7), 396–405. https://doi.org/10.1089/jop.2015.0057

Schaefer, H., Marcus, K., Sickmann, A., Herrmann, M., Klose, J., & Meyer, HelmutE. (2003). Identification of phosphorylation and acetylation sites in alpha-A crystallin of the eye lens (mus musculus) after two-dimensional gel electrophoresis. *Analytical and Bioanalytical Chemistry*, *376*(7), 966–972. https://doi.org/10.1007/s00216-003-1983-1

Schey, K. L., Anderson, D. M., & Rose, K. L. (2013). Spatially-Directed Protein Identification from Tissue Sections by Top-Down LC-MS/MS with Electron Transfer Dissociation. *Analytical Chemistry*, *85*(14), 6767–6774. https://doi.org/10.1021/ac400832w

Schey, K. L., & Finley, E. L. (2000). Identification of Peptide Oxidation by Tandem Mass Spectrometry. *Accounts of Chemical Research*, *33*(5), 299–306. https://doi.org/10.1021/ar9800744

Schey, K. L., Gletten, R. B., O'Neale, C. V. T., Wang, Z., Petrova, R. S., & Donaldson, P. J. (2022). Lens Aquaporins in Health and Disease: Location is Everything! *Frontiers in Physiology*, *13*, 882550. https://doi.org/10.3389/fphys.2022.882550

Schey, K. L., Gutierrez, D. B., Wang, Z., Wei, J., & Grey, A. C. (2010). Novel Fatty Acid Acylation of Lens Integral Membrane Protein Aquaporin-0. *Biochemistry*, *49*(45), 9858–9865. https://doi.org/10.1021/bi101415w

Schey, K. L., Petrova, R. S., Gletten, R. B., & Donaldson, P. J. (2017). The Role of Aquaporins in Ocular Lens Homeostasis. *International Journal of Molecular Sciences*, *18*(12). https://doi.org/10.3390/ijms18122693

Schey, K. L., Wang, Z., Friedrich, M. G., Garland, D. L., & Truscott, R. J. W. (2020). Spatiotemporal changes in the human lens proteome: Critical insights into long-lived proteins. *Progress in Retinal and Eye Research*, *76*, 100802. https://doi.org/10.1016/j.preteyeres.2019.100802

Schmid, P. W. N., Lim, N. C. H., Peters, C., Back, K. C., Bourgeois, B., Pirolt, F., Richter, B., Peschek, J., Puk, O., Amarie, O. V., Dalke, C., Haslbeck, M., Weinkauf, S., Madl, T., Graw, J., & Buchner, J. (2021). Imbalances in the eye lens proteome are linked to cataract formation. *Nature Structural & Molecular Biology*, *28*(2), 143–151. https://doi.org/10.1038/s41594-020-00543-9

Searle, B. C., Pino, L. K., Egertson, J. D., Ting, Y. S., Lawrence, R. T., MacLean, B. X., Villén, J., & MacCoss, M. J. (2018). Chromatogram libraries improve peptide detection and quantification by data independent acquisition mass spectrometry. *Nature Communications*, *9*(1). https://doi.org/10.1038/s41467-018-07454-w

Searle, B. C., Swearingen, K. E., Barnes, C. A., Schmidt, T., Gessulat, S., Kuster, B., & Wilhelm, M. (2019). Generating high-quality libraries for DIA-MS with empirically-corrected peptide predictions. *BioRxiv*. https://doi.org/10.1101/682245

Searle, B. C., Swearingen, K. E., Barnes, C. A., Schmidt, T., Gessulat, S., Küster, B., & Wilhelm, M. (2020). Generating high quality libraries for DIA MS with empirically corrected peptide predictions. *Nature Communications*, *11*(1), 1548. https://doi.org/10.1038/s41467-020-15346-1

Segal, D., Ohana, E., Besser, L., Hershfinkel, M., Moran, A., & Sekler, I. (2004). A role for ZnT-1 in regulating cellular cation influx. *Biochemical and Biophysical Research Communications*, *323*(4), 1145–1150. https://doi.org/10.1016/j.bbrc.2004.08.211

Sen, P. C., Krebsbach, R. J., & Pfeiffer, D. R. (1986). Persistent stimulation of lens fiber cell Na,K-ATPase by sodium thiocyanate. *Experimental Eye Research*, *43*(3), 315–327. https://doi.org/10.1016/s0014-4835(86)80069-0

Serang, O., & Noble, W. (2012). A review of statistical methods for protein identification using tandem mass spectrometry. *Statistics and Its Interface*, *5*(1), 3–20. https://doi.org/10.4310/sii.2012.v5.n1.a2

Shahidullah, M., Mandal, A., & Delamere, N. A. (2012). TRPV4 in porcine lens epithelium regulates hemichannel-mediated ATP release and Na-K-ATPase activity. *American Journal of Physiology-Cell Physiology*, *302*(12). https://doi.org/10.1152/ajpcell.00010.2012

Shahidullah, M., Mandal, A., & Delamere, N. A. (2018). Activation of TRPV1 channels leads to stimulation of NKCC1 cotransport in the lens. *American Journal of Physiology. Cell Physiology*, *315*(6), C793–C802. https://doi.org/10.1152/ajpcell.00252.2018

Shestopalov, V. I., & Bassnett, S. (2000). Three-dimensional organization of primary lens fiber cells. *Investigative Ophthalmology & Visual Science*, *41*(3), 859–863.

Shi, Y., Barton, K., De Maria, A., Petrash, J. M., Shiels, A., & Bassnett, S. (2009). The stratified syncytium of the vertebrate lens. *Journal of Cell Science*, *122*(Pt 10), 1607–1615. https://doi.org/10.1242/jcs.045203

Shi, Y., De Maria, A. B., Wang, H., Mathias, R. T., FitzGerald, P. G., & Bassnett, S. (2011). Further analysis of the lens phenotype in Lim2-deficient mice. *Investigative Ophthalmology & Visual Science*, *52*(10), 7332–7339. https://doi.org/10.1167/iovs.11-7724

Shin, D.-M., Jeon, J.-H., Kim, C.-W., Cho, S.-Y., Kwon, J.-C., Lee, H.-J., Choi, K.-H., Park, S.-C., & Kim, I.-G. (2004). Cell Type-specific Activation of Intracellular Transglutaminase 2 by Oxidative Stress or Ultraviolet Irradiation. *Journal of Biological Chemistry*, *279*(15), 15032–15039. https://doi.org/10.1074/jbc.M308734200

Shridas, P., Sharma, Y., & Balasubramanian, D. (2001). Transglutaminase-mediated cross-linking of α-crystallin: Structural and functional consequences. *FEBS Letters*, *499*(3), 245–250. https://doi.org/10.1016/S0014-5793(01)02565-0

Sindhu Kumari, S., Gupta, N., Shiels, A., FitzGerald, P. G., Menon, A. G., Mathias, R. T., & Varadaraj, K. (2015). Role of Aquaporin 0 in lens biomechanics. *Biochemical and Biophysical Research Communications*, *462*(4), 339–345. https://doi.org/10.1016/j.bbrc.2015.04.138

Sindhu Kumari, S., & Varadaraj, K. (2013). Aquaporin 5 knockout mouse lens develops hyperglycemic cataract. *Biochemical and Biophysical Research Communications*, *441*(2), 333–338. https://doi.org/10.1016/j.bbrc.2013.10.058

Slavi, N., Wang, Z., Harvey, L., Schey, K. L., & Srinivas, M. (2016). Identification and Functional Assessment of Age-Dependent Truncations to Cx46 and Cx50 in the Human Lens. *Investigative Opthalmology & Visual Science*, *57*(13), 5714. https://doi.org/10.1167/iovs.16-19698

Slingsby, C., & Clout, N. J. (1999). Structure of the crystallins. *Eye (London, England)*, *13 (Pt 3b)*, 395–402. https://doi.org/10.1038/eye.1999.113

Slingsby, C., & Wistow, G. J. (2014). Functions of crystallins in and out of lens: Roles in elongated and post-mitotic cells. *Progress in Biophysics and Molecular Biology*, *115*(1), 52–67. https://doi.org/10.1016/j.pbiomolbio.2014.02.006

Slingsby, C., Wistow, G. J., & Clark, A. R. (2013). Evolution of crystallins for a role in the vertebrate eye lens. *Protein Science: A Publication of the Protein Society*, *22*(4), 367–380. https://doi.org/10.1002/pro.2229

Smith, B., Varadaraj, R., Krushinski, A., Donaldson, P., Mathias, R., & Kistler, J. (2002). Glucose Transport In the Lens. *Investigative Ophthalmology & Visual Science*, *43*(13), 4646–4646.

Specht, H., Emmott, E., Petelski, A., Huffman, R. G., Perlman, D. H., Serra, M., Kharchenko, P., Koller, A., & Slavov, N. (2019). Single-cell mass-spectrometry quantifies the emergence of macrophage heterogeneity. *BioRxiv*. https://doi.org/10.1101/665307

Srivastava, O. P., McEntire, J. E., & Srivastava, K. (1992). Identification of a 9 kDa γ-crystallin fragment in human lenses. *Experimental Eye Research*, *54*(6), 893–901. https://doi.org/10.1016/0014-4835(92)90153-J

Srivastava, O. P., & Srivastava, K. (2003). BB2-crystallin undergoes extensive truncation during aging in human lenses. *Biochemical and Biophysical Research Communications*, *301*(1), 44–49. https://doi.org/10.1016/S0006-291X(02)02975-3

Stahl, E., Buhl, R., Schnaudigel, O., Steinkamp, G., Fries, U., Gümbel, H., & Ohrloff, C. (1996). [Regulation of glutathione level in venous plasma and aqueous humor in cataracta senilis provecta]. *Der Ophthalmologe: Zeitschrift Der Deutschen Ophthalmologischen Gesellschaft*, *93*(1), 54–58.

Straub, B. K., Boda, J., Kuhn, C., Schnoelzer, M., Korf, U., Kempf, T., Spring, H., Hatzfeld, M., & Franke, W. W. (2003). A novel cell-cell junction system: The cortex adhaerens mosaic of lens fiber cells. *Journal of Cell Science*, *116*(Pt 24), 4985–4995. https://doi.org/10.1242/jcs.00815

Subramanian, A., Tamayo, P., Mootha, V. K., Mukherjee, S., Ebert, B. L., Gillette, M. A., Paulovich, A., Pomeroy, S. L., Golub, T. R., Lander, E. S., & Mesirov, J. P. (2005). Gene set enrichment analysis: A knowledge-based approach for interpreting genome-wide expression profiles. *Proceedings of the National Academy of Sciences*, *102*(43), 15545–15550. https://doi.org/10.1073/pnas.0506580102

Swarup, A., Bell, B. A., Du, J., Han, J. Y. S., Soto, J., Abel, E. D., Bravo-Nuevo, A., FitzGerald, P. G., Peachey, N. S., & Philp, N. J. (2018). Deletion of GLUT1 in mouse lens epithelium leads to cataract formation. *Experimental Eye Research*, *172*, 45–53. https://doi.org/10.1016/j.exer.2018.03.021

Swearingen, K. E., & Moritz, R. L. (2012). High-field asymmetric waveform ion mobility spectrometry for mass spectrometry-based proteomics. *Expert Review of Proteomics*, *9*(5), 505–517. https://doi.org/10.1586/epr.12.50

Sweeney, M. H., & Truscott, R. J. (1998). An impediment to glutathione diffusion in older normal human lenses: A possible precondition for nuclear cataract. *Experimental Eye Research*, *67*(5), 587–595. https://doi.org/10.1006/exer.1998.0549

Takemoto, L. (1996). Increase in the Intramolecular Disulfide Bonding of Alpha-A Crystallin During Aging of the Human Lens. *Experimental Eye Research*, *63*(5), 585–590. https://doi.org/10.1006/exer.1996.0149

Takemoto, L. J. (1995). Identification of the *in vivo* truncation sites at the C-terminal region of alpha-A crystallin from aged bovine and human lens. *Current Eye Research*, *14*(9), 837–841. https://doi.org/10.3109/02713689508995806

Tamiya, S., Dean, W. L., Paterson, C. A., & Delamere, N. A. (2003). Regional Distribution of Na,K-ATPase Activity in Porcine Lens Epithelium. *Investigative Opthalmology & Visual Science*, *44*(10), 4395. https://doi.org/10.1167/iovs.03-0287

Tang, D., Borchman, D., Yappert, M. C., Vrensen, G. F. J. M., & Rasi, V. (2003). Influence of Age, Diabetes, and Cataract on Calcium, Lipid-Calcium, and Protein-Calcium Relationships in Human Lenses. *Investigative Opthalmology & Visual Science*, *44*(5), 2059. https://doi.org/10.1167/iovs.02-0345

Tanimura, S., & Takeda, K. (2017). ERK signalling as a regulator of cell motility. *The Journal of Biochemistry*, *162*(3), 145–154. https://doi.org/10.1093/jb/mvx048

Tao, Y., & Julian, R. R. (2014). Identification of Amino Acid Epimerization and Isomerization in Crystallin Proteins by Tandem LC-MS. *Analytical Chemistry*, *86*(19), 9733–9741. https://doi.org/10.1021/ac502296c

Tao, Y., Quebbemann, N. R., & Julian, R. R. (2012). Discriminating D -Amino Acid-Containing Peptide Epimers by Radical-Directed Dissociation Mass Spectrometry. *Analytical Chemistry*, *84*(15), 6814–6820. https://doi.org/10.1021/ac3013434

Taverner, T., Hall, N. E., O'Hair, R. A. J., & Simpson, R. J. (2002). Characterization of an Antagonist Interleukin-6 Dimer by Stable Isotope Labeling, Cross-linking, and Mass Spectrometry. *Journal of Biological Chemistry*, *277*(48), 46487–46492. https://doi.org/10.1074/jbc.M207370200

Taylor, A. (1992). Role of Nutrients in Delaying Cataracts. *Annals of the New York Academy of Sciences*, *669*(1), 111–123. https://doi.org/10.1111/j.1749-6632.1992.tb17093.x

Taylor, V. L., al-Ghoul, K. J., Lane, C. W., Davis, V. A., Kuszak, J. R., & Costello, M. J. (1996). Morphology of the normal human lens. *Investigative Ophthalmology & Visual Science*, *37*(7), 1396–1410.

Teo, G. C., Polasky, D. A., Yu, F., & Nesvizhskii, A. I. (2021). Fast Deisotoping Algorithm and Its Implementation in the MSFragger Search Engine. *Journal of Proteome Research*, *20*(1), 498–505. https://doi.org/10.1021/acs.jproteome.0c00544

The, M., MacCoss, M. J., Noble, W. S., & Käll, L. (2016). Fast and Accurate Protein False Discovery Rates on Large-Scale Proteomics Data Sets with Percolator 3.0. *Journal of the American Society for Mass Spectrometry*, *27*(11), 1719–1727. https://doi.org/10.1007/s13361-016-1460-7

Thinon, E., Serwa, R. A., Broncel, M., Brannigan, J. A., Brassat, U., Wright, M. H., Heal, W. P., Wilkinson, A. J., Mann, D. J., & Tate, E. W. (2014). Global profiling of co- and post-translationally N-myristoylated proteomes in human cells. *Nature Communications*, *5*, 4919. https://doi.org/10.1038/ncomms5919

Thomas, P. D. (2003). PANTHER: A Library of Protein Families and Subfamilies Indexed by Function. *Genome Research*, *13*(9), 2129–2141. https://doi.org/10.1101/gr.772403

Thornell, E., & Aquilina, A. (2015). Regulation of αA- and αB-crystallins via phosphorylation in cellular homeostasis. *Cellular and Molecular Life Sciences*, *72*(21), 4127–4137. https://doi.org/10.1007/s00018-015-1996-x

Timmons, J. A., Szkop, K. J., & Gallagher, I. J. (2015). Multiple sources of bias confound functional enrichment analysis of global -omics data. *Genome Biology*, *16*(1). https://doi.org/10.1186/s13059-015-0761-7

Ting, Y. S., Egertson, J. D., Bollinger, J. G., Searle, B. C., Payne, S. H., Noble, W. S., & MacCoss, M. J. (2017). PECAN: Library-free peptide detection for data-independent acquisition tandem mass spectrometry data. *Nature Methods*, *14*(9), 903–908. https://doi.org/10.1038/nmeth.4390

Tong, J., Canty, J. T., Briggs, M. M., & McIntosh, T. J. (2013). The water permeability of lens aquaporin-0 depends on its lipid bilayer environment. *Experimental Eye Research*, *113*, 32–40. https://doi.org/10.1016/j.exer.2013.04.022

Trudgian, D. C., Fischer, R., Guo, X., Kessler, B. M., & Mirzaei, H. (2014). GOAT - A simple LC-MS/MS gradient optimization tool. *PROTEOMICS*, *14*(12), 1467–1471. https://doi.org/10.1002/pmic.201300524

Truscott, R. J. W. (2005). Age-related nuclear cataract—Oxidation is the key. *Experimental Eye Research*, *80*(5), 709–725. https://doi.org/10.1016/j.exer.2004.12.007

Truscott, R. J. W., Comte-Walters, S., Ablonczy, Z., Schwacke, J. H., Berry, Y., Korlimbinis, A., Friedrich, M. G., & Schey, K. L. (2011). Tight binding of proteins to membranes from older human cells. *AGE*, *33*(4), 543–554. https://doi.org/10.1007/s11357-010-9198-9

Truscott, R. J. W., & Friedrich, M. G. (2019). Molecular Processes Implicated in Human Age-Related Nuclear Cataract. *Investigative Opthalmology & Visual Science*, *60*(15), 5007. https://doi.org/10.1167/iovs.19-27535

Truscott, R. J. W., Mizdrak, J., Friedrich, M. G., Hooi, M. Y., Lyons, B., Jamie, J. F., Davies, M. J., Wilmarth, P. A., & David, L. L. (2012). Is protein methylation in the human lens a result of non-enzymatic methylation by S-adenosylmethionine? *Experimental Eye Research*, *99*, 48–54. https://doi.org/10.1016/j.exer.2012.04.002

Truscott, R. J. W., Schey, K. L., & Friedrich, M. G. (2016). Old Proteins in Man: A Field in its Infancy. *Trends in Biochemical Sciences*, *41*(8), 654–664. https://doi.org/10.1016/j.tibs.2016.06.004

Tsai, C.-F., Zhao, R., Williams, S. M., Moore, R. J., Schultz, K., Chrisler, W. B., Pasa-Tolic, L., Rodland, K. D., Smith, R. D., Shi, T., Zhu, Y., & Liu, T. (2020). An Improved Boosting to Amplify Signal with Isobaric Labeling (iBASIL) Strategy for Precise Quantitative Single-cell Proteomics. *Molecular & Cellular Proteomics: MCP*, *19*(5), 828–838. https://doi.org/10.1074/mcp.RA119.001857

Tsou, C.-C., Avtonomov, D., Larsen, B., Tucholska, M., Choi, H., Gingras, A.-C., & Nesvizhskii, A. I. (2015). DIA-Umpire: Comprehensive computational framework for data-independent acquisition proteomics. *Nature Methods*, *12*(3), 258–264, 7 p following 264. https://doi.org/10.1038/nmeth.3255

Turner, C. E., Glenney, J. R., & Burridge, K. (1990). Paxillin: A new vinculin-binding protein present in focal adhesions. *The Journal of Cell Biology*, *111*(3), 1059–1068. https://doi.org/10.1083/jcb.111.3.1059

Ubaida-Mohien, C., Lyashkov, A., Gonzalez-Freire, M., Tharakan, R., Shardell, M., Moaddel, R., Semba, R. D., Chia, C. W., Gorospe, M., Sen, R., & Ferrucci, L. (2019). Discovery proteomics in aging human skeletal muscle finds change in spliceosome, immunity, proteostasis and mitochondria. *ELife*, *8*. https://doi.org/10.7554/eLife.49874

Ueda, Y., Duncan, M. K., & David, L. L. (2002). Lens proteomics: The accumulation of crystallin modifications in the mouse lens with age. *Investigative Ophthalmology & Visual Science*, *43*(1), 205–215.

Umapathy, A., Donaldson, P., & Lim, J. (2013). Antioxidant Delivery Pathways in the Anterior Eye. *BioMed Research International*, *2013*, 1–10. https://doi.org/10.1155/2013/207250

Vaghefi, E., & Donaldson, P. J. (2018). The lens internal microcirculation system delivers solutes to the lens core faster than would be predicted by passive diffusion. *American Journal of Physiology-Regulatory, Integrative and Comparative Physiology*, *315*(5), R994–R1002. https://doi.org/10.1152/ajpregu.00180.2018

Vaghefi, E., Kim, A., & Donaldson, P. J. (2015). Active Maintenance of the Gradient of Refractive Index Is Required to Sustain the Optical Properties of the Lens. *Investigative Opthalmology & Visual Science*, *56*(12), 7195. https://doi.org/10.1167/iovs.15-17861

Vaghefi, E., Pontre, B. P., Jacobs, M. D., & Donaldson, P. J. (2011). Visualizing ocular lens fluid dynamics using MRI: Manipulation of steady state water content and water fluxes. *American Journal of Physiology-Regulatory, Integrative and Comparative Physiology*, *301*(2), R335–R342. https://doi.org/10.1152/ajpregu.00173.2011

Vaghefi, E., Walker, K., Pontre, B. P., Jacobs, M. D., & Donaldson, P. J. (2012). Magnetic resonance and confocal imaging of solute penetration into the lens reveals a zone of restricted extracellular space diffusion. *American Journal of Physiology-Regulatory, Integrative and Comparative Physiology*, *302*(11), R1250–R1259. https://doi.org/10.1152/ajpregu.00611.2011

Valiunas, V., & White, T. W. (2020). Connexin43 and connexin50 channels exhibit different permeability to the second messenger inositol triphosphate. *Scientific Reports*, *10*(1), 8744. https://doi.org/10.1038/s41598-020-65761-z

van Rheede, T. (2003). Lactate Dehydrogenase A as a Highly Abundant Eye Lens Protein in Platypus (Ornithorhynchus anatinus): Upsilon (upsilon)-Crystallin. *Molecular Biology and Evolution*, *20*(6), 994–998. https://doi.org/10.1093/molbev/msg116

Varadaraj, K., Kumari, S. S., & Mathias, R. T. (2007). Functional expression of aquaporins in embryonic, postnatal, and adult mouse lenses. *Developmental Dynamics: An Official Publication of the American Association of Anatomists*, *236*(5), 1319–1328. https://doi.org/10.1002/dvdy.21125

Varadaraj, K., Kumari, S. S., & Mathias, R. T. (2010). Transgenic expression of AQP1 in the fiber cells of AQP0 knockout mouse: Effects on lens transparency. *Experimental Eye Research*, *91*(3), 393–404. https://doi.org/10.1016/j.exer.2010.06.013

Varadaraj, K., Kumari, S., Shiels, A., & Mathias, R. T. (2005). Regulation of Aquaporin Water Permeability in the Lens. *Investigative Opthalmology & Visual Science*, *46*(4), 1393. https://doi.org/10.1167/iovs.04-1217

Varadaraj, K., Kushmerick, C., Baldo, G. J., Bassnett, S., Shiels, A., & Mathias, R. T. (1999). The Role of MIP in Lens Fiber Cell Membrane Transport. *Journal of Membrane Biology*, *170*(3), 191–203. https://doi.org/10.1007/s002329900549

Venable, J. D., Dong, M.-Q., Wohlschlegel, J., Dillin, A., & Yates, J. R. (2004). Automated approach for quantitative analysis of complex peptide mixtures from tandem mass spectra. *Nature Methods*, *1*(1), 39–45. https://doi.org/10.1038/nmeth705

Verrastro, I., Pasha, S., Jensen, K. T., Pitt, A. R., & Spickett, C. M. (2015). Mass spectrometry-based methods for identifying oxidized proteins in disease: Advances and challenges. *Biomolecules*, *5*(2), 378–411. https://doi.org/10.3390/biom5020378

Vetter, C. J., Thorn, D. C., Wheeler, S. G., Mundorff, C. C., Halverson, K. A., Wales, T. E., Shinde, U. P., Engen, J. R., David, L. L., Carver, J. A., & Lampi, K. J. (2020). Cumulative deamidations of the major lens protein ΓS -crystallin increase its aggregation during unfolding and oxidation. *Protein Science*, *29*(9), 1945–1963. https://doi.org/10.1002/pro.3915

von Mering, C., Huynen, M., Jaeggi, D., Schmidt, S., Bork, P., & Snel, B. (2003). STRING: A database of predicted functional associations between proteins. *Nucleic Acids Research*, *31*(1), 258–261. https://doi.org/10.1093/nar/gkg034

Walker, J., & Menko, A. S. (2009). Integrins in lens development and disease. *Experimental Eye Research*, *88*(2), 216–225. https://doi.org/10.1016/j.exer.2008.06.020

Wang, B., Hom, G., Zhou, S., Guo, M., Li, B., Yang, J., Monnier, V. M., & Fan, X. (2017). The oxidized thiol proteome in aging and cataractous mouse and human lens revealed by ICAT labeling. *Aging Cell*, *16*(2), 244–261. https://doi.org/10.1111/acel.12548

Wang, K., Ma, W., & Spector, A. (1995). Phosphorylation of alpha-crystallin in rat lenses is stimulated by H2O2 but phosphorylation has no effect on chaperone activity. *Experimental Eye Research*, *61*(1), 115–124. https://doi.org/10.1016/s0014-4835(95)80065-4

Wang, S., Yu, M., Yan, H., Liu, J., & Guo, C. (2022). MiR-34a-5p Negatively Regulates Oxidative Stress on Lens Epithelial Cells by Silencing GPX3 – A Novel Target. *Current Eye Research*, *47*(5), 727–734. https://doi.org/10.1080/02713683.2022.2029905

Wang, W.-L., Li, Q., Xu, J., & Cvekl, A. (2010). Lens fiber cell differentiation and denucleation are disrupted through expression of the N-terminal nuclear receptor box of NCOA6 and result in p53-dependent and p53-independent apoptosis. *Molecular Biology of the Cell*, *21*(14), 2453–2468. https://doi.org/10.1091/mbc.e09-12-1031

Wang, Z., Cantrell, L. S., & Schey, K. L. (2021). Spatially Resolved Proteomic Analysis of the Lens Extracellular Diffusion Barrier. *Investigative Ophthalmology & Visual Science*, *62*(12), 25. https://doi.org/10.1167/iovs.62.12.25

Wang, Z., Friedrich, M. G., Truscott, R. J. W., & Schey, K. L. (2019). Cleavage C-terminal to Asp leads to covalent crosslinking of long-lived human proteins. *Biochimica et Biophysica Acta (BBA) - Proteins and Proteomics*, *1867*(9), 831–839. https://doi.org/10.1016/j.bbapap.2019.06.009

Wang, Z., Han, J., David, L. L., & Schey, K. L. (2013). Proteomics and Phosphoproteomics Analysis of Human Lens Fiber Cell Membranes. *Investigative Opthalmology & Visual Science*, *54*(2), 1135. https://doi.org/10.1167/iovs.12-11168

Wang, Z., Han, J., & Schey, K. L. (2008). Spatial Differences in an Integral Membrane Proteome Detected in Laser Capture Microdissected Samples. *Journal of Proteome Research*, *7*(7), 2696–2702. https://doi.org/10.1021/pr700737h

Wang, Z., Lyons, B., Truscott, R. J. W., & Schey, K. L. (2014). Human protein aging: Modification and crosslinking through dehydroalanine and dehydrobutyrine intermediates. *Aging Cell*, *13*(2), 226–234. https://doi.org/10.1111/acel.12164

Wang, Z., Obidike, J. E., & Schey, K. L. (2010). Posttranslational Modifications of the Bovine Lens Beaded Filament Proteins Filensin and CP49. *Investigative Opthalmology & Visual Science*, *51*(3), 1565. https://doi.org/10.1167/iovs.09-4565

Wang, Z., Ryan, D. J., & Schey, K. L. (2020). Localization of the lens intermediate filament switch by imaging mass spectrometry. *Experimental Eye Research*, *198*, 108134. https://doi.org/10.1016/j.exer.2020.108134

Wang, Z., & Schey, K. L. (2018). Proteomic Analysis of S-Palmitoylated Proteins in Ocular Lens Reveals Palmitoylation of AQP5 and MP20. *Investigative Opthalmology & Visual Science*, *59*(13), 5648. https://doi.org/10.1167/iovs.18-25312

Wang, Z., & Schey, K. L. (2021). *Spatially-Resolved Proteomic Analysis of the Lens Extracellular Diffusion Barrier* [Preprint]. Biochemistry. https://doi.org/10.1101/2021.02.23.432581

Watanabe, M., Kobayashi, H., Rutishauser, U., Katar, M., Alcala, J., & Maisel, H. (1989). NCAM in the differentiation of embryonic lens tissue. *Developmental Biology*, *135*(2), 414–423. https://doi.org/10.1016/0012-1606(89)90190-5

Webb, K. F., Merriman-Smith, B. R., Stobie, J. K., Kistler, J., & Donaldson, P. J. (2004). Cl $^-$ Influx into Rat Cortical Lens Fiber Cells Is Mediated by a Cl $^-$ Conductance That Is Not ClC-2 or -3. *Investigative Opthalmology & Visual Science*, *45*(12), 4400. https://doi.org/10.1167/iovs.04-0205

Wei, M., Xing, K.-Y., Fan, Y.-C., Libondi, T., & Lou, M. F. (2015). Loss of Thiol Repair Systems in Human Cataractous Lenses. *Investigative Ophthalmology & Visual Science*, *56*(1), 598–605. https://doi.org/10.1167/iovs.14-15452

Wenke, J. L., McDonald, W. H., & Schey, K. L. (2016). Spatially Directed Proteomics of the Human Lens Outer Cortex Reveals an Intermediate Filament Switch Associated With the Remodeling Zone. *Investigative Ophthalmology & Visual Science*, *57*(10), 4108–4114. https://doi.org/10.1167/iovs.16-19791

Wenke, J. L., Rose, K. L., Spraggins, J. M., & Schey, K. L. (2015). MALDI Imaging Mass Spectrometry Spatially Maps Age-Related Deamidation and Truncation of Human Lens Aquaporin-0. *Investigative Ophthalmology & Visual Science*, *56*(12), 7398–7405. https://doi.org/10.1167/iovs.15-18117

Whitson, J. A., Sell, D. R., Goodman, M. C., Monnier, V. M., & Fan, X. (2016). Evidence of Dual Mechanisms of Glutathione Uptake in the Rodent Lens: A Novel Role for Vitreous Humor in Lens Glutathione Homeostasis. *Investigative Ophthalmology & Visual Science*, *57*(8), 3914–3925. https://doi.org/10.1167/iovs.16-19592

Wilmarth, P. A., Tanner, S., Dasari, S., Nagalla, S. R., Riviere, M. A., Bafna, V., Pevzner, P. A., & David, L. L. (2006). Age-Related Changes in Human Crystallins Determined from Comparative Analysis of Post-translational Modifications in Young and Aged Lens: Does Deamidation Contribute to Crystallin Insolubility? *Journal of Proteome Research*, *5*(10), 2554–2566. https://doi.org/10.1021/pr050473a

Wood, T. E., Dalili, S., Simpson, C. D., Hurren, R., Mao, X., Saiz, F. S., Gronda, M., Eberhard, Y., Minden, M. D., Bilan, P. J., Klip, A., Batey, R. A., & Schimmer, A. D. (2008). A novel inhibitor of glucose uptake sensitizes cells to FAS-induced cell death. *Molecular Cancer Therapeutics*, *7*(11), 3546–3555. https://doi.org/10.1158/1535-7163.MCT-08-0569

Wride, M. A. (2011). Lens fibre cell differentiation and organelle loss: Many paths lead to clarity. *Philosophical Transactions of the Royal Society of London. Series B, Biological Sciences*, *366*(1568), 1219–1233. https://doi.org/10.1098/rstb.2010.0324

Wu, H., Lin, L., Giblin, F., Ho, Y.-S., & Lou, M. F. (2011). Glutaredoxin 2 knockout increases sensitivity to oxidative stress in mouse lens epithelial cells. *Free Radical Biology & Medicine*, *51*(11), 2108–2117. https://doi.org/10.1016/j.freeradbiomed.2011.09.011

Wu, S.-Y., Zou, P., Fuller, A. W., Mishra, S., Wang, Z., Schey, K. L., & Mchaourab, H. S. (2016). Expression of Cataract-linked γ-Crystallin Variants in Zebrafish Reveals a Proteostasis Network That Senses Protein Stability. *The Journal of Biological Chemistry*, *291*(49), 25387–25397. https://doi.org/10.1074/jbc.M116.749606

Wu, X., Liu, Z., Zhang, X., Wang, D., Long, E., Wang, J., Li, W., Lai, W., Cao, Q., Hu, K., Chen, W., Lin, H., & Liu, Y. (2017a). Proteomics analysis and proteogenomic characterization of different physiopathological human lenses. *BMC Ophthalmology*, *17*(1). https://doi.org/10.1186/s12886-017-0642-9

Wu, X., Liu, Z., Zhang, X., Wang, D., Long, E., Wang, J., Li, W., Lai, W., Cao, Q., Hu, K., Chen, W., Lin, H., & Liu, Y. (2017b). Proteomics analysis and proteogenomic characterization of different physiopathological human lenses. *BMC Ophthalmology*, *17*(1), 253. https://doi.org/catara

Yang, B., & Verkman, A. S. (1997). Water and glycerol permeabilities of aquaporins 1-5 and MIP determined quantitatively by expression of epitope-tagged constructs in Xenopus oocytes. *The Journal of Biological Chemistry*, *272*(26), 16140–16146. https://doi.org/10.1074/jbc.272.26.16140

Yang, B., Wu, Y.-J., Zhu, M., Fan, S.-B., Lin, J., Zhang, K., Li, S., Chi, H., Li, Y.-X., Chen, H.-F., Luo, S.-K., Ding, Y.-H., Wang, L.-H., Hao, Z., Xiu, L.-Y., Chen, S., Ye, K., He, S.-M., & Dong, M.-Q. (2012). Identification of cross-linked peptides from complex samples. *Nature Methods*, *9*(9), 904–906. https://doi.org/10.1038/nmeth.2099

Yang, F., Kawedia, J. D., & Menon, A. G. (2003). Cyclic AMP regulates aquaporin 5 expression at both transcriptional and post-transcriptional levels through a protein kinase A pathway. *The Journal of Biological Chemistry*, *278*(34), 32173–32180. https://doi.org/10.1074/jbc.M305149200

Yasunaga, G., Pastene, L. A., Bando, T., Hakamada, T., & Fujise, Y. (2017). Age estimation of Antarctic minke whales Balaenoptera bonaerensis based on aspartic acid racemization technique. *Fisheries Science*, *83*(6), 947–954. https://doi.org/10.1007/s12562-017-1122-0

Yonova-Doing, E., Forkin, Z. A., Hysi, P. G., Williams, K. M., Spector, T. D., Gilbert, C. E., & Hammond, C. J. (2016). Genetic and Dietary Factors Influencing the Progression of Nuclear Cataract. *Ophthalmology*, *123*(6), 1237–1244. https://doi.org/10.1016/j.ophtha.2016.01.036

Young, M. A., Tunstall, M. J., Kistler, J., & Donaldson, P. J. (2000). Blocking chloride channels in the rat lens: Localized changes in tissue hydration support the existence of a circulating chloride flux. *Investigative Ophthalmology & Visual Science*, *41*(10), 3049–3055.

Yu, N. T., DeNagel, D. C., Pruett, P. L., & Kuck, J. F. (1985). Disulfide bond formation in the eye lens. *Proceedings of the National Academy of Sciences*, *82*(23), 7965–7968. https://doi.org/10.1073/pnas.82.23.7965

Zahraei, A., Guo, G., Perwick, R. D., Donaldson, P. J., Demarais, N. J., & Grey, A. C. (2021). Mapping glucose metabolites in the normal bovine lens: Evaluation and optimisation of a matrix-assisted laser desorption/ionisation imaging mass spectrometry method. *Journal of Mass Spectrometry*, *56*(4). https://doi.org/10.1002/jms.4666

Zahraei, A., Guo, G., Varnava, K. G., Demarais, N. J., Donaldson, P. J., & Grey, A. C. (2022). Mapping Glucose Uptake, Transport and Metabolism in the Bovine Lens Cortex. *Frontiers in Physiology*, *13*, 901407. https://doi.org/10.3389/fphys.2022.901407

Zavalin, A., Yang, J., Haase, A., Holle, A., & Caprioli, R. (2014). Implementation of a Gaussian beam laser and aspheric optics for high spatial resolution MALDI imaging MS. *Journal of the American Society for Mass Spectrometry*, *25*(6), 1079–1082. https://doi.org/10.1007/s13361-014-0872-5

Zhang, F., Ge, W., Ruan, G., Cai, X., & Guo, T. (2020). Data-Independent Acquisition Mass Spectrometry-Based Proteomics and Software Tools: A Glimpse in 2020. *PROTEOMICS*, *20*(17–18), 1900276. https://doi.org/10.1002/pmic.201900276

Zhang, Y., Bilbao, A., Bruderer, T., Luban, J., Strambio-De-Castillia, C., Lisacek, F., Hopfgartner, G., & Varesio, E. (2015). The Use of Variable Q1 Isolation Windows Improves Selectivity in LC–SWATH–MS Acquisition. *Journal of Proteome Research*, *14*(10), 4359–4371. https://doi.org/10.1021/acs.jproteome.5b00543

Zhao, H., Brown, P. H., Magone, M. T., & Schuck, P. (2011). The molecular refractive function of lens γ-Crystallins. *Journal of Molecular Biology*, *411*(3), 680–699. https://doi.org/10.1016/j.jmb.2011.06.007

Zhao, S., Li, C.-I., Guo, Y., Sheng, Q., & Shyr, Y. (2018). RnaSeqSampleSize: Real data based sample size estimation for RNA sequencing. *BMC Bioinformatics*, *19*(1), 191. https://doi.org/10.1186/s12859-018-2191-5

Zhao, Y., Wilmarth, P. A., Cheng, C., Limi, S., Fowler, V. M., Zheng, D., David, L. L., & Cvekl, A. (2019). Proteome-transcriptome analysis and proteome remodeling in mouse lens epithelium and fibers. *Experimental Eye Research*, *179*, 32–46. https://doi.org/10.1016/j.exer.2018.10.011

Zheng, X., Deng, L., Baker, E. S., Ibrahim, Y. M., Petyuk, V. A., & Smith, R. D. (2017). Distinguishing d- and l-aspartic and isoaspartic acids in amyloid β peptides with ultrahigh resolution ion mobility spectrometry.

Chemical Communications (Cambridge, England), *53*(56), 7913–7916. https://doi.org/10.1039/c7cc03321d

Zhu, Y., Piehowski, P. D., Zhao, R., Chen, J., Shen, Y., Moore, R. J., Shukla, A. K., Petyuk, V. A., Campbell-Thompson, M., Mathews, C. E., Smith, R. D., Qian, W.-J., & Kelly, R. T. (2018). Nanodroplet processing platform for deep and quantitative proteome profiling of 10–100 mammalian cells. *Nature Communications*, *9*(1). https://doi.org/10.1038/s41467-018-03367-w

Zilg, B., Alkass, K., Berg, S., & Druid, H. (2009). Postmortem identification of hyperglycemia. *Forensic Science International*, *185*(1–3), 89–95. https://doi.org/10.1016/j.forsciint.2008.12.017